# The role of the Sigma1 receptor (σ1R) in Store-operated calcium entry (SOCE) microdomains

Petra Visic

A thesis submitted to the University of Sussex for the degree of

Doctor of Philosophy

University of Sussex

September 2019

I hereby declare that this thesis has not been and will not be, submitted in whole or in part to another University for the award of any other degree.

Signature:_____

**Abstract**

The Sigma1 receptor (σ1R) is an endoplasmic reticulum (ER) chaperone targeted to mitochondrion associated ER membranes (MAMs). The upregulation of σ1R is associated with various cancers, whereas the decreased expression and mutant forms of σ1R are associated with neurodegenerative disorders. The underlying cellular mechanism by which σ1R exerts such a versatile impact remains elusive. At MAMs, σ1R is reported to regulate inter-organelle $Ca^{2+}$ levels. Following translocation to ER-plasma membrane junctions, σ1R is reported to interact with various ion channels, including the key regulators of store-operated $Ca^{2+}$ entry (SOCE).

I have investigated the role of σ1R in the regulation of SOCE within a population of cells and within the SOCE microdomains of single cells. In a population of cells, overexpression of σ1R profoundly inhibited both $Ca^{2+}$ store content and SOCE. Although these measurements of global $[Ca^{2+}]_{cyt}$ provide essential information about the functional role of σ1R in the regulation of SOCE, they do not provide detailed information about the effects of σ1R on temporal and spatial aspects of SOCE within the microdomain of the ER-plasma membrane junction. Recently developed, the G-GECO1.2-Orai1 construct encodes for a fully functional Orai1 protein with a genetically encoded fluorescent $Ca^{2+}$ reporter protein. The Orai1 channel is a key regulator of SOCE. GECO1.2-Orai1 allows for the monitoring of Orai1 channel activity in SOCE microdomains. Within the SOCE microdomains, overexpression of σ1R reduced the frequency of highly-activated G-GECO1.2-Orai1 clusters, which resulted in cumulatively low SOCE. Overexpression of $σ1R^{E102Q}$, an

ALS-causing mutant, failed to inhibit SOCE. *In situ*, σ1R was shown to interact with another key regulator of SOCE, STIM1 and its less-studied homolog STIM2. Overexpression of σ1R resulted in the inhibition of STIM2.2-mediated SOCE triggered by the ER $Ca^{2+}$ store depletion. σ1R failed to inhibit STIM2.2-mediated SOCE during basal conditions, suggesting that regulation of SOCE by σ1R requires a greater drop in ER [$Ca^{2+}$] than occurs under basal conditions.

**Acknowledgements**

I would like to express my gratitude to Dr. Ruth Murrell-Lagnado for providing me with an opportunity to be a part of her research group. During my doctoral training, Ruth encouraged me to challenge scientific hypothesis and data with confidence, helping me to grow and develop as a scientist. I am also immensely grateful to the past members of the lab, specifically Dr. Stephanie Chadet for her unconditional support in research and at the personal front during the initial two years of my PhD training.

I would like to thank members of my thesis committee, Dr. Erika Mancini, Professor Martin Gosling, and Dr. Andrew Penn for their time and guidance throughout this project. I am sincerely thankful for every “half-an-hour” meeting that slipped into two hours of constructive discussions, suggestions, and invaluable insights into the experimental design and analysis. All of them were also remarkably kind in providing access to valuable lab resources that helped in the successful completion of my PhD project.

I would also like to thank Professor Leon Lagnado and acknowledge his team, specifically Sofie Seibel for helping me with essential molecular biology tools and resources, Dr Chen Qian for building TIRF microscope and re-building it every once in a while, after my experiments, Kate Hampden-Smith for organizing cell culture facilities, Dr. Tristan Heintz and Dr. Paul Pitchler for their tips in data analysis.

Special thanks to Sussex Drug Discovery Centre and their extraordinary team who provided training in Flexstation III, as well as facilities and resources for calcium

assays. I am incredibly thankful to Dr. Anthony Oliver and his research team, and Dr. Lihong Zhou from Genome Damage and Stability Centre who helped in the development of baculovirus. Also, I would like to thank Professor Guy Richardson and his research team for sharing their cell culture facilities with me.

At the personal front, big hooray to my everyday support system, the source of motivation, and the waffle-masters Marwa Elmasri and Sofie Seibel. Thank you for listening, for laughing with me, and for being there.

Furthermore, I extend my sincere, immense gratitude to my parents Petar and Marija, who have always put their children first providing me with the resources and freedom to chase my dreams. Special thanks to my little brother Luka, who would complain if I left him out. I would also like to thank all members of Višić and Jozić families, as well as friends, former supervisors, mentors, and colleagues for their unconditional support, patience, and understanding.

**Dedication**

*For my father, who taught me laughter.*

*For my mother, who taught me faith.*

## Abbreviations

| | |
|---|---|
| ALS | amyotrophic lateral sclerosis (ALS) |
| AMPAR | α-amino-3-hydroxy-5-methyl-4-isoxazole propionic acid receptor |
| ANOVA | analysis of variance |
| ATP | adenosine triphosphate |
| AUC | area under curve |
| BiP | binding immunoglobulin protein |
| $Ca^{2+}$ | calcium |
| $[Ca^{2+}]_{cyt}$ | cytosolic $Ca^{2+}$ concentration |
| CAD | channel-activating domain |
| CDI | $Ca^{2+}$-dependent inactivation |
| CNS | central nervous system |
| CPA | cyclopiazonic acid |
| CRAC | calcium release activated channel |
| ER | endoplasmic reticulum |
| F | fluorescence |
| $F_{MAX}$ | maximum fluorescence |
| $F_{MIN}$ | minimum fluorescence |
| $GD^{3+}$ | gadolinium |
| GCaMP | genetically encoded $Ca^{2+}$-indicator |
| GECO | genetically encoded $Ca^{2+}$-indicators for optical imaging |
| GFP | green fluorescent protein |
| GPCRs | G-protein-coupled receptors |
| HEK | human embryonic kidney |
| ICRAC | calcium release activated calcium currentsl |
| IP3R | IP3 receptor |
| kDa | kilodaltons |
| MAM | mitochondrion-associated ER membrane |
| mCh | mCherry |
| MOI | multiplicity of infection |
| NFAT | nuclear factor of activated T cells |
| NMDAR | N-methyl-D-aspartate receptor |
| nSOCE | neuronal SOCE |
| PM | plasma membrane |
| PLA | proximity ligation assay |
| PLC | phospholipase C |
| ROS | reactive oxygen species |
| SARAF | SOCE-associated regulatory factor |
| SD | standard deviation |
| SCID | severe combined immunodeficiency |
| SEM | standard error of the mean |
| SERCA | Sarco/ER $Ca^{2+}$-ATPase pump |
| SOAR | STIM-Orai activating region |
| σ1R | sigma1 receptor |
| σ2R | sigma2 receptor |
| SOCE | store-operated $Ca^{2+}$ entry |
| SOD1 | superoxide dismutase |
| STIM | stromal interaction molecule |
| Tg | thapsigargin |
| TIRFM | total internal reflection fluorescence microscopy |
| TMEM97 | transmembrane protein 97 |
| TRP | transient receptor potential channels |
| WT | wild-type |
| $WT^{VC}$ | viral control |

# Table of Contents

# 1 Chapter I: Introduction

## 1.1 Sigma1 receptor (σ1R)

### 1.1.1 Historical overview of Sigma (σ)-receptors

σ-receptors are pharmacologically well-defined, transmembrane proteins that are targeted by compounds from the variety of structural classes. The existence of "sigma" (σ) site was first proposed by Martin et al. (1976) during pharmacological studies using SKF-10,047 and related benzomorphans[1]. This historical, ground-breaking study was performed in morphine-dependent and non-dependent chronic spinal dogs. Based on the behavioural effects that occurred following the application of benzomorphans, several types of novel opioid receptors were proposed: μ (Mu), κ (Kappa) and σ (Sigma).

Further pharmacological and photo-labelling studies demonstrated that SKF-10,047 interacted with several distinct sites, resulting in opioid and non-opioid related effects[2–5]. Separate evaluation of SKF-10,047 (+)- and (-)-isomers explained these observations. It was demonstrated that (-)-isomers of benzomorphans account for the opioid-mediated effects, including the effects reported by Martin et al. study which used a racemic mixture of benzomorphans. Today, it is considered that observed opioid-effects during Martin et al. study were the result of benzomorphans binding to μ- and κ- sites as opioid antagonists failed to modulate the effects of σ-ligands. Hence, σ-receptors were eventually reclassified as non-opioid receptors with high affinity for (+)-isomers of benzomorphans.

In addition to pharmacological and photo-labelling studies, development of molecular and cell biology techniques has provided new insights into σ-site, demonstrating that σ-receptors have different architecture, as well as pharmacology when compared to opioid receptors[6]. Based on the different tissue distribution, protein size and drug selectivity, two

subtypes of σ-receptors were proposed; σ1R - with a molecular mass of 25.3 kDa, and σ2R – with a molecular mass of 18-21.5 kDa [6–8].

As most of the pharmacologically described receptors during the 20th century, σ1R was cloned by the end of the 1990s. The original σ1R clone was from guinea pig, but it has also been cloned from numerous other species, including humans, rats, and mice[7,9,10]. Contrary, the identification of σ2R sequence took forty years of scientific wandering until σ2R was finally purified from calf liver by Alon et al. in 2017– two years after the beginning of this doctoral work - and identified as previously known human transmembrane protein 97 (TMEM97)[11].

Two σ-subtypes appear to be distinct physical entities. Following sequence identification, σ1R has shown no homology to other mammalian proteins. It shares approximately 30.3% sequence identity with ERG2, a fungal gene encoding for a C8-C7 sterol isomerase. However, σ1R itself is not found in yeast, and it also lacks sterol isomerase activity[7]. As such, and in the absence of σ2R identity sequence, σ1R has been used as a starting point in the characterization of both σ-receptors, placing them into distinct protein family. However, recent sequence identity of σ2R/TMEM97 has shown that σ2R has EXPERA domain which makes it a distant homolog of human TM6SF1, TM6SF2, EBP, and EBPL proteins – proteins implicated in cholesterol biology[11].

Currently, there is a growing scientific interest in functional and molecular mechanisms of both σ-subtypes as promising therapeutic targets in various cancers and neurodegenerative diseases[12]. However, while recent cloning of σ2R/TMEM97 has merely just opened doors for mechanistic studies of this subtype, the σ1R subtype has been made the focus of this doctoral work.

### 1.1.2 Anatomical and subcellular distribution of σ-receptors

σ-receptors are widely expressed within various peripheral tissues, including heart, kidney, pancreas, liver, lung, spleen, and adrenal glands, as well as the central nervous system (CNS) where they exhibit neuroprotective properties[12]. The expression of both σ-subtypes is also upregulated in the various cancers with functional implications in cell proliferation and migration[13–16].

Within CNS, particularly within the brain, σ1Rs have been associated with the areas involved in the regulation of memory (memory deficit), pain, sensory and motor functions, such as the hippocampus, the dentate gyrus, cortical layers, pons, the central grey, locus ceruleus, the substantia nigra pars compacta, hypothalamus, dorsal raphe, olfactory bulb the red nucleus, and motor cranial nerve nuclei[17]. The expression of σ2Rs is also detected within the brain, including the cerebellum, motor cortex, hippocampus, and the substantia nigra[18]. The current body of research suggests that within these areas σ-receptors are involved in various neural mechanisms, including calcium ($Ca^{2+}$) signalling, cell survival and function, , neurotransmitter release, and synaptogenesis, but their precise mode of action remains elusive[19].

At the subcellular level, the σ1R is detected in the membrane of the endoplasmic reticulum (ER), microsome, mitochondrion, nucleus, and the plasma membrane (PM)[17]. In the rat hypothalamic and hippocampal neurons, electron microscopy studies showed the association of σ1Rs with neuronal perikarya, the membranes of mitochondria, cisternae of the ER, and dendrites[20,21]. However, σ-receptors are predominately ER transmembrane proteins which accumulate at the ER-mitochondrion contact sites known as the MAM (mitochondrion associated ER membranes; Figure 1.11)[22]. The formation of MAM junctions occurs in the area where membranes of two organelles are estimated to be within 25nm of

each other, enabling their protein complexes to interact and regulate inter-organelle signalling pathways, which are crucial for cellular “housekeeping” functions such as the non-vesicular movement of phospholipids, proteins, and ions[23,24]. The functional role of σ1R at the MAM is described in the latter part of this chapter (Section 1.15).

In a series of studies[22,23,25], Hayashi and Su demonstrated that σ1Rs accumulate in the lipid domains of the ER. These domains, also known as lipid microdomains, lipid rafts or lipid droplets, are cholesterol- and sphingolipid-enriched areas present in the external leaflet of the membranes. Upregulation of σ1Rs in human neuroblastoma cells reduced free cholesterol and glycosphingolipids in the ER and mitochondrion membranes, indicating that at the MAM, σ1Rs participate in the lipid-based signalling pathways[17].

σ2Rs have also been detected in the lipid microdomains of rat liver membranes[26]. Contrary to σ1Rs that possess the ability to translocate from MAM to either nuclear envelope or ER-PM junctions, σ2Rs seem to be exclusively lipid raft proteins with the ability to affect $Ca^{2+}$ signalling via sphingolipid products.

### 1.1.3 Molecular and structural features of σ1R

σ1Rs are 223 amino acids long transmembrane proteins. Early hydrophobicity study of the σ1R sequence detected a high hydrophobicity of its segment close to its N-terminus, and correctly predicted single transmembrane helix between ~9–30 residues of the receptor[7]. However, in the absence of the σ1R crystal structure, another model of σ1R was proposed and became widely embraced within the scientific community. This latter model predicted two-transmembrane domains of σ1R based on the homology of the receptor with a database of known TM segments, as well as immunostaining experiments with antibodies targeting green fluorescent protein (GFP) fused to either N- or C-terminus of σ1R. During

these immunostaining experiments, the N and C termini of σ1R have been observed to be on the same side of the PM of *Xenopus* oocytes or of the ER membrane of CHO cells[27]. Contrary, the first crystal structure of σ1R published in 2016 revealed single transmembrane pass, and thus, confirmed the initial predictions[28].

The crystal structure of human σ1R was published forty years after the original proposal of σ-site. In their first publication, the crystal structures of the human σ1R were reported in the complex with two chemically divergent, but experimentally uncommon σ1R ligands, PD144418 and 4-IBP[28]. However, in the following publication, σ1R was crystallized bound to its classical antagonists – haloperidol (Figure 1.11) and NE-100, as well as thoroughly-studied agonist - (+)-pentazocine[29]. Using lipid cubic phase crystallization method, σ1R was crystallized as a trimer where each protomer was binding a single ligand at the centre of its C-terminal domain while showing unusual fold[28]. Each protomer included a single transmembrane domain (6-31 aa) flanked by α cytosolic domain made of a β-barrel (81–176 aa) and flanking α-helices[28,29].

The existence of σ1R as homotrimer was not predicted by previous studies. Before publication of σ1R's crystal structure, numerous binding and fluorescent studies indicated an even-number of σ1R subunits during oligomerization[2,30–33]. As similar studies also suggested that σ1R oligomerization states may regulate its function(s), the full significance of σ1R as homotrimer has yet to be determined [32,33].

σ1Rs are regulated by a structurally diverse array of compounds that are used for different therapeutic applications, including benzomorphans, neuroleptics, antitussives, antidepressants, drugs of abuse, and drugs used to treat pain, psychosis, anxiety , and neurodegenerative diseases[33,34]. Thus, another unexpected insight into the novel σ1R structure was the discovery that the site for ligand-binding is sterically occluded[29]. Kinetic

analysis of ligands association and dissociation to σ1Rs revealed that the ligand-binding to σ1R occurs very slowly and in multiple steps, requiring a conformational change of the protein and dynamic exposure of its binding pocket[29].

A unique domain within σ1R named the Sterol Binding Domain Like region (SDBL) plays an important role in the protein- and ligand-binding to σ1R[35]. Photo-affinity experiments identified two SBDL domains spanning between 91-109 (SBDL1) and 176-194 (SBDL2) residues of σ1R[2]. A considerable number of mutational studies demonstrated that SBDL1 and SBDL2 of σ1R form at least a portion of the ligand- or specialized lipid-binding site[35]. Residues spanning between amino acid 119-149 and 208-223 of σ1R have been established as crucial for ligand-binding and functional interaction with partner proteins[33]. These results are firmly in agreement with the novel σ1R structure; the most mutations with significant impact on ligand-binding affinity, such as juvenile amyotrophic lateral sclerosis (ALS)-causing mutation E102Q, are found to be in the proximity of structurally demonstrated ligand-binding site.

The cytosolic portion of σ1R also contains two cholesterol-binding domains located between residues 161-180 and 191-210. These domains contain two unique motifs, VEYGER and LFYTLRSYAR, which have been identified as essential for the functional role of σ1R in lipid trafficking and lipid-based signalling pathways[27]. Additionally, removal of residues 2-8 from the N-terminus results in the impairment of σ1R interaction with ER lipids and cholesterol, leading towards an increase in the lipid and cholesterol content of the ER and decreased cholesterol content in the PM[23].

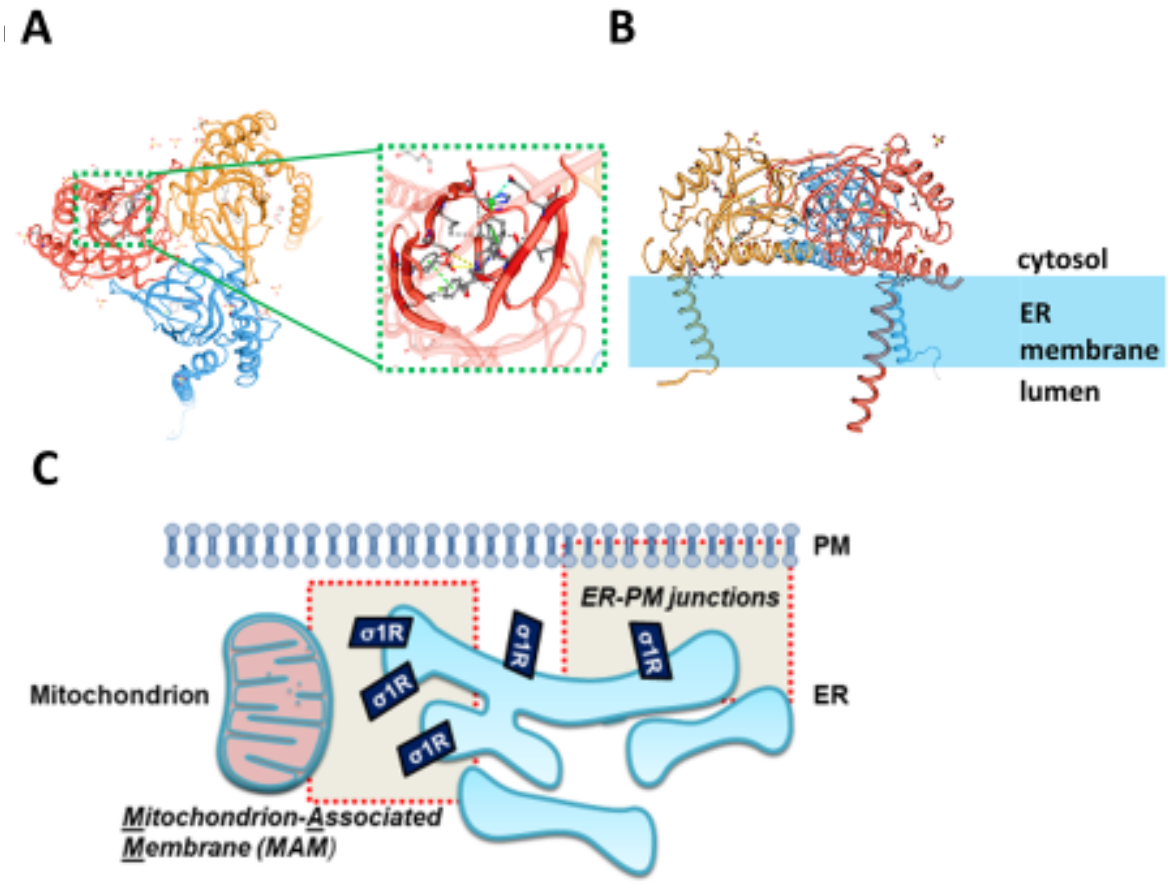


**Fig1.11 Features of σ1R.** A) Cartoon of σ1R trimer from cytosolic perspective created using Swiss PDB viewer. σ1R monomers are bound to their classical antagonist haloperidol. B) Cartoon of σ1R trimer from side perspective. σ1R monomer has a single transmembrane domain with the largest portion of the protein being located in the cytosol, including protein's ligand binding and cholesterol binding domains. C) At subcellular level, σ1Rs are predominately found at MAMs regions, but can also translocate to the regions known as ER-PM junctions.

### 1.1.4 Therapeutic potential of σ1Rs

A rich history of scientific inquiry into σ1R established its therapeutic potential in two major pathological areas: (1) neurodegenerative diseases and (2) cancers.

#### *1.1.4.1 The implication of σ1Rs in neurodegenerative diseases*

Neurodegenerative disease is a term for a range of pathological conditions that damage the neuronal integrity within CNS, including Huntington's disease Alzheimer's disease, amyotrophic lateral sclerosis (ALS), Parkinson's diseases, and multiple sclerosis.

ALS is a motor neuron disease that manifests as the death of neurons required for controlling voluntary muscles. One of identified, underlying causes of diagnosed ALS are mutations in the gene for the copper-zinc superoxide dismutase (SOD1). A treatment of ALS mouse-model, SOD1-G93A, with the PRE084 - selective σ1R agonist - improved survival and function of spinal motor neurons and the locomotor performance, as well as the maintenance of muscle action potential amplitudes, and motor neuron number of the spinal cord[33]. In contrast, a global knockout of σ1R in the same mouse model resulted in the acceleration of motor deficiency and the decreased longevity of the mouse model[33].

Genotyping studies that used a single nucleotide polymorphism (SNP) approach identified E102Q-mutant of σ1R in the genomic DNA of patients diagnosed with juvenile-onset of ALS[36]. Overexpression of $\sigma1R^{E102Q}$ in motor neuron-like cell line NSC34 resulted in a shift of the $\sigma1R^{E102Q}$ to membranes of lower density during sucrose gradient fractionation[36]. Interestingly, during the Western blot analysis, $\sigma1R^{E102Q}$ was detected as a complex at ~ 50kDa (instead of ~25kDa) even in the buffers containing 150mM DTT and

2% Triton-X. This result indicates that σ1R$^{E102Q}$ forms dimers with the strong hydrophobic interaction between the monomers. Additionally, the overexpression of σ1R$^{E102Q}$ reduced viability of NSC34 cell line. Further investigations of σ1R$^{E102Q}$ have shown that it also aggregates at the subcellular level, leading to mislocalisation of the major pathological protein in sporadic ALS known as TDP43, and thus, an increase in cytoxicity[37].

Alzheimer's disease is a neurological disorder characterised by a slow, increasing decline in cognitive functions as well as the pathological self-assembly of amyloid-beta (Aβ) plaques and tangles. The predominant hypothesis about development and advancement of Alzheimer's disease, so-called "amyloid hypothesis", proposes that alteration in cleavage, processing, and clearance of the amyloid precursor protein (APP) causes the disease. The Aβ plaques form during proteolysis of APP[33].

A memory deficit is one of the symptoms of Alzheimer's disease[38]. The role of σ1Rs in the memory deficits was investigated using an $A\beta_{25-35}$-infusion mouse. In a dose-dependent manner, the selective σ1R agonist (+)-pentazocine attenuated memory deficits that were caused by amyloid $\beta_{25-35}$ injection[33].

Current therapy of Alzheimer's disease uses acetylcholinesterase inhibitor donepezil. Donepezil enhances the cognitive functions disturbed during the disease. In the brain, donepezil binds to σ1Rs[39]. Activation of σ1Rs has been reported as a by-product of donepezil-treatment, contributing to overall neuroprotective and anti-amnesic effects of donepezil. Donepezil also significantly improves neurite outgrowth in PC12 cells, which can be countered by the treatment with NE-100, the σ1R antagonist[40].

Overall, these results demonstrate that expression and activation of σ1R confer a neuroprotective role in pre-clinical models of neurodegenerative disorders. However, the

mechanisms by which σ1R exhibits its neuroprotective role yet remain to be fully understood.

#### *1.1.4.2 The implication of σ1Rs in cancers*

Although there are currently no clinically approved σ1R ligands in cancer treatment, the study of σ1Rs' involvement in cancers represents a growing and exciting area of research.

Enhanced expression of both σ-subtypes has been reported in a variety of cancer tissues, including small- and non-small-cell lung carcinoma, colon carcinoma, sarcoma, renal carcinoma, breast cancer, prostate cancer, melanoma and neuroblastoma.[13,41–46]. In neoplastic breast cancer cells, treatment with σ1R antagonists, haloperidol and progesterone, inhibited cell viability in dose-dependent manner[13]. Additionally, Aydar et al.[47] demonstrated that overexpression of σ1R-targeted siRNA reduced breast cancer proliferation and cell adhesion.

In breast cancer and colorectal cancer cells, downregulation of σ1R as well as the treatment with its antagonist, igmesine, resulted in reduced cell migration[14]. This result is of particular interest for this doctoral work as Gueguinou et al.[14] proposed the regulatory mechanism of cell migration in which expression of σ1R promotes SK3-dependent $Ca^{2+}$ influx through Orai1 channel – the main channel of store-operated $Ca^{2+}$ entry (SOCE). Therefore, the mechanism that proposes interplay of SK3, σ1R and Orai1 is discussed in the latter part of this thesis (Section 1.2.11).

To summarise, current inquiries in the role of σ1Rs in cancers suggest their "cancer-protective" role. Enhanced levels of σ1Rs promote proliferation, cell adhesion, and

migration, whereas the downregulation of σ1Rs and the treatment with σ1R antagonist reduces cancer cell viability.

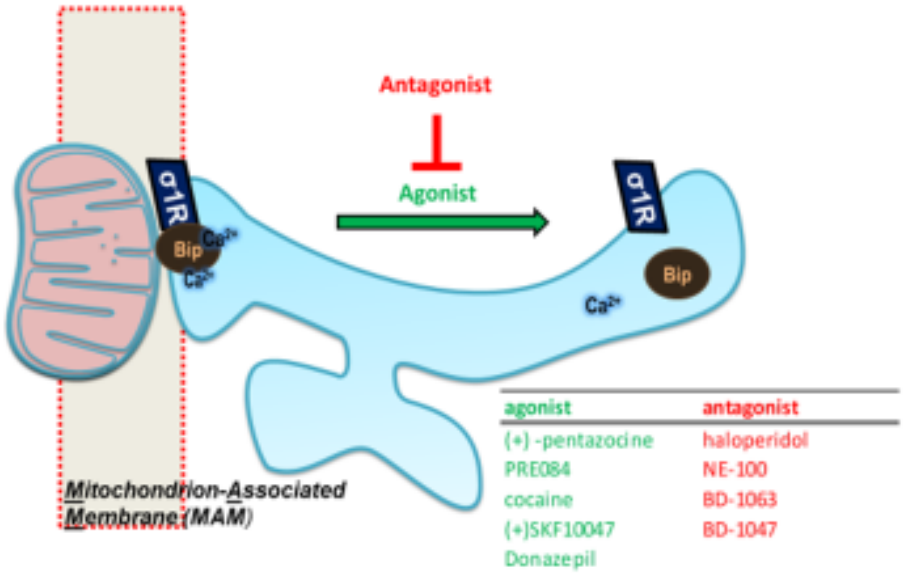


**Fig1.12 Mechanism of σ1R.** A schematic illustrating the effects exerted by σ1R agonists and antagonists that were mentioned in literature review. σ1R are found predominantly within MAMs and associated with binding immunoglobulin protein (BiP). Treatment with σ1R agonists disrupts σ1R/BiP interaction, freeing σ1R to interact with other proteins. The antagonist deters the dissociation of σ1R/BiP interactive complex resulting in inactive σ1R.

### 1.1.5 The functional roles of σ1R

#### *1.1.5.1 The functional roles of σ1R at the MAMs*

σ1R was initially identified as a receptor[1,3,7]. However, an increasing body of evidence suggests it primarily acts as an intracellular ER chaperone aiding in the proper folding and stabilisation of proteins[22,48,49].

Co-immunoprecipitation and co-localisation studies in CHO cells identified σ1R in a complex with binding immunoglobulin protein or BiP (Fig1.12)[22]. BiP is a well-characterized intraluminal chaperone that binds newly stabilised proteins upon their translocation into the ER and facilitates their maintenance in a state of competence for post-translational modification and oligomerization[50]. BiP is also $Ca^{2+}$ buffering chaperone as it binds luminal $Ca^{2+}$ and contributes to the storage of $Ca^{2+}$ within the ER[51]. Dissociation of the σ1R-BiP complex occurs during stress, such as serum starvation, a significant decline in ER $Ca^{2+}$ levels or treatment with σ1R agonists, and results in active σ1R allowing its interaction with other ER proteins or proteins at the ER contact sites. Hence, σ1R-BiP interaction is considered inhibitory for σ1R and its functional roles, and it is stabilized by intraluminal $Ca^{2+}$[22].

ER is a dynamic organelle that forms contact sites with mitochondria, at MAM, and with PM, at ER-PM junctions. Following dissociation from BiP, σ1R was reported to interact with ion channels at MAM and ER-PM junctions[22,34]. At MAMs, σ1R was shown to stabilize the subtype 3 of inositol 1,4,5-trisphosphate receptors (IP3R). By chaperoning IP3Rs, σ1Rs promote the $Ca^{2+}$ flux from the ER to the mitochondria by increasing the sensitivity of IP3Rs for their endogenous ligand, IP3 [22,48]. This movement of $Ca^{2+}$ from ER to mitochondria is essential for the regulation of bioenergetics, as well as the free radical formation in mitochondria[48]. A downregulation of σ1R protein levels was shown to enhance the

proteasomal degradation of IP3R, type 3, at the MAMs, resulting in dysregulation of $Ca^{2+}$ homeostasis between the ER and mitochondria[22].

More recently, Brailoiu et al.[52] have demonstrated that the functional interaction between σ1Rs and IP3Rs is potentiated by binding of choline to σ1Rs in an agonist-like manner. The activation of G-protein-coupled receptors (GPCRs) at the PM stimulates phospholipase C (PLC) and the downstream production of IP3. IP3 binds to IP3Rs and activates the release of $Ca^{2+}$ from the ER through IP3Rs. Additionally, the activation of GPCRs stimulates phospholipase D (PLD), leading to the formation of choline which as endogenous ligand binds σ1Rs, and thus, potentiates $Ca^{2+}$ signals evoked by IP3-activated IP3Rs. This proposed mechanism combines the initially proposed role of σ1Rs as a receptor with its widely demonstrated role as a chaperone.

As a chaperone, σ1Rs has also been reported to regulate cytoskeletal adaptor protein ankyrin-B, which is localized in the ER lumen. In several cell types, including cardiomyocytes ad striated muscle cells, ankyrin-B has been shown to regulate the localization and membrane stabilization of ion transporters and ion channels, including $Na^+/Ca^{2+}$ exchanger, $Na^+/K^+$ ATPases ATP1A1 and ATP1A2 and IP3R3. The regulation of ankyrin-B by σ1Rs is demonstrated to be coupled with σ1R's regulatory role of IP3Rs. At MAMs, ankyrin-B interacts with subtype 3 of IP3Rs. This interaction can be modulated by treatment with σ1R ligands where the application of agonists reduces ankyrin-B/IP3R interaction whilst the application of σ1R antagonists has the opposite effect. The cellular expression of ankyrin-B is reduced by downregulation of σ1Rs which results in the prolonged activation of IP3R3 at MAMs, triggering apoptosis[53].

At MAMs, σ1Rs also regulate the inositol requiring enzyme-1 (IRE1)[48]. IRE1 is a serine/threonine-protein kinase, and endoribonuclease that acts as a sensor for the ER

unfolded protein response (UPR), and thus, assumes the role of the ER stress response protein[51,54,55]. Similar to σ1R, the luminal domain of IRE1 interacts with BiP during unstressed conditions[54]. Increase in misfolded protein content within the ER promotes BiP and IRE1 dissociation and leads to subsequent activation of IRE1 endonuclease activity. Mori et al. have demonstrated that under ER stress conditions IRE1 accumulates at the MAMs to respond to reactive oxygen species (ROS) released from the mitochondria[56]. Following σ1R and IRE1 dissociation from BiP, σ1R stabilises IRE-1 at the MAM, enhancing the stress response and promoting cell survival which seems to be one of the underlying mechanisms of σ1R's neuroprotective effect in the brain[48,56]. These studies demonstrate the essential role of σ1Rs in the regulation of the ER-mitochondria inter-organelle signalling at MAMs where σ1R with its interacting partners regulates underlying mechanisms of bioenergetics, as well as the response to ROS during ER stress conditions.

#### *1.1.5.2 The functional roles of σ1R at the ER-PM junctions*

The ER-PM junctions are membrane contact sites (MCS) between ER and PM that serve as a regulatory platform for important physiological functions of the mammalian cells, including non-vesicular lipid transfer between the ER and the PM, excitation–contraction coupling, and store-operated $Ca^{2+}$ entry (SOCE)[57]. These junctions are distinct subcellular regions where smooth, peripheral parts of ER membrane form close appositions with PM, allowing the tethering of their protein complexes. Recent imaging of HeLa cells by super-resolution microscopy described ER–PM junctions as oblong-shaped contact sites with the size of 120x80nm[57,58].

Early inquiries into the subcellular distribution of σ1Rs in mouse neuroblastoma NG108-15 cells marked their ability to translocate to ER-PM junctions just by placing cells in Hank's balancing solution[22,59]. The localisation of σ1Rs to the PM was confirmed through

various studies that included surface biotinylation followed by Western blot analysis and total internal reflection fluorescence microscopy (TIRFM)[34,60,61]. Since then, σ1R has been described to interact with mechanistically diverse types of ion channels at MCSs, including voltage-operated ion channels (VOICs), receptor-operated ion channels (ROICs), volume-operated and acid-sensitive ion channels (ASICs), and store-operated ion channels (SOCs).

#### 1.1.5.2.1 Regulation of VOICs by σ1R

VOICs are channels formed by transmembrane proteins that allow the passage of ions across the membrane in response to changes in the electrical membrane potential in the channel's proximity. σ1Rs have been reported to interact, directly and/or indirectly with following VOICs: (1) sodium ($Na^+$) channels, such as Nav1.5, (2) potassium ($K^+$) channels, including Kv1.3, Kv1.4, Kv1.5, and Kv11.1 (hERG)[62], and (3) N, L, P, Q and R types of $Ca^{2+}$ channels. Additionally, σ1Rs have been reported to regulate small-conductance $Ca^{2+}$-activated $K^+$ channel called SK. Although SK channels are not purely voltage-dependent their activity can control the membrane potential, subsequently affecting the activity of other transmembrane proteins and inducing changes in the cellular metabolism[63].

#### 1.1.5.2.2 Regulation of voltage-operated sodium channels by σ1R

Using co-immunoprecipitation studies and atomic force microscopy (AFM), Balasuriya et al. provided evidence that σ1Rs interact directly with Nav1.5 channel in MDA-MB-231 cells, where σ1R has been shown to regulate Nav1.5 channel currents and subsequently, promote the invasiveness of cancer cells[64]. Direct interaction of σ1R with Nav1.5 channel resulted in the inhibition of Nav1.5 channel currents. Interestingly, σ1Rs have also been shown to inhibit $Na^+$ current indirectly. In slice preparation of the prefrontal cortex, σ1Rs were activated by the neurosteroids dehydroepiandrosterone sulphate

(DHEAS), which was followed by the inhibition of a persistent $Na^+$ currents[65,66]. As in numerous studies demonstrated before, this effect of σ1Rs was also successfully modulated by treatment with different σ1Rs ligands[64].

#### 1.1.5.2.3 Regulation of voltage-operated potassium channels by σ1R

Co-immunoprecipitation studies in HEK293 cells precipitated σ1R with the human ether-a-gogo-$K^+$ channel (hERG), which is essential for cardiac repolarization[67]. In a chaperone-like manner, σ1Rs also increased the stability of the $K^+$ channel subunit, as well as $K^+$ currents in leukemic cells[68].

The regulatory role of σ1R has also been reported in another type of $K^+$ channels, in SK channels. SK channels are involved in the variety of physiological processes by regulating $Ca^{2+}$ influx through the control of the membranes' resting potential and $Ca^{2+}$ driving force. Martina et al. demonstrated that targeting σ1Rs with agonist (+)-pentazocine prevented SK channels from opening In CA1 pyramidal cells of rat hippocampus. Inhibitory effect of σ1R on SK channels modulated and enhanced $Ca^{2+}$ influx via N-methyl-D-aspartate receptors (NMDAR), which are essential for the regulation of synaptic plasticity and memory[69].

#### 1.1.5.2.4 Regulation of voltage-operated calcium channels by σ1R

Pharmacological studies of σ1R identified that agonists of σ1R are broadly neuroprotective. Voltage-operated $Ca^{2+}$ channels are predominantly present in excitable cells and activated as a response to depolarization of the PM. Based on the degree of PM depolarization necessary to activate the channel, voltage-operated $Ca^{2+}$ channels can be categorized in two distinct groups: (1) a high degree includes L,N,P, Q and R subtype, and (2) a low degree includes T channel subtype.

Treatment by the agonists of σ1R was shown to block $Ca^{2+}$ currents mediated by N,L,P,Q and R type voltage-operated $Ca^{2+}$ channels, guarding against the cytotoxic $Ca^{2+}$ overload which often characterizes neurodegenerative diseases[70,71]. An extensive increase in cytosolic [$Ca^{2+}$] can cause the saturation of mitochondrial buffering capacity, mitochondrial damage and, eventually, neuronal death[72,73]. Treatment of rat sympathetic and parasympathetic neurons by σ1R agonists diminished currents of almost all $Ca^{2+}$ channel subtypes. This effect suggested that σ1R attenuates all subtypes of voltage-operated $Ca^{2+}$ channels found on the cell body of these neurons.[70] Co-localization and co-immunoprecipitation studies of the role of σ1Rs in the regulation of L-type voltage-operated $Ca^{2+}$ channels, suggests that σ1R exerts this inhibitory effect through direct interaction with voltage-operated $Ca^{2+}$ channels at the PM[60].

#### 1.1.5.2.5 Regulation of ROICs by σ1R

ROICs are structurally and functionally diverse ion channels, predominantly found in the secretory cells and synapses. ROICs are activated by ligand binding to the receptor which induces conformational changes of the channel, opening the channel pore. Examples of ROIC include purinergic (P2X) receptors, serotonin (5-HT3 receptors, and ionotropic glutamate receptors, such as AMPAR and NMDAR.

NMDAR is a heterotetrameric ionotropic receptor which is activated by the binding of two ligands: glutamate and glycine[74]. A pioneering study by Monnet et al. identified the effect of σ1R and its agonists on NMDAR-induced $Ca^{2+}$ influx in CA3 hippocampal neurons[75]. NMDAR-potentiated $Ca^{2+}$ influx can be regulated through σ1Rs inhibitory effect on the SK-channels, but more recent proximity ligation studies also reveal that σ1R interacts directly with the GluN1, subunit of NMDARs[69,76]. In mice, the impairment of learning can be

induced by the treatment with NMDAR antagonist. A treatment with σ1R's agonist PRE084 attenuates the effects of induced NMDAR antagonists, improving learning and memory[77].

These studies clearly demonstrate that in addition to its role at MAMs, σ1R also exhibits an essential role at ER-PM junctions. Although it is currently accepted that σ1Rs are predominately located at MAMs, experimentally-demonstrated interactions of σ1R with Nav1.5, SK, L-type voltage-operated $Ca^{2+}$ channels, and NMDARs suggests that σ1R can either be located at the PM or translocate to the ER-PM junctions from MAM regions. However, while the functional interactions of σ1R with various ion channels have been identified through pharmacological studies and the receptor's implication in a wide variety of disease, underlying mechanisms of σ1R role at ER-PM junctions still remain poorly understood.

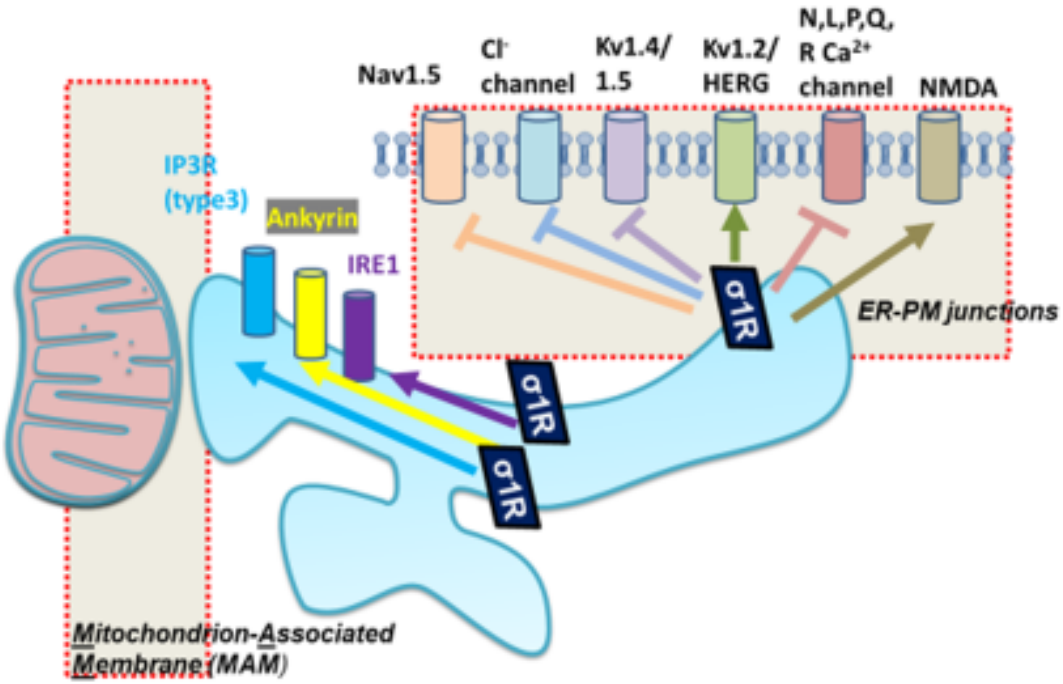


**Fig1.13 Interactions of σ1R with proteins at MAM and ER-PM junctions.** Upon dissociation from BiP, σ1R can chaperone proteins at MAM, or translocate to ER-PM junctions where it interacts with different channels. At MAM, σ1R stabilizes 1) type 3 IP3R which allows $Ca^{2+}$ from the ER to mitochondria, 2) Ankyrin which stabilizes ER $Ca^{2+}$ homeostasis, and 3) IRE1 which stabilizes ER during stress through physical interaction. At ER-PM junctions, σ1R has been identified to inhibit 4) Nav1.5, Kv1.4/1.5 channels, voltage operated $Ca^{2+}$ channels, and to enhance activity of 5) Kv1.2/HERG channels and NMDA gated $Ca^{2+}$ channels.

## 1.2 The store-operated calcium entry (SOCE)

### 1.2.1 Introduction to $Ca^{2+}$ signalling

$Ca^{2+}$ ions are ubiquitous and versatile intracellular messengers. At a cellular level, $Ca^{2+}$ ions modulate various cellular processes, such as cell proliferation, gene transcription, neurotransmitter release, cellular plasticity, exocytosis, endocytosis, cellular viability, and apoptosis[78,79]. At the anatomical level, $Ca^{2+}$ is a crucial regulator of numerous physiological functions, including muscle contractions, sensory perceptions, learning, memory formation, fertilisation, and aging[78,79].

Under resting conditions, cytosolic $Ca^{2+}$ concentration ($[Ca^{2+}]_{cyt}$) is tightly regulated at 50-100 nM, which varies between the cell types and their microenvironment. The imbalance in $Ca^{2+}$ regulation often characterises various neurodegenerative diseases, including Alzheimer's disease, Huntington disease, and ALS[70,71,80–83]. Dysregulation of $Ca^{2+}$ signalling is also considered hallmarks of various cancers, contributing to the cancer progression and invasiveness[84]. Mammalian cells adapted a finely coordinated network of $Ca^{2+}$ regulators to buffer, compartmentalise and extrude excess in $[Ca^{2+}]_{cyt}$, which makes $Ca^{2+}$ homeostasis an energy costly process. Due to the energy investment, the maintenance of $Ca^{2+}$ homeostasis became evolutionary interlinked with the regulation of numerous, often simultaneous, and essential cellular processes.

The elevated $[Ca^{2+}]_{cyt}$ can be toxic for the cells over long period of time, and thus, the increase in $[Ca^{2+}]_{cyt}$ results in the prompt activation of two distinct classes of proteins: (1) $Ca^{2+}$ buffering proteins, and (2) $Ca^{2+}$ sensitive signalling proteins. $Ca^{2+}$ buffering proteins, such as calretinin, calbindin-$D_{28K}$, and parvalbumin, buffer $Ca^{2+}$ ions to maintain cytosolic $Ca^{2+}$. $Ca^{2+}$ sensitive proteins, such as calmodulin, annexins, synaptotagmin, troponin C, and

calcineurin, are triggered into the action mode by their binding to $Ca^{2+}$. In contact with $Ca^{2+}$-binding motifs, $Ca^{2+}$ ions alter the conformation of $Ca^{2+}$ sensitive proteins, initiate the transduction of $Ca^{2+}$ encoded signals, and subsequently, trigger the specific, downstream cellular processes. $Ca^{2+}$-binding motifs of both $Ca^{2+}$ buffering proteins and $Ca^{2+}$ sensitive signalling proteins also vary in their affinities for $Ca^{2+}$ over a million-fold range (nM to mM). As a consequence, proteins with low-affinity motifs are unresponsive to global $Ca^{2+}$ fluctuations whilst proteins with high-affinity motifs are unresponsive to low, elementary $Ca^{2+}$ fluctuations, also known as quarks, puffs, or sparks. Hence, distinct frequencies and amplitudes of $Ca^{2+}$ transient signals activate a specific combination of the $Ca^{2+}$ buffering proteins and $Ca^{2+}$ sensitive signalling proteins. As a result, the formation of $Ca^{2+}$ microdomains occurs at the mere point of $Ca^{2+}$ entry, allowing a precise, spatiotemporal organisation of $Ca^{2+}$ signalling.

### 1.2.2 $Ca^{2+}$ microdomains

$Ca^{2+}$ microdomains are formed at the point of $Ca^{2+}$ entry to the cell. An influx of $Ca^{2+}$ to cytosol can originate from two primary sources: the extracellular environment, which contains ~ 1.2 mM $Ca^{2+}$ in physiological conditions, and intracellular stores, where $[Ca^{2+}]$ varies from μM to mM range [85].

Most of the $Ca^{2+}$ influx occurs through $Ca^{2+}$-permeable PM channels, such as voltage-operated $Ca^{2+}$ channels, receptor-operated $Ca^{2+}$ channels, the store-operated $Ca^{2+}$ channels (SOC) and the transient receptor potential (TRP) channels.

During maintenance of cellular $Ca^{2+}$ homeostasis, the excess in $[Ca^{2+}]_{cyt}$ is compartmentalised to the intracellular $Ca^{2+}$ stores, which also serve as a source of $Ca^{2}$. ER is the main $Ca^{2+}$ store in mammalian cells with luminal free $[Ca^{2+}]$ in the region of 100 – 300

μM. Other organelles, including the nucleus, mitochondria, or the organelles of the secretory pathway, such as the Golgi apparatus and lysosomes, can also act as the intracellular source of $Ca^{2+}$.

From both sources, $Ca^{2+}$ moves readily to the cytosol after the opening of the ion-channel pores, and down the steep concentration gradient around the entry site which gives rise to nonhomogeneous activation of $Ca^{2+}$-buffering and $Ca^{2+}$-sensitive signalling proteins with similar $Ca^{2+}$ affinities[86]. $Ca^{2+}$ binding triggers signal transduction cascade, whilst additional excess in $[Ca^{2+}]_{cyt}$ is compartmentalised to the intracellular stores in the proximity of $Ca^{2+}$ entry, or finally, extruded out the cell. Thus, the freedom of $Ca^{2+}$ ions is measured in nano- and microseconds, localising the effect of generated $Ca^{2+}$ signal within its microdomain.

$Ca^{2+}$ microdomains consist of the elementary, local $Ca^{2+}$ events which can also combine and serve as building blocks of larger microdomains. Such local $Ca^{2+}$ microdomains allow for the spatial organisation of $Ca^{2+}$ signalling and functional specificity in the different regions of the cell. In neurons, pre- and postsynaptic events are organized in the form of highly localised pulses of $Ca^{2+}$, allowing a single neuron to process a remarkable amount of information. This miniaturisation of $Ca^{2+}$ signalling allows for individual synapses to be selectively modified to activate specific postsynaptic events while leaving their neighbouring synapses unchanged. In T cells, the activation of $Ca^{2+}$-dependent transcription factor called nuclear factor of activated T cells (NFAT) depends on the formation of $Ca^{2+}$ microdomains during a process known as store-operated $Ca^{2+}$ entry (SOCE). An increase in $[Ca^{2+}]_{cyt}$ during SOCE activates calmodulin which in turn activates calmodulin-dependent phosphatase calcineurin. Once activated, calcineurin dephosphorylates NFAT triggering its nuclear translocation, and subsequent cytokine production, proliferation, and immune competence.

### 1.2.3 History of store-operated $Ca^{2+}$ entry (SOCE)

In 1986, Putney proposed a concept of "capacitative $Ca^{2+}$ entry", a biphasic and sustained $Ca^{2+}$ influx to cytosol that began as IP3-activated $Ca^{2+}$- mobilisation through intracellular "pool" and continued as influx across PM after IP3 degradation and the "pool" closure[87]. Per the scientific understanding of the time, Putney referred to the ER as intracellular "pool" or "$Ca^{2+}$ capacitor" working under the assumption that the ER was in the continuity with the extracellular compartment. Following discoveries that $Ca^{2+}$ crosses the PM before reaching the ER and that $Ca^{2+}$ entry by emptying ER compartment of $Ca^{2+}$could be activated, independently of IP3, Putney revised his initial model of "capacitative $Ca^{2+}$ entry". Instead, the new model was proposed which would come to be known as "store-operated $Ca^{2+}$ entry" (SOCE) – a $Ca^{2+}$ influx induced by depletion of ER $Ca^{2+}$ stores[88,89].

Following the publication of Putney's revised "capacitative Ca2+ entry", SOCE was still merely speculation. In 1992, the whole-cell electrophysiology experiments in rat mast cells finally provided the evidence for Putney's SOCE model[90]. After depleting ER $Ca^{2+}$ stores by application of IP3, the ionophore ionomycin or the excess of the $Ca^{2+}$ chelator EGTA, Hoth and Penner described $Ca^{2+}$ release-activated $Ca^{2+}$ current (ICRAC) which had the following characteristics: (1) slow development, (2) voltage–independent gating, (3) small amplitude (pA range) and unitary conductance, (4) inwardly rectifying current-voltage relationship, (5) very high $Ca^{2+}$ selectivity over $Ba^{2+}$, $Sr^{2+}$ and $Mn^{2+}$ ions, (6) sensitivity to heavy metals such as $Gd^{3+}$, $La^{3+}$, $Ni^{2+}$ and $Cd^{2+}$, (7) potentiation by extracellular $Ca^{2+}$, and (8) inhibition by intracellular $Ca^{2+}$, named "$Ca^{2+}$–dependent inhibition" (CDI). However, the mechanism by which depleted intracellular $Ca^{2+}$ stores activated SOCE remained unknown for the following decade.

Development of RNA interference (RNAi) led towards the discovery of the key SOCE regulators. In 2005, two independent publications identified stromal cell surface protein Stromal Interaction Molecule 1 (STIM1) as the ER $Ca^{2+}$ sensor and regulator of SOCE in both *Drosophila melanogaster* S2 and mammalian HeLa cells[91,92]. Further genomic screenings in S2 cells also identified SOCE/CRAC channel unit-forming protein – Orai1[93–95]. Today, the scientific community acknowledges members of STIM and Orai protein family as key regulators of SOCE.

### 1.2.4 Key regulators of SOCE

#### *1.2.4.1 STIM protein family*

STIM proteins are $Ca^{2+}$ binding proteins that act as ER $Ca^{2+}$ sensors. STIM proteins belong to type 1A single-span membrane protein family characterised by unique anchor sequence motif targeted to the lipid membrane and N-terminal domain targeted to the ER lumen during synthesis. In response to ER $Ca^{2+}$ store-depletion, STIM proteins trigger the opening of Orai/SOCE channels allowing $Ca^{2+}$ to enter the cytosol, which results in the formation of $Ca^{2+}$ microdomain at STIM-Orai interaction site[89].

STIM proteins are highly conserved across species from *Drosophila melanogaster* to humans[96,97] Two STIM homologs are identified in vertebrates: 685 amino acids long STIM, and 748 amino acids long STIM2, also known as STIM2.2[89]. Human STIM homologs exhibit ~65% sequence similarity. Both homologs are ubiquitously expressed throughout the tissues, whilst the expression of STIM2 predominates in the brain[98].

STIM1 is the most studied member of protein of STIM family as it was first discovered at the PM through the signal-sequence trap screening on the stromal cell surface [99]. Since

its discovery, the presence of both STIM homologs has been confirmed at the PM, but they are predominately found at the ER[89,100,101].

#### 1.2.4.1.1 Molecular mechanisms of STIM1 and STIM2.2 proteins' activation

The crystal structure of full-length STIM protein in resting-state remains elusive. However, smaller portions of STIM proteins have been structurally assessed and support current scientific consensus stating that in resting bound-to-$Ca^{2+}$ state, both STIM homologs form dimers while undertaking the conformational form where channel-activating regions are hidden from the Orai/SOCE channel[102].

The $Ca^{2+}$ binding region of STIM protein is located in its luminal portion (Fig1.21), while channel activating region can be found in its cytosolic portion. The luminal portion of STIM proteins consists of N-terminal ER targeting signal sequence (SS), canonical EF (cEF) and non-canonical or "hidden" EF (hEF) hands followed by a sterile alpha motif (SAM) and the transmembrane domain. cEF hand serves as ER $Ca^{2+}$ sensor while SAM is required for protein-protein interaction[96]. The cytosolic portion of STIM proteins consists of three coiled-coil domains (CC1, CC2 and CC3), an inhibitory domain (ID), and a polybasic (lysine-rich) tail. Following ER store-depletion, polybasic tail anchors STIM protein at the PM through the tail's interaction with PIP2[89,91,103,104]. Three coiled-coil regions contain the STIM-Orai activating region (SOAR) that has also been identified as CAD (CRAC activation domain), required for Orai1 binding and activation[105].

Despite the high similarity of STIM homologues, reported divergences in luminal and cytosolic portions of STIM1 and STIM2 reflect through their different functional properties. In resting state, $Ca^{2+}$ is bound to the cEF-hand of both homologs via negatively charged aspartates and glutamates promoting a compact monomeric state of EF-SAM domain, which

is stabilised by hEF-hand[102]. When intraluminal $Ca^{2+}$ drops below the threshold, EF-SAM domain undergoes yet undefined conformational change and dimerises[106]. However, what is currently accepted as “dimerisation” of the two monomeric luminal domains of STIM proteins can also be explained as a simultaneous reorientation of two EF-SAM domains which are already in contact[106]. Mutations in EF-SAM domain incapacitate $Ca^{2+}$ association of STIM proteins causing constitutive SOCE [89].

The first main difference between STIM1 and STIM2 lies in the affinity of their EF-hands for $Ca^{2+}$. Due to higher $Ca^{2+}$ dissociation constant (Kd) in comparison to STIM1, STIM2 is more sensitive to low changes in ER [$Ca^{2+}$] (EC50 of 406 μM) while functional activation of STIM1 proteins in SOCE requires a more significant drop in ER $Ca^{2+}$ (EC50 of 210 μM)[107]. Once $Ca^{2+}$ dissociates from cEF, STIM proteins oligomerize before relocating to the peripheral ER where at ER-PM junctions they form distinct PM puncta[105,108].

Oligomerisation is caused by the unfolding of the monomeric EF-SAM domain, which is a key mediator of resting conformational stability[109]. The combination of high-resolution structural data and live-cell functional analyses for STIM1 and STIM2 respective EF-SAM domains helped to identify functionally relevant differences in the stability of two homologues. In comparison to STIM2, STIM1 possesses lower SAM stability and less robust EF-SAM interface. Hence, STIM1 exhibits increased kinetics of oligomerisation compared to STIM2[106,108]. Also, the increased stability of STIM2 EF-SAM domain decreases protein’s propensity for oligomerisation, which attenuates STIM2-association kinetics and prevents hyperactivation of SOCE due to low drops in intraluminal $Ca^{2+}$[106].

The conformational changes of STIM proteins that begin within the luminal domain, dimerisation and oligomerisation propagate to the cytosolic domain through the mechanism that is not yet entirely understood[106]. However, the conformational change in a cytosolic

portion of STIM protein has been widely proposed to expose protein's C-terminal polybasic (lysine-rich) PM-targeting tail, as well as SOAR/CAD domain to the proteins at the PM, including SOCE channel major forming unit Orai1[91,105,106,108]. After oligomerisation, the C-terminal polybasic (lysine-rich) tails anchors STIM proteins at the PM through interaction with PIP2[110]. Deletion of the tail of STIM1 prevents proteins translocation to peripheral ER sites and distinct PM puncta after store depletion[105]. Hence, the polybasic tail of STIM proteins plays a crucial role in stabilising STIM proteins at contact sites between ER and PM allowing STIM proteins to interact with the proteins at the PM. In comparison to STIM1, STIM2 has a higher affinity of the polybasic tail for lipids that stabilises protein's localisation at the PM even at the resting conditions[111].

As a result of the higher sensitivity to intraluminal $Ca^{2+}$ drops, increased EF-SAM stability, decreased the propensity for oligomerisation, and higher affinity of the C-terminal polybasic (lysine-rich) tail for PIP2, STIM2 homolog has been proposed as a weaker regulator of SOCE with the more homeostatic role during discrete drops in the ER [$Ca^{2+}$]. Contrary, STIM1 is considered the primary activator of SOCE during prominent $Ca^{2+}$ store depletion. However, during the dissociation of $Ca^{2+}$ from their respective EF-hands, both STIM homologs can also interact with each other forming heterooligomers, which further adds to the complexity of SOCE activation[103].

#### 1.2.4.1.2 STIM2.2 and its splice variant STIM2.1

Due to its latter discovery and the more prominent activation of SOCE by STIM1, STIM2 homolog has been understudied. During early siRNA screenings of the human signalling proteome, STIM2 was proposed as a feedback regulator of basal cytosolic and ER $Ca^{2+}$ concentrations that activated $Ca^{2+}$ influx upon smaller decreases in ER $Ca^{2+}$, but also, similarly to STIM1, caused $Ca^{2+}$ influx via activation of Orai1[112]. In this study,

downregulation of STIM2, but not STIM1, significantly lowered basal cytosolic [$Ca^{2+}$] as well as basal ER $Ca^{2+}$ levels. However, another study described an inhibitory effect of STIM2 on STIM1-mediated SOCE, including its constitutive and store-independent activation of Orai1[113].

A more recent study of STIM2 revealed that neurons from STIM2$^{(-/-)}$ mice had significantly increased viability under hypoxic conditions compared to neurons from wild-type controls, both in culture and in acute hippocampal slice preparations[114]. While initially, SOCE was considered a major $Ca^{2+}$ signalling pathway of non-excitable cells, in recent years, the proposal of neuronal SOCE (nSOCE) has gained much attention for influencing a variety of nerve cell responses[114,115]. With an increased scientific interest in nSOCE, more studies have focused on STIM2 homolog which expression predominates in CNS.

The initial inquiries in SOCE activation by STIM2 resulted in conflicting conclusions reporting both channel activation and inhibition by STIM2. In 2015, Mierderer et al. characterised splice variant of STIM2, known as STIM2.1[116]. Initially, STIM2.1 was characterised as the first member of the STIM protein family that negatively regulated SOCE. The inhibitory effect of STIM2.1 on SOCE was proposed to be due to the insertion of the additional exon (VAASYLIQ) into the channel-activating domain (CAD), which made STIM2.1-Orai1 interaction impaired. However, in the following study, this initial proposal was re-assessed and replaced with another, suggesting that STIM2.1 exerts a potent, inhibitory effect on SOCE most likely through preventing Orai1 channel cross-linking[117].

A remarkable contribution of Mierderer et al. study was in providing a mechanistic explanation for the previous controversies regarding STIM2 regulation of SOCE. STIM2.1 was found to express in many cell types, where its relative expression ratio to the known variant STIM2, also known as STIM2.2, can differ up to eightfold[116]. Overexpression of

STIM2.2 in HEK293 increased basal $Ca^{2+}$ and still elicited additional activation of Orai1 channel. Co-expression of STIM2.1 with STIM2.2 significantly decreased Orai1-mediated SOCE. In further parts of this thesis, terminology introduced by Mierderer et al., which refers to STIM2 as STIM2.2, is adopted when it is possible to make a distinction between two STIM2 variants.

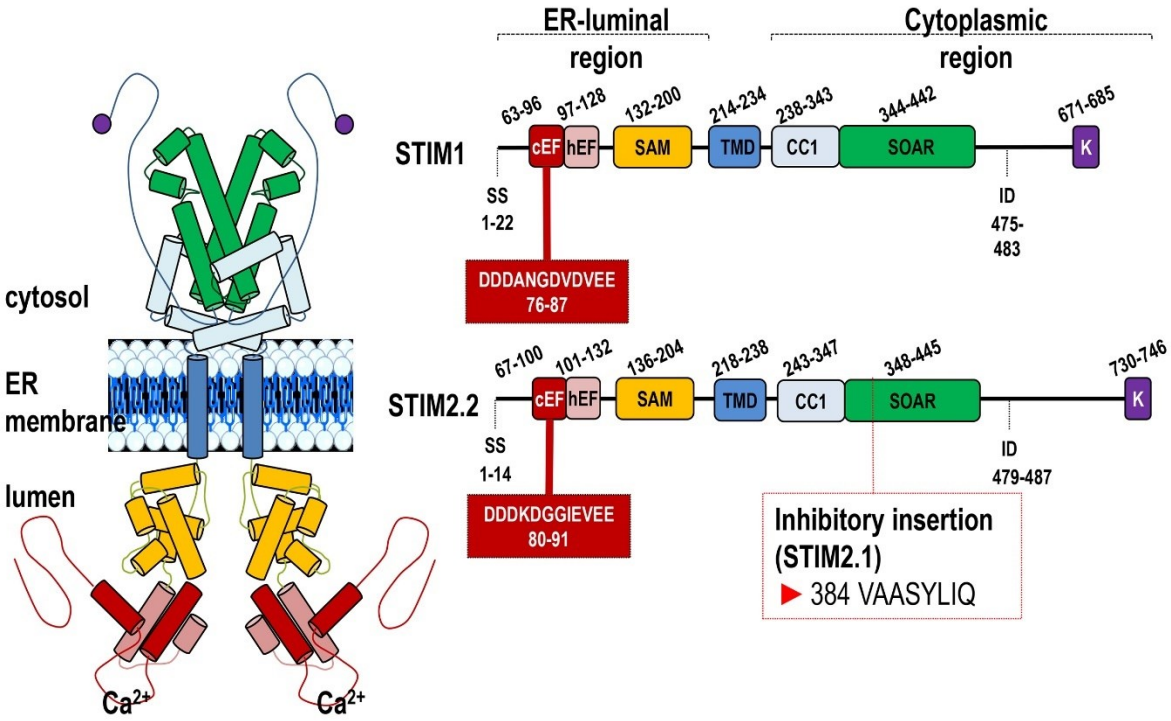


**Fig1.21 Features of STIM protein family.** Schematic illustrates proposed bound-to-$Ca^{2+}$ STIM dimer. STIM proteins consist of an EF hand which binds luminal $Ca^{2+}$ and serves as a $Ca^{2+}$ sensor. EF hand is followed by sterile alpha motif (SAM) which is required for protein-protein interaction and transmembrane domain. The cytosolic portion of STIM proteins consists of three coiled-coil domains (CC1,CC2, and CC3), inhibitory domain (ID) and polybasic (lysine-rich) tail. Following ER store-depletion, polybasic tail anchors STIM protein at the PM through the tail's interaction with PIP2. Three coiled-coil regions contain the STIM-Orai activating region (SOAR) that has also been identified as CAD (CRAC activation domain), required for Orai1 binding and activation. The main difference between STIM1 and STIM2 lies in the affinity of their EF-hands for $Ca^{2+}$, which makes STIM2 more sensitive to the low drops in ER [$Ca^{2+}$]. STIM2 has two splice variants: STIM2.2 and STIM2.1. STIM2.1 has been proposed as first STIM protein that exerts inhibitory effect on SOCE.

### 1.2.5 Orai protein family

Another key regulator of SOCE is the primary forming unit of CRAC channel, Orai1. Orai1 is a member of a highly conserved Orai protein family with no discernible homology with other ion channel proteins[118]. Orai proteins possess four putative transmembrane domains (M1-M4) with the N- and C-termini located inside the cytosol [94,118]. A SOAR region of STIM1 interacts with the cytosolic extension of the M4 segment (residues 263 to 301) of human Orai1. Human Orai1 also has second STIM1-binding site in proximity of its N-terminal region (residues 70 to 91)[105]. Crystallographic studies confirmed initial predictions that gating of Orai1-channels occurred through STIM1-binding across this two sites[105,118]

The crystal structure of *Drosophila* Orai1 revealed a hexameric arrangement of subunits around a central channel pore with a ring of glutamate residues forming the selectivity filter[118]. The hexameric assembly of Orai1 subunits was further demonstrated by AFM studies in HEK293 cells using recombinant human full-length Orai1. Balasuriya at el. showed that human Orai1 form hexamers at both resting and store-depleted conditions[119]. In store-depleting conditions, Orai1 hexamers clustered at ER-PM contact sites in STIM1-dependent manner[119]. More recently, functional analysis of Orai1 concatemers also supported Orai1 hexameric assembly[120].

In humans, the Orai family consists of three isomers with approximately 62% sequence identity: Orai1, Ora2, and Orai3[109]. In comparison to Orai1, the upregulation of its homologs Orai2 and Orai3 yields smaller ICRAC and is unable to substitute Orai1[121]. While Orai1 is considered the primary forming unit of the CRAC channel, Vaeth et al. demonstrated that Orai1 and Orai2 also form heteromeric CRAC channels, in which the Orai2 subunit fine-tuned the magnitude of SOCE to modulate immune responses[122]. Orai1 and Orai3 have

been found to form STIM1-independent CRAC channel that requires activation by arachidonic acid in receptor-operated manner[121].

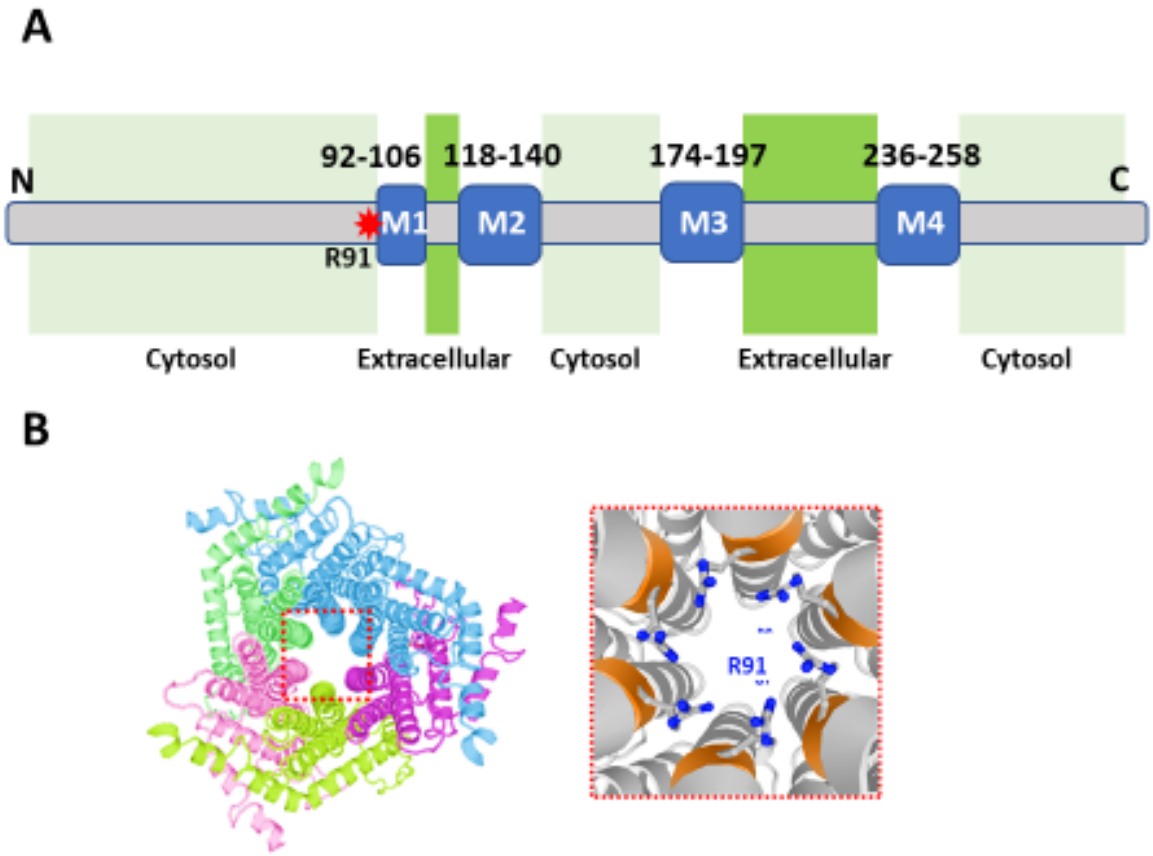


**Fig1.22 Features of Orai1. A)** Schematic illustrates location of cytosolic, transmembrane (M1-M4) and extracellular domains of Orai1 protein. A location of native variant Arg (R) 91 is marked in red before the M1. B) Cartoon of Orai1 hexameric arrangement of subunits around a central channel pore from cytosolic side created using Swiss PDB viewer. Location of Arg (R) is shown within the Orai1 channel pore. A change of Arg to tryptophan (W) results in a sizeable aromatic side chain within the channel pore, presumably preventing channel from opening.

### 1.2.6 The molecular mechanism of SOCE activation

STIM and Orai1 proteins are key regulators of SOCE, and the mechanism of their functional interaction can be explained in a stepwise manner, as shown in Fig1.23.

1. The current body of evidence suggests that at the resting state STIM proteins form homodimers[108,123,124]. The formation of STIM1 homodimers is supported NMR crystallography, STIM2.2 homodimers are proposed based on STIM1 homology modelling[116]. Although functional studies provide evidence that STIM2.1 interacts with other STIM proteins, its resting assembly remains unknown[116]. In resting state, STIM and Orai1 proteins localise diffusely at the ER and PM, respectively[120].
2. The hydrolysis of phosphatidylinositol 4, 5-bisphosphate PI (4, 5) P2 (PIP2) at the PM, induced by ligand activation of GPCRs and tyrosine kinase receptors, generates IP3[125].
3. $IP_3$ acts as a secondary messenger and binds to the IP3Rs at the ER membrane. Upon IP3 binding, $Ca^{2+}$ leaves ER through the IP3R.
4. Following a drop in ER [$Ca^{2+}$] below the threshold, $Ca^{2+}$ dissociates from STIM proteins initiating the conformational change via EF-SAM domain[102].
5. Unfolding and interaction of EF-SAM domains promote an extended conformation of the cytosolic portion of STIM proteins and exposure of CRAC-channel activating domain (SOAR/CAD) and polybasic tail[110].
6. Conformational change of STIM proteins promotes their oligomerisation via coiled-coil domains and consequently, their translocation to ER-PM contact sites. Polybasic K-rich tail of STIM proteins interacts directly with lipids of PM, anchoring proteins at ER-PM contact sites[108,110].

7. Accumulated at ER-PM contact sites, STIM proteins tether and activate Orai1 channel via SOAR/CAD domain [117].
8. Binding of SOAR/CAD domains of STIM proteins to the assembled Orai1-hexamer opens the CRAC channel, allowing a $Ca^{2+}$ to enter cytosol[105,108]**.** Current evidence suggests that at least 6 binding sites of Orai1 hexamer have to be occupied to detect signature CRAC properties (high $Ca^{2+}$ affinity, low unitary conductance and high CDI)[126]**.**
9. Sarco/ER $Ca^{2+}$-ATPase (SERCA) pumps the excess in $[Ca^{2+}]_{cyt}$ against a dominant-negative concentration gradient from the cytosol to ER.

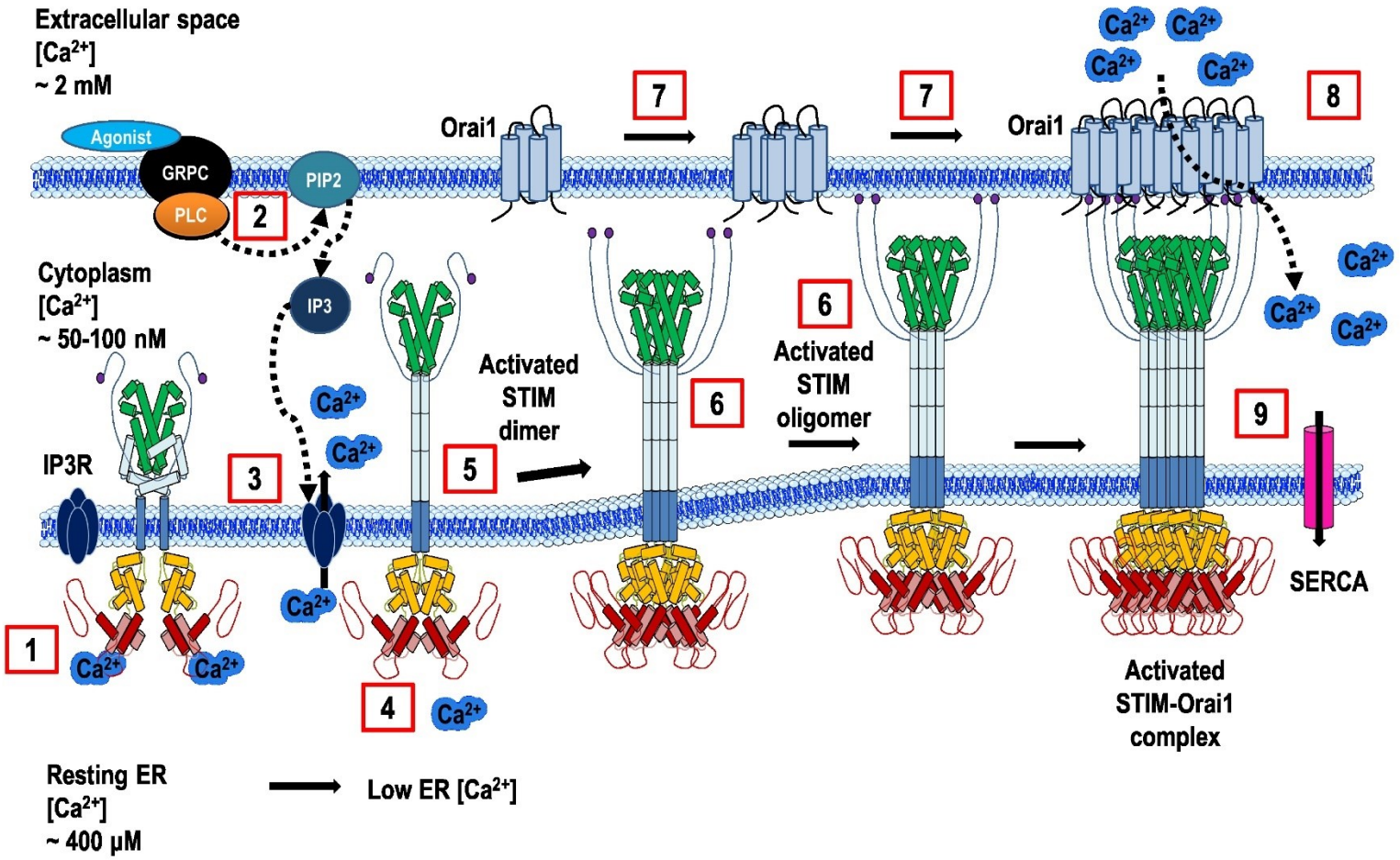


**Fig1.23 The molecular mechanism of SOCE activation as described in Section 1.26 of this chapter.**

### 1.2.7 SERCA-STIM1 complex

Sarco/ER Ca2+-ATPase (SERCA) pump is an ATP dependent $Ca^{2+}$ pump which refills ER $Ca^{2+}$ stores. Several different mechanisms can deplete ER $Ca^{2+}$ stores. The first mechanism is introduced in the earlier section, where IP3 binding to IP3Rs promotes $Ca^{2+}$ efflux from ER, activating SOCE. SOCE can also be activated independently of IP3Rs by inhibition of SERCA pump which promotes $Ca^{2+}$ leak through ER $Ca^{2+}$ leak channels, such as Sec61 and presenilins while blocking the movement of $Ca^{2+}$ to ER[127,128]. A substantial leak of ER $Ca^{2+}$ subsequently leads to the store-depletion and activation of SOCE. Experimentally, the SERCA inhibition can be realized by the application of thapsigargin – a sesquiterpene lactone from Thapsia garganica, and cyclopiazonic acid (CPA) – which is a toxic fungal metabolite.

In HEK293 cells, depletion of ER $Ca^{2+}$ stores also stimulated the formation of STIM1-SERCA complex at ER-PM junctions which was identified using co-immunoprecipitation techniques and TIRF microscopy[129]. Downregulation of STIM1 reduced ER $Ca^{2+}$ uptake, which suggested that the formation of STIM1-SERCA complex activated SERCA pump during SOCE allowing for the immediate $Ca^{2+}$ transfer from SOCE microdomain directly to ER[129]. However, upregulation of Orai1 reduced ER $Ca^{2+}$ store content, suggesting that Orai1 may act as an inhibitor of STIM1-SERCA complex[129].

### 1.2.8 The molecular mechanism of SOCE inactivation

To prevent excessive $Ca^{2+}$-influx, Orai1 channel is additionally regulated through a negative feedback mechanism known as $Ca^{2+}$-dependent inactivation (CDI). CDI can be subdivided into (1) slow CDI (SCDI), and (2) fast CDI (FCDI), which possess different sites of action and kinetics.

Following SOCE activation, global increases in [$Ca^{2+}$] activate SCDI that then occurs gradually in tens of seconds. SCDI is reported to be regulated by various proteins, including SARAF, caveolin, E-syt1, septin4, and PI(4,5)P2[130,131]. For SARAF-STIM1 interaction and the SARAF-regulation of SCDI, STIM1-Orai1 complex has to form within SOCE microdomain which is tethered by E-syt1, stabilised by septin4 and enriched in PI(4,5)P2[132]. More recently, calmodulin has been reported to bind STIM1 following SOCE activation, disassembling STIM1-Orai1 complexes and STIM oligomers[133].

FCDI is activated by $Ca^{2+}$ binding to a site located ~8 nm from the channel pore. Thus, FCDI occurs within several milliseconds after channel activation, and is modulated by a range of factors, including a negatively charged amino acid region of STIM1 (residues 475–483), the intracellular loop of Orai1 between M2-M3, the STIM1-Orai1 expression ratio, and the N-terminus of Orai1 (residues 68–91).

### 1.2.9 The role of TRPC in SOCE

The transient receptor potential canonical (TRPC) channels are channels that permeate $Ca^{2+}$, as well as $Na^{+}$ and $Mg^{2+}$. TRPCs are activated downstream of PLC activation and PIP2 hydrolysis. Besides the STIM and Orai protein families, TRPCs were also identified as a molecular component of SOCE, but none of the seven isoforms of TRPCs (1- 7) displays currents that resemble ICRAC[134]. However, various reports suggest that TRPC1 forms ternary complexes with STIM1 and Orai1 at ER-PM junctions[135]. Kim et al. have shown that the simultaneous expression of siRNAs targeted to TRPC1 and Orai1 diminished SOCE in HEK293 cells[136]. Overexpression of either Orai1 or TRPC alone failed to restore SOCE[136]. However, while overexpression of Orai1 in TRPC1 stable HEK293 cell line potentiated $Ca^{2+}$ entry, several studies detected no change in ICRAC during either upregulation or downregulation of TRPC1 levels[94,135]. More recent studies show that STIM1 can directly

activate both Orai1 and TRPC1, but via distinct residues[135]. The activation of TRPC1 occurs via C-terminal polybasic domain of STIM1, whilst Orai1 is activated by the Orai1-activating domain, SOAR[126,137]. Additionally, the activation of TRPC1s required Orai1-mediated $Ca^{2+}$ entry to trigger their recruitment at PM, where they were then activated by STIM1[138]. Expression of dominant-negative mutant and natural variant $Orai1^{R91W}$ attenuated TRPC1-STIM1 dependent SOCE, whilst overexpression of Orai1 potentiated it[138]. Together, these studies suggest that TRPC1-STIM1-mediated SOCE functional requires Orai1. However, additional work is still necessary for further understanding of TRPCs' involvement in SOCE.

### 1.2.10 STIM and ORAI1 related disorders

ORAI1 and STIM proteins are ubiquitously expressed throughout the tissues, where they act as key regulators of SOCE process, and subsequently, of physiological processes downstream of SOCE. Numerous studies, including studies of human patients, have discovered severe irregularities of SOCE process in various immunopathies, cancers and diseases of CNS[14,93,122,139].

#### *1.2.10.1 SOCE in the immune system*

Linkage analysis in an extended consanguineous family of patients diagnosed with the severe combined immunodeficiency (SCID) identified ORAI1, bearing R91W mutation, as a loss-of-function mutant that abolishes CRAC currents[93,140]. The crystal structure of *Drosophila* Orai provided an insight into the location of the K163 residue, the equivalent of R91 in human Orai1. K163 residue was found in the elongated pore of the channel with its side chain constricting the channel's pore diameter (Fig1.22)[118,122]. This observation suggested that the mutation of R91 to tryptophan resulted in a sizeable aromatic side chain within the channel pore, presumably preventing the channel from opening[141]. Additionally,

the R91W mutation was found undisruptive of ORAI1 expression at the PM or ORAI1 interaction with STIM1[140,141]. Hence, R91W mutation of Orai1 abolished CRAC and SOCE by impairing Orai1 channel function. In SCID patients, heterozygous expression of $Orai1^{R91W}$ had a dominant-negative effect on the CRAC channel, suggesting that mere incorporation of mutant into the hexameric channel structure was sufficient to impair the channel function[141].

Loss-of-function STIM1 mutants have also been detected in immunodeficient patients. STIM1 bearing R429C mutation located in its CAD/SOAR domain abolished SOCE in patient B cells[142]. As CAD/SOAR domain is essential for STIM1-Orai1 interaction, expression of $STIM1^{R429C}$ abolished STIM1-ORAI1 interactions. Additionally, expression of $STIM1^{R429C}$ also impaired the oligomerization of STIM1 cytosolic portion, suggesting that R429C mutation most likely altered the conformation of the STIM1 C terminus.

#### *1.2.10.2 SOCE in cancers*

STIM and ORAI proteins have become associated with various oncogenic processes such as apoptosis, proliferation, angiogenesis, antitumor immunity, and metastasis. Dysregulation of SOCE has been implicated in the tumour initiation stage, promoting genetic changes in premalignant cells and promoting malignant transformation[143]. In human prostate cancer cells, Orai1 represents the major molecular component of SOCE, which serves as a primary source of $Ca^{2+}$ during cellular apoptosis[144]. The downregulation of Orai1 and overexpression of its dominant-negative mutant $Orai1^{R91W}$ decreased the rate of thapsigargin-induced apoptosis in prostate cancer cells. Contrary to this finding, other evidence suggests that STIM/Orai-mediated SOCE actually promotes tumour growth and metastasis in a variety of cancer types. Upregulation of ORAI1 and STIM1, which led to the enhanced SOCE, were reported in therapy-resistant ovarian carcinoma cells[145].

Downregulation or pharmacological targeting of STIM1/ORAI1 complex has been demonstrated to restrain the growth and metastasis of breast, colorectal, cervical, liver, nasopharyngeal, epidermoid, glioma, and melanoma[13,146–148].

#### *1.2.10.3 SOCE in neurodegenerative disorders*

While SOCE is the main $Ca^{2+}$ entry pathway of non-excitable cells, accumulating evidence also indicates its role in the CNS, particularly in the hippocampal pyramidal neurons, cortical pyramidal neurons, and cerebellar Purkinje neurons[149–152]. The expression of both STIM homologs has been reported in hippocampal neurons where STIM1 was observed to colocalized Orai1 upon depletion of intracellular $Ca^{2+}$ stores in dendrites and soma[114,151,152]. Activation of STIM1 and nSOCE was achieved via activation of type I metabotropic glutamate receptors (mGluR) or muscarinic acetylcholine receptors[153,154]. However, in hippocampal neurons, STIM1 was also reported to exert nSOCE-independent functions[154]. The mice with engineered forebrain-specific knockout exhibited a mild learning delay during STIM1 knockout, whilst the effect on learning and memory in STIM2 knockout mice was insignificant[155]. However, simultaneous knockout of both STIM homologs caused a pronounced impairment in spatial learning and memory and in enhanced long-term potentiation at CA3-CA1 hippocampal synapses[155].

STIM2 is predominately expressed in the hippocampus where it has been reported to regulate nSOCE in hippocampal synapse essential for the long-term maintenance of mushroom spines[139,156]. In Alzheimer disease mice model, treatment with novel nSOCE modulator NSN21778 rescued mushroom spine loss and synaptic plasticity impairment[156]. Furthermore, downregulation of STIM2 was observed in cells from AD patients, suggesting that STIM2 may have a protective role in amyloid synaptotoxicity[157]. These studies suggest that underlying mechanisms of SOCE and SOCE-responsive proteins may be a potential

therapeutic target in various pathological systems. However, considering the ubiquitous expression of ORAI1 and STIM proteins, as well as differential roles of STIM homologs, further inquiries and understanding of SOCE and SOCE-responsive proteins are required before designing target-specific treatment.

### 1.2.11 The role of σ1R in SOCE

In 2016 and 2017, several studies demonstrated the ability of σ1R to regulate SOCE but disagreed about the underlying mechanism of σ1R's involvement. Brailoiu et al. have shown that treatment of rat brain endothelial cells with cocaine, which is a σ1R agonist, inhibited SOCE[158]. Pre-treatment with the selective σ1R antagonists BD-1063 and NE-100 eliminated cocaine-induced SOCE inhibition, which suggested that it most likely occurred in σ1R-dependent manner[158]. This study was followed by another where Srivats et al. demonstrated that following store-depletion σ1R formed a complex with STIM1 and Orai1 at ER-PM junctions of HEK293 cells[34]. TIRFM, AFM and immunoprecipitation results showed that σ1Rs translocated in STIM1-dependent manner to the ER-PM junctions where they reduced the effectiveness of STIM1 to Orai1 interaction. Additionally, calcium functional assays showed that upregulation of σ1R in HEK293 cells inhibited SOCE. Treatment of CHO cells, which expressed σ1Rs endogenously, with (+)SKF10047, σ1R agonist, increased binding of STIM1 to σ1R and resulted in reduced SOCE, whereas treatment with BD1047, the antagonist, had the opposite effects.

Gueguinou et al. reported the potentiation of Orai1-mediated $Ca^{2+}$ influx by σ1R[14]. In breast cancer and colorectal cancer cells, silencing or inhibiting σ1R using either siRNA or σ1R ligands prevented functional coupling of calcium-activated $K^+$ channel SK3 with Orai1, and subsequently, resulted in lower Orai1-mediated $Ca^{2+}$ influx. Hence, this study reported the opposite effect of σ1R in comparison to earlier studies, proposing that the role of σ1Rs

in the regulation of SOCE could also depend on the cellular dynamics and the expression and availability of its interactive partners. Studying the effect of σ1R bearing ALS-inducing E102Q mutation, Dreser et al. also reported that overexpression of wild-type σ1R potentiated SOCE in MCF-7 breast cancer cell line[159]. Contrary, the overexpression of $\sigma1R^{E102Q}$ failed to affect SOCE, but significantly reduced STIM1 proteins levels in MCF-7 cells. These conflicting results suggest that σ1R possesses the ability to regulate SOCE, but the underlying mechanisms of its action require further investigation.

## 1.3 Aims

This thesis investigates the role of the σ1R in regulating SOCE microdomains and the underlying mechanism of action. The main objectives of this thesis are as follows:

(1) ***To determine how enhanced expression of σ1R affects SOCE.*** This was investigated by creating σ1R baculovirus and the appropriate viral control. Cytosolic $Ca^{2+}$ signals were measured in response to store-depletion and during $Ca^{2+}$ influx in the population of HEK293 cells using fluorescent $Ca^{2+}$ dyes and genetically encoded $Ca^{2+}$ indicator GCaMP6f. This is discussed in Chapter III.

(2) ***To develop a reliable method to measure the Orai1-mediated $Ca^{2+}$ signal within the SOCE microdomain, and to compare the effect of the σ1R on the amplitude of this signal.*** This was achieved by utilising targeted $Ca^{2+}$ reporter protein fused to the Orai1 channel, named G-GECO1.2-Orai1, and applying the semi-automated approach in G-GECO1.2-Orai1 detection, signal extraction and analysis. Cytosolic $Ca^{2+}$ signals were measured in response to store-depletion and during $Ca^{2+}$ influx using TIRFM. This is discussed in Chapter IV.

(3) ***To determine whether the enhanced expression of $σ1R^{E102Q}$ ALS-inducing mutant affects SOCE.*** This was investigated by creating σ1R bearing E102Q mutation. Cytosolic $Ca^{2+}$ signals were measured in response to store-depletion and during $Ca^{2+}$ influx using both GCaMP6f and G-GECO1.2-Orai1. This is discussed in Chapter V.

(4) ***To determine whether σ1R interacts with STIM1 and STIM2 proteins in situ.*** This was investigated using proximity ligation assay (PLA) and imaging techniques. This is discussed in Chapter VI.

(5) ***To determine how enhanced expression of σ1Rs affects STIM2.2/Orai1 mediated SOCE.*** This was investigated by upregulation of STIM2.2 in HEK293 cells transduced with σ1R baculovirus. Cytosolic $Ca^{2+}$ signals were measured in response to store-depletion and during $Ca^{2+}$ influx using both GCaMP6f and G-GECO1.2-Orai1. This is discussed in Chapter VII.

# 2 Chapter II:

# Methods

## 2.1 Cell Culture

### 2.1.1 Cell lines

Four immortalised cell lines were used in this study: Flp-In™ human embryonic kidney (HEK) 293, HEK293, HEK293-IP3R$^{-/-}$ and HeLa cell lines. Flp-In™-HEK293 cell line was a generous gift from Sussex Drug Discovery Center (SDDC). HEK293 and HEK293-IP3R$^{-/-}$ cell lines were a generous gift from Collin W. Taylor's Lab (University of Cambridge). Flp-In™-HEK293 cell line was used for $Ca^{2+}$ measurements in response to store-depletion by thapsigargin using Flexstation III, and for NFAT translocation. This cell line was used due to good transfection yield via PEI method. HEK293 and HEK293-IP3R$^{-/-}$ cell lines were used for $Ca^{2+}$ measurements in response to store-depletion by ATP and carbachol (ATP/Cch) using Flexstation III. Additionally, HEK293 cell line was used for TIRFM experiments as it had a flatter footprint in comparison to Flp-In™-HEK293 cell line, which facilitated TIRFM recordings. HeLa cell line was used to visualise protein-protein interaction *in situ* (proximity ligation assay; PLA) and subcellular distribution of proteins.

### 2.1.2 Cell maintenance

Flp-In™-293 and HeLa cell lines were cultured in Dulbecco's modified Eagle's medium (DMEM; ThermoFisher), supplemented with 10% foetal bovine serum (FBS, Gibco) and 1% penicillin/streptomycin (P/S, Hyclone). HEK293 and HEK293-IP3R$^{-/-}$ cell lines were cultured in DMEM/F-12 with GlutaMAX (ThermoFisher) supplemented with 10% FBS and 1% P/S. All cells lines were maintained in 75cm$^2$ flasks (T75) at 37°C in humidified air with 5% $CO_2$ and passaged every 3–4 days using in-house-made PBS and 0.05% Trypsin-EDTA (ThermoFisher). Approximately 1.5 million cells were passaged to a new T75 flask to obtain 75-80% confluency in 3-4 days.

| PBS | 1L, pH=7.40 |
|---|---|
| NaH2PO4* H2O | 1.3 mM |
| Na2HPO4 | 8.1 mM |
| NaCl | 145 mM |

**Table 2.1-1 Composition of phosphate buffered saline (PBS)**

## 2.2 Molecular biology

### 2.2.1 Plasmid DNA Preparation

Plasmid DNA was isolated from a bacterial culture grown from a single transformed colony in 3 ml of LB medium with appropriate antibiotics at 37°C. overnight. For this purpose, Monarch Miniprep kit was used according to the manufacturer's instructions.

### 2.2.2 2.3.2 Polymerase chain reaction (PCR)

The PCR reaction mix was prepared in a final volume of 50 µl using 20ng of DNA and NEB reagents (Table 2.21). A general thermocycling condition can be found in Table 2.22. Annealing Tm temperature was calculated for each set of primers using NEB Tm calculator. All primers used within this study can be found in Table 2.23. All PCR products were analysed using agarose gel electrophoresis.

| COMPONENT | FINAL CONCENTRATION |
|---|---|
| 5X Q5 Reaction Buffer | 1X |
| 10 mM dNTPs | 200 µM |
| 10 µM Forward Primer | 0.5 µM |
| 10 µM Reverse Primer | 0.5 µM |
| Template DNA | < 1,000 ng |
| Q5 High-Fidelity DNA Polymerase | 0.02 U/µl |
| 5X Q5 High GC Enhancer (optional) | (1X) |
| Nuclease-Free Water | |

**Table 2.2-1 List of NEB PCR reagents**

| STEP | TEMPERATURE | TIME |
|---|---|---|
| Initial Denaturation | 98°C | 30 seconds |
| 25–35 Cycles | 98°C<br>*50–72°C<br>72°C | 5–10 seconds<br>10–30 seconds<br>20–30 seconds/kb |
| Final Extension | 72°C | 2 minutes |
| Hold | 4–10°C | |

**Table 2.2-2 Thermocycling PCR conditions**

### 2.2.3 Agarose gel electrophoresis

A custom made 0.8% agarose gels were used for analysis of PCR products. Agarose was added to 1x TBE buffer (89 mM Tris base, 89 mM g/l boric acid, 2.5 mM EDTA,) at final concentration of 0.8%. The solution was repeatedly microwaved until boiling and swirled until the agarose had dissolved. The agarose was cooled for 10-15min at room temperature before 5 µl ethidium bromide was added to the solution. The solution was poured into a mini gel cast with a gel comb and allowed to polymerize for 45 min minutes at room temperature. To load samples, the comb was removed, and the gel was submerged in 1x TBE buffer. Samples were diluted in DNAse free-water, where appropriate, and mixed with 5x loading buffer before loading into wells. The sample on the gel was run at 100V for 30–45 minutes.

### 2.2.4 Site directed mutagenesis

GeneArt Site Direct Mutagenesis kit (ThermoFisher) was used to induce mutations. Complementary primers were designed using GeneArt® Primer and Construct Design Tool. Primers (Table 2.23) contain mutagenic sequence flanked on either side by 15 nucleotides which complement the template sequence. AccuPrime™ Pfx (2.5 U/µL) polymerase was used in a 50µl reaction according to manufacturer guidelines. Negative control reaction was set up for each PCR containing no primers. 5 µL of the PCR product was analyzed on a 0.8% agarose gel as above. Following confirmation of PCR product, 4 µL of the product was used in recombination reaction. Recombination mix was incubated at room temperature for 10 min when the recombination reaction was stopped by adding 1 µL 0.5 M EDTA. 2 µL from the recombination reaction was used for transformation.

Transformation reaction was performed using One Shot® MAX Efficiency® DH5αTM-T1R competent cells supplied with the GENEART® Site-Directed Mutagenesis

System. 50-µL vial of DH5αTM-T1R cells was thawed for 5- 7 minutes on ice for each transformation. 2 µL of the Recombination mix was transferred directly into each vial of cells and incubated on ice for 12 minutes. Following incubation, vials were heat-shocked for exactly 30 seconds at 42°C using Eppendorf Thermo-Mixer C, then incubated on ice for additional 2 min. After incubation, the vials were removed from ice. 250 µL of pre-warmed SOC medium was added to each vial, using aseptic conditions. For kanamycin-resistant plasmids, the vials containing SOC medium were placed sideways in the Infors HT Ecotron shaking incubator at 225 rpm and 37$^{o}$C for exactly 1 hour. 1h-incubation was not necessary for ampicillin-resistant plasmids, and we proceeded to the next step immediately after addition of pre-warmed SOC medium. 10 µL of each transformation reaction was additionally diluted with 90 µL of SOC medium, and then transferred to the pre-warmed agar plates with appropriate antibiotic resistance Plates were inverted and incubated in SciQuip Incu-50S incubator at 37°C for 16–20 hours. Following incubation, plasmid DNA isolation as performed as above (Section 2.21). Plasmids were sequenced by Eurofins-Genomics.

| Primer name | Sequence |
|---|---|
| **DNA Cloning Primers** | |
| **σ1R-V5-FWD** | **5'-CACCATGCAGTGGGCCGTGG-3'** |
| **σ1R-V5-REV** | **5'-TCAATGGTGATGGTGATGATG-3'** |
| **PCR Analysis Primers** | |
| **M13-FWD** | **5'-GTTTTCCCAGTCACGAC-3'** |
| **M13-REV** | **5'-CAGGAAACAGCTATGAC-3'** |
| **Mutagenesis Primers** | |
| **Orai1$^{R91W}$-FWD** | **5'- CTTAAAGCCTCCAGCTGGACCTCGGCTCTGC-3'** |
| **Orai1$^{R91W}$-REV** | **5'- GCAGAGCCGAGGTCCAGCTGGAGGCTTTAAG-3'** |
| **σ1R$^{EndCodon}$-FWD** | **5'- TTTGGCCAGGACCCTTGACTAGAGGGCCCGCGG -3'** |
| **σ1R$^{EndCodon}$-REV** | **5'- CCGCGGGCCCTCTAGTCAAGGGTCCTGGCCAAA-3'** |
| **σ1R$^{E102Q}$-FWD** | **5'-CACGCCTCGCTGTCCCAGTATGTGCTGCTCT-3'** |
| **σ1R$^{E102Q}$-REV** | **5'- AGAGCAGCACATACTGGGACAGCGAGGCGTG-3'** |

**Table 2.2-3 List of primers**

### 2.2.5 Bacmid transposition and recombinant bacmid DNA isolation

σ1R-V5/BacMam pCMV-DEST transfer vector was utilized to generate the recombinant σ1R-V5 baculovirus. This transfer vector was generated as described in ViraPower™ BacMam Expression System and BacMam pCMV-DEST Vector Kit protocol[160] (Life Technologies) using following DNA cloning primers: σ1R-V5-FWD (5'-CACCATGCAGTGGGCCGTGG-3') and σ1R-V5-REV (5'-TCAATGGTGATGGTGATGATG-3'). BacMam pCMV-DEST transfer vector without insertion was employed to generate appropriate viral control - WT$^{VC}$ baculovirus. σ1R-V5 was transposed into bacmid using *E.coli* DH10 MultiBac competent cells (Invitrogen). 1 µg of σ1R-V5/BacMam pCMV-DEST and BacMam pCMV-DEST was incubated on ice for 30 min with 100 µl of E.coli DH10 MultiBac competent cells. Each mix was heat-shocked for 45 seconds at 42˚C, returned to the ice for 2min. resuspended in 900 µl of S.O.C medium

(Invitrogen). Insertion of σ1R-V5 into bacmid occurred by Tn7 transposition mediated by the Tn7 transposase. Each mix was incubated at 37˚C at 225rpm for 6 hours. After 6 hours, the cultures were plated onto bacmid transposition plates (agar plates with 50 μg/ml kanamycin, 10 μg/ml tetracycline, 7 μg/ml gentamycin, 100 μg/ml Bluo-gal, and 40 μg/ml IPTG) and incubated for 48 hours. The positive transposition was determined using blue-white screening. Successful transposition of fragment via Tn-7 sites disrupts the lacZα gene coding for β-galactosidase – an enzyme which is necessary to hydrolyse Bluo-gal, allowing growth of the blue colonies. Therefore, individual white colonies were picked and replated onto bacmid transposition plates for additional 24 hours to verify positive transposition. Individual white colonies were picked to inoculate bacmid transposition medium (LB medium with 50 μg/ml kanamycin, 10 μg/ml tetracycline, 7 μg/ml gentamycin). The cultures were incubated at 37˚C at 225rpm for 24 hours. After 24 hours, bacmid cultures were harvested by centrifugation (4000rpm for 10 minutes). Cell pellets were resuspended in 0.4ml of Buffer P1 and Buffer P2 (QIAprep Spin MiniPrep kit) and incubated at room temperature for 5 minutes, following by incubation with 0.4ml 3M potassium acetate (pH 5.5) and additional incubation on ice for 10 min. The supernatant was resuspended in 0.8ml of ice-cold isopropanol, incubated at -20°C for 10 minutes, and then centrifuged at room temperature for 15 minutes at 13000rpm. The pellet was washed in 0.7ml 70% ethanol and centrifuged at room temperature for 15 minutes at 13000rpm. The supernatant was carefully discarded. The DNA pellet was air-dried for 20 minutes and dissolved in 40 μl DNAse and RNAse-free water. Transposition was verified by PCR analysis of the pellet.

### 2.2.6 Insect cells transfection and baculovirus amplification

The bacmid contains the polyhedrin (polH) promoter sequence required for protein expression in the insect cells. To express a σ1R-V5 protein, Sf9 insect cells were selected.

Sf9 cells were transfected with the recombinant bacmid DNA, according to manufacturer instructions[160], to start production of recombinant baculovirus particles containing DNA of interest. To amplify the $WT^{VC}$ and σ1R-V5 P1 recombinant baculovirus particles, Sf9 insect cells were placed in a 35-mm petri dish and diluted with antibiotic-free SF900IISFM medium (ThermoFisher) to achieve cell density of $1 \times 10^6$ cells/ml. Following dilution, Sf9 cells were left to adhere during incubation at 27°C for 1 hour. Following incubation, 2 ml of the P1 (passage 1) baculovirus was used to transfect the cells during further incubation at 27°C for 3–5 days. To check for contamination and for the number of insect cells infected, transfected Sf9 cells were monitored every 24 hours. 5 days after transfection, newly generated generation of baculovirus was collected from supernatant and transferred to sterile cryotubes containing 1% heat-inactivated FCS (Gibco). The cryotubes containing now P2 baculovirus were stored at 4°C in the dark. Whole-cell extracts were prepared to check protein expression levels by western blotting. P2 recombinant baculovirus has been amplified as above, to achieve a higher volume of P3 recombinant baculovirus – which was then used for transduction. Infected Sf9 cultures were incubated at 28°C, at 150 rpm for 72 hours. 100ml of P3 recombinant baculovirus was obtained in Sf-900 II SFM medium (w/o antibiotic). During baculovirus amplification, the pellet was harvest and analyzed by Western Blotting (Fig2.21).

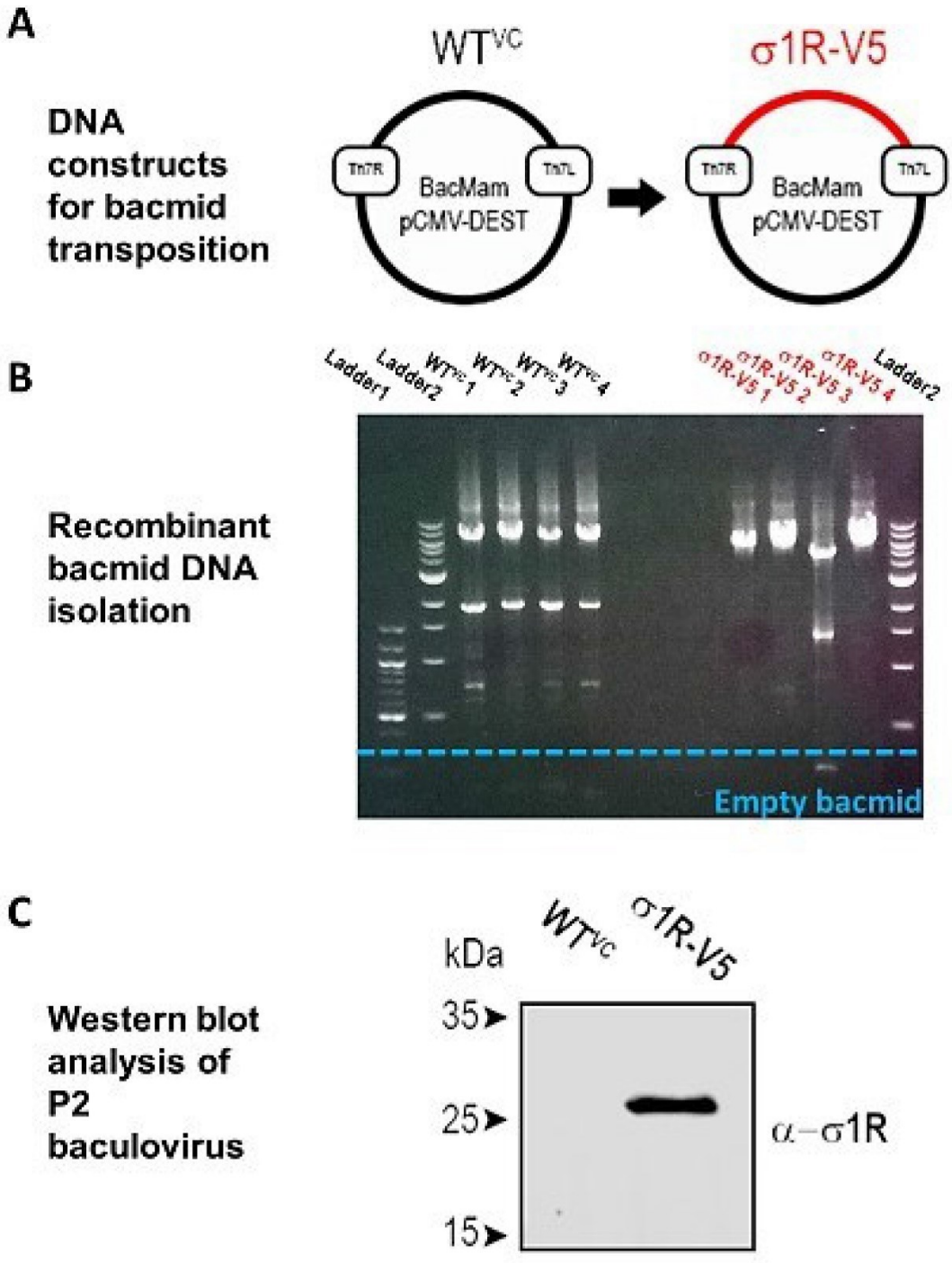


**Fig2.21. A)** Schematics of Bacmam pCMV-DEST constructs used to generate $WT^{VC}$ and σ1R-V5 baculovirus. **B)** A PCR confirmation of transposition of $WT^{VC}$ and σ1R-V5 coding sequences using M13 primers that align upstream/downstream of Tn7 sites of insertion into bacmid. Empty bacmid was expected at 300bp (dashed blue line). PCR products $WT^{VC}$ (2) and σ1R-V5 (4) were used for transfection of Sf9 cells. Ladder 1=100bp NEB. Ladder 2 = 1kb NEB. C) Western blot analysis of P2 baculovirus generation. σ1R-V5 was detected ~ above 25kD using monoclonal α-σ1R.

### 2.2.7 Plaque assay

Plaque assays were performed to determine the viral titer (pfu/ml). The viral titer [plaque-forming units per ml (pfu/ml)] was determined for each P3 baculovirus stock. The P3 viral stock was diluted from $10^6$ to $10^7$-fold, of which 100 µl was added into plates for plaque assay containing Sf9 insect cells in SF900IISFM media. Plates were incubated at room temperature for 1 hour. Liquid medium was removed and replaced with 1% agarose containing medium, which was allowed to polymerise. 1 ml of SF900IISFM medium was added on the agarose in the plates before the plates were incubated at 27°C for 3–4 days. Cells were stained by adding 0.02% neutral red per plate and incubated at 27°C in the dark for 2 hours before removing all the liquid. Plates were stored overnight at room temperature. Viral plaques were identified as “clear zones” in the agarose generated by infection of Sf9 insect cells. The number of plaques was calculated as a viral titer. The results of the plaque assay are recorded below. P3 baculovirus stock was stored at 4˚C and protected from light. Expression of σ1R-V5 baculovirus after transduction using 15 multiplicity of infection (MOI15) of P3 baculovirus generation was verified in HEK293 using immunostaining (Fig2.21). Calculation and transduction protocol can be found in Section 2.4 of this chapter.

| Bacmid | Plaque count in $10^7$ dilution | | Plaque count in $10^6$ dilution | | Average viral titer |
|---|---|---|---|---|---|
| | Calculated titer in original stock | | | | |
| First P3 Stock | | | | | |
| $WT^{VC}$ | 14 | 5 | 72 | 49 | $2.75x10^8$ |
| | $2.5x10^8$ | | $3x10^8$ | | |
| σ1R-V5 | 6 | 10 | 50 | 59 | $2.85x10^8$ |
| | $3x10^8$ | | $2.7x10^8$ | | |
| Second P3 Stock | | | | | |
| $WT^{VC}$ | | 2 | 21 | | $1.05x10^8$ |
| | $1 x10^8$ | | $1.1 x10^8$ | | |
| σ1R-V5 | | 3 | | 23 | $1.3x10^8$ |
| | $1.5 x10^8$ | | $1.2 x10^8$ | | |

**Table 2.2-4 Viral titer of $WT^{vc}$ and σ1R-V5 baculovirus stock. Viral titer is estimated by number of plaque-forming units per l ml of (pfu/ml) based on number of plaques counted 96 hours after infection of Sf9 cells using series of dilutions. Initial dilution of baculovirus stock before plaque essay was 5x in Sf-900 II SFM medium. Titer of original stock is calculated using following formula: Plaque count Average x Dilution x Initial Dilution.**

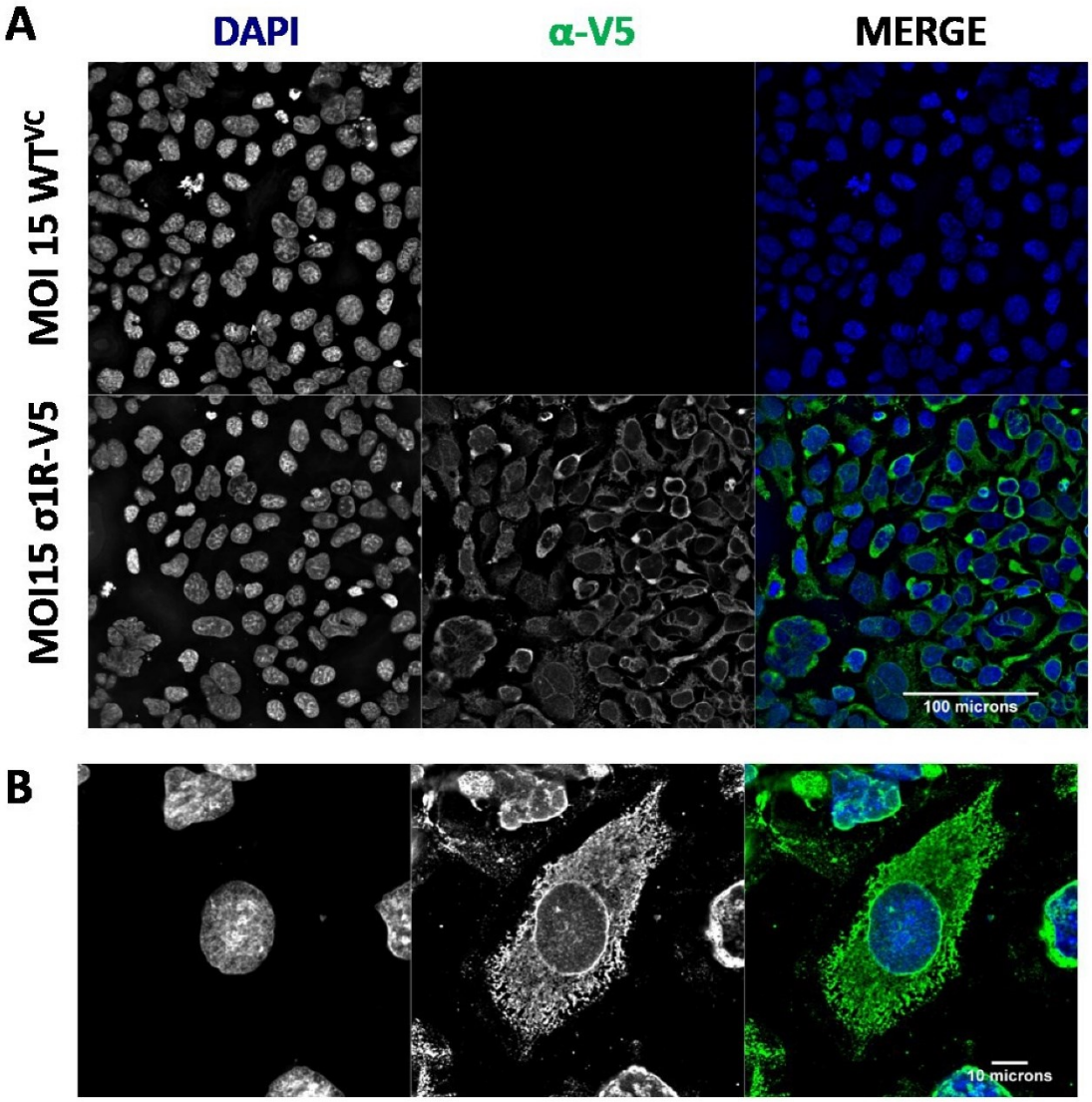


**Fig2.22 σ1R-V5 expresses in HEK293 cells 24h post-transduction with σ1R-V5 baculovirus. A)** Images of HEK293 cells transduced with MOI15 of $WT^{VC}$ and σ1R-V5 baculovirus particles and fixed in 4% PFA 24 hours post-transduction. HEK293 cells transduced with σ1R-V5 baculovirus express V5-tagged σ1R (primary antibody: α-V5; secondary antibody: anti-mouse IgG (H+L) ALexaFluor Plus 488). V5-tagged σ1R was not detected in HEK293 cells transduced with control $WT^{VC}$ baculovirus. Nucleus is stained with DAPI. Scale bar = 100 µm. **B)** Subcellular localization of V5-tagged σ1R 24h after transduction of HEK293 cells with MOI15 of σ1R-V5 baculovirus. V5-tagged σ1R expresses in characteristic reticular shape from nuclear envelope towards the periphery of the cell. Scale bar = 10 µm.

## 2.3 Transfection

### 2.3.1 Poly-ethyl enimine (PEI) method

PEI method was used for Flexstation and NFAT translocation assays. HEK293 cells were grown to 80-85% confluence. For one well of a 6-well plate, 1µg of plasmid DNA was mixed with 1µl of 1.3µg/µl PEI aqueous solution (Polysciences, Inc.) and then diluted with 150µl of OptiMEM (Gibco). This mixture was incubated for 15min at room temperature and added to wells containing 1mL of serum-free DMEM. A transfection media was replaced 4-6 hours after incubation with fresh DMEM growth medium. Cells were incubated for a further 40-48 hours before being used for experiments.

### 2.3.2 Lipofectamine method

Lipofectamine method was used for TIRFM and imaging assays. HEK293 and HeLa cells were grown to 70% confluence and transfected using lipofectamine 2000 (Life Technologies). For one well of a 6-well plate, 1µg of plasmid DNA was mixed with 50 µl of Opti-MEM (Gibco). This mixture was incubated at room temperature for 5 min and combined with another 50 µl of Opti-MEM containing 2µL of lipofectamine. A new mixture was incubated for a further 20 minutes at room temperature. This mixture was then added to cells in 1 ml of serum-free DMEM. A transfection media was replaced 4-6 hours after incubation with fresh DMEM growth medium. Cells were incubated for either 24h or 48 hours at 37ºC, depending on the experimental requirements.

| Plasmid | Description | Reference |
|---|---|---|
| **BacMam Gene Delivery System** | | |
| σ1R-V5 | Plasmid coding for V5-tagged human σ1R created using pcDNA3.1/V5-His-TOPO using HindIII and AgeI. | 34 |
| pENTR/dTOPO | Linearized pENTR/dTOPO vector used as an entry vector for σ1R-V5 Gateway cloning and bacmid | 160 |
| BacMam pCMV-Dest | BacMam pCMV-Dest Vector used as destination vector for Gateway cloning and bacmid generation | 160 |
| **NFAT translocation assay** | | |
| NFAT1-GFP | The expression plasmid for mouse NFAT1-GFP which was a gift from A. Parekh (University of Oxford, Oxford, England) | 161 |
| **Calcium assays** | | |
| pGP-CMV-GCaMP6f | Vector for mammalian expression of ultrasensitive protein calcium sensor. | 162 |
| mCh-STIM1 | Human STIM1 subcloned into mCherry-C1 (Takara Bio Inc.) using XbaI and NotI. | 34 |
| mCh-STIM-CAD | mCherry-targeted human STIM CAD domain | 34 |
| HA-STIM1 | HA-tagged human STIM1 | 163 |
| STIM2.2 | The expression plasmid for human STIM2.2 which was a gift from B. Niemeyer (School of Medicine, Saarland University, Germany). | 116 |
| STIM2.2-mCh | The expression plasmid for mCherry-tagged human STIM2.2 where mCherry-coding sequence replaced the variable domain (I648-K711), retaining 121 C-terminal aa residues. | 116 |
| STIM2.1-mCh | The expression plasmid for mCherry-tagged human STIM2.1 where mCherry-coding sequence. | |
| Orai1$^{R19W}$ | The expression plasmid for human dominant-negative mutant of Orai1 which was a gift from C.Taylor (University of Cambridge, Cambridge, England). | 164 |
| σ1R-mKate | mKate-targeted human σ1R | 34 |
| σ1R-EGFP | EGFP-targeted human σ1R | 34 |
| ER-dsRED | ER-targeted marker | |
| PMEM-td-Tomato | PM-targeted marker | |

**Table 2.3-1 List of plasmids**

## 2.4 Transduction

Cells were plated at 80-90% confluence allowed to adhere. After cell adhesion, media si removed and baculovirus was added at an MOI (Multiplicity of Infection)15 in infection medium (Sf-900 II SFM medium and DMEM without any antibiotic and serum). Appropriate volume for MOI 15 is calculated using titer results (table) and equation below:

**Equation 2.4-1 Calculation of volume for transduction with baculovirus particles**

$$MOI\ (pfu/number\ of\ cells) \times number\ of\ cells = titer\ (pfu/ml) \times volume\ (ml)$$

Cells were incubated at 37 C for 12 h before using where appropriate (transfection, calcium imaging assays, biochemistry).

## 2.5 Calcium imaging assays

### 2.5.1 Measurements of $[Ca^{2+}]_c$ in the cell population

For measurements of $[Ca^{2+}]_c$ in the cell population, Flp-In™ HEK 293, HEK293, HEK293-IP3R$^{-/-}$ cells were seeded into poly-L-lysine coated 96-well plates. 6 hours after seeding, cells were transduced with the multiplicity of infection (MOI) 15 of $WT^{VC}$ or σ1R-V5 baculovirus particles and used for experiments 24- or 72-hours post-transduction using $Ca^{2+}$ fluorescent dyes or genetically encoded $Ca^{2+}$ indicator GCaMP6f.

#### *2.5.1.1 Using $Ca^{2+}$ fluorescent dyes*

After 24 hours, cells were incubated with 2μM Fluo-4-AM (Life technologies) or Fluo-8-AM (ATT Bioquest) in house-prepared HEPES-buffered saline (NES) for 40 min at room temperature. In nominal $Ca^{2+}$-free NES, $Ca^{2+}$ was omitted, and 1 mM EGTA was added.

Fluorescence (excitation 490 nm, emission 520 nm) was measured at room temperature using Flexstation III plate-reader with automatic additions. At the beginning of the assay, extracellular $Ca^{2+}$ was quenched using 1 mM EGTA and $Ca^{2+}$ stores were depleted using either 1 μM thapsigargin (Thermo Fisher), CPA (Tocris) or 100 μM ATP and carbachol (Sigma). Subsequently, 2mM $Ca^{2+}$ was added to assess $Ca^{2+}$ entry. $F_{max}$ and $F_{min}$ are the fluorescence values determined after addition of Triton X-100 (0.1%) in NES with 10 mM $Ca^{2+}$ and EGTA respectively. The composition of NES can be found in Table.2.31.

| NES | 1L, pH=7.40 |
|---|---|
| NaCl | 150 mM |
| KCl | 10 mM |
| $MgCl_2$ | 1 mM |
| $CaCl_2$ | 2 mM |
| Glucose | 10 mM |
| HEPES | 10 mM |

**Table 2.5-1 Composition of NES buffer**

### *2.5.1.2 Using GCaMP6f*

After 24 hours, cells were transfected with GCaMP6f using PEI method. 48h after transfection cells fluorescence (excitation 485 nm, emission 520 nm) was measured at room temperature using Flexstation III plate-reader with automatic additions. At the beginning of the assay, extracellular $Ca^{2+}$ was quenched using 1 mM EGTA, and $Ca^{2+}$ stores were depleted using 1 μM thapsigargin (Thermo Fisher). Subsequently, 2mM $Ca^{2+}$ was added to assess $Ca^{2+}$ entry. $F_{max}$ and $F_{min}$ are the fluorescence values determined after the addition of Triton X-100 (0.1%) in NES with 10 mM $Ca^{2+}$ and EGTA respectively.

| HBSS | 1L, pH=7.40 |
|---|---|
| 1 powder flask | Sigma H1387 |
| HEPES | 2.383g (10 mM) |
| HBSS wo Ca2+/Mg2+ | 1L, pH=7.40 |
| 1 powder flask | Sigma H4891 |
| MgCl2 | 0.095g (1mM) |
| HEPES | 2.383g (10 mM) |

**Table 2.5-2 Composition of HBSS buffers**

## 2.5.2 Measurements of $[Ca^{2+}]_c$ in the single cells

### *2.5.2.1 Using G-GECO1.2-Orai1*

For measurements of $[Ca^{2+}]_c$ in the single cells, HEK293 cells were seeded onto poly-L-lysine coated coverslips (16mm for epifluorescence microscopy, 24mm for TIRFM). 6 hours after seeding, cells were transduced with the multiplicity of infection (MOI) 15 of $WT^{VC}$ or σ1R-V5 baculovirus particles and used for experiments 48- or 72-hours post-transduction using genetically encoded G-GECO1.2-Orai1 (Kd value of 1,150 nM; Addgene). After 24 hours, cells were transfected with G-GECO1.2-Orai1 using lipofectamine method. 48h after transfection cells fluorescence (excitation 488 nm, emission 535 nm) was measured at room temperature using epifluorescence microscope and TIRFM. The exception was made during simultaneous overexpression of G-GECO1.2-Orai1 with STIM constructs to avoid prolonged constitutive $Ca^{2+}$ influx and cytotoxicity; these cells were used from 15h (mCh-STIM-CAD construct) to 30h from transfection. At the beginning of the assay, extracellular $Ca^{2+}$ was quenched using 0.1 mM EGTA, and $Ca^{2+}$ stores were depleted using 1 μM thapsigargin (Thermo Fisher). Subsequently, 2mM $Ca^{2+}$ was added to assess $Ca^{2+}$ entry. $F_{max}$ is the fluorescence value determined after the addition of 5μM ionomycin in HBSS containing 2mM $Ca^{2+}$. The analysis of recordings using G-GECO1.2-Orai1 is more

thoroughly assessed in Chapter IV, Section 4.21. The composition of HBSS can be found in Table 2.32.

### 2.5.3 NFAT translocation assay

HEK293 cells were seeded onto poly-L-lysine-coated 24-mm coverslips, mock-transduced (WT) or transduced with 15 MOI of either $WT^{VC}$ or σ1R-V5 baculovirus, transfected with GFP-NFAT plasmid using PEI method and used after 48 hours. The rate of NFAT nuclear translocation was measured as the distribution of GFP fluorescence before and after addition of thapsigargin (5 μM) to cells at 37ºC in NES. Fluorescence (excitation at 488 nm, emission at 510-540 nm) was collected using a Leica SP8 confocal microscope with an oil-immersion 40x objective (NA 1.25). Analyses of nuclear translocation of GFP-NFAT were performed as a blinded study by two independent analysts. In total, 6 coverslips per group were analysed from 3 independent experiments (n=3) with ~ 20 cells within the field of view.

## 2.6 Biochemistry

### 2.6.1 Analysis of protein expression

HEK293 and HeLa cells were grown in 1 well of 6W plate. Where appropriate, cells were transduced and transfected as previously described. At appropriate timepoints, cells were washed 3x in 1ml of ice-cold PBS and collected in 80μl of 1X RIPA buffer (Sigma) containing 1X of protease inhibitor cocktail (Sigma). Collected cells were then agitated at +4ºC for 60 min. The samples were centrifuged at 16000xg at +4ºC for 10 min. Supernatant was transferred in a clean tube for storage at -20ºC and the pellet was discarded. Protein expression was analysed by protein gel electrophoresis followed by immunoblotting.

### 2.6.2 Western blot

Precast NuPAGE Bis-Tris gels (Invitrogen, 4-12%) and 1XMES buffer (Thermo Fisher) were used for protein electrophoresis to separate proteins based on their size. The wells were loaded with 40µl of total volume for each protein sample, alongside with 5µl of ladder (PageRuler Plus, Prestained; Thermo Fisher). Total loading volume was made using 4X laemlli (0.25 M Tris-HCl pH6.8, 8 % SDS, 40 % glycerol, 0.04 % Bromophenol blue, 10 % B-mercaptoethanol), PBS and calculated sample volume for ~20µg of protein. Protein transfer was made using IBlot2 system and nitrocellulose membrane transfer packs (Invitrogen). Membranes were blocked with 5% milk dissolved in TBS-Tween at +4ºC overnight, followed by the incubation with the primary antibody made up in 2.5% milk in TBS-Tween for 2 hours at room temperature. Membranes were washed with TBS-Tween and incubated for 1h with secondary antibody coupled to horseradish peroxidase made up in 2.5% milk. Membranes were washed with TBS-Tween and protein was detected using ECL Western blotting substrate (Thermo Fisher). The images were captured using DNR Bioimaging systems.

| **TBS** | **1L, pH=7.40** |
|---|---|
| **Tris-HCl** | **25 mM** |
| **NaCl** | **150mM** |
| **EDTA** | **10mM** |

**Table 2.6-1Composition of Tris-buffered saline (TBS)**

| Primary Antibody | Concentration | Manufacturer |
|---|---|---|
| α-σ1R | 1:500 | Santa Cruz Biotechnology |
| α-STIM1 | 1:1000 | Protein Tech |
| α-STIM2 | 1:200 | Alomone |
| α-Orai1 | 1:500 | Sigma |
| α-βactin | 1:1500 | Sigma |
| **Secondary Antibody** | | |
| α-mouse HRP | 1:1000 | Dako |
| α-rabbit HRP | 1:1000 | Bio-rad |

**Table 2.6-2 List of antibodies used in Western blotting**

## 2.7 Microscopy

### 2.7.1 Immunofluorescence

Protocol for immunofluorescence can be found in Chapter VI, Section 6.21.

### 2.7.2 Proximity ligation assay (PLA)

Protocol for PLA can be found in Chapter VI, Section 6.22.

### 2.7.3 Total internal reflection microscopy (TIRFM)

TIRF imaging was performed on a custom-built inverted TIRF microscope. Cells were seeded onto poly-L-lysine-coated 24-mm coverslips at 70-80% confluency. The microscope system consisted of 60x oil-immersion objective (Olympus, NA 1.45), the electron-multiplying charged-coupled device camera (Photometrics Cascade 512B), Thorlabs SC10 - Optical Beam Shutter Controller, 535/50 and 630/60 emission filters, and 488-nm (70 mW output measured, Cobolt MLD) and 561-nm (55 mW output measured, Cobolt Jive) diode lasers. The system was controlled using Micro-Manager Open Source

Microscopy Software. Using the 60× TIRF objective, a pixel corresponded to a 240-nm by 240-nm square. Single channel images were acquired at the rate of image/5 seconds. Two channel images were acquired sequentially (colour-stack/5 seconds) with exposure time of 100 ms.

### 2.7.4 Data analysis

Most of results are presented as mean±SEM from “n” independent experiments as indicated in the figure legends. Number of biological replicates is marked with “N”. Statistical analysis for dataset from normal population ( D'Agostino-Pearson normality test, $P>0.05$) used unpaired Student’s test or ANOVA followed by Tukey’s post hoc test, as appropriate. Statistical analysis for dataset significantly different from normal population ( D'Agostino-Pearson normality test, $P<0.05$) used unpaired Mann-Whitney test or Kruskal-Wallis test followed by Dunn-Bonferroni post hoc test, as appropriate. Line and bar graphs, and statistical analysis were generated using GraphPad Prism v6.

# 3 Chapter III

## Measurements of $[Ca^{2+}]_{cyt}$ in the population of cells and the functional role of σ1R in regulation of SOCE

## 3.1 Introduction

Tight and precise regulation of changes in $[Ca^{2+}]_{cyt}$ is crucial for numerous cellular processes. Store-operated $Ca^{2+}$ entry (SOCE) is a key pathway for the replenishment of intracellular $Ca^{2+}$ in non-excitable cells, and recently, it has emerged as an important pathway for the maintenance of $Ca^{2+}$ homeostasis in excitable cells[115,139].

σ1R, a neuroprotective ER chaperone with established therapeutic potential, has been proposed as a functional regulator of Orai1-mediated SOCE[14,34]. However, σ1R has been reported to inhibit, promote, and even potentiate SOCE in different cell lines requiring further investigation[14,34,158,159].

### 3.1.1 Use of fluorescent $Ca^{2+}$ dyes and GCaMP6f to measure SOCE

$Ca^{2+}$ indicators are molecules that increase in fluorescence upon $Ca^{2+}$ binding. The current understanding of cellular $Ca^{2+}$ signals can be contributed to the continuous improvements in $Ca^{2+}$ indicators, including fluorescent (synthetic) $Ca^{2+}$ dyes and genetically encoded $Ca^{2+}$ indicators (GECI).

The fluorescent $Ca^{2+}$ dyes were first introduced by Dr. Roger Tsien, together with instructions for loading fluorescent dyes into the cells via membrane-permeant ester forms [165–167]. Fluo-4-AM and Fluo-8-AM are fluorescent $Ca^{2+}$ dyes that are used in this chapter. Both Fluo-AM dyes are the non-polar esters that readily cross live cell membranes; upon crossing both dyes are hydrolysed by cellular esterases and, thus, “trapped” inside mammalian cells, allowing for measurements of $[Ca^{2+}]_{cyt.}$ On binding of $Ca^{2+}$, Fluo-4-AM and Fluo-8-AM exhibit substantial changes in fluorescence that can be normalized by ratio of

chelated fluorescence ($F_{min}$) to fluorescence obtained after saturating levels of cytosolic $Ca^{2+}$($F_{max}$).

In parallel to fluorescent $Ca^{2+}$ dyes, GECI were developed as promising *in vivo* sensors for imaging of changes in neuronal $[Ca^{2+}]_{cyt}$[168]. A significant advantage of GECI over fluorescent $Ca^{2+}$ dyes includes targeting to distinct populations of cells and/or subcellular locations using cell-specific promoters and targeting sequences over indiscriminate uptake[168]. GCaMP6f is GECI used in this chapter. It is a more recent iteration of the original GCaMP sensor which consists of green fluorescent protein (GFP) fused to the calmodulin (CaM) binding region of chicken myosin light kinase (M13)[168]. On binding of $Ca^{2+}$, GCaMP6f undergoes conformational change resulting in the interaction of its CaM and M13 regions and consequently, an increase in fluorescence.

GCaMP6f has been reported to outcompete various synthetic indicator dyes when compared to their sensitivity and dynamic range[162,168]. The dissociation constant ($K_d$) describes how tightly a $Ca^{2+}$ indicator binds $Ca^{2+}$ [169], and GCaMP6f has several reported $K_d$ values ranging from 290 to 375nM[170,171]. In comparison, Fluo-4-AM has a $K_d$ value of 345nM, and Fluo-8-AM has a $K_d$ value of 389nM, suggesting similar buffering affinity. To investigate the functional role of σ1R in the regulation of SOCE, Fluo-4-AM, Fluo-8-AM, and GCaMP6f were utilized as $Ca^{2+}$ indicators while performing $Ca^{2+}$ functional assay using Flexstation III microplate reader.

### 3.1.2 Use of BacMam gene-delivery system to express σ1R

Various research tools may be used to manipulate the expression levels of a gene of interest in mammalian cell lines. In recent years, the modified insect cell baculovirus

(BacMam virus) has emerged as an efficient gene delivery technology to mammalian cells resulting in very little to no microscopically observable cytotoxicity[172].

BacMam virus carries cDNA of gene of interest under the control of the CMV promoter. The transduction of mammalian cells by BacMam virus requires small liquid addition to the culturing media after which BacMam particles enter the cell via endocytosis[6]. After endocytosis, the BacMam DNA is trafficked to the nucleus where the mammalian transcriptional machinery transcribes the CMV-promoted gene but fails to recognize baculovirus promoters. The transcription of BacMam-delivered gene under CMV promoter begins within 4–6 hours after transduction and in most of the cell types is completed overnight.

In the drug discovery environment, BacMam gene-delivery system is routinely used to achieve the transient and controllable expression of target proteins in cell-based assays for high-throughput screenings (HTS)[172,173]. While the development of a stable-cell line is a time-costly process which can result in several shortcomings, including the accumulation of mutations due to continuous selection pressure required to maintain the transgene, BacMam gene-delivery system allows for highly reproducible and titratable transient expression within 24 hours from transduction[172,173].

To express σ1R in mammalian cell lines and asses its role within SOCE, I have developed σ1R baculovirus carrying cDNA for expression of σ1R tagged with small V5 epitope (σ1R-V5). Also, I have developed appropriate viral control named $WT^{VC}$ using BacMam vector without σ1R-V5 cDNA.

### 3.1.3 Use of HEK293 cell line as an experimental system

Human embryonic kidney (HEK) 293 is immortalized cell line extensively used in research, including studies of neuronal related diseases. First HEK293 cells were cultured by transforming the primary cultures of HEK cells with sheared Adenovirus 5 DNA[174]. As embryonic kidneys consist of heterogeneous mix of cell types, the precise type of kidney or kidney-adjacent cell that gave rise to HEK293 cell line has been unknown. For decades, this immortalized cell line was considered kidney epithelial or even fibroblasts[175,176], but subsequent studies, as well as advances in immunocytochemistry and transcriptomics, have revealed that HEK 293 cells express markers of renal progenitor cells, adrenal gland, and neuronal cells[177,178]. Cell-type unspecific phenotype of HEK293 cells that includes expression of over sixty neuron-specific proteins, such as neurofilaments, subunits of neuron-specific ion channels, neuroreceptors, and synaptic-vesicle-associated proteins, have led towards current hypothesis that HEK 293 and neurons originate from the same precursor line[177,179].

As a choice of experimental system, HEK293 do not provide identical cellular and sub-cellular organization nor biochemistry associated with neuronal cells and tissue preparations. Moreover, HEK293 cells are devoid of several ion channels, chaperons, receptors, and enzymes crucial for neuronal biology. However, preserved functionality of both endogenous and exogenous neuron-specific proteins in HEK293 cells has been experimentally demonstrated, suggesting high similarity of fundamental biological processes and regulatory mechanisms between HEK293 cells and neurons. For example, currents of endogenously expressed voltage-gated $Ca^{2+}$, $K^{+}$, and $Na^{2+}$ channels have been recorded[179]. HEK293 cells were also found sensitive to agonists implicated in neuronal signaling, such as histamine, neurotensin, and ATP[179]. Additionally, HEK293 cells

underwent synaptogenesis in a mixed assay cultures with neurons after exogenous protein expression of neuronal-specific proteins[179]. This evidence suggests that HEK293 cells represent a good “low-noise” model for studying basic cellular mechanism of neuroprotective chaperone, such as σ1R.

In this thesis, HEK293 cells are used as experimental system to determine how enhanced expression of σ1R affects SOCE regulated by a) endogenous levels of STIM and Orai1 proteins, and b) following upregulation in STIM and Orai1 expression levels.

### 3.1.4 Aims

(1) To determine how enhanced expression of σ1R affects SOCE

## 3.2 Methods

### 3.2.1 Experimental timeline of Chapter III

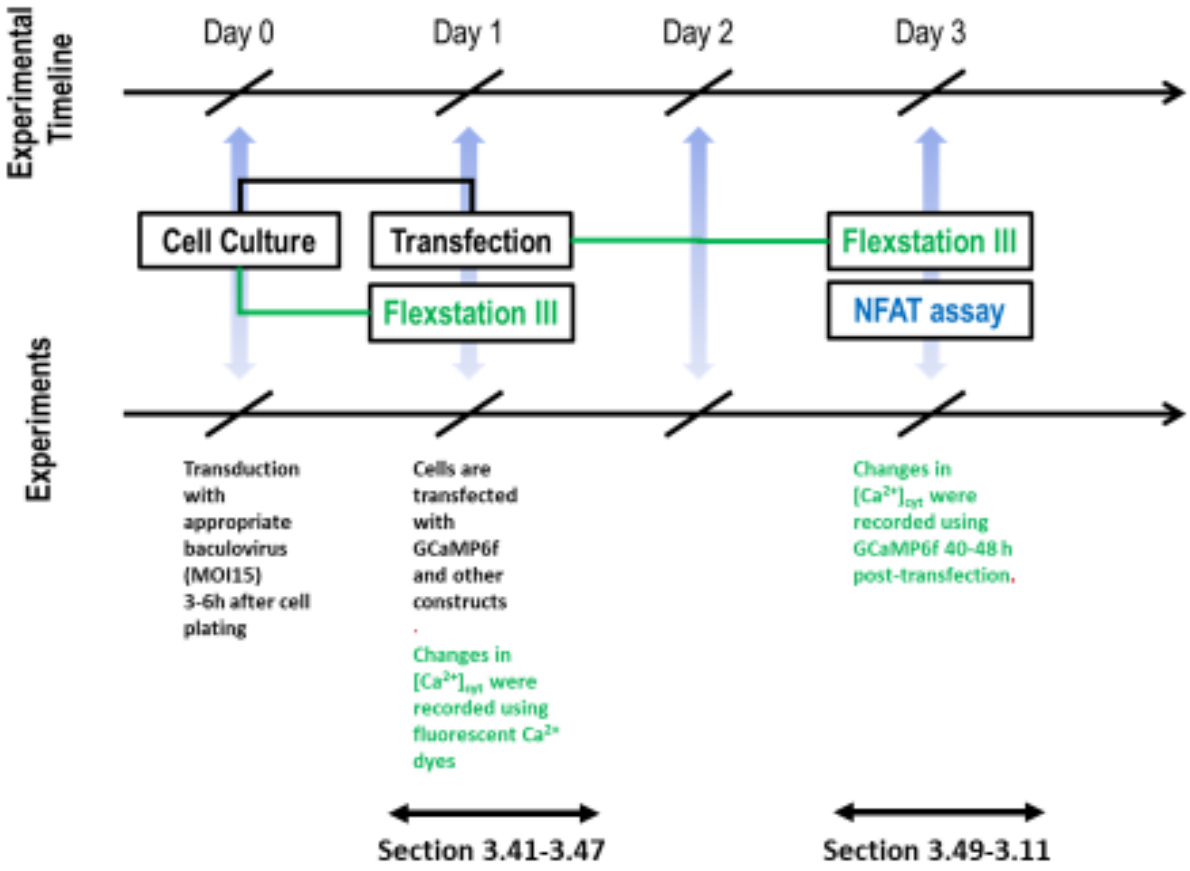


**Fig3.21 Experimental timeline of calcium assays in Chapter III.** Day (0) Cell culture and plating of cells on the appropriate recording dishes, followed by baculovirus transduction. (Day 1) Transfection using PEI/Flexstation III experiments using fluorescent $Ca^{2+}$ dyes. (Day 3) Flexstation III and NFAT translocation assay experiments.

## 3.3 Results

### 3.3.1 Overexpression of σ1R-V5 significantly inhibits store-depletion and SOCE

For initial testing of the functional role of σ1R in the regulation of SOCE, σ1R-V5 was transiently expressed in HEK293 cells using PEI transfection method. Plasmid for expression of σ1R-V5 was developed by Srivats et al[34]. 48 h post-transfection, cells were loaded with Fluo-4-AM for 45 min and tested using Flexstation III microplate reader. Cells were put in nominal $Ca^{2+}$-free NES and treated with 1 μM thapsigargin to induce store depletion, which can be observed as the first rise in cytosolic $Ca^{2+}$ ($1^{st}$ peak). This was followed by the restoration of 2 mM extracellular $Ca^{2+}$ where $Ca^{2+}$ influx (SOCE) was recorded as the second rise in cytosolic $Ca^{2+}$ ($2^{nd}$ peak). Additionally, at this stage of the assay, cell were treated with either 1 μM $Gd^{3+}$, a known SOCE inhibitor, or the equivalent volume of DMSO.

Fig3.31 shows Fluo-4-AM traces of mock-transfected and σ1R-V5 HEK293 cells treated with 1μM of thapsigargin in nominal $Ca^{2+}$-free NES followed by the restoration of 2 mM extracellular $Ca^{2+}$ with either 1μM $Gd^{3+}$ or the equivalent volume of DMSO. Store-depletion and SOCE peaks of each experimental group were obtained and compared with one-way ANOVA using α of 0.05. The overexpression of σ1R-V5 resulted in a significant decrease in both store-depletion and SOCE when compared to mock-transfected HEK293 cells (Fig3.31B, ****, $P < 0.0001$), which suggests that σ1R-V5 inhibits store-depletion and SOCE. Addition of 1μM $Gd^{3+}$ significantly inhibited SOCE in both mock-transfected and σ1R-V5 cells, suggesting that experimentally measured $Ca^{2+}$ influx occurs through CRAC channel. These results agree with the previously reported[34]. Results of statistical analysis have been summarized in Table3.31.

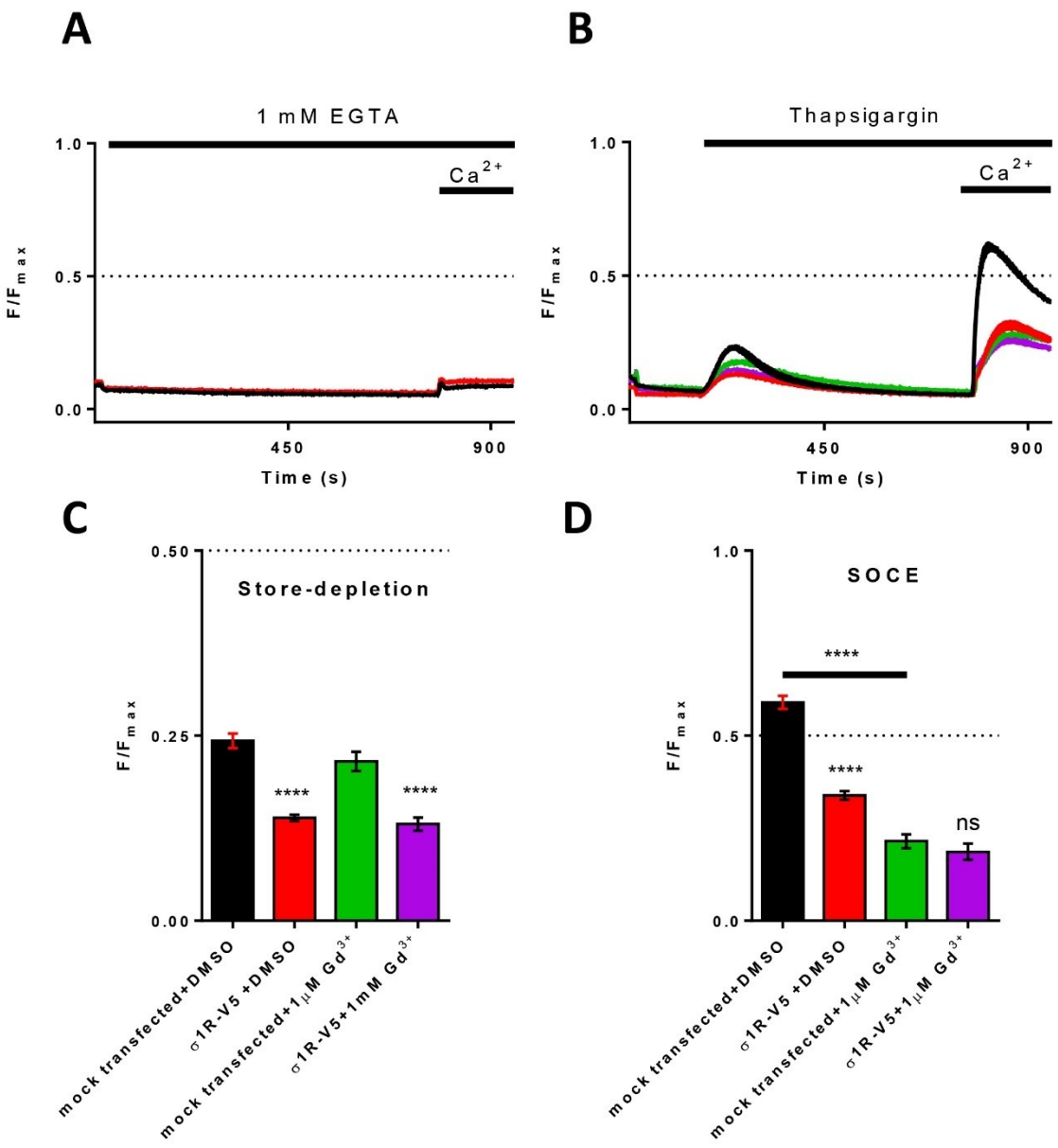


**Fig3.31 Overexpression of σ1R-V5 and treatment with 1μM $Gd^{3+}$ inhibit SOCE in HEK293 cells. A)** Representative average±SEM traces of mock-transfected and σ1R-V5 HEK293 cells treated with nominal $Ca^{2+}$-free NES which contains $Ca^{2+}$ chelator EGTA (1mM) followed by the restoration of 2 mM extracellular $Ca^{2+}$ . No significant changes in $[Ca^{2+}]_{cyt}$ were detected**. B)** Representative average±SEM traces of mock-transfected and σ1R-V5 HEK293 cells treated with 1μM thapsigargin in nominal $Ca^{2+}$-free NES followed by the restoration of 2 mM extracellular $Ca^{2+}$ with either DMSO (black and red) or 1μM $Gd^{3+}$ (green and purple). **C) and D)** Results summary of thapsigargin-evoked store-depletion ($1^{st}$ peak, B) and SOCE ( $2^{nd}$ peak, C) values across n=3. One-way ANOVA. N.s., P> 0.05; **, P < 0.01;****, P < 0.0001.

.

| Group | Store-depletion Mean±SEM | SOCE Mean±SEM | N | Tukey summary of store-depletion σ1R-V5+DMSO | Tukey summary of SOCE σ1R-V5+DMSO |
|---|---|---|---|---|---|
| Mock-transfected + DMSO | 0.2431 ± 0.009906 | 0.5901± 0.01768 | 23 | ****, P < 0.0001 | ****, P < 0.0001 |
| σ1R-V5+DMSO | 0.1391± 0.004416 | 0.3386± 0.01159 | 24 | | |
| Mock-transfected + $Gd^{3+}$ | 0.2152± 0.01294 | 0.2149± 0.01890 | 18 | *, P < 0.05 | ****, P < 0.0001 |
| σ1R-V5+$Gd^{3+}$ | 0.1306± 0.008676 | 0.1863± 0.02192 | 17 | n.s, P > 0.05 | ****, P < 0.0001 |
| **Group** | **Store-depletion Mean±SEM** | **SOCE Mean±SEM** | **N** | **Tukey summary of store-depletion Mock-transfected + $Gd^{3+}$** | **Tukey summary of SOCE Mock-transfected + $Gd^{3+}$** |
| Mock-transfected + DMSO | 0.2431 ± 0.009906 | 0.5901± 0.01768 | 23 | n.s, P > 0.05 | ****, P < 0.0001 |

**Table 3.3-1 Summary of one-way ANOVA for the thapsigargin-evoked increase in $[Ca^{2+}]_{cyt}$ during store-depletion and either DMSO or $Gd^{3+}$ treatment during SOCE.** Store-depletion and SOCE measurements (Peaks, Fig 3.31) were taken 48h post-transfection with σ1R-V5 construct across three independent experiments (n=3). A population of HEK293 cells within one well of 96W plate was used as a biological replicate (N) for statistical analysis.

### 3.3.2 Sustained store-depletion is not sufficient to inhibit SOCE

σ1R promotes $Ca^{2+}$ influx from ER to mitochondria by stabilizing IP3Rs at the MAM[22]. Thus, enhanced expression of σ1R can result in sustained efflux of luminal $Ca^{2+}$ and $Ca^{2+}$ overload of mitochondria. Up-to-date evidence shows that mitochondria possesses unknown mechanism to inhibit SOCE during mitochondrial depolarisation[180]. Hence, the observed ability of σ1R to inhibit SOCE could be linked with its ability to promote efflux of luminal $Ca^{2+}$ and cause sustained store-depletion before even before experimental assessment. To test whether sustained store-depletion might itself cause downregulation of SOCE, HEK293 cells were treated with cyclopiazonic acid (CPA) to reversibly inhibit the ER $Ca^{2+}$ pump for 2 and 18h.

Fig3.32 shows Fluo-4-AM traces of mock-treated, 2h CPA-treated and 18 h CPA-treated HEK293 cells treated with 1μM of Thapsigargin in nominal $Ca^{2+}$-free NES followed by the restoration of 2 mM extracellular $Ca^{2+}$. Store-depletion and SOCE peaks of each experimental group were obtained and compared with one-way ANOVA using α of 0.05. In comparison to the mock-treated cells, the treatment with CPA for 2h and 18h resulted in a significant decrease in store-depletion (Fig3.32B, ****, $P < 0.0001$), indicating the sustained store-depletion by CPA-treatment. However, no significant inhibition of SOCE was detected, suggesting that sustained store-depletion is not sufficient to inhibit SOCE. These results agree with the previously reported[34]. Results of statistical analysis have been summarized in Table3.32.

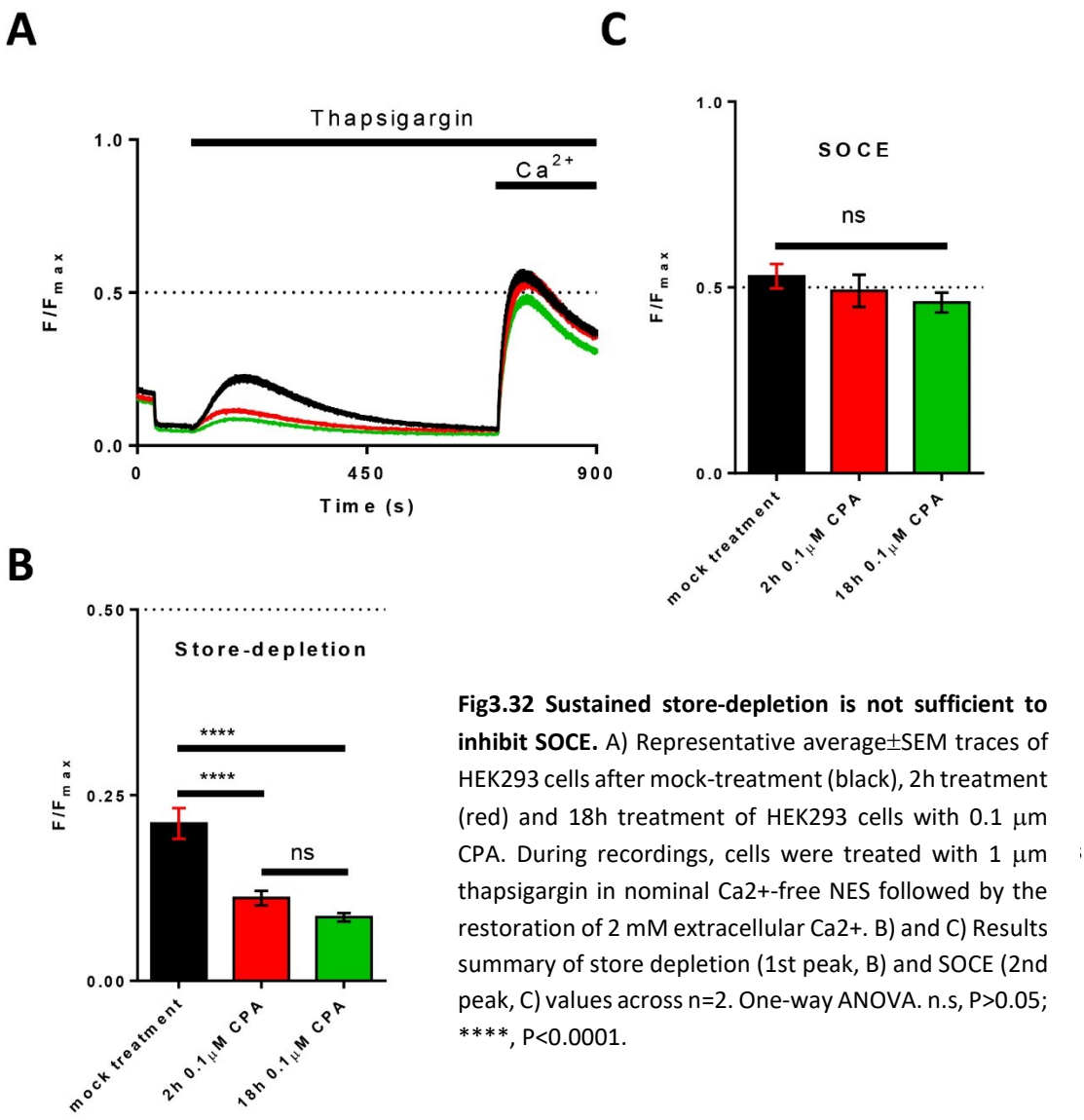


**Fig3.32 Sustained store-depletion is not sufficient to inhibit SOCE.** A) Representative average±SEM traces of HEK293 cells after mock-treatment (black), 2h treatment (red) and 18h treatment of HEK293 cells with 0.1 μm CPA. During recordings, cells were treated with 1 μm thapsigargin in nominal Ca2+-free NES followed by the restoration of 2 mM extracellular Ca2+. B) and C) Results summary of store depletion (1st peak, B) and SOCE (2nd peak, C) values across n=2. One-way ANOVA. n.s, P>0.05; ****, P<0.0001.

### 3.3.3 Overexpression of σ1R-V5 using BacMam gene delivery system inhibits store-depletion and SOCE 24 h post-transduction

After determining that the overexpression of σ1R-V5 inhibits SOCE, the cDNA of σ1R-V5 was inserted into the BacMam pCMV-Dest vector which was used to develop σ1R-V5 baculovirus. A viral control ($WT^{VC}$) was developed using BacMam pCMV-Dest vector without σ1R-V5 cDNA. To functionally assess the BacMam gene delivery system, HEK293 were transduced with MOI15 of $WT^{VC}$ and σ1R-V5 baculovirus particles. To test whether σ1R-V5 inhibits SOCE 24h post-transduction, cells were loaded with Fluo-8-AM for 30 min and tested using Flexstation III microplate reader.

Fig3.33 shows Fluo-8-AM traces of $WT^{VC}$ and σ1R-V5 HEK293 cells treated with 1μM of Thapsigargin in nominal $Ca^{2+}$-free NES followed by the restoration of 2 mM extracellular $Ca^{2+}$. Store-depletion and SOCE peaks of each experimental group were obtained and compared with Student's t-test using α of 0.05. The overexpression of σ1R-V5 using BacMam gene delivery system resulted in a significant decrease in both store-depletion and SOCE when compared to $WT^{VC}$ HEK293 cells (Fig3.33B, **, $P < 0.01$; Fig3.33C, ****, $P < 0.0001$ ), which suggests that σ1R-V5 inhibits store-depletion and SOCE. Results of statistical analysis have been summarized in Table3.33.

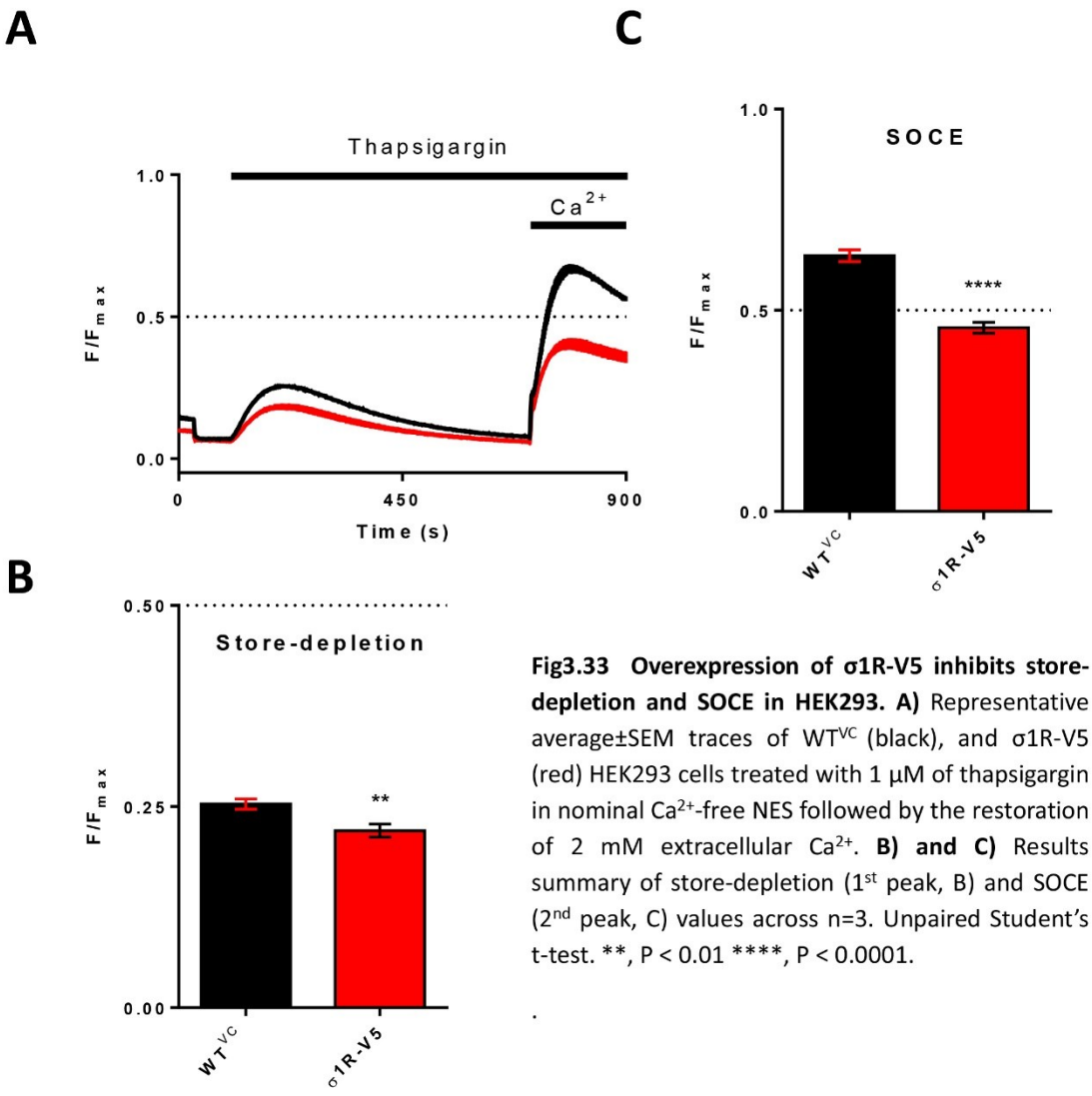


**Fig3.33 Overexpression of σ1R-V5 inhibits store-depletion and SOCE in HEK293. A)** Representative average±SEM traces of $WT^{VC}$ (black), and σ1R-V5 (red) HEK293 cells treated with 1 μM of thapsigargin in nominal $Ca^{2+}$-free NES followed by the restoration of 2 mM extracellular $Ca^{2+}$. **B) and C)** Results summary of store-depletion (1st peak, B) and SOCE (2nd peak, C) values across n=3. Unpaired Student's t-test. **, $P < 0.01$ ****, $P < 0.0001$.

.

| Group | Store-depletion Mean± SEM | SOCE Mean± SEM | N | t-test summary of store-depletion σ1R-V5 | t-test summary of SOCE σ1R-V5 |
|---|---|---|---|---|---|
| $WT^{VC}$ | 0.2531 ± 0.006405 | 0.6358± 0.01461 | 30 | **, P < 0.01 | ****, P < 0.0001 |
| σ1R-V5 | 0.2200 ± 0.008220 | 0.4563± 0.01345 | 24 | | |

**Table 3.3-3 Summary of unpaired Student's t-test for the thapsigargin-evoked increase in $[Ca^{2+}]_{cyt}$ during store-depletion and SOCE 24h post-transduction.** Store-depletion and SOCE measurements (Peaks, Fig 3.33) were taken across three independent experiments (n=3). A population of HEK293 cells within one well of 96W plate was used as a biological replicate (N) for statistical analysis.

### 3.3.4 Overexpression of σ1R-V5 in HEK293 cells inhibits SOCE independently of efflux of intracellular potassium ($K^+$)

Gueguinou et al[14]. reported that σ1R modulates SK3-dependent $Ca^{2+}$ homeostasis by promoting Orai1:SK3 coupling in colorectal and breast cancer cells, which leads to an increase in thapsigargin-evoked and constitutive Orai1-mediated $Ca^{2+}$ influx [15]. SK3 is small conductance $Ca^{2+}$ activate potassium ($K^+$) channel that activated by high intracellular $Ca^{2+}$ hyperpolarizes cell by allowing $K^+$ efflux. To test whether σ1R modulates SOCE in HEK293 cells independently of $K^+$ efflux, $WT^{VC}$ and σ1R-V5 transduced HEK293 cells were tested in nominal $Ca^{2+}$-free NES with increased concentration of extracellular $K^+$ (142 mM).

Fig3.34 shows Fluo-8-AM traces of $WT^{VC}$ and σ1R-V5 HEK293 cells treated with 1μM of Thapsigargin in nominal $Ca^{2+}$-free NES (high $K^+$) followed by the restoration of 2 mM extracellular $Ca^{2+}$. Store-depletion and SOCE peaks of each experimental group were obtained and compared with Student's t-test using α of 0.05. The overexpression of σ1R-V5 resulted in a significant decrease in SOCE when compared to $WT^{VC}$ HEK293 cells (Fig3.34C, ****, $P < 0.0001$ ), which suggests that in HEK293 cells, σ1R-V5 modulates SOCE via a different mechanism than reported by Gueguinou et al[14]. Results of statistical analysis have been summarized in Table3.34.

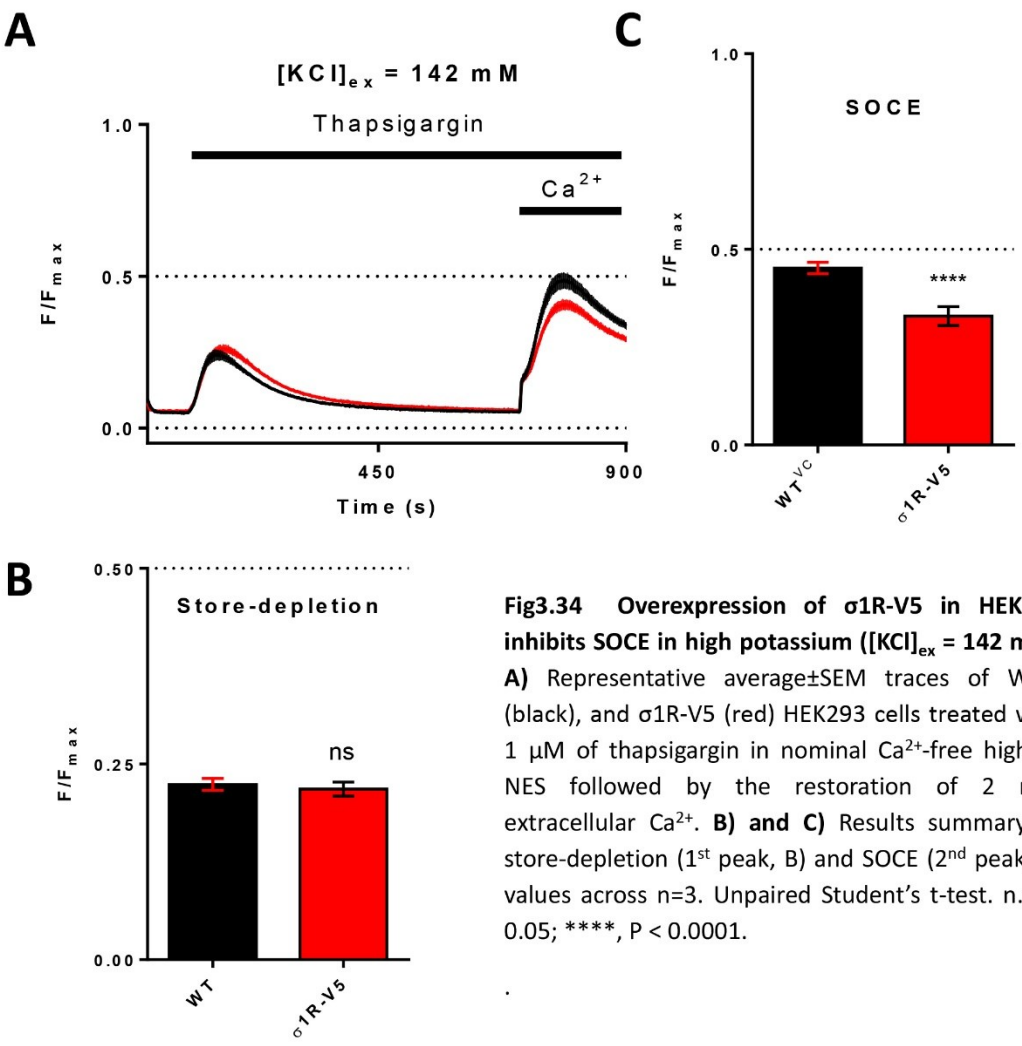


**Fig3.34 Overexpression of σ1R-V5 in HEK293 inhibits SOCE in high potassium ($[KCl]_{ex}$ = 142 mM)** **A)** Representative average±SEM traces of $WT^{VC}$ (black), and σ1R-V5 (red) HEK293 cells treated with 1 µM of thapsigargin in nominal $Ca^{2+}$-free high $K^+$ NES followed by the restoration of 2 mM extracellular $Ca^{2+}$. **B) and C)** Results summary of store-depletion (1st peak, B) and SOCE (2nd peak, C) values across n=3. Unpaired Student's t-test. n.s. > 0.05; ****, P < 0.0001.

.

| Group | Store-depletion Mean± SEM | SOCE Mean± SEM | N | t-test summary of store-depletion σ1R-V5 | t-test summary of SOCE σ1R-V5 |
|---|---|---|---|---|---|
| $WT^{VC}$ | 0.2241 ± 0.007425 | 0.4522 ± 0.01467 | 24 | n.s., P > 0.05 | ****, P < 0.0001 |
| σ1R-V5 | 0.2180 ± 0.008954 | 0.3294 ± 0.02434 | 24 | | |

**Table 3.3-4 Summary of unpaired Student's t-test for the thapsigargin-evoked increase in $[Ca^{2+}]$cyt during store-depletion and SOCE following membrane depolarization (high KCl).** Store-depletion and SOCE measurements (Peaks, Fig 3.34) were taken across three independent experiments (n=3). A population of HEK293 cells within one well of 96W plate was used as a biological replicate (N) for statistical analysis.

### 3.3.5 σ1R-V5 reduces ATP/Cch-evoked increase in $[Ca^{2+}]_{cyt}$ during store-depletion and SOCE

In HEK293 cells, the depletion of intracellular $Ca^{2+}$ stores can be induced by the inhibition of the SERCA ATPase pump by thapsigargin, or by the stimulation of endogenous receptors that activate PLC using adenosine triphosphate (ATP) and carbachol (Cch). To test whether the overexpression of σ1R-V5 reduces store-depletion and SOCE after activation of PLC and downstream activation of IP3Rs, HEK293 cells were transduced with either $WT^{VC}$ or σ1R-V5 baculovirus. 24h post-transduction, the populations of $WT^{VC}$ and σ1R-V5 HEK293 cells were treated with the addition of 100μM of ATP/Cch, and changes in $[Ca^{2+}]_{cyt}$ were measured using Fluo-8-AM and Flexstation III microplate reader.

HEK293 cells in this section and following sections 3.36 and 3.37 of this chapter were a gift from C. Taylor lab (University of Cambridge), and are also a control cell line for $IP3R^{-/-}$ HEK293 cell line introduced in the following section.

Fig3.35 shows Fluo-8-AM traces of $WT^{VC}$ and σ1R-V5 HEK293 cells treated with 100μM of ATP/Cch in nominal $Ca^{2+}$-free NES followed by the restoration of 2 mM extracellular $Ca^{2+}$. Store-depletion and SOCE peaks of $WT^{VC}$ and σ1R-V5 HEK293 cells were compared with unpaired Student's t-test using α of 0.05. The overexpression of σ1R-V5 resulted in a significant decrease in both store-depletion and SOCE when compared to $WT^{VC}$ HEK293 cells (Fig3.35B, ****, $P < 0.0001$). This result suggests that σ1R-V5 inhibits SOCE following active store-depletion via PLC pathway. Also, a significantly lower efflux of luminal $Ca^{2+}$ to cytosol agrees with the previously reported results[34]. Results of statistical analysis have been summarized in Table 3.35.

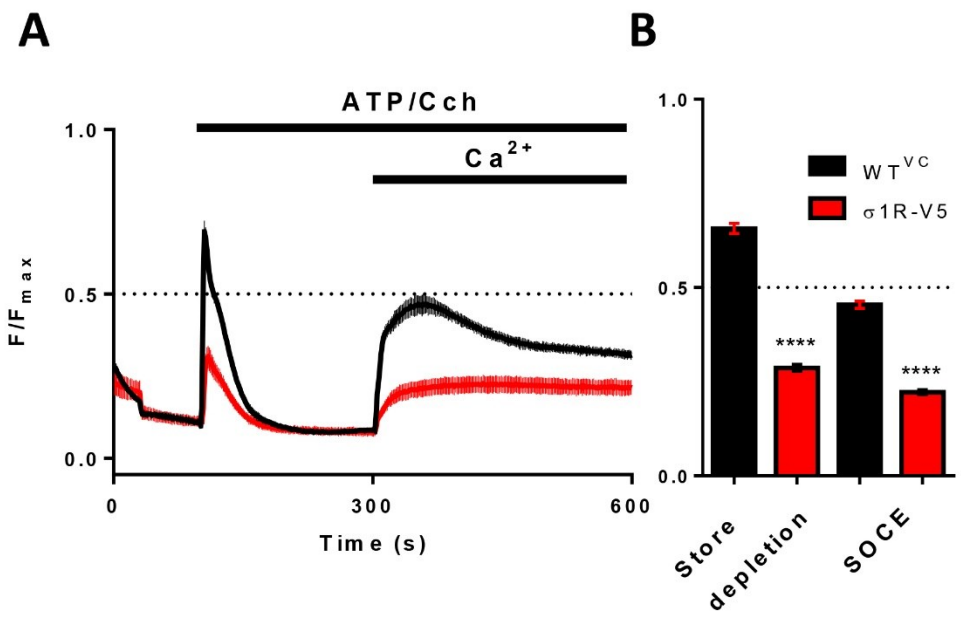


**Fig3.35 σ1R-V5 inhibits ATP/Cch-evoked store-depletion and SOCE. A)** Representative average±SEM traces of $WT^{vc}$(black), and σ1R-V5(red) transduced HEK293 cells treated with 100µM of ATP/Cch in nominal $Ca^{2+}$-free NES followed by the restoration of 2 mM extracellular $Ca^{2+}$. **B)** Results summary of store-depletion (1st peak) and SOCE (2nd peak) values across n=3. Unpaired Student t-test. ****, P < 0.0001.

.

| Group | Store-depletion Mean± SEM | SOCE Mean± SEM | N | t-test summary of store-depletion σ1R-V5 | t-test summary of SOCE σ1R-V5 |
|---|---|---|---|---|---|
| $WT^{VC}$ | 0.6569 ± 0.01376 | 0.4543 ± 0.009763 | 18 | ****, P < 0.0001 | ****, P < 0.0001 |
| σ1R-V5 | 0.2867 ± 0.009353 | 0.2219 ± 0.006639 | 18 | | |

**Table 3.3-5 Summary of unpaired Student's t-test for ATP/Cch-evoked increase in $[Ca^{2+}]_{cyt}$ during store-depletion and SOCE.** Store-depletion and SOCE measurements (Peaks, Fig 3.35) were taken across three independent experiments (n=3). A population of HEK293 cells within one well of 96W plate was used as a biological replicate (N) for statistical analysis.

### 3.3.6 Treatment with ATP/Cch fails to evoke store-depletion and SOCE in IP3R$^{-/-}$ HEK293 cells

To further characterize the role of σ1R within the SOCE pathway, IP3R$^{-/-}$ HEK293 cell line was obtained from Taylor Lab[181] with its appropriate control which is used in Section 3.35 of this chapter. Subtype three of IP3Rs has been introduced in Section 1.151 of Chapter I as interactive partner of σ1R at the MAM where activated, promotes $Ca^{2+}$ influx from ER to mitochondria. In IP3R$^{-/-}$ stable cell line, all three subtypes of IP3R have been knocked-out eliminating IP3R-mediated store-depletion and SOCE activation. Before using IP3R$^{-/-}$ HEK293 cells in experiments with WT$^{VC}$ and σ1R-V5 baculovirus, IP3R$^{-/-}$ stable cell line was briefly characterized during $Ca^{2+}$ functional assay by applying 100μM of ATP/Cch treatment, which is upstream stimuli of IP3R-mediated store-depletion and SOCE activation.

Fig3.36 shows Fluo-8-AM traces of WT (black) and IP3R$^{-/-}$ (red) HEK293 treated with 100μM of ATP/Cch in nominal $Ca^{2+}$-free NES followed by the restoration of 2 mM extracellular $Ca^{2+}$. Store-depletion (1$^{st}$ peak) and SOCE (2$^{nd}$ peak) of experimental groups were compared with unpaired Student's t-test using α of 0.05. ATP/Cch treatment failed to induce store-depletion and to activate SOCE in IP3R-/- cell line, confirming absence of IP3Rs.

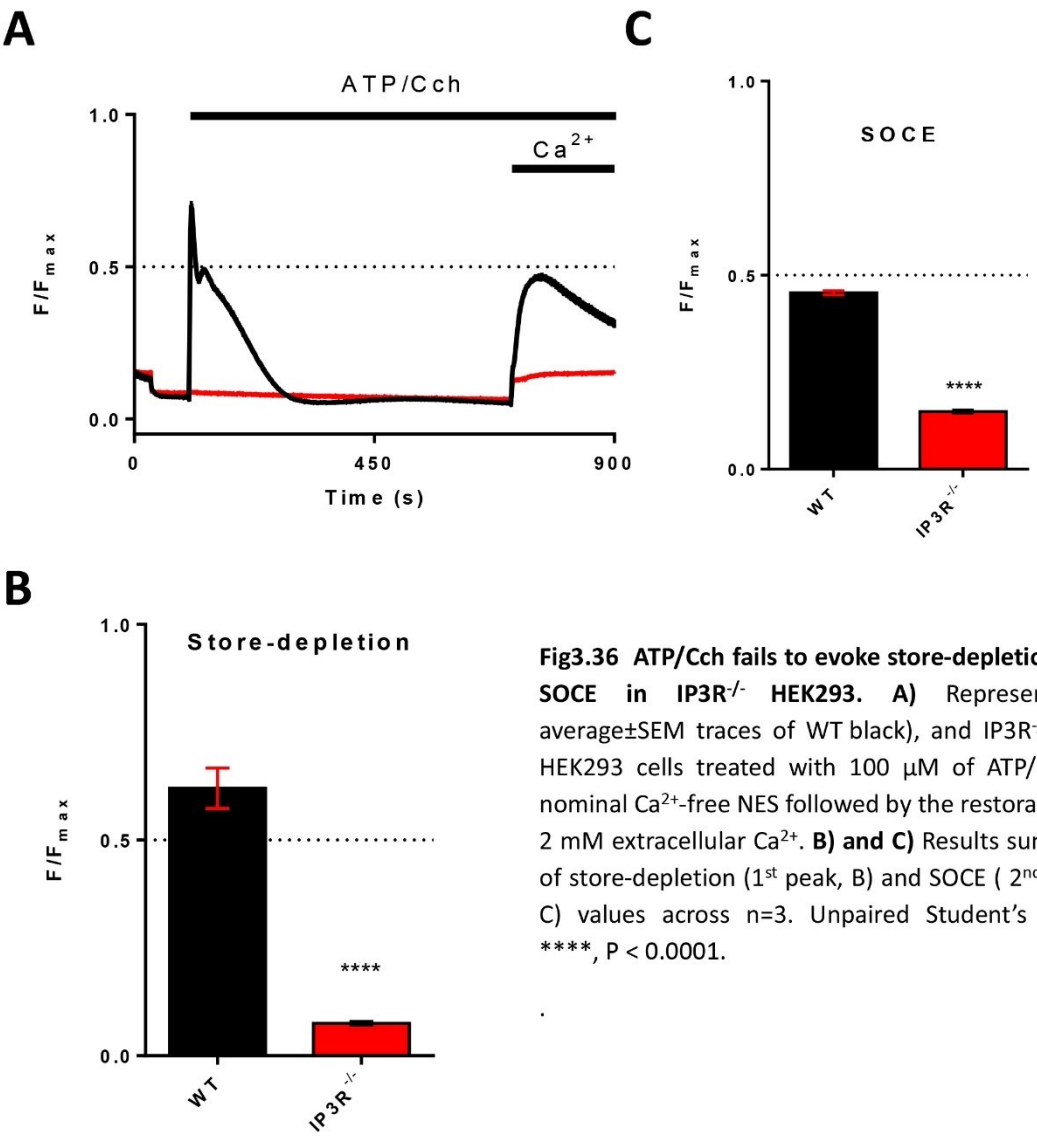


**Fig3.36 ATP/Cch fails to evoke store-depletion and SOCE in IP3R$^{-/-}$ HEK293. A)** Representative average±SEM traces of WT black), and IP3R$^{-/-}$ (red) HEK293 cells treated with 100 µM of ATP/Cch in nominal $Ca^{2+}$-free NES followed by the restoration of 2 mM extracellular $Ca^{2+}$. **B) and C)** Results summary of store-depletion (1$^{st}$ peak, B) and SOCE ( 2$^{nd}$ peak, C) values across n=3. Unpaired Student's t-test. ****, P < 0.0001.

.

### 3.3.7 σ1R-V5 inhibits SOCE in IP3R$^{-/-}$ HEK293 cells, but fails to reduce store-depletion

A significant drop in $[Ca^{2+}]_{ER}$ promotes dissociation of σ1R from BiP and its translocation to the MAM where it promotes flux of $Ca^{2+}$ from ER to mitochondria by stabilizing IP3Rs. Recently, two groups reported that depletion of intracellular stores by the activation of IP3Rs also promotes IP3R-STIM1 association at ER-PM junctions[181,182]. These results prompt us to address whether previously observed functional interaction of σ1Rs with IP3Rs at the MAM plays a role in underlying cellular mechanism of SOCE inhibition by σ1R. To determine whether the functional role of σ1R in the regulation of ER $Ca^{2+}$ content and SOCE is IP3R-dependent, HEK293 cell line deficient for all three subtypes of IP3Rs (IP3R$^{-/-}$ HEK293 cells) was transduced with WT$^{VC}$ and σ1R-V5 baculovirus. 24h post-transduction, the populations of WT$^{VC}$ and σ1R-V5 IP3R$^{-/-}$ HEK293 cells were treated with 1μM of thapsigargin, and changes in $[Ca^{2+}]_{cyt}$ were measured using Fluo-8-AM $Ca^{2+}$ dye and Flexstation III microplate reader.

Fig3.37 shows Fluo-8-AM traces of WT$^{VC}$ and σ1R-V5 IP3R$^{-/-}$ HEK293 cells treated with 1μM of thapsigargin in nominal $Ca^{2+}$-free NES followed by the restoration of 2 mM extracellular $Ca^{2+}$. Store-depletion and SOCE peaks of WT$^{VC}$ and σ1R-V5 HEK293 cells were compared with unpaired Student's t-test using α of 0.05. The overexpression of σ1R-V5 resulted in a significant decrease of SOCE, but not the store-depletion when compared to WT$^{VC}$ HEK293 cells (Fig3.37C, ****, $P < 0.0001$; Fig3.37B, n.s., $P > 0.05$). This result suggests that σ1R-V5 inhibits SOCE independently of IP3Rs. Also, this result suggests that previously demonstrated inhibition of store-depletion by σ1R-V5 could be the result of the increased efflux of luminal $Ca^{2+}$ to mitochondria via IP3Rs. Results of statistical analysis have been summarized in Table 3.36.

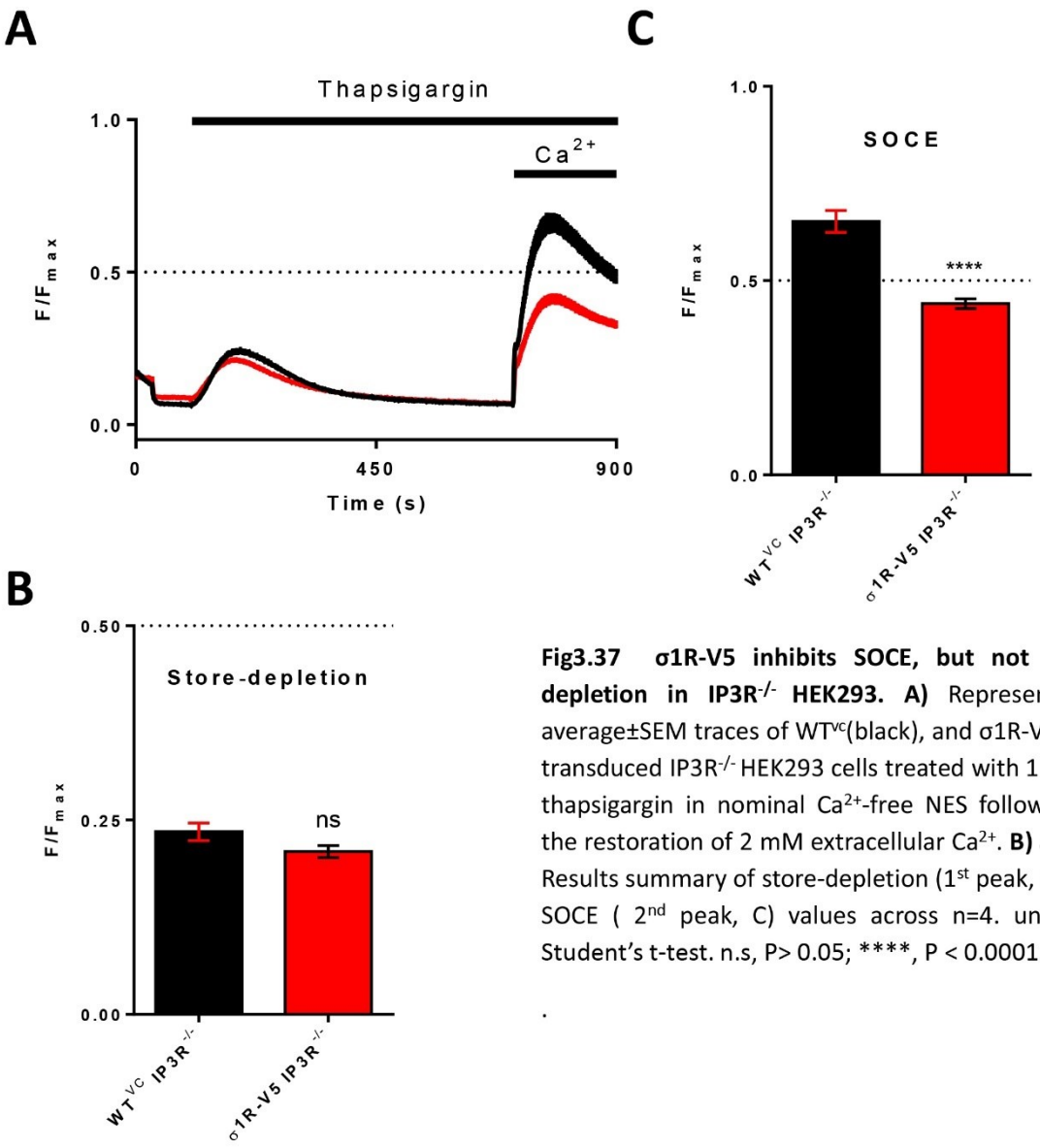


**Fig3.37 σ1R-V5 inhibits SOCE, but not store-depletion in IP3R$^{-/-}$ HEK293. A)** Representative average±SEM traces of WT$^{vc}$(black), and σ1R-V5(red) transduced IP3R$^{-/-}$ HEK293 cells treated with 1 µM of thapsigargin in nominal $Ca^{2+}$-free NES followed by the restoration of 2 mM extracellular $Ca^{2+}$. **B) and C)** Results summary of store-depletion (1$^{st}$ peak, B) and SOCE ( 2$^{nd}$ peak, C) values across n=4. unpaired Student's t-test. n.s, P> 0.05; ****, P < 0.0001.

.

| Group | Store-depletion Mean± SEM | SOCE Mean± SEM | N | t-test summary of store-depletion σ1R-V5 | t-test summary of SOCE σ1R-V5 |
|---|---|---|---|---|---|
| $WT^{VC}$ | 0.2349± 0.01123 | 0.6523 ± 0.02816 | 24 | n.s., P > 0.05 | ****, P < 0.0001 |
| σ1R-V5 | 0.2093± 0.007734 | 0.4408 ± 0.01266 | 24 | | |

**Table 3.3-6 Summary of unpaired Student's t-test for Tg-evoked increase in $[Ca^{2+}]_{cyt}$ during store-depletion and SOCE in $IP3R^{-/-}$ HEK293 cells.** Store-depletion and SOCE measurements (Peaks, Fig 3.37) were taken across four independent experiments (n=4). A population of HEK293 cells within one well of 96W plate was used as a biological replicate (N) for statistical analysis.

### 3.3.8 Overexpression of σ1R-V5 does not significantly reduce endogenous levels of STIM1 and STIM2.2 proteins in HEK293 cells

The regulation of SOCE is dependent on expression levels of ER $Ca^{2+}$ sensor proteins, STIM1 and STIM2.2, and thus, the inhibition of SOCE can be achieved by downregulation of STIM levels[183]. To determine whether the overexpression of σ1R reduces expression of endogenous STIM proteins, lysates of HEK293 cells were transduced with either $WT^{VC}$ or σ1R-V5 baculovirus and collected 24, 48 and 72h post-transduction –at time points that reflect conditions of different $Ca^{2+}$ functional assays used in this thesis. Collected lysates were analysed by Western blotting.

Fig3.38 shows endogenous levels of STIM1 and STIM2.2 in lysates collected 48h post-transduction with either $WT^{VC}$ and σ1R-V5 baculovirus. Endogenous levels of STIM1 and STIM2.2 were compared to overexpression of HA-STIM1 and STIM2.2, respectively. Lysates of HA-STIM1 and STIM2.2 HEK293 cells were collected 48h post-transfection with STIM constructs. This comparison was performed to test the specificity of STIM1 and STIM primary antibodies.

Fig3.39 shows Western blot analysis of endogenous levels of STIM homologs 24, 48 and 72h post-transduction with either $WT^{VC}$ or σ1R-V5 baculovirus. Fig3.39B, C and D summarize normalized STIM2.2, STIM1, and σ1R-V5 intensity across three independent experiments (n=3) analysed with one-way ANOVA using α of 0.05. No significant difference in endogenous levels of STIM proteins was detected between $WT^{VC}$ or σ1R-V5 HEK293 cells.

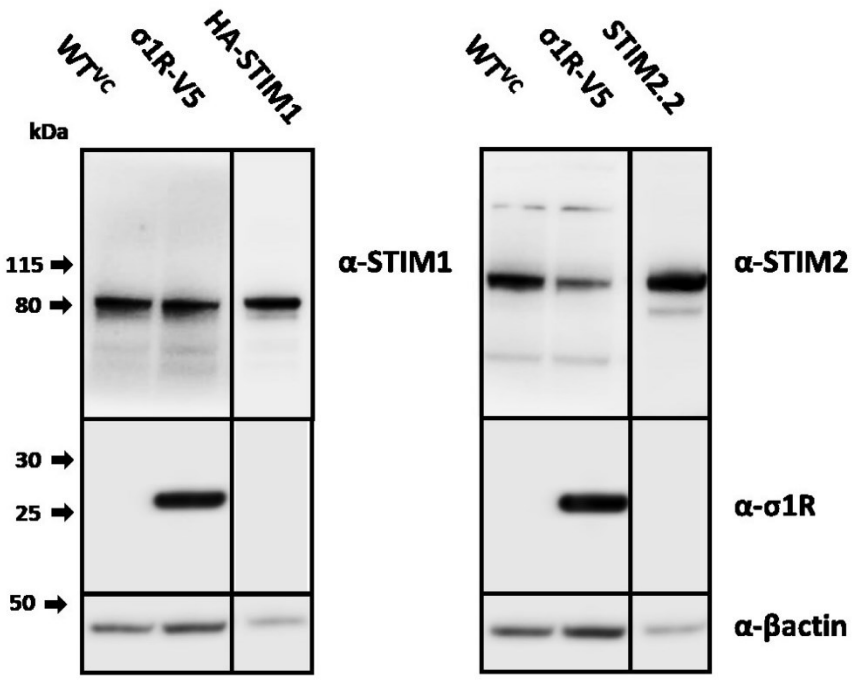


**Fig3.38 Western blot of endogenous STIM1 and STIM2 expression in $WT^{VC}$ and σ1R-V5 HEK293 cells 48h post-transduction compared to HEK293 cells expressing HA-STIM1 and STIM2.2 48h post-transfection.** Nitrocellulose membranes blotted with α-STIM2, α-STIM1, α-σ1R and α-βactin showing protein levels of endogenous STIM1 and STIM2.2 compared to expression of HA-STIM1 and STIM2.2, respectively (Row1), overexpressed σ1R-V5 (Row 2), and endogenous βactin (Row 3). 20 µg of $WT^{VC}$ and σ1R-V5 HEK293 lysates was loaded to assess endogenous levels of STIM proteins. 10 µg of HA-STIM1 and STIM2.2 lysates was loaded to assess overexpression of STIM proteins. To visualize location of the STIM bands for endogenous and overexpressed STIM proteins, different brightness and contrast settings were applied.

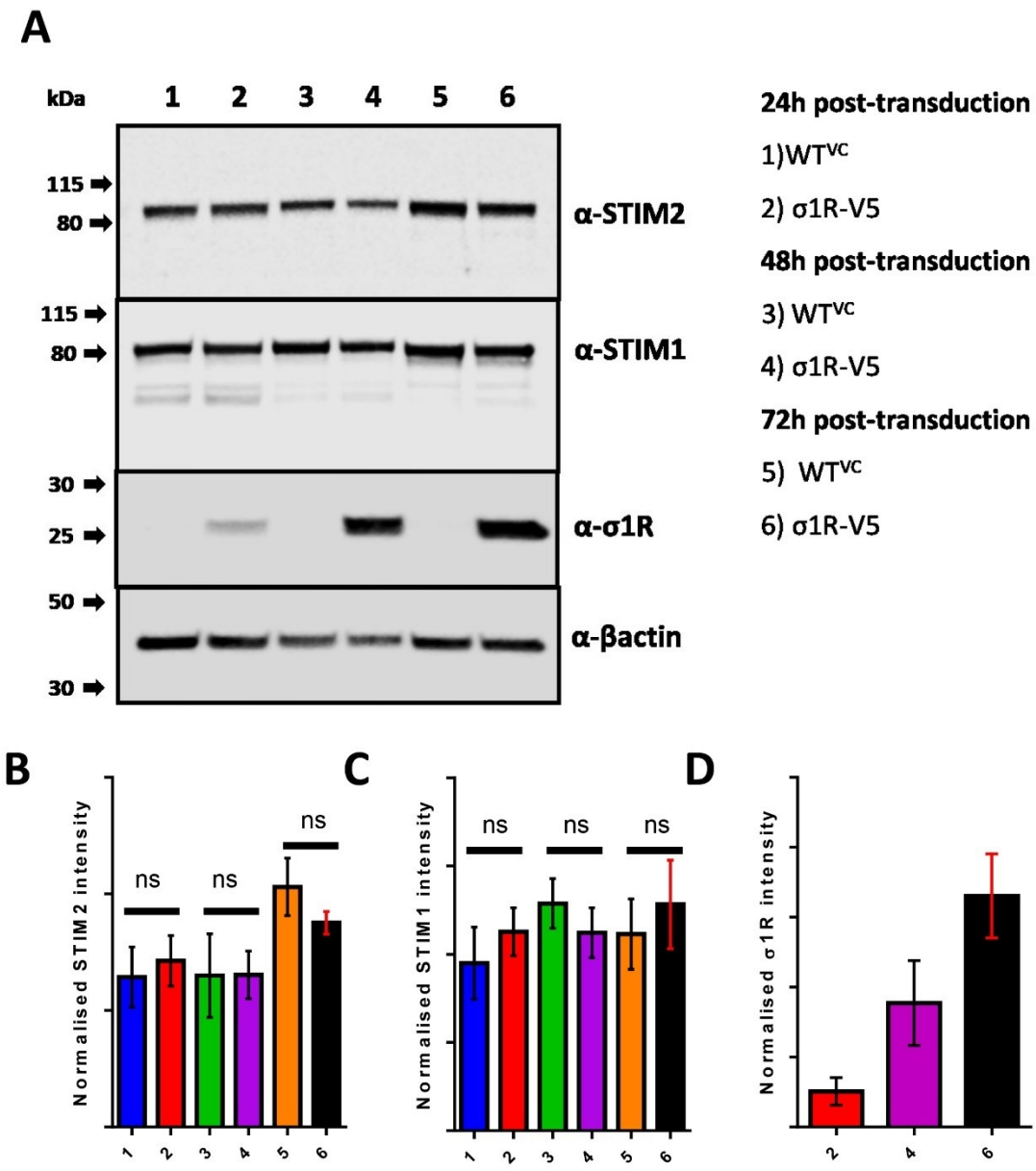


**Fig3.39 Western blot analysis of endogenous STIM1 and STIM2 expression in WT$^{VC}$ and σ1R-V5 HEK293 cells 24, 48 and 72h post-transduction. A)** Nitrocellulose membranes blotted with α-STIM2, α-STIM1, α-σ1R and α-βactin showing protein levels of endogenous STIM2 (Row1), endogenous STIM1 (Row2), overexpressed σ1R-V5 (Row 3), and endogenous βactin (Row 4). Lanes 1,2 contain lysates of WT$^{VC}$ and σ1R-V5 HEK293 cells 24 hours post-transduction. Lanes 3,4 contain lysates of WT$^{VC}$ and σ1R-V5 HEK293 cells 48 hours post-transduction. Lanes 5,6 contain lysates of WT$^{VC}$ and σ1R-V5 HEK293 cells 72 hours post-transduction. kDa = molecular weight markers in kilodaltons. B) C) and D) show normalized STIM2, STIM1, and σ1R-V5 intensities, respectively. Results are mean ± SEM. n = 3. ns, P> 0.05; relative to control. ANOVA with Tukey's posthoc analysis.

### 3.3.9 Overexpression of dominant-negative mutant Orai1$^{R91W}$ diminishes majority of GCaMP6f-measured SOCE

After investigating the functional effect of σ1R on SOCE using fluorescent $Ca^{2+}$ dyes, SOCE was also measured using GCaMP6f. A benefit of GECI approach over using fluorescent $Ca^{2+}$ dyes presented itself in measurements from only transfected cells. To determine the amount of SOCE mediated by Orai1, dominant-negative mutant Orai1$^{R91W}$ was co-expressed with GCaMP6f and ER $Ca^{2+}$ sensors mCh-STIM1 and STIM2.2-mCh. 48h post-transfection, HEK293 cells were treated with 1μM of thapsigargin, and changes in $[Ca^{2+}]_{cyt}$ were measured using GCaMP6f and Flexstation III microplate reader.

Fig3.310 shows GCaMP6f traces of HEK293 cells expressing GCaMP6f-only (WT; black), Orai1$^{R91W}$ (red), mCh-STIM1 (blue), mCh-STIM1+Orai1$^{R91W}$ (orange), STIM2.2-mCh (green), and STIM2.2-mCh+Orai1$^{R91W}$ (pink). Cells were treated with 1μM of thapsigargin in nominal $Ca^{2+}$-free NES followed by the restoration of 2 mM extracellular $Ca^{2+}$. SOCE peaks of HEK293 cells were compared with one-way ANOVA using α of 0.05. The overexpression of Orai1$^{R91W}$ resulted in a significant decrease of SOCE (Fig3.310, ****, $P < 0.0001$). The overexpression of two STIM homologs potentiated SOCE which was also diminished in the presence of dominant negative mutant Orai1$^{R91W}$. These results suggest that majority of GCaMP6f-measured SOCE occurs in association with functional Orai1 subunit. Results of statistical analysis have been summarized in Table 3.37.

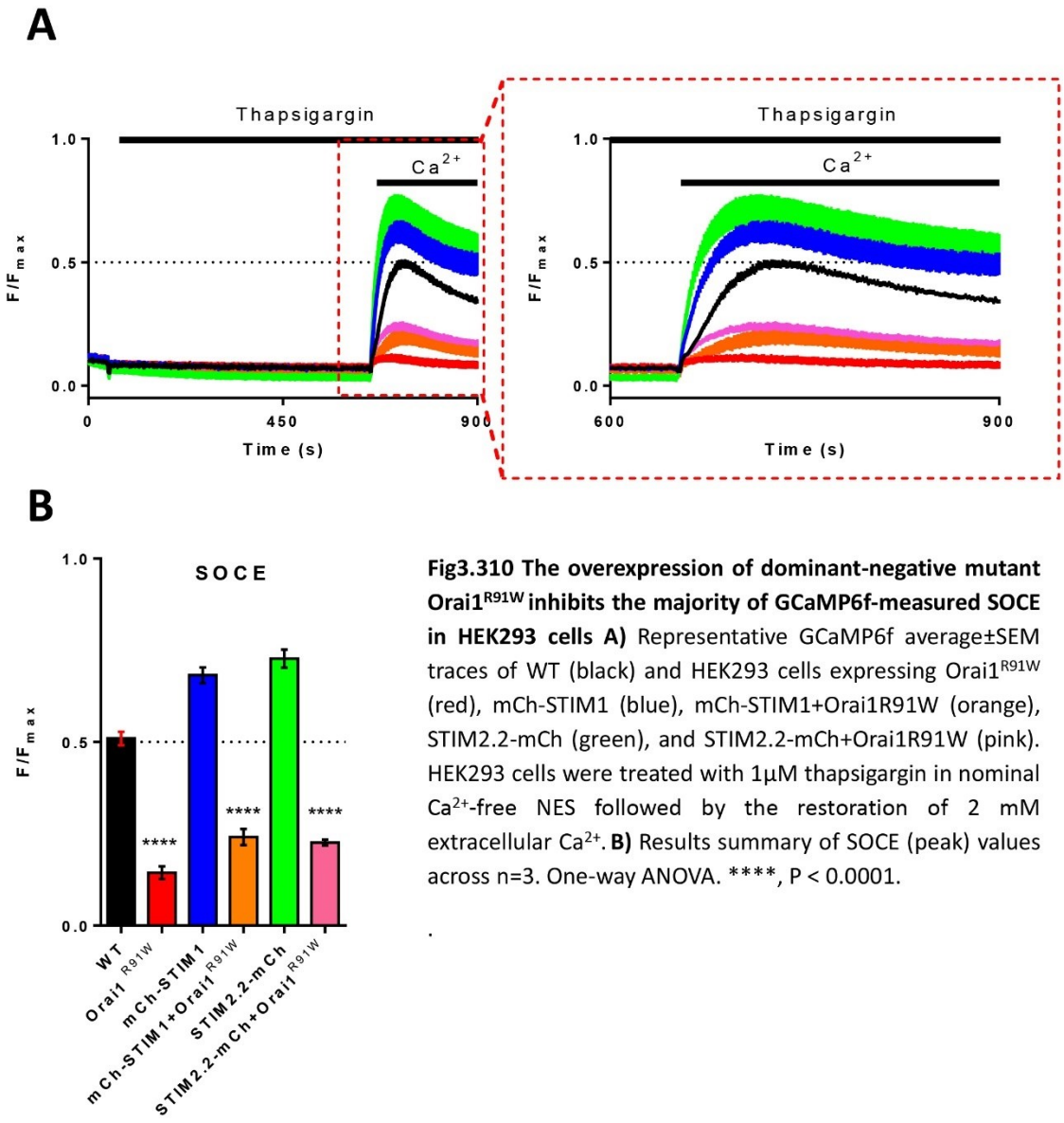


**Fig3.310 The overexpression of dominant-negative mutant Orai1$^{R91W}$ inhibits the majority of GCaMP6f-measured SOCE in HEK293 cells A)** Representative GCaMP6f average±SEM traces of WT (black) and HEK293 cells expressing Orai1$^{R91W}$ (red), mCh-STIM1 (blue), mCh-STIM1+Orai1R91W (orange), STIM2.2-mCh (green), and STIM2.2-mCh+Orai1R91W (pink). HEK293 cells were treated with 1µM thapsigargin in nominal $Ca^{2+}$-free NES followed by the restoration of 2 mM extracellular $Ca^{2+}$. **B)** Results summary of SOCE (peak) values across n=3. One-way ANOVA. ****, P < 0.0001.

.

| Group | SOCE Mean± SEM | N | ANOVA SOCE Orai1$^{R91W}$ | ANOVA SOCE mCh-STIM1 + Orai1$^{R91W}$ | ANOVA SOCE STIM2.2-mCh + Orai1$^{R91W}$ |
|---|---|---|---|---|---|
| WT | 0.5099± 0.01808 | 18 | ****, P < 0.0001 | ****, P < 0.0001 | ****, P < 0.0001 |
| Orai1$^{R91W}$ | 0.1441± 0.01747 | 18 | | | |
| mCh-STIM1 | 0.6822± 0.02132 | 18 | ****, P < 0.0001 | ****, P < 0.0001 | ****, P < 0.0001 |
| mCh-STIM1+ Orai1$^{R91W}$ | 0.2413± 0.022 | 18 | **, P < 0.01 | | n.s, P > 0.5 |
| STIM2.2-mCh | 0.7276± 0.02456 | 18 | ****, P < 0.0001 | ****, P < 0.0001 | ****, P < 0.0001 |
| STIM2.2-mCh+ Orai1$^{R91W}$ | 0.2263± 0.008085 | 18 | *, P < 0.05 | n.s, P > 0.5 | |

**Table 3.3-7 Summary of one-way ANOVA tests for GCaMP6f-measured SOCE during overexpression of dominant-negative Orai1$^{R91W}$.** SOCE measurements (Peaks, Fig 3.310) were taken across three independent experiments (n=3). A population of HEK293 cells within one well of 96W plate was used as a biological replicate (N) for statistical analysis.

### 3.3.10 σ1R-V5 inhibits GCaMP6f-measured SOCE

After establishing that the majority of GCaMP6f-measured SOCE occurs through the Orai1 channel, SOCE was measured in $WT^{VC}$ and σ1R-V5 HEK293 cells 72h post-transduction with baculovirus particles and 48h post-transfection with GCaMP6f. HEK293 cells were treated with 1μM of thapsigargin, and changes in $[Ca^{2+}]_{cyt}$ were measured using GCaMP6f and Flexstation III microplate reader.

Fig3.311 shows GCaMP6f traces of HEK293 cells transduced with $WT^{VC}$ (black) or σ1R-V5 (red) baculovirus particles. Cells were treated with 1μM of thapsigargin in nominal $Ca^{2+}$-free NES followed by the restoration of 2 mM extracellular $Ca^{2+}$. SOCE peaks of $WT^{VC}$ and σ1R-V5 HEK293 cells were compared with unpaired Student's t-test using α of 0.05. The overexpression of σ1R-V5 resulted in a significant decrease of SOCE (Fig3.311B, ****, $P < 0.0001$), suggesting that σ1R inhibits GCaMP6f-measured SOCE. Results of statistical analysis have been summarized in Table 3.38.

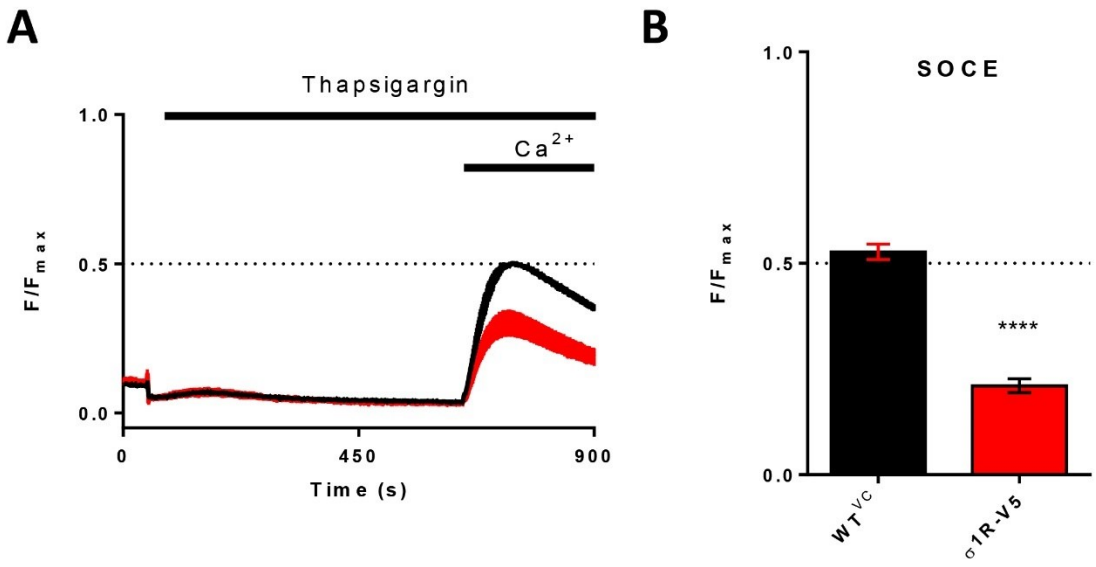


**Fig3.311 σ1R-V5 inhibits GCaMP6f-measured SOCE in HEK293 cells. A)** Representative average±SEM traces of $WT^{VC}$ and σ1R-V5-transduced HEK293 cells treated with 1µM thapsigargin in nominal $Ca^{2+}$-free NES followed by the restoration of 2 mM extracellular $Ca^{2+}$. **B)** Results summary of SOCE ( peak) values across n=3. Unpaired Student's t-test.****, P < 0.0001.

| Group | SOCE Mean±SEM | N | t-test summary of SOCE σ1R-V5 |
|---|---|---|---|
| $WT^{VC}$ | 0.5271 ± 0.01807 | 36 | ****, P < 0.0001 |
| σ1R-V5 | 0.2105 ± 0.01646 | 36 | |

**Table 3.3-8 Summary of unpaired Student's t-test for GCaMP6f-measured SOCE in $WT^{VC}$ and σ1R-V5-transduced HEK293 cells.** Store-depletion and SOCE measurements (Peaks, Fig 3.311) were taken across three independent experiments (n=3). A population of HEK293 cells within one well of 96W plate was used as a biological replicate (N) for statistical analysis.

### 3.3.11 σ1R-V5 inhibits NFAT nuclear-translocation

Nuclear factor of activated T cells (NFAT) is a $Ca^{2+}$-dependent transcription factor that translocates from the cytosol to nucleus in response to activated SOCE[161,184]. In SCID T-cells, cells with a defect in SOCE due to the expression of $Orai1^{R91W}$, NFAT nuclear-translocation is impaired and associated with immunodeficiency[185]. To further test the functional effect of σ1R on SOCE, the rate of nuclear translocation of GFP-tagged NFAT was measured in WT, $WT^{VC}$ and σ1R-V5 HEK293 cells 72h post-transduction with baculovirus particles and 48h post-transfection with NFAT-GFP. HEK293 cells were treated with 5μM of thapsigargin for 15 minutes while kept in 2 mM $Ca^{2+}$ NES, and changes in the rate of NFAT-GFP nuclear translocation were measured using confocal microscopy.

Fig3.312 summarizes results of NFAT nuclear translocation experiment. Fig3.312A shows images of NFAT-GFP expressing HEK293 cells before (Basal) and after (SOCE) treatment with 5μM of thapsigargin in 2mM $Ca^{2+}$ NES. The rate of NFAT nuclear translocation was measured using Time Series V3 Analyzer in Fiji/ImageJ; For purposes of analysis, an oval (height = 10px, width = 10px) region of interest (ROI) was placed within nuclei of NFAT-GFP transfected cells to measure changes in nuclear fluorescence, and within the cytosol to measure changes in cytosolic fluorescence. Measured traces were normalized using nuclear/cytosolic fluorescence ratio (N/C). The rate of NFAT nuclear translocation was calculated using the area under the curve (AUC).

Fig3.312B and C summarize the rate of NFAT-GFP translocation in WT (blue), $WT^{VC}$ (black) and σ1R-V5 (red) HEK293 cells across three independent (n=3) experiments. The rate of NFAT-GFP translocation between experimental groups was compared with one-way ANOVA using α of 0.05. The overexpression of σ1R-V5 resulted in a significant decrease in

the rate of NFAT nuclear-translocation (Fig3.312C, **, $P < 0.01$), suggesting the inhibitory effect of σ1R upstream of the activation of NFAT nuclear-translocation.

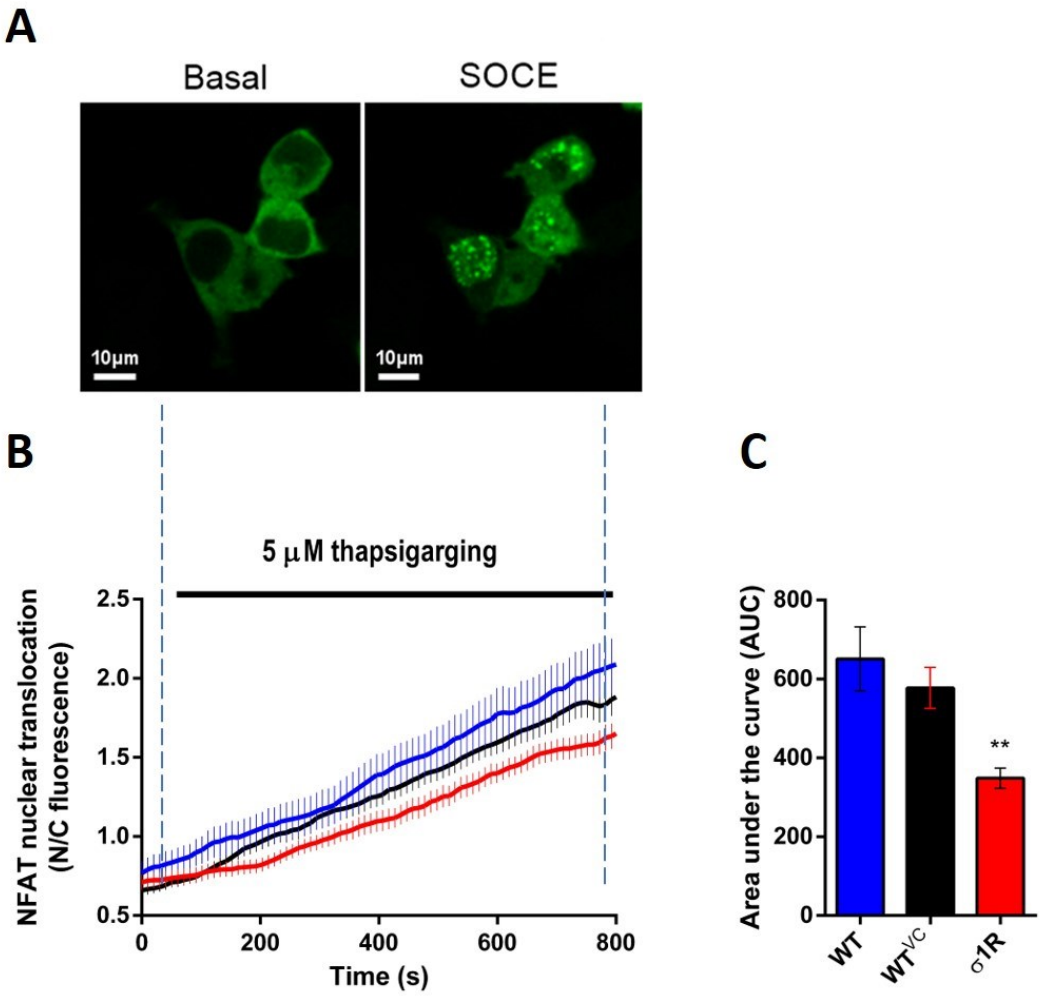


**Fig3.312 σ1R-V5 inhibits rate of NFAT-nuclear translocation in HEK293 cells .** A) Representative images of HEK293 cells before (basal) and after 15-min treatment with 5 µM thapsigargin (SOCE). B) Average±SEM traces of NFAT fluorescence (nuclear/cytosolic) in WT (blue), WTVC (black) and σ1R-V5 HEK293 cells. C) Results summary of NFAT translocation calculated using area under the curve (AUC) values across three independent experiments (n=3). One-way ANOVA. **, P<0.01.

.

## 3.4 Discussion

### 3.4.1 σ1R inhibits SOCE in HEK293 cells

Enhanced expression of σ1R-V5 in HEK293 cells significantly inhibited $Ca^{2+}$ influx 24h post-transduction – as measured by $Ca^{2+}$ fluorescent dyes, and 72h post-transduction – as measured by GCaMP6f. This $Ca^{2+}$ influx was characterised as SOCE as it was a) dependent on the store-depletion, b) inhibited by the addition of 1μM $Gd^{3+}$, and c) diminished by the expression of dominant-negative mutant $Orai^{R91W}$. Additionally, overexpression of σ1R reduced store-depletion, indicating reduced $Ca^{2+}$ content of intracellular stores. However, chronically reduced ER $Ca^{2+}$ content after treatment with reversible SERCA blocker CPA failed to inhibit SOCE, which suggests reduced store-depletion is not sufficient to inhibit SOCE and that σ1R exerts its inhibitory role as SOCE regulator via different mechanism.

These results are consistent with two of previous reports. Brailoiu et al. have shown that treatment of rat brain endothelial cells with cocaine, which is a σ1R agonist, inhibited SOCE[158]. Similar results were obtained by Srivats et al. in CHO cells where treatment with another σ1R agonist, (+)SKF10047, yielded similar results[34]. In both studies, treatments with unrelated σ1R antagonist exerted opposite effect on the regulation of SOCE. σ1R agonists promote dissociation of σ1R/BiP complex, allowing σ1R to interact with proteins at MAMs and ER-PM junctions, and forming of monomeric and lower oligomeric forms of σ1R [48]. Contrary, σ1R antagonist oppose agonist effect preserving σ1R/BiP complex and favouring higher oligomeric forms[186].

Srivats et al. also demonstrated that enhanced expression of σ1R inhibited thapsigargin-evoked SOCE in the σ1R-HEK293 stable-cell line[34]. Thapsigargin is the

irreversible blocker of the SERCA ATPase pump at the ER, and its administration promotes a substantial leak of ER $Ca^{2+}$, subsequently causing store-depletion. A substantial drop in ER [$Ca^{2+}$] also promotes dissociation of σ1R/BiP complex, suggesting that observed inhibitions of SOCE in these two studies occurred during the availability of σ1Rs for interaction with other SOCE regulators[22]. Moreover, upregulation of σ1R reduced the rate of NFAT nuclear translocation. Natively, NFAT proteins are found in the cytoplasm of the T cells[187]. To translocate from cytoplasm to nucleus, NFAT requires direct dephosphorylation by the $Ca^{2+}$-regulated phosphatase calcineurin which is activated by CRAC-mediated $Ca^{2+}$ influx. Hence, the rate of NFAT translocation is often used as an independent measure for the possible action of protein on SOCE activity. Previously, a negative regulator of SOCE called SARAF was characterised by measuring of rate of NFAT translocation[131]. As part of STIM-Orai1 complex, SARAF promoted a slow inactivation of STIM-dependent SOCE activity, possibly by facilitating the de-oligomerization of STIM proteins, and thus, turning off Orai-channel to prevent the overload of the cell with excessive $Ca^{2+}$. During ER $Ca^{2+}$ depletion by SERCA inhibitor BHQ, the rate of NFAT nuclear translocation was inhibited after upregulation of SARAF in HEK293 cells and downstream of its regulation of SOCE. Upregulation of σ1R yielded equivalent results, suggesting that σ1R inhibited SOCE and subsequently, reduced rate of NFAT translocation as a downstream effect of SOCE regulation. From pharmacological aspect, this ability of σ1R to reduce NFAT translocation is of particular interest as cocaine, known σ1R agonist, compromises immune system[188]. Hence, this result provides an insight into a possible mechanism how the administration of σ1R agonist can affect immune system, and what approach, such as administration of σ1R antagonist, should be considered to counteract/prevent it.

### 3.4.2 σ1R inhibits SOCE independently of $K^+$ efflux in HEK293 cells

Gueguinou et al[14]. reported that σ1R modulates SK3-dependent $Ca^{2+}$ homeostasis by promoting Orai1:SK3 coupling in colorectal and breast cancer cells[14]. SK3 is small conductance $Ca^{2+}$ activate potassium ($K^+$) channel that hyperpolarizes cell by allowing $K^+$ efflux. In mechanism proposed by Gueguinou et al., hyperpolarization of PM via SK3 channel enhances $Ca^{2+}$ influx through Orai1 channel. In HEK293 cells, SK3 channels are not normally expressed. Nonetheless, for further characterization of regulation of SOCE by σ1R in HEK293 and whether it is coupled to $K^+$ efflux, HEK293 cells expressing σ1R were placed in high extracellular $K^+$ (142nM). Firstly, reduced SOCE in $WT^{VC}$ HEK293 cells was observed when compared to the previous experiments. This was expected due to depolarization of the membrane potential in high extracellular $K^+$ which reduced the electrical driving force for $Ca^{2+}$ entry through Orai1 channels. However, under those conditions, enhanced expression of V5-tagged σ1R still inhibited SOCE, suggesting that inhibitory effect of σ1R on SOCE in HEK293, as observed by this study, is independent of $K^+$ efflux.

### 3.4.1 σ1R inhibits SOCE independently of IP3Rs in HEK293 cells

Enhanced expression of σ1Rs reduced efflux of $Ca^{2+}$ from the intracellular stores, suggesting reduced ER [$Ca^{2+}$] concentration. A reduction in ER [$Ca^{2+}$] might arise from σ1R stabilizing type 3 of IP3Rs at MAMs and thereby, enhanced movement of $Ca^{2+}$ from the ER to mitochondria[22]. Also, σ1R may indirectly promote $Ca^{2+}$ leak via Sec61 channels. Interaction of ER chaperone BiP with Sec61 inhibits ER $Ca^{2+}$ leak[189]. Upregulation of σ1R might result in increased number of σ1R/BiP complexes and consequently, enhance Sec61-mediated $Ca^{2+}$ leak. Another possibility is that σ1R could also attenuate basal SOCE through interaction with STIM2 proteins based on the model by Srivats et al. where σ1R attenuated SOCE through interaction with STIM1[34].

The results of this study suggest that reduced $Ca^{2+}$content of intracellular stores by σ1R was most likely a consequence of its interaction with IP3Rs. In $IP3R^{-/-}$ HEK293 stable cell line, enhanced expression of σ1R resulted in inhibition of thapsigargin-evoked SOCE but failed to significantly reduce store-depletion. Recent study using ER $Ca^{2+}$ indicator Mag-Fluo-4 showed enhanced $Ca^{2+}$ depletion during upregulation of IP3R in HEK293 cells, which could also be observed as enhanced rise in cytosolic [$Ca^{2+}$ ][182]. By stabilizing IP3Rs at MAMs, σ1R promotes efflux of luminal $Ca^{2+}$ to mitochondria. Thus, non-significant reduction in ER [$Ca^{2+}$] content in the absence of IP3Rs could be a result of σ1R inability to promote $Ca^{2+}$ flux from ER to mitochondria. However, this data set lacks additional experiments, such as ionomycin-evoked store depletion or measurements using combination of ER- and mitochondria-targeted $Ca^{2+}$ indicators for more precise evaluation of σ1R's role in the regulation of $Ca^{2+}$ content of intracellular stores.

Interestingly, these results also show that σ1R can inhibit SOCE in the absence of IP3Rs. While a role of IP3Rs as a channel of ER $Ca^{2+}$ release is well understood, recent studies also demonstrated that IP3R could associate with STIM1 proteins which results in the modulation of SOCE[181,182]. Moreover, a subdivision of IP3Rs into "mobile" and "immobile" fractions has been proposed to explain the underlying mechanism of IP3Rs regulation of $Ca^{2+}$ influx[181]. These "immobile" IP3Rs were detected at ER-PM junctions where they served as sites of frequent STIM1 accumulation after store-depletion, but precise molecular explanation behind this mechanism, or what causes differentiation of "mobile" and "immobile" IP3Rs remains unknown. However, combination of FRET experiments with $Ca^{2+}$ assays revealed that association of IP3Rs with STIM1 resulted in reduced intraluminal $Ca^{2+}$ environment at the sites of IP3R/STIM1 interaction which subsequently, increased diameter of STIM1/Orai1 puncta and enhanced SOCE[182]. Hence, current evidence suggests that IP3Rs are incorporated into SOCE complex at ER-PM junctions with ability to modulate

$Ca^{2+}$. Both IP3R (type 3) and STIM1 have been reported as σ1R interactive proteins and σ1R has been reported in same immunoprecipitated complex with STIM1 and Orai1[22,34]. While results in Chapter III do not exclude possibility that σ1R may participate or perhaps, modulate the association between IP3R and STIM1, they do demonstrate that the inhibitory role of σ1R in the regulation of SOCE is independent of IP3R, its known interactive partner.

# 4 Chapter IV:

## Measurements of $[Ca^{2+}]_{cyt}$ at ER-PM junctions and the functional role of σ1R in SOCE microdomains

## 4.1 Introduction

We have shown in Chapter III that σ1R inhibits SOCE during measurements of $[Ca^{2+}]_{cyt}$ in a population of cells. Although these measurements of global $[Ca^{2+}]_{cyt}$ provide essential information about the functional role of σ1R in the regulation of SOCE, they do not provide detailed information about the effects of σ1R on temporal and spatial aspects of SOCE within the microdomain of the ER-plasma membrane junction. It is changes here which are of key importance for triggering downstream signalling events.

SOCE occurs at contact sites between the PM and ER membranes, where the distance separating the two membranes is below 40 nm. This allows proteins embedded in the ER to interact with proteins embedded in the PM[190]. These ER-PM junctions are essential for store-dependent $Ca^{2+}$ entry. Upon depletion of the ER $Ca^{2+}$ store, the STIM family of ER transmembrane proteins accumulate at the ER-PM junctions where they directly interact with phospholipids and PM proteins, in particular, the Orai family of $Ca^{2+}$ channels. This interaction causes the docking, tethering and activation of the Orai1 channel[117,191]. The restricted STIM-Orai1 microdomains result in local $Ca^{2+}$ entry and the formation of $Ca^{2+}$ microdomains, a key feature of $Ca^{2+}$ signalling that gives a raise to specific cellular processes in different regions of the cell[192].

To investigate how σ1R affects Orai1-mediated SOCE, we utilized a targeted $Ca^{2+}$ reporter protein fused to the Orai1 channel, named G-GECO1.2-Orai1[193]. The G-GECO1.2-Orai1 construct encodes for a fully functional Orai1 protein with a genetically encoded fluorescent $Ca^{2+}$ reporter protein, G-GECO1.2, attached to its N-terminal domain. This was shown previously to allow the monitoring of Orai1 channel activity in transfected mammalian cells. Advantages of utilizing such a construct over electrophysiological techniques include

reduced invasiveness and improved spatial information with regards to the location of the SOCE response. Combined with total internal reflection fluorescence microscopy (TIRFM), that allows for optical sectioning of fluorescent molecules within the immediate vicinity of the PM, and a fast EMCCD camera, this approach provides spatial and temporal resolution of Orai1 mediated $Ca^{2+}$ signals within the SOCE microdomain[194].

### 4.1.1 Aims

The aim was (1) to develop a reliable method to measure the Orai1-mediated $Ca^{2+}$ signal within the SOCE microdomain and (2) to compare the effect of the σ1R on the amplitude of this signal.

## 4.2 Methods

### 4.2.1 Analysis procedures for optical recordings with G-GECO1.2-Orai1 and TIRFM

For the analysis of optical measurements of G-GECO1.2-Orai1, we defined and implemented several stages of analysis (Figure 4.2.1) that allowed us an efficient and semi-automated approach for detection, extraction and analysis of G-GECO1.2-Orai1 fluorescent traces.

#### *4.2.1.1 Pre-processing of G-GECO1.2-Orai1 TIRFM recordings*

TIRFM recordings were generated via MicroManager (*ome* format) and imported into Fiji/ImageJ for pre-processing. The pre-processing step consisted of background-subtraction that was performed by subtracting the baseline image (median filtered, 2x pixel radius) from the recording. This step corrected for uneven illumination and camera deficiencies. A baseline image and pre-processed recording (BS stack) were saved in an original folder (.tiff format).

#### *4.2.1.2 ROI detection using thresholding based on the Laplace operator*

ROIs were detected in the pre-processed recording in IgorPro7 using an integrated set of software tools, named SARFIA (Semi-Automated Routines for Functional Image Analysis)[195]. The segmentation of the recordings was carried out using a threshold calculated as a multiple of the standard deviation (SD) of all the pixel values in the Laplace operator[196]. ROIs were then displayed in a temporary window allowing us to verify whether ROIs corresponded to visible G-GECO1.2-Orai1 puncta, and to adjust the threshold with immediate feedback. In our experiments, we used the threshold of 2.5-3 × SD.

#### *4.2.1.3 Fluorescence analysis*

Selected ROIs were converted in the mask that we applied on the G-GECO1.2-Orai1 pre-processed recording. SARFIA allowed us to extract and compare dynamic fluorescent traces for each ROI. Fluorescent traces were extracted as changes in the relative fluorescence (RFUs) over a period of time. We normalised each individual trace using two methods of normalization. First, we used SARFIA in-built ΔF/F formula where the baseline was defined as the bin centre of the highest peak of a histogram of all fluorescence values in a given trace. The number of bins was 1 + log2 N, where N was the number of points in a given trace.

As a second normalisation approach, we considered the nature of our $Ca^{2+}$ reporter targeted to Orai1 protein. ROI of G-GECO1.2-Orai1 can consist of a) different number of G-GECO1.2-Orai1 per active Orai1 channel (1 to 6), and b) clusters of Orai1 channels. Therefore, we decided to implement an additional point of reference into our recordings that would maximise fluorescent signal for each ROI – $F_{max}$. $F_{max}$ was recorded immediately after SOCE by treating cells with 5 μM Ionomycin in 2 mM $Ca^{2+}$, allowing us to acknowledge the variation in the number of G-GECO1.2-Orai1 per ROI and normalise each extracted G-GECO1.2-Orai1 trace using $F/F_{max}$ formula.

#### *4.2.1.4 Hierarchical clustering*

Implementing SARFIA for data analysis allowed us to perform hierarchical clustering with extracted and normalised G-GECO1.2-Orai1 traces. Clustering methods are often utilized for sorting functional classes of the response. SARFIA allows for comparison of traces using different metrics: Pearson's r, Euclidean, normalised Euclidean, Manhattan, or Chebyshev. To sort G-GECO1.2-Orai1 traces into functional classes, we opted for

Euclidean metric that has been commonly used for sorting of time-series traces. G-GECO1.2-Orai1 traces were compared pair-wise to yield a distance matrix where the distance between traces provided qualification for the dissimilarity between two traces. Within the distance matrix, a distance of 0 indicated a perfect correlation between the traces. A cut-off for grouping traces into the same functional cluster was chosen manually as a percentage of the highest distance. We used a cut-off of 15% to detect dissimilar G-GECO1.2-Orai1 traces. Considering the majority of examined traces were grouped within the same cluster, suggesting a very similar response, we used hierarchical clustering option within SARFIA to define and exclude artefacts from the overall analysis.

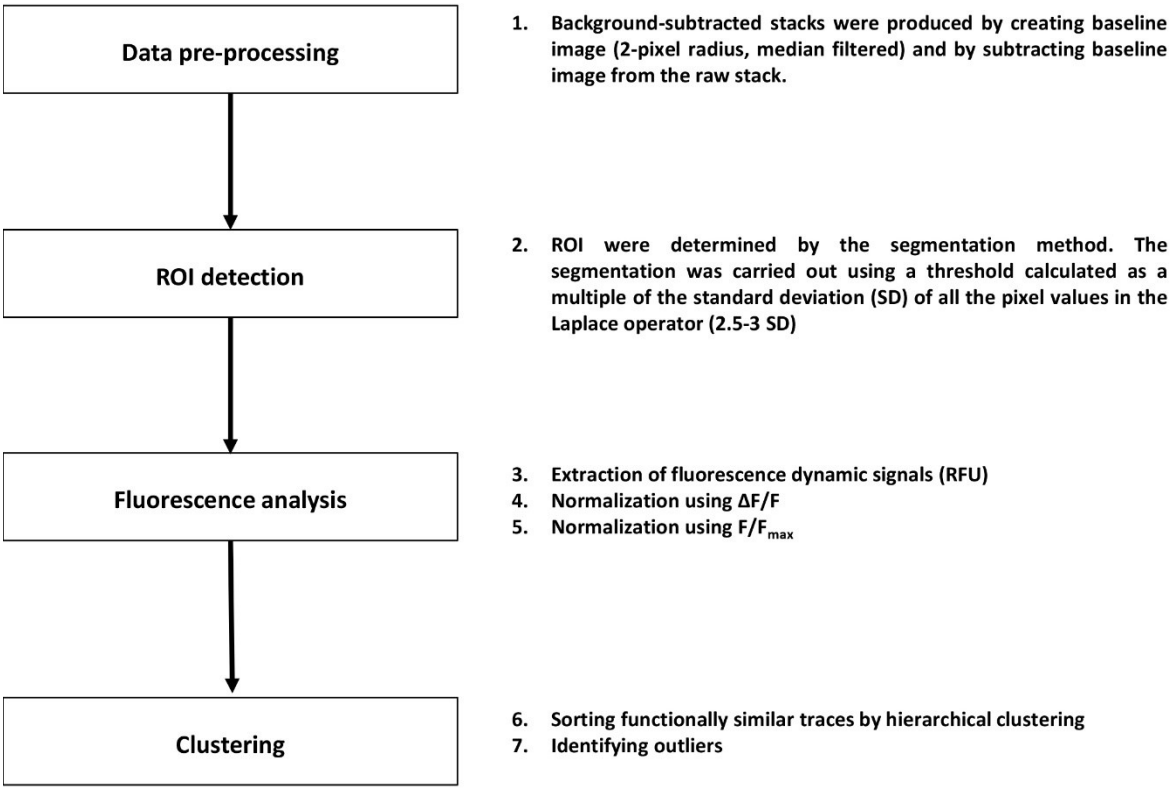


**Figure 4.21 Outline of analysis procedures for optical recordings with G-GECO1.2-Orai1 and TIRFM.** Data pre-processing was performed using Fiji/ImageJ. The integrated set of software tools, named SARFIA, was implemented using IgorPro7 for ROI detection, extraction and analysis of G-GECO1.2-Orai1 fluorescent traces.

## 4.3 Results

### 4.3.1 Determining the angle for TIRFM recordings in ER-PM junctions using G-GECO1.2-Orai1 and ER-DsRed co-expression in HEK293 cells

To perform TIRFM recordings, the angle of incidence has to surpass the critical angle. However, the critical angle depends on the refractive index of the sample, and biological samples have unknown and variable refractive indices[197]. Therefore, we co-expressed G-GECO1.2-Orai1 with ER-DsRed to estimate the angle of incidence for TIRFM recordings in ER-PM junctions.

Figure 4.3.1 shows HEK293 cells expressing G-GECO1.2-Orai1 (green) and ER-DsRed (red) in epifluorescent and TIRF mode. ER-dsRED is genetically encoded fluorescent marker for ER. In the epifluorescent mode, ER-DsRed was distributed in a typical, reticular, ER manner, surrounding nuclei and extending towards edges of the cells. However, once we manually adjusted the angle for TIRF, surpassing the critical angle, only near-PM ER was visible over the entire footprint of the cell. Simultaneously, the distribution of G-GECO1.2-Orai1 went from uneven and blurry within the epifluorescent mode of our TRIFM, to a sharper and more even distribution across the entire footprint of the cell in TIRF mode. These changes in both channels were accompanied by a noticeable change in signal-to-noise ratios (SNRs) between the biological sample and the background immediately after surpassing the critical angle. Across our TIRFM experiments, we used both morphological and SNR changes as guidelines for angle adjustments when moving from epifluorescent to TIRF mode.

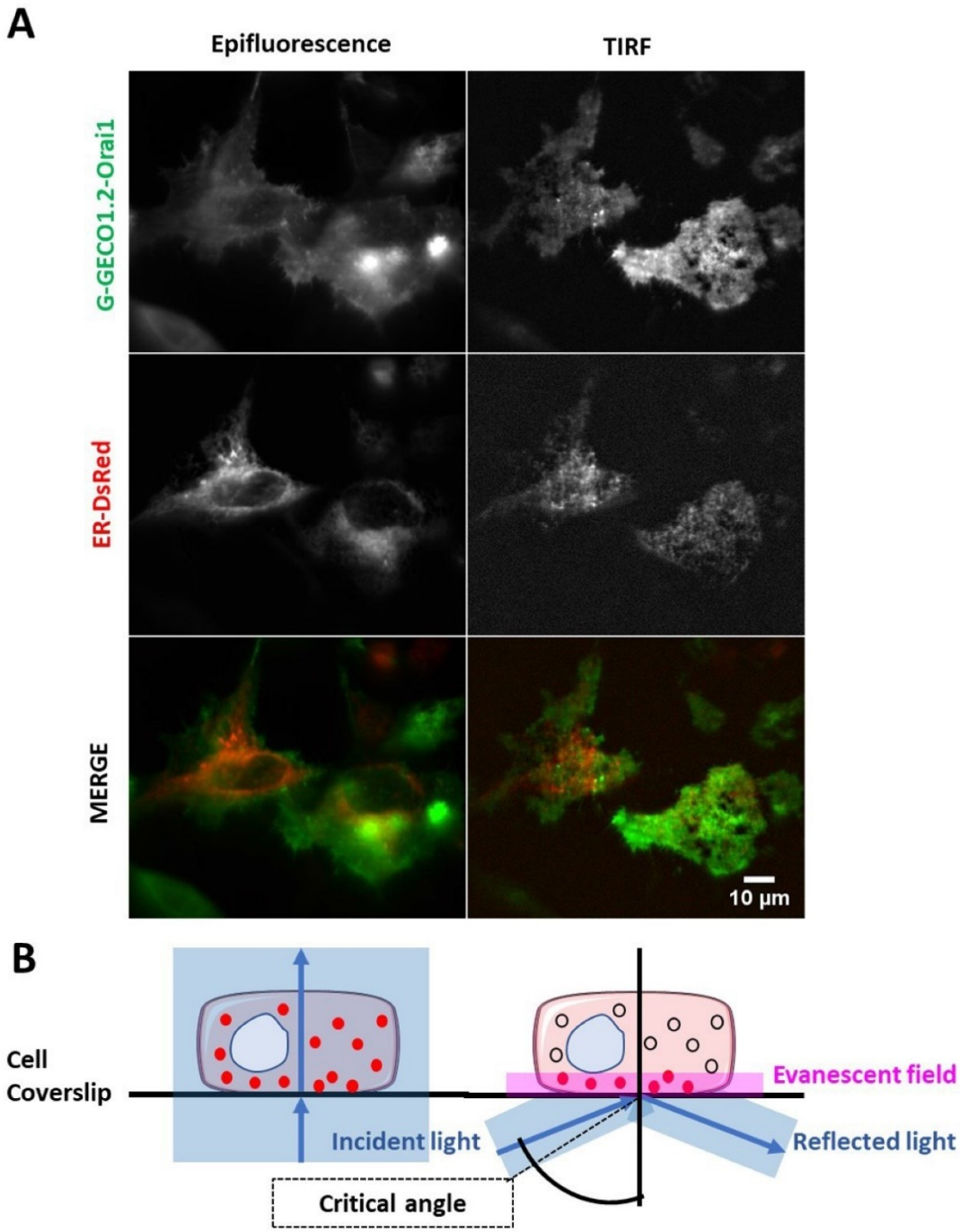


**Fig4.31 Epifluorescent and TIRF mode of G-GECO1.2-Orai1 co-expressed with ER-DsRed in HEK293 cells.** (A) HEK293 cells expressing G-GECO1.2-Orai1 (green) and ER-DsRed (red) in Epifluorescent (column 1) and TIRF (column 2) mode. Cells were imaged in HBSS. (B) Schematics of Epifluorescent (column 1) and TIRF (column 2) mode. In TIRF mode, the angle of incident light surpasses critical angle (dashed line), creating the evanescent field. Recordings in the evanescent field allow for optical sectioning of the narrow area at the cell-coverslip interface. Scale bar = 10µm.

### 4.3.2 Local $Ca^{2+}$ entry recorded at the PM using G-GECO1.2-Orai1 co-expressed with PMEM-dTomato in HEK293 cells

After establishing the angle for TIRFM recordings in ER-PM junctions by G-GECO1.2-Orai1 and ER-DsRed, we wanted to test whether we could record local $Ca^{2+}$ influx in sub-PM regions, using G-GECO1.2-Orai1. Therefore, G-GECO1.2-Orai1 was co-expressed with PM marker PMEM-dTomato in HEK293 cells.

Figure4.3.2 shows HEK293 cells co-expressing G-GECO1.2-Orai1 and PMEM-dTomato in 0.1 mM EGTA, before treatment (column 1), and in 2 mM $Ca^{2+}$, after treatment with 1 μM Thapsigargin for 6 minutes (column 2). A change of extracellular [$Ca^{2+}$] to 2mM increased G-GECO1.2-Orai1 fluorescence intensity at the PM. Under the same conditions, the fluorescence intensity of PMEM-dTomato remained relatively unchanged, suggesting that the observed changes in the fluorescence of G-GECO1.2-Orai1 were due to shifting in the indicator's calmodulin domain caused by $Ca^{2+}$-binding. As G-GECO1.2 is attached to the intracellular N-termini of Orai1 protein[193], a change in the fluorescent intensity also suggests a change in [$Ca^{2+}$] in the proximity of the intracellular domain of G-GECO1.2-Orai1 – thus, a local $Ca^{2+}$ entry.

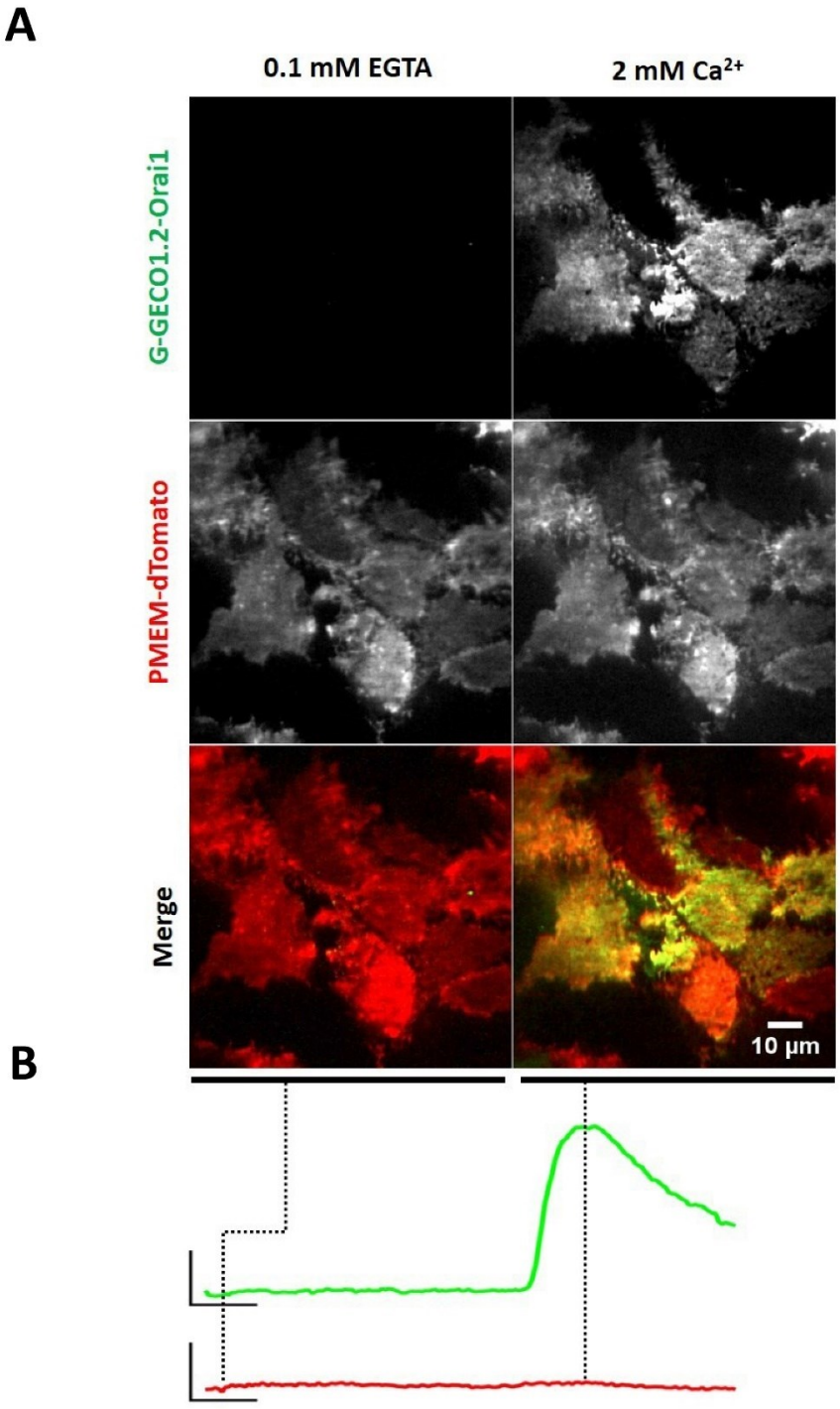


**Fig4.32 Changes in fluorescence of G-GECO1.2-Orai1 co-expressed with PMEM-dTomato in HEK293 cells.** (A) HEK293 cells expressing G-GECO1.2-Orai1 (green) and PMEM-dTomato (red) in 0.1mM EGTA (column 1), and in 2mM extracellular $Ca^{2+}$ 6 min post-Thapsigargin treatment (column 2). (B) Traces show changes in total fluorescence of G-GECO1.2-Orai1 (green) and PMEM-dTomato (red) during changes of extracellular [$Ca^{2+}$]. Scale bar = 50 RFUs (y-direction) and 100 s (x-direction).

### 4.3.3 Local $Ca^{2+}$ entry recorded using G-GECO1.2-Orai1 co-expressed with mCh-STIM-CAD in HEK293 cells

For further testing of G-GECO1.2-Orai1 on our home-built TIRFM system, G-GECO1.2-Orai1 was co-expressed with mCh-STIM-CAD what was sufficient to induce clustering and activation of Orai1 channels, independently of $Ca^{2+}$ stores depletion (Figure 4.34). Considering that co-expression of Orai1 proteins with STIM-CAD domains results in the constitutively active $Ca^{2+}$ entry – which under prolonged conditions is toxic for cells – we attempted TIRFM recordings 10-, 15- and 20-hours post-transfection (data not shown). At 15 hour-point post-co-transfection of HEK293 cells with mCh-STIM-CAD, G-GECO1.2-Orai1 was expressed at sufficient levels to obtain TIRFM images from healthy-looking cells.

In the presence of mCh-STIM-CAD and G-GECO1.2-Orai1, we tested for store-independent $Ca^{2+}$ dynamics at ER-PM junctions in response to changes in extracellular [$Ca^{2+}$] while recording at a rate of one frame every 5s. Figure 4.33A shows representative images of G-GECO1.2-Orai1 (green) and mCh-STIM-CAD (red) co-expressed in HEK293 cells in 0.2 mM $Ca^{2+}$ (column 1), 2mM $Ca^{2+}$ (column 2) and 2 mM EGTA (column 3). Figure4.33B shows an average change in the relative fluorescence (RFU) of G-GECO1.2-Orai1 (green) and mCh-STIM-CAD (red) during a recording. Dashed lines indicate the precise time point of image extraction from the recording.

A change of $[Ca^{2+}]_{ex}$ from 0.2 mM to 2mM resulted in the robust elevation of G-GECO1.2-Orai1 fluorescence intensity, while the addition of 2 mM EGTA diminished G-GECO1.2-Orai1 signal. This result was consistent with previously reported CAD-evoked and Orai1-mediated $Ca^{2+}$ influx[105,193]. Under the same conditions, the fluorescence intensity of mCh-STIM-CAD remained relatively unchanged, suggesting that the observed changes in the fluorescence of G-GECO1.2-Orai1 were due to a local $Ca^{2+}$ entry.

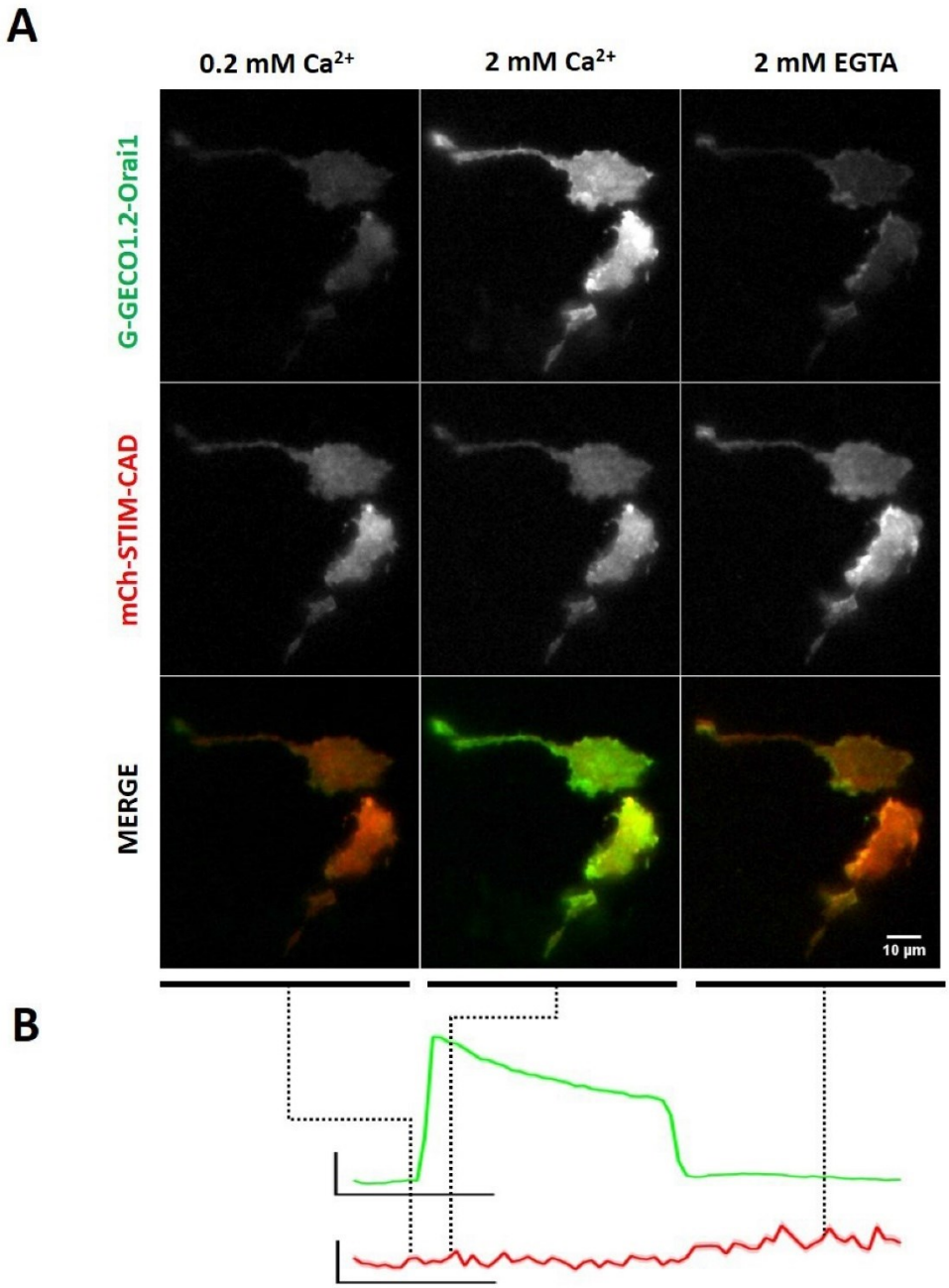


**Figure 4.33 Changes in fluorescence of G-GECO1.2-Orai1 co-expressed with mCh-STIM-CAD in HEK293 cells.** A) HEK293 cells expressing G-GECO1.2-Orai1 (green) and mCh-STIM-CAD (red) in 0.2mM (column 1) and 2mM extracellular $Ca^{2+}$ (column 2), and 2mM EGTA (column 3). B) Traces show changes in relative fluorescence of G-GECO1.2-Orai1 (green) and mCh-STIM-CAD (red) during changes of extracellular [$Ca^{2+}$]. Scale bar = 50 RFUs (y-direction) and 100 s (x-direction). This recording is also used to demonstrate different stages of analysis as shown in Figures 4.34, 4.35, and 4.36.

### 4.3.4 A subtraction of initial local background allows for the extraction of comparable G-GECO1.2-Orai1 traces

The TIRFM recordings occur in the evanescent field, which is not discrete, but exponentially decays with a distance from the coverslip[194,198]. Thus, the excitation intensity is dependent on the distance of fluorophore from the coverslip, as well as the penetration depth of the evanescent field. The advantage of G-GECO1.2-Orai1 is that it is localized in the PM (Figure 4.32), resulting in discrete fluorophore distribution and limiting the error of data interpretation that can occur due to the distance of fluorophore from the coverslip. However, the position and relative fluorescence of the fluorophore can be additionally affected by the "flatness" of the cell footprint against the coverslip, as well as uneven illumination across the field of view and camera deficiencies.

To correct for these numerous factors that could impact quantification and comparison of G-GECO1.2-Orai1 responses, the initial local background was subtracted. We created the median-filtered (2-pixel radius) baseline image and subtracted it from the rest of the stack.

Figure 4.34 compares average images of recordings before (Raw-Stack) and after (BS stack) background subtraction. Uneven illumination during TIRFM is apparent in the average image of the Raw-Stack (Figure4.34A) where the background intensity (white trace) decreased going from left to right of the image. The average image of the BS stack had a more even background.

Figure4.34B compares plot profiles across two cells in 0.2mM and 2mM extracellular $Ca^{2+}$ and 2 mM EGTA. Baseline intensity across two cells in 0.2mM $Ca^{2+}$ (low $Ca^{2+}$, Raw Stack) resembles an intensity across two cells in 2mM EGTA. After background-subtraction,

these intensities were almost nullified within the recording (Figure4.34B, BS-stack), allowing us to focus on the change in fluorescence caused by the addition of physiological [$Ca^{2+}$] (2 mM).

Figure4.34C compares G-GECO1.2-Orai1 traces along the plot-line of two cells in the field of view (Cell1 and Cell2). In the original recording (Raw image column), G-GECO1.2-Orai1 traces had a different baseline in 0.2 mM $Ca^{2+}$, peak in 2 mM $Ca^{2}$, and fluorescent intensity after chelation with 2 mM EGTA. After pre-processing (BS-stack column), traces were very similar in 0.2 mM $Ca^{2+}$ and after chelation with 2 mM EGTA, allowing us a better comparison of their peaks in physiological [$Ca^{2+}$] (2 mM).

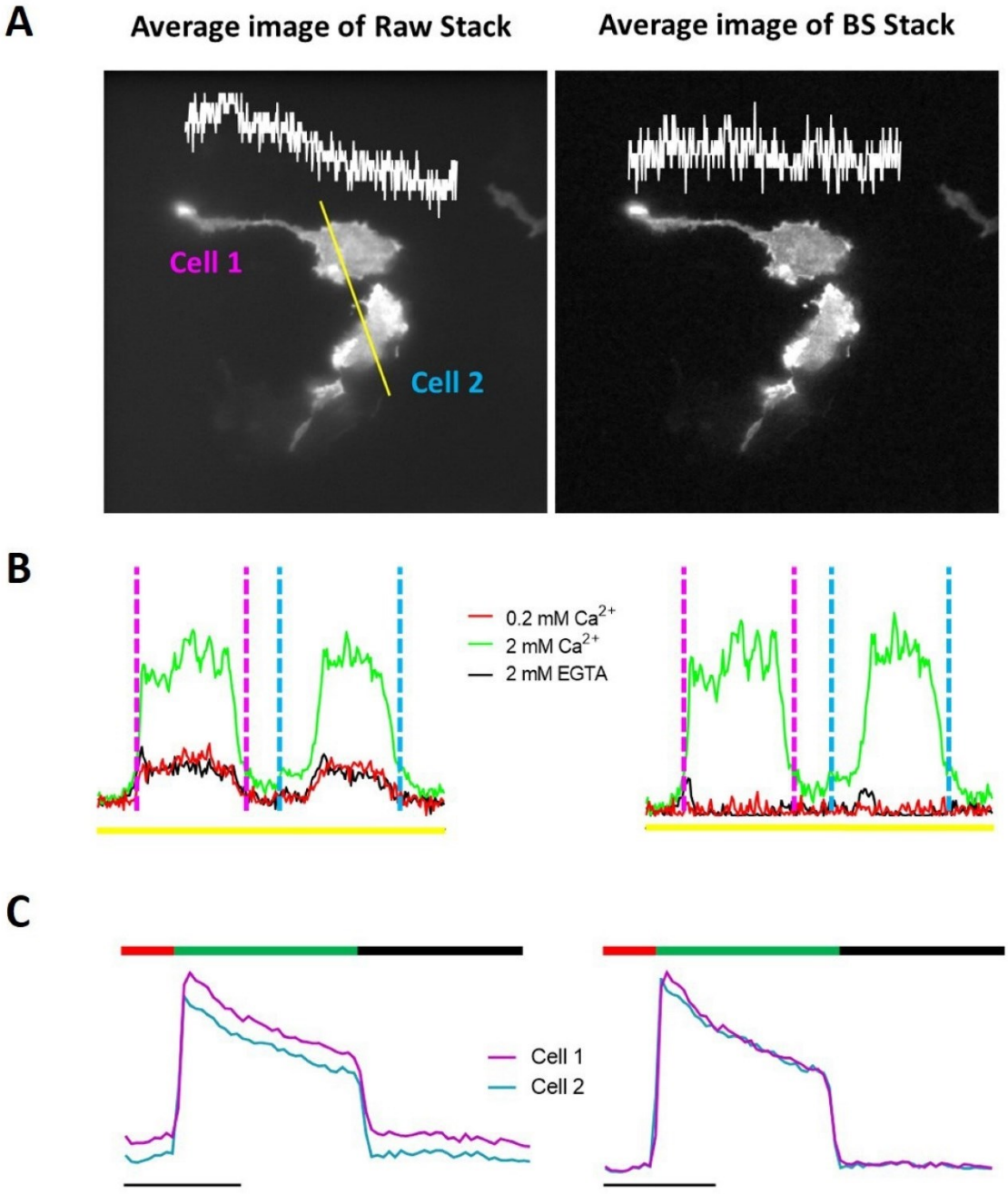


**Fig4.34 A comparison of raw and pre-processed TIRFM recordings of G-GECO1.2-Orai1 in HEK293 cells.** A) Average images of Raw and BS stacks of G-GECO1.2-Orai1 co-expressed with STIM-CAD in HEK293. White traces above the cells show background intensity in the marked area. A yellow line marks 55 µM long plot profiles shown under (B). B) Plot profiles of G-GECO1.2-Orai1 intensity in raw and BS image stacks in 0.2 mM $Ca^{2+}$ (red), 2 mM $Ca^{2+}$ (green) and 2 mM EGTA (black). Dashed lines mark the boundaries of cell 1 (purple) and cell 2 (blue). C) Changes in fluorescence of G-GECO1.2-Orai1 of cell 1 (purple) and cell 2 (blue) in 0.2 mM $Ca^{2+}$ (red), 2 mM $Ca^{2+}$ (green) and 2 mM EGTA (black) along the profile line. Scale bar = 100 s.

### 4.3.5 Implementation of SARFIA for analysis facilitates the detection, extraction, and analysis of G-GECO1.2-Orai1 fluorescent traces

Manual detection of ROIs is a time-consuming process that can introduce bias and reduce the consistency and accuracy of the obtained dataset, especially when the position and relative fluorescence of the fluorophore can affect data quantification. To minimize personal bias and increase the consistency, we implemented a set of tools called SARFIA for semi-automatic analysis of dynamic imaging experiments using G-GECO1.2-Orai1.

Figure 4.35 shows an example of ROI detection of G-GECO1.2-Orai1 puncta in HEK293 cells. ROIs were obtained using a full focal plane and a threshold calculated as a multiple of the standard deviation (SD) of all the pixel values in the Laplace operator (3 x SD). During segmentation in SARFIA, a temporary SD-image was produced to allow visual comparison between detected ROIs and visible G-GECO1.2-Orai1 puncta. The position and size of each ROI were then saved in the ROI mask with the same x and y dimensions as the initial image sequence. Based on their position within the focal plane, ROIs were coloured and indexed (Figure 4.35A). A visual comparison of SD-image with detected ROIs confirmed that chosen ROIs corresponded to the G-GECO1.2-Orai1 in puncta-like structures.

Overall, 164 ROIs were detected within the representative recording, and further analysis of the ROI mask showed that ROIs varied in size. Considering that our segmentation parameters excluded ROIs ≤ 2px to exclude off-target regions, our smallest ROI consisted of 3 px (~0.72 µm) while the largest was 157 px (~37.56 µm). Frequency distribution of ROIs' size revealed that majority of ROIs were smaller in size (25% percentile = 4 px, median = 7 px, 75% percentile = 13 px). However, in comparison to the previously reported sizes across the Orai1 hexamer (8 nm) and Orai1 clusters (100 – 200 nm)[117], the

size of our ROIs suggested that detected G-GECO1.2-Orai1 puncta-like structures corresponded to clusters of G-GECO1.2-Orai1 clusters.

Once ROIs were detected, we applied the ROI mask to the recording to extract G-GECO1.2-Orai1 time-series information. SARFIA allowed us to assess this information in the form of individual traces and fluorescent data showing a change in fluorescence per ROI over time.

Figure 4.36 shows the extracted time series of G-GECO1.2-Orai1 in both formats – individual traces and fluorescent data of changes in relative fluorescence (RFU) per ROI over time. Individual traces were then normalized using the ΔF/F formula (Figure 4.36B, see 4.2 Methods). Following normalization, we performed hierarchical clustering of time-series to differentiate between potential functional clusters.

Figure 4.36C summarizes exemplary responses of G-GECO1.2-Orai1 in the presence of mCh-STIM-CAD domain into three distinct categories. The most abundant category (Category-1) consisted of traces that were consistent with previously reported CAD-evoked and Orai1-mediated $Ca^{2+}$ influx[105,193]. The other two categories (Category-2 and Category-3) made 4.3% of overall traces and consisted of traces exhibiting unusual shape due to very slow $Ca^{2+}$ influx, as well as a slow response to chelation with 2 mM EGTA. We traced these traces to the two groups of ROIs, with each category corresponding to the particular area at the edge of the cell, which would suggest that the measured functional responses within these two categories were most likely results of motion artifact. Led by this example, we later performed hierarchical clustering to all G-GECO1.2-Orai1 recordings post-normalization. We individually assessed whether detected functional clusters were actual SOCE responses – and to be included in the analysis - or a consequence of motion

artefact. Recordings with over 5% of traces that resembled noise or motion artefacts were not included in the analysis.

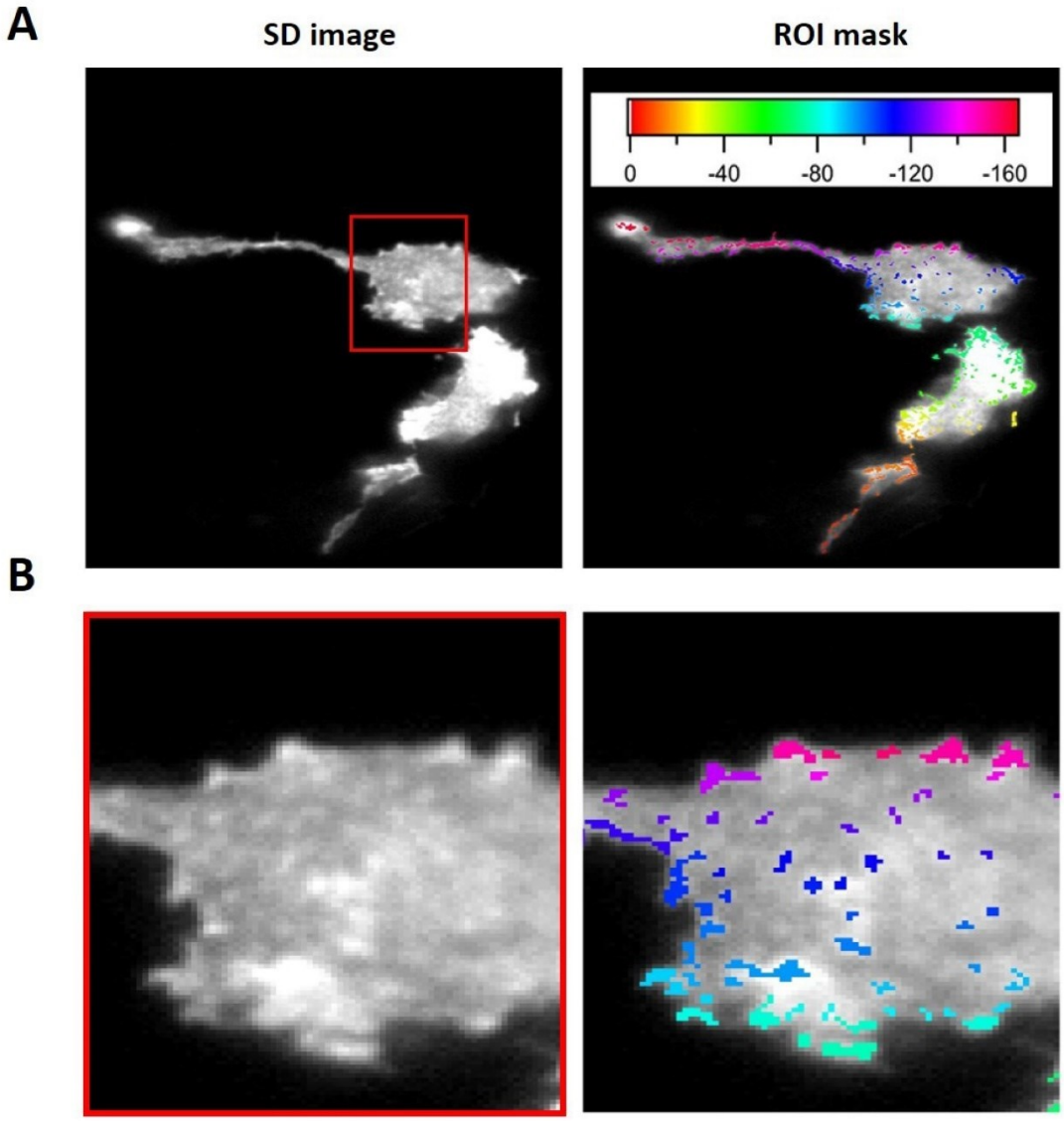


**Figure 4.35 ROI detection of G-GECO1.2-Orai1 puncta in HEK293 cells using SARFIA in IgorPro.** A) SD image of the full focal plane created by segmentation using a threshold calculated as a multiple of the SD of all pixel values in the Laplace operator. The ROIs were colored, numbered and stored in a matrix, termed "ROI mask" with the same x and y dimensions as the initial image sequence: Pixels that were outside ROIs were assigned a value of 1, whereas pixels inside an ROI were assigned a negative value based on their index number. B) Enlarged SD image with visible G-GECO1.2-Orai1 puncta. Selected ROI regions correspond to visible G-GECO1.2-Orai1 puncta.

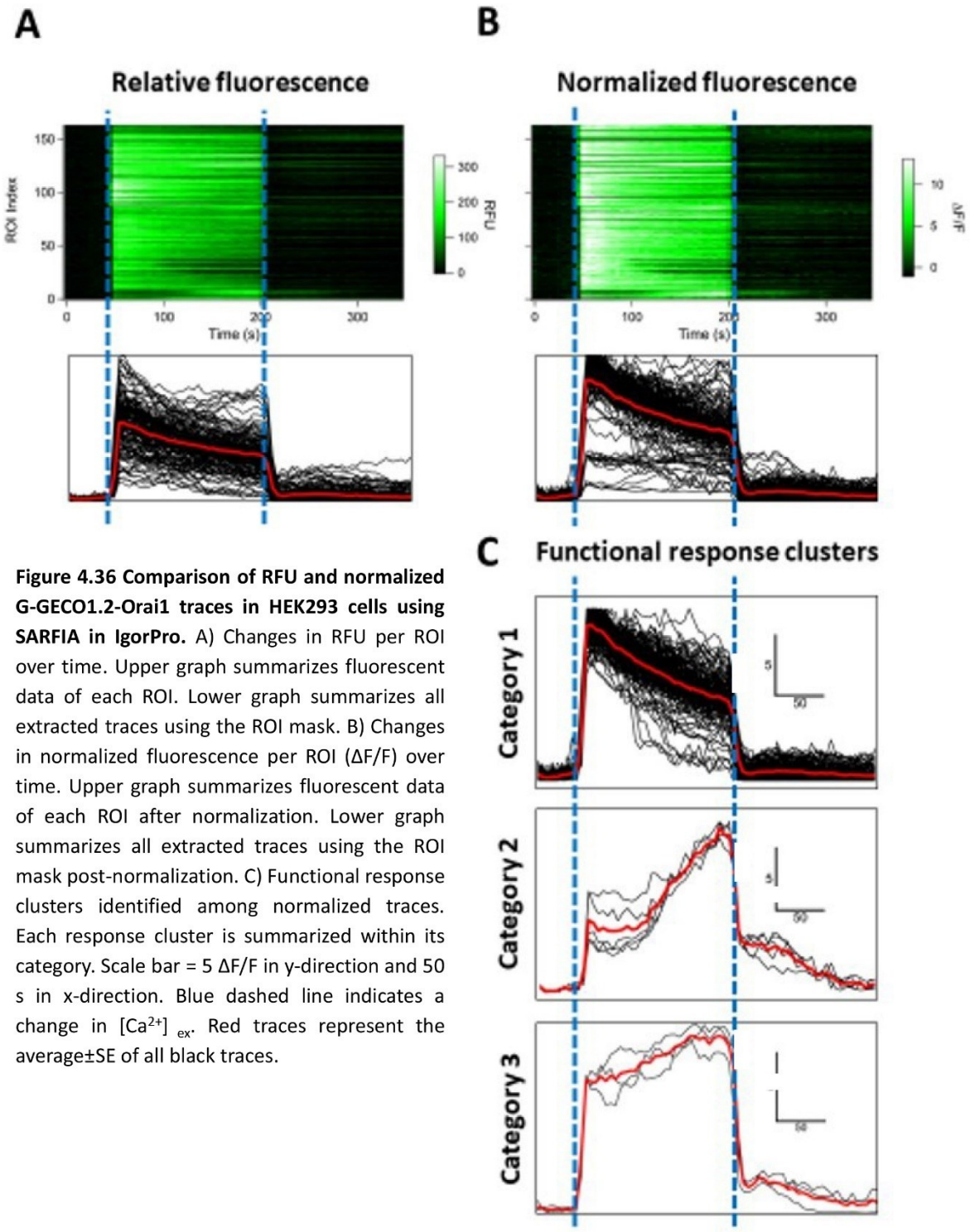


**Figure 4.36 Comparison of RFU and normalized G-GECO1.2-Orai1 traces in HEK293 cells using SARFIA in IgorPro.** A) Changes in RFU per ROI over time. Upper graph summarizes fluorescent data of each ROI. Lower graph summarizes all extracted traces using the ROI mask. B) Changes in normalized fluorescence per ROI (ΔF/F) over time. Upper graph summarizes fluorescent data of each ROI after normalization. Lower graph summarizes all extracted traces using the ROI mask post-normalization. C) Functional response clusters identified among normalized traces. Each response cluster is summarized within its category. Scale bar = 5 ΔF/F in y-direction and 50 s in x-direction. Blue dashed line indicates a change in $[Ca^{2+}]_{ex}$. Red traces represent the average±SE of all black traces.

### 4.3.6 Comparison of the expression and subcellular distribution of G-GECO1.2-Orai1 and G-GECO1.2-Orai1$^{R91W}$

Having established the criteria for obtaining reliable TIRFM recordings and the analysis of G-GECO1.2-Orai1 datasets, we wanted to ensure that changes in fluorescence, as measured with G-GECO1.2-Orai1, genuinely corresponded to the local SOCE mediated by Orai1. We therefore looked to generate a non-functional mutant of Orai1 which would have similar PM expression but fail to allow $Ca^{2+}$ influx, thus acting as a negative control. The R91W mutation in Orai1 occurs in the region of the channel that lines the pore and it was originally identified as a naturally occurring mutation that caused severe combined immune deficiency (SCID) syndrome[93]. Homozygous expression of Orai1$^{R91W}$ mutant diminishes CRAC currents, and is shown to have a dominant-negative effect on Orai1 mediated $Ca^{2+}$ entry[93,199,200].

The R91W mutation was introduced into G-GECO1.2-Orai1 and initially, the expression of this mutant compared to the wild-type G-GECO1.2-Orai1 was done using Western blot analysis of HEK293 lysates collected 24h post-transfection with either G-GECO1.2-Orai1 or G-GECO1.2-Orai1$^{R91W}$ construct (Figure 4.37). Nitrocellulose membranes were blotted with primary antibodies targeted to Orai1, and βactin anti-Orai1 antibody.

The Western blot in Figure 4.37 shows bands of very similar intensity at the predicted size for G-GECO1.2-Orai1 (~80kDa) for the wild-type protein (lane 1) and R91W mutant protein (lane 2). There is more than one band which are likely to correspond to the different glycosylation states of Orai1[201]. β-actin was used as a loading control. The predicted size for endogenous Orai1 protein is ~30 kDa for non-glycosylated and ~50 kDa for glycosylated Orai1 and we also detected similar levels of the endogenous Orai1 protein. Thus, we

conclude that introducing the mutation into Orai1 does not disrupt expression of the reporter-tagged channel.

To compare the subcellular distribution of the wild-type and mutant G-GECO1.2-Orai1, HEK293 cells expressing these proteins were imaged by confocal fluorescence microscopy, 24h after transfection. Cells were treated with 5 μM ionomycin in 2mM $Ca^{2+}$ HBSS, to saturate the $Ca^{2+}$ binding sites of G-GECO1.2 and maximize the fluorescence signal and images obtained as shown in Figure 4.38. These single confocal optical sections show that both proteins exhibited a similar distribution. Plot profiles of the relative fluorescence intensity for G-GECO1.2-Orai1 and G-GECO1.2- Orai1$^{R91W}$ (Fig4.38B) demonstrated intensity peaks at the edges of the cells, suggesting plasma membrane targeting for both for G-GECO1.2-Orai1 and G-GECO1.2- Orai1$^{R91W}$.

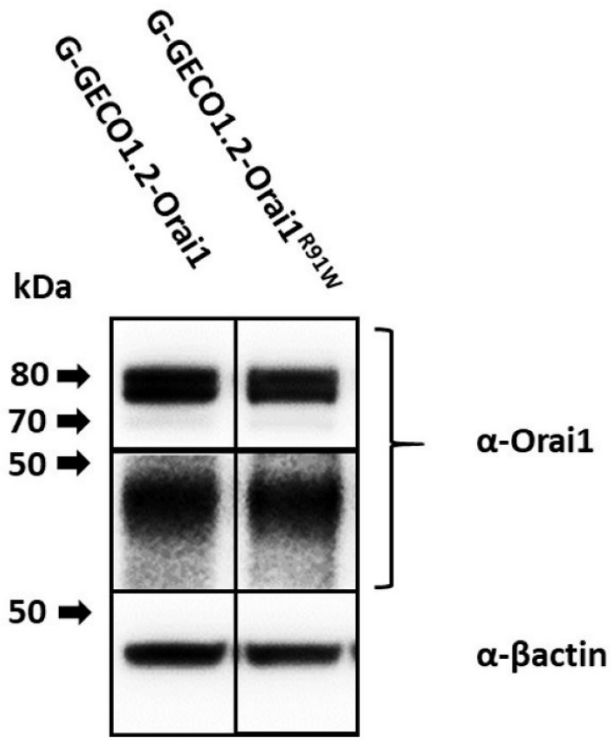


**Figure4.37 Western blot analysis of G–GECO1.2–Orai1 and G-GECO1.2-Orai1$^{R91W}$ in HEK293 cells.** Nitrocellulose membranes blotted with primary antibodies targeted to Orai1, and βactin. Detected bands correspond to protein levels of recombinant Orai1 – G-GECO1.2-Orai1 or G-GECO1.2-Orai1$^{R91W}$ (Row1), endogenous Orai1 (Row2), and endogenous βactin (Row 3). HEK293 lysates were collected 24 hours after transfection with G-GECO1.2-Orai1 or G-GECO1.2-Orai1$^{R91W}$. kDa = molecular weight markers in kilodaltons.

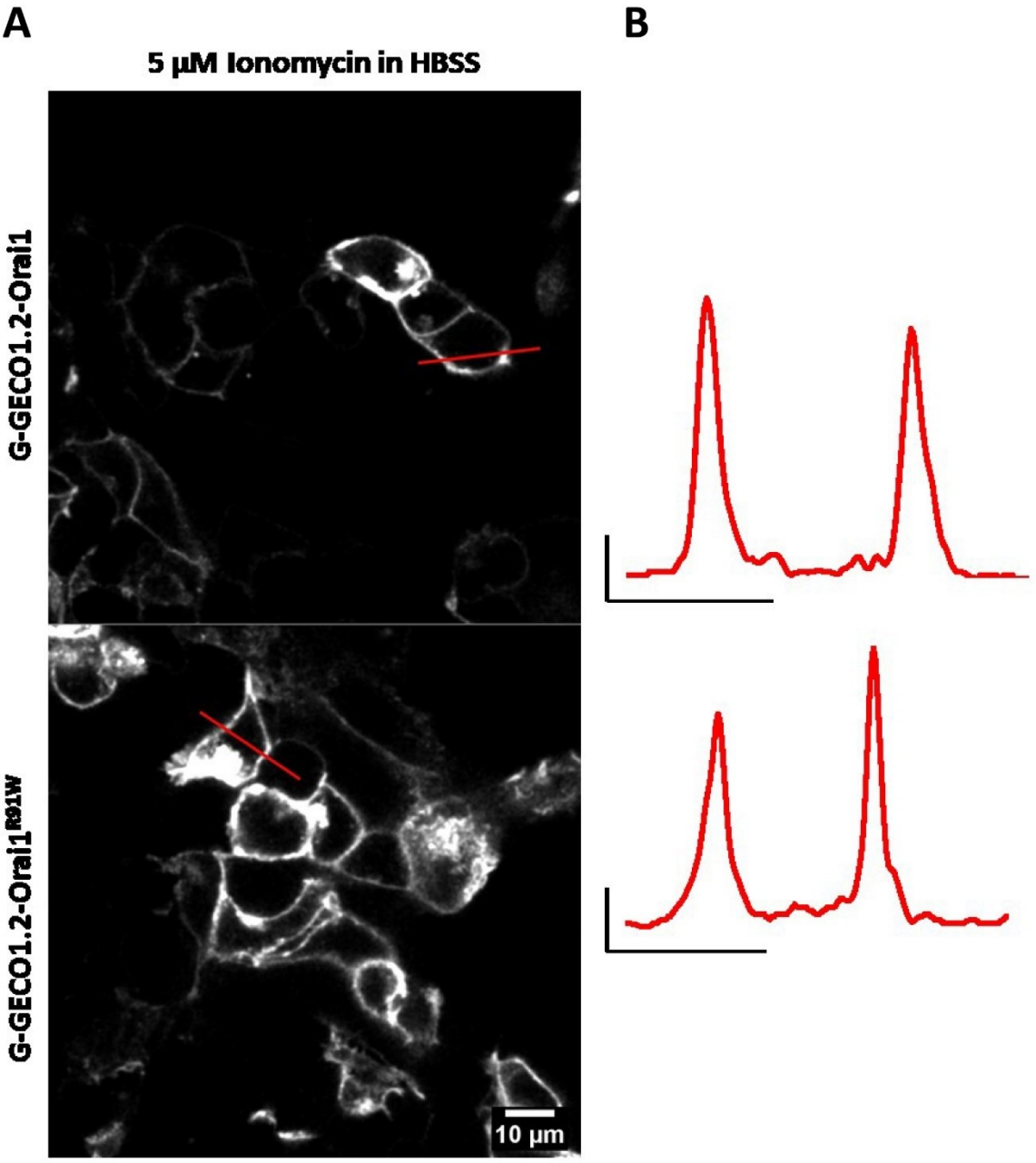


**Figure 4.38 Membrane targeting of G–GECO1.2–Orai1 and G-GECO1.2-Orai1$^{R91W}$.** A) Single confocal optical sections of HEK293 cells transfected with G–GECO1–Orai1 and G-GECO1.2-Orai1$^{R91W}$ 1 min after treatment with 5 µM ionomycin in HBSS. B) Plot profiles of the relative fluorescence intensity as a function of distance along the red line in A. Scale bar, 10 RFUs in y-direction a 10 µm in the x-direction.

### 4.3.7 G-GECO1.2-Orai1$^{R91W}$ blocked Orai1-mediated SOCE

Before testing the effect of G-GECO1.2-Orai1$^{R91W}$ on Orai1-mediated SOCE by TIRFM, we utilized an epifluorescent microscope which allowed us to have more cells per field of view (~ 30 cells), and to record at a faster rate (1 frame/s) while avoiding photobleaching. Recordings were made 24 hours after transfection of HEK293 cells with G-GECO1.2-Orai1 constructs by putting cells in $Ca^{2+}$-free HBSS with 0.1 mM EGTA for 1 min and applying 1 μM thapsigargin for an additional 5 min. Following this, 2 mM $Ca^{2+}$ was applied for 5 min to measure SOCE, and finally 5 μM ionomycin was added to provide the maximal response ($F_{max}$) (Figure 4.39).

Representative images for G-GECO1.2-Orai1 and GECO1.2-Orai1 $^{R91W}$ are shown in Figure 4.39. Following 5-min treatment with 1 μM thapsigargin, the addition of extracellular 2 mM $Ca^{2+}$ caused very little or no change in intensity of GECO1.2-Orai1 $^{R91W}$ whilst clearly increasing G-GECO1.2-Orai1 fluorescence. Only after addition of 5 μM ionomycin was there an increase in intensity for both constructs. This suggests that the R91W mutation blocks the Orai1-mediated SOCE response.

Figure 4.310B shows representative traces for G-GECO1.2-Orai1 and GECO1.2-Orai1 $^{R91W}$ and each grey trace corresponds to the change of intensity within a single ROI normalized to its $F_{max}$ value ($F/F_{max}$). Black and red traces show average ± SEM traces for G-GECO1.2-Orai1 and GECO1.2-Orai1 $^{R91W}$, respectively. Only the last two-minutes of thapsigargin treatment and five minutes post $Ca^{2+}$ addition are shown, to illustrate the difference in SOCE. The box-and-whiskers plot in Figure 4.310C compares the peak amplitude of the SOCE response for G-GECO1.2-Orai1 and GECO1.2-Orai1 $^{R91W}$. The data was analysed using the Mann–Whitney test and α of 0.05; SOCE measured with G-

GECO1.2-Orai1 (0.4343) was significantly higher in comparison to SOCE measured with GECO1.2-Orai1 $^{R91W}$ (0.03863; ****, P < 0.0001).

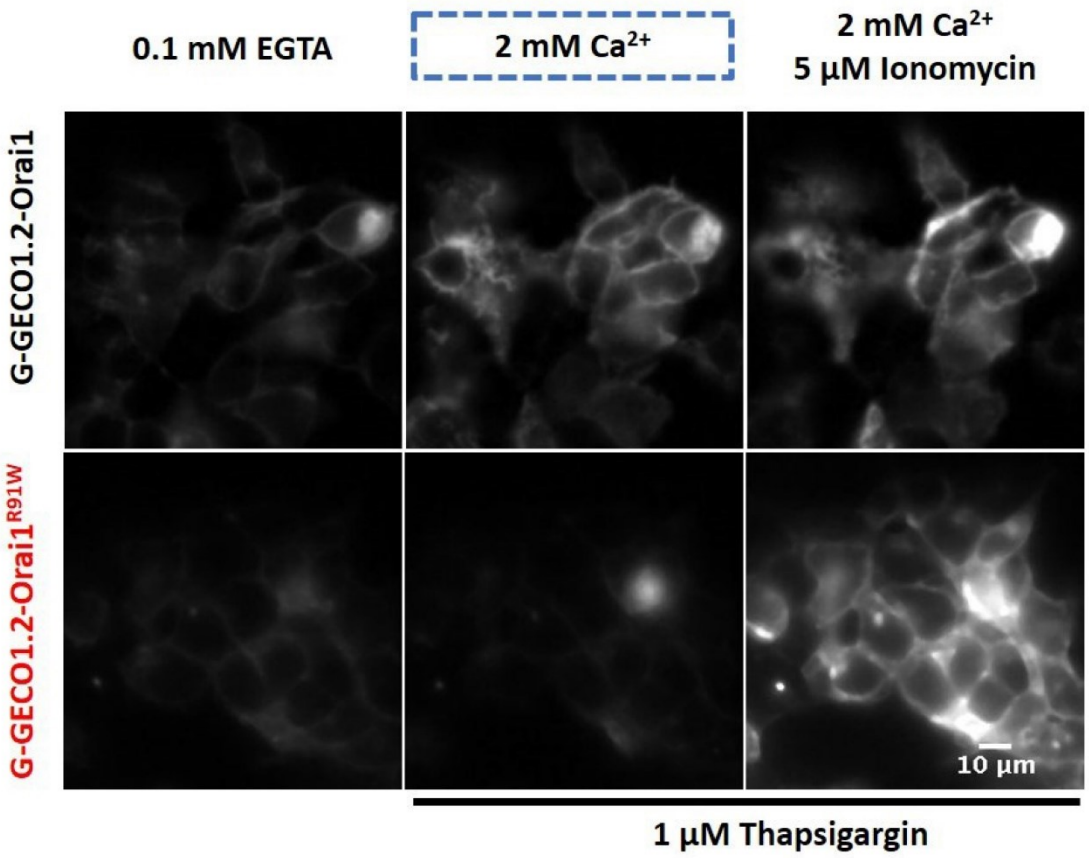


**Fig4.39 G-GECO1.2-Orai1$^{R91W}$ blocks SOCE in HEK293 cells.** Epifluorescent images of G-GECO1.2-Orai1 and G-GECO1.2-Orai1$^{R91W}$ in 0.1 mM EGTA (pre-treatment; column 1), 2mM $Ca^{2+}$ (post-treatment with 1 µM Thapsigargin; column 2) and 2mM $Ca^{2+}$ with 5 µM Ionomycin (column 3).

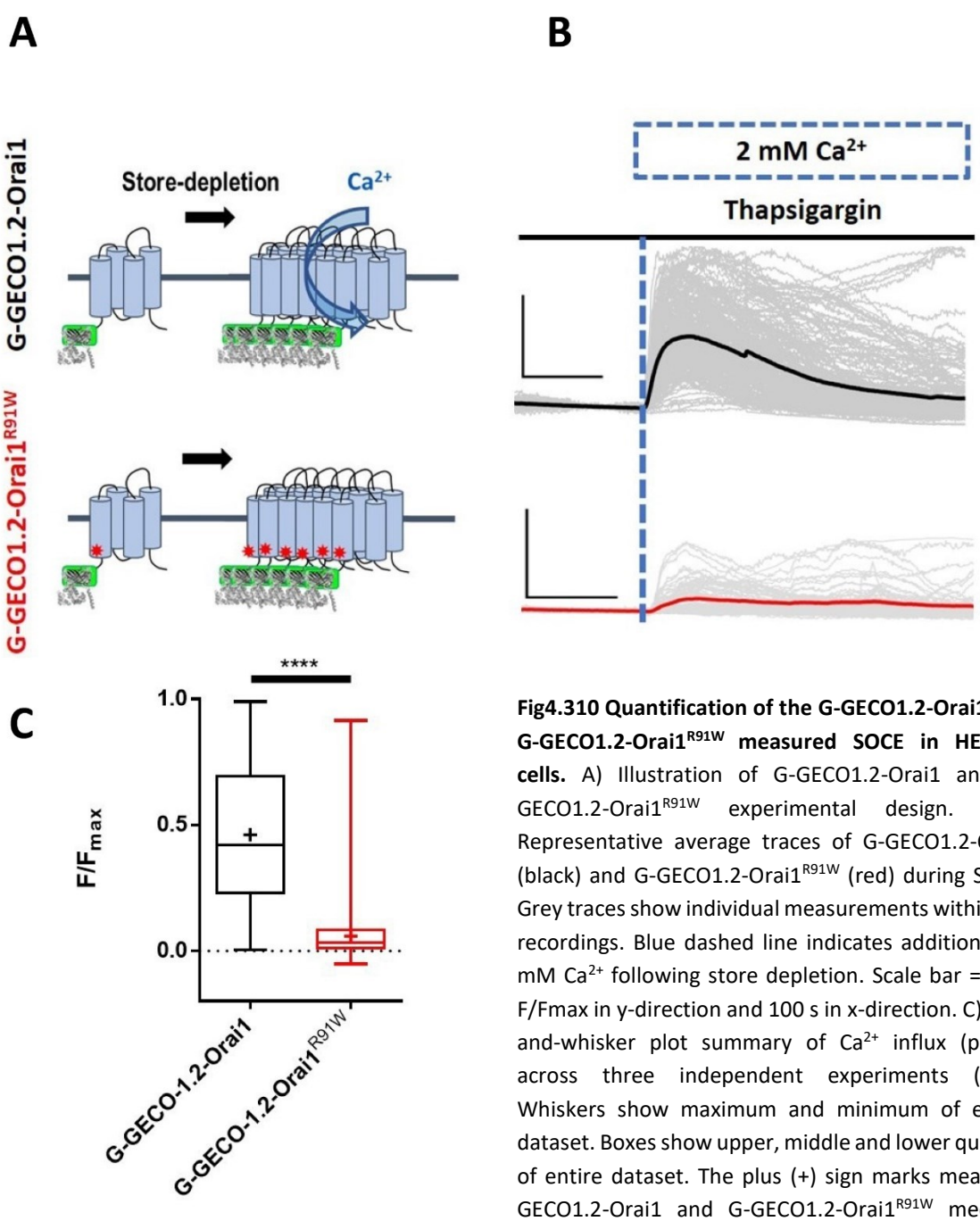


**Fig4.310 Quantification of the G-GECO1.2-Orai1 and G-GECO1.2-Orai1$^{R91W}$ measured SOCE in HEK293 cells.** A) Illustration of G-GECO1.2-Orai1 and G-GECO1.2-Orai1$^{R91W}$ experimental design. B) Representative average traces of G-GECO1.2-Orai1 (black) and G-GECO1.2-Orai1$^{R91W}$ (red) during SOCE. Grey traces show individual measurements within the recordings. Blue dashed line indicates addition of 2 mM $Ca^{2+}$ following store depletion. Scale bar = 50% F/Fmax in y-direction and 100 s in x-direction. C) Box-and-whisker plot summary of $Ca^{2+}$ influx (peaks) across three independent experiments (n=3). Whiskers show maximum and minimum of entire dataset. Boxes show upper, middle and lower quartile of entire dataset. The plus (+) sign marks mean. G-GECO1.2-Orai1 and G-GECO1.2-Orai1$^{R91W}$ medians (0.4343 and 0.03863, respectively) were compared with the Mann-Whitney test. ****,P<0.0001.

### 4.3.8 G-GECO1.2-Orai1$^{R91W}$ blocked Orai1-mediated SOCE at ER-PM junctions

To confirm G-GECO1.2-Orai1 also measures Orai1-mediated SOCE at ER-PM junction microdomains, TIRFM was used. Figure 4.311 shows representative images from cells expressing either G-GECO1.2-Orai1 or GECO1.2-Orai1 $^{R91W}$. Following 5-min treatment with 1 μM thapsigargin, the addition of extracellular 2 mM $Ca^{2+}$ caused very little or no change in the intensity of GECO1.2-Orai1$^{R91W}$ and only following the addition of 5 μM ionomycin did fluorescence increase. The intensity of each ROI normalized locally using ΔF/F (B) or F/$F_{max}$ (C) formula is shown in Figure 4.311 B and C.

Both normalization methods of TIRFM data obtained using the G-GECO1.2-Orai1 constructs yielded very similar results. Therefore, we proceeded with the quantification of G-GECO1.2-Orai1 and GECO1.2-Orai1 $^{R91W}$ traces obtained using TIRFM in the same manner as we did with G-GECO1.2-Orai1 and GECO1.2-Orai1 $^{R91W}$ traces obtained using epifluorescent microscopy; we normalized each trace with its local $F_{max}$ using F/$F_{max}$ formula. Figure 4.312 shows representative traces for G-GECO1.2-Orai1 and GECO1.2-Orai1 $^{R91W}$. Each grey trace corresponds to the change of intensity within a single ROI normalized to its $F_{max}$ value (F/$F_{max}$). Black and red traces show average traces ±SEM for G-GECO1.2-Orai1 and GECO1.2-Orai1 $^{R91W}$, respectively. Figure 4.312B summarizes the effects of the R91W mutation on the SOCE response and again, SOCE measured with G-GECO1.2-Orai1 was significantly higher compared to SOCE measured with GECO1.2-Orai1 $^{R91W}$ (****, $P < 0.0001$). This indicates that using G-GECO1.2-Orai1, the fluorescence signal recorded following the addition of $Ca^{2+}$, is dominated by $Ca^{2+}$ entry through the G-GECO1.2-Orai1 channel itself. There is minimal contamination of the response by $Ca^{2+}$ entry through a different route.

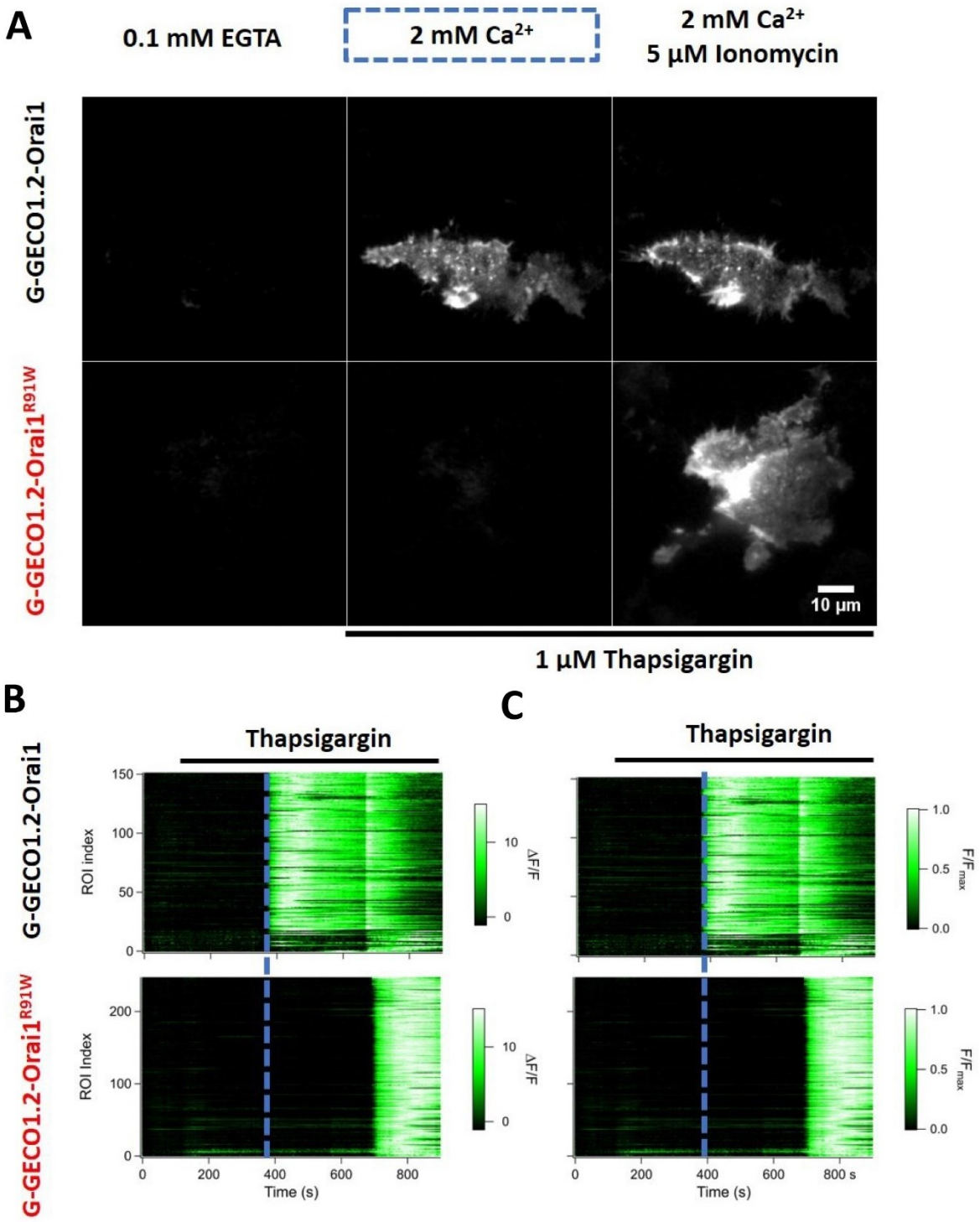


**Fig4.311 G-GECO1.2-Orai1$^{R91W}$ blocks SOCE in ER-PM microdomains of HEK293 cells.** A) TIRFM images of G-GECO1.2-Orai1 and G-GECO1.2-Orai1$^{R91W}$ in 0.1 mM EGTA (pre-treatment; column 1), 2mM $Ca^{2+}$ (post-treatment with 1 µM Thapsigargin; column 2) and 2mM $Ca^{2+}$ with 5 µM Ionomycin (column 3). B) Fluorescence data of G-GECO1.2-Orai1 and G-GECO1.2-Orai1$^{R91W}$ per ROI normalized using ΔF/F formula. C) Fluorescence data of G-GECO1.2-Orai1 and G-GECO1.2-Orai1$^{R91W}$ per ROI normalized using $F/F_{max}$ formula. Blue dashed line indicates addition of 2 mM $Ca^{2+}$ following store depletion.

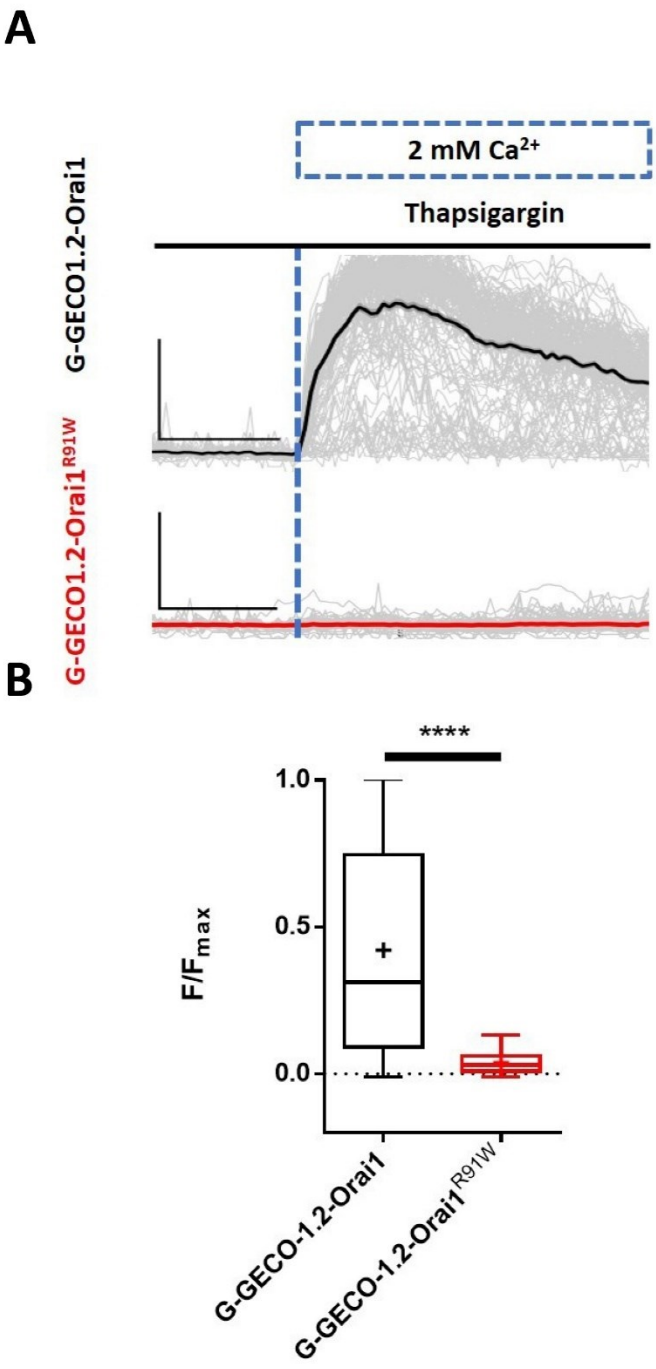


**Fig4.312 Quantification of SOCE (peak) for G-GECO1.2-Orai1 and G-GECO1.2-Orai1$^{R91W}$ in HEK293 cells.** A) Representative average traces of G-GECO1.2-Orai1 (black) and G-GECO1.2-Orai1$^{R91W}$ (red) during SOCE. Grey traces show individual measurements within the TIRFM recordings. Scale bar = 50% F/Fmax in y-direction and 100 s in x-direction. B) Box-and-whisker plot summarizing all peak values of $Ca^{2+}$ influx across three independent experiments (n=3) for G-GECO1.2-Orai1 (black) and G-GECO1.2-Orai1$^{R91W}$ (red) using TIRFM. Result shows difference between medians (0.2487, G-GECO1.2-Orai1; 0.03439, G-GECO1.2-Orai1$^{R91W}$ ) compared with the Mann-Whitney test. ****, $P < 0.0001$.

### 4.3.9 σ1R-V5 reduces Orai1-mediated SOCE in ER-PM microdomains

Utilizing this approach, the effects of σ1R expression on Orai1-mediated SOCE were tested. HEK293 cells were transduced 6h after plating using $WT^{VC}$ and σ1R-V5 baculovirus and the following day transfected with G-GECO1.2-Orai1. TIRFM recordings were made 24h later.

Figure 4.313 shows representative images and fluorescent data of G-GECO1.2-Orai1 after infection with either $WT^{VC}$ or σ1R-V5. Following 6-min treatment with 1 μM thapsigargin, the addition of extracellular 2 mM $Ca^{2+}$ caused an increase in the intensity of GECO1.2-Orai1 in both $WT^{VC}$ and σ1R-V5 HEK293 cells. The intensity as well as the kinetics of the SOCE response appeared to be different in cells expressing σ1R-V5**.**

Figure 4.314A shows representative traces with each grey trace corresponds to the change of intensity within a single ROI normalized to its $F_{max}$ value ($F/F_{max}$) and the average traces shown in black and red as before. The results are summarized in the box-and-whiskers plot in Figure 4.314B and SOCE measured in cells transduced with σ1R-V5 was significantly lower than in cells infected with the control virus ($P < 0.0001$), suggesting σ1R-V5 reduces Orai1-mediated SOCE in ER-PM microdomains**.**

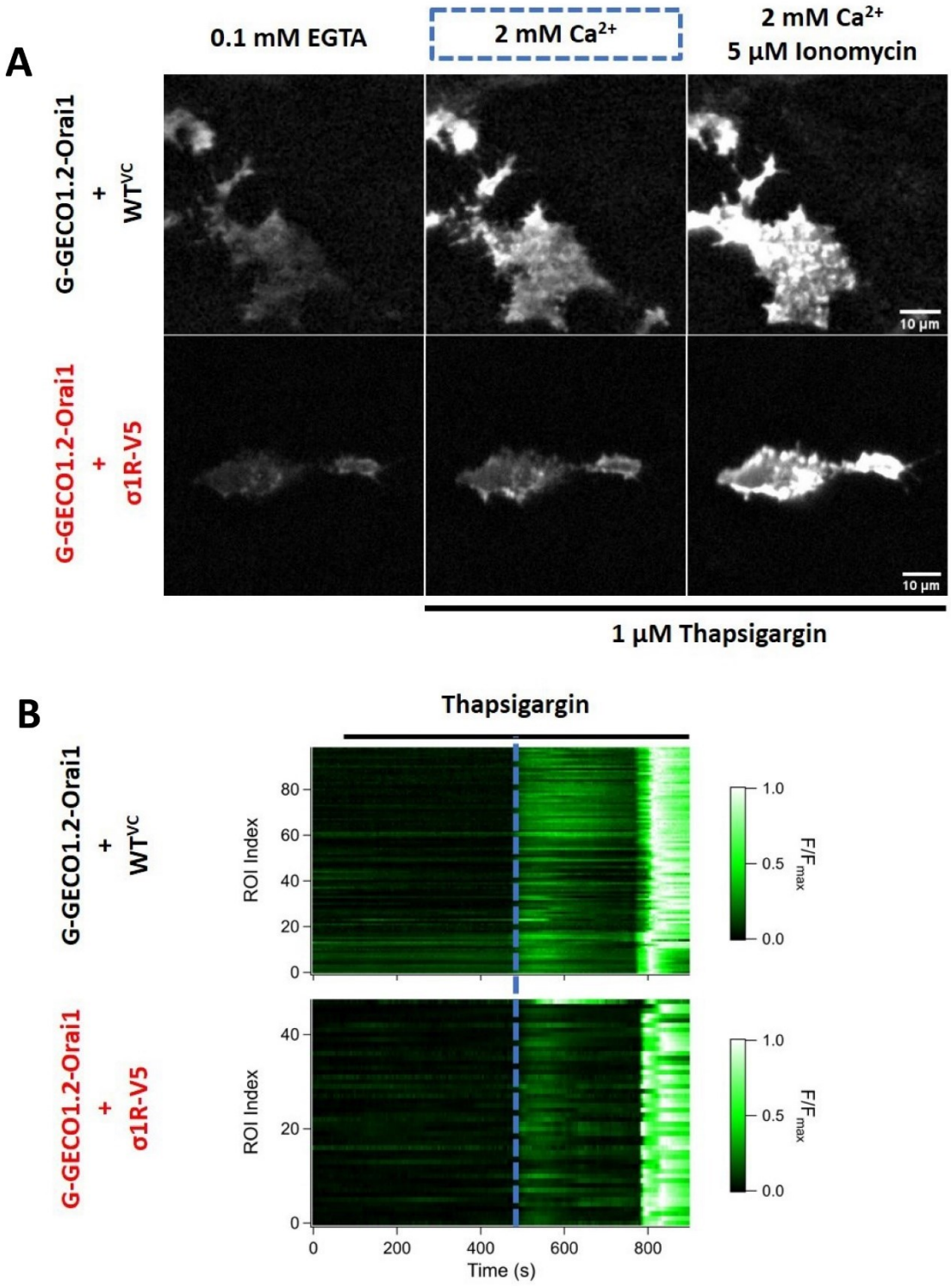


**Fig4.313 σ1R-V5 reduces G-GECO1.2-Orai1-mediated SOCE in HEK293 cells.** A) TIRFM images of G-GECO1.2-Orai1-measured SOCE in $WT^{VC}$ and σ1R-V5 HEK293 cells in 0.1 mM EGTA (pre-treatment; column 1), 2mM $Ca^{2+}$ (post-treatment with 1 µM Thapsigargin; column 2) and 2mM $Ca^{2+}$ with 5 µM Ionomycin (column 3). B) Representative fluorescence data of G-GECO1.2-Orai1 per ROI normalized using $F/F_{max}$ formula. Blue dashed line indicates addition of 2 mM $Ca^{2+}$ following store depletion.

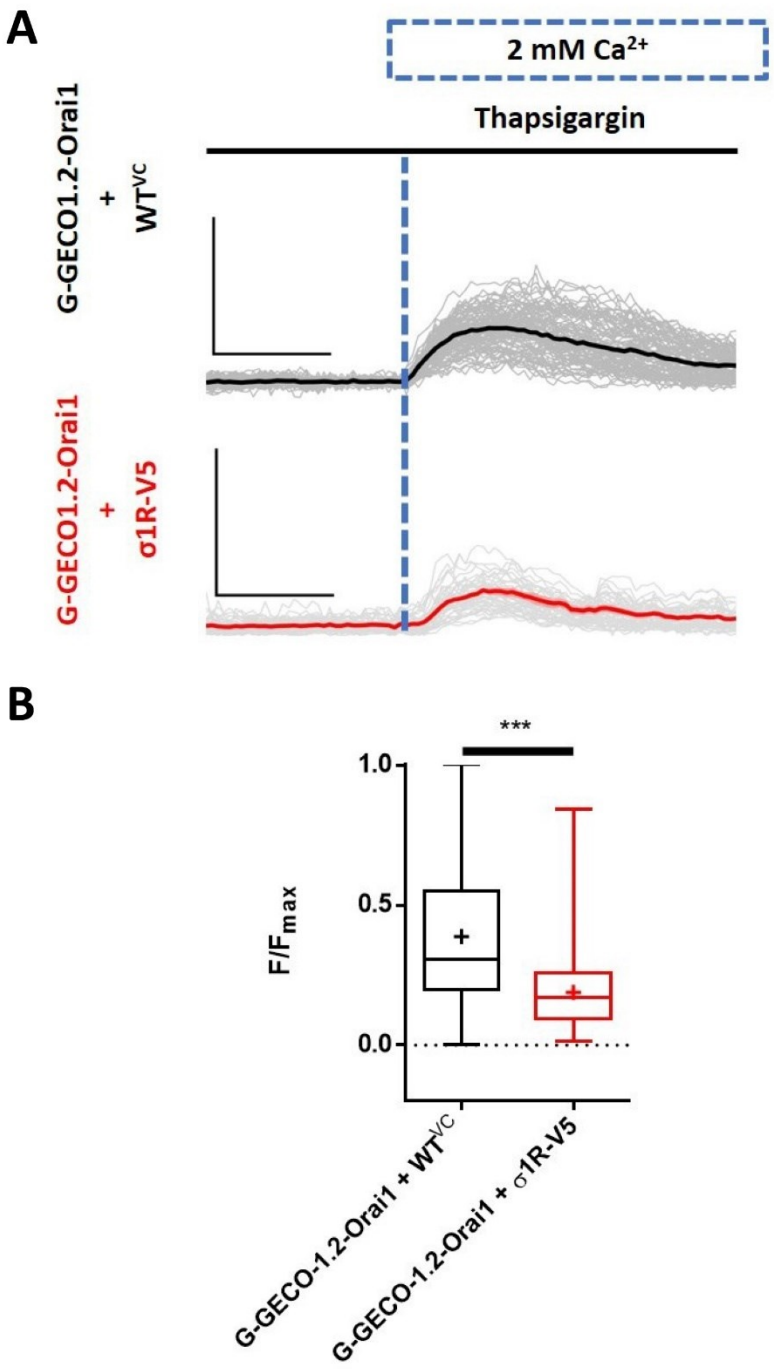


**Fig4.314 Quantification of G-GECO1.2-Orai1-mediated SOCE in $WT^{VC}$ and σ1R-V5 HEK293 cells.** A) Representative average traces of G-GECO1.2-Orai1-measured SOCE in $WT^{VC}$ (black) and σ1R-V5 (red) HEK293 cells. Grey traces show individual measurements within representative TIRFM recordings. Scale bar = 50% F/Fmax in y-direction and 100 s in x-direction. B) Box-and-whisker plot summarizing all peak values of $Ca^{2+}$ influx across three independent experiments (n=3) for $WT^{VC}$ (black) and σ1R-V5 (red) HEK293 cells using TIRFM. The result shows the difference between medians (0.2171, $WT^{VC}$; 0.1402, σ1R-V5) compared with the Mann-Whitney test. ***, $P < 0.001$.

### 4.3.10 Segmentation and ROI size does not affect the final result

In section 4.35 of this chapter, we reported how segmentation as a method of semi-automated determination of G-GECO1.2-Orai1 puncta yielded ROIs of different sizes. Following the result that σ1R reduced local Orai1-mediated SOCE, we wanted to test whether the method of segmentation and ROI size had an impact on the quantification of local SOCE in $WT^{VC}$ and σ1R-V5 HEK293 cells.

Figure 4.315A shows relative frequencies of G-GECO1.2-Orai1 ROI sizes (pixels) in $WT^{VC}$ (black) and σ1R-V5 (red) HEK293 cells. Relative frequencies of G-GECO1.2-Orai1 ROI sizes were obtained using three different SD values. As before, the threshold for ROI detection was calculated as a multiple of the standard deviation (SD) of all the pixel values in the Laplace operator; (1) 2xSD (SD2), (2) 3x SD (SD3), and (3) 4xSD (SD4). Under all three conditions of segmentation, ROI sizes were very similar and predominantly small in size.

Figure 4.315B and C show a comparison of G-GECO1.2-Orai1 traces from $WT^{VC}$ (B) and σ1R-V5 (C) HEK293 cells obtained using threshold of SD2 (column 1), SD3 (column 2) and SD4 (column 3). The SD criteria for segmentation did not affect the final shape of G-GECO1.2-Orai1 traces. Also, the quantification of SOCE as the ratio between local SOCE intensity and local $F_{max}$ intensity resulted in a 3% difference between SD2 and SD4 traces for G-GECO1.2-Orai1 in both $WT^{VC}$ and σ1R-V5 HEK293 cells. Figure 4.315D shows the average±SD ROI sizes in $WT^{VC}$ and σ1R-V5 HEK293 cells while using different threshold levels during segmentation.

Considering that for analysis we used SD values between 2.5 and 3 SDs and that previously reported the difference in SOCE between $WT^{VC}$ and σ1R-V5 HEK293 cells was

~8%, the results summarized in Figure 4.315 suggest that the segmentation method and ROI size did not affect the final result in section 4.39.

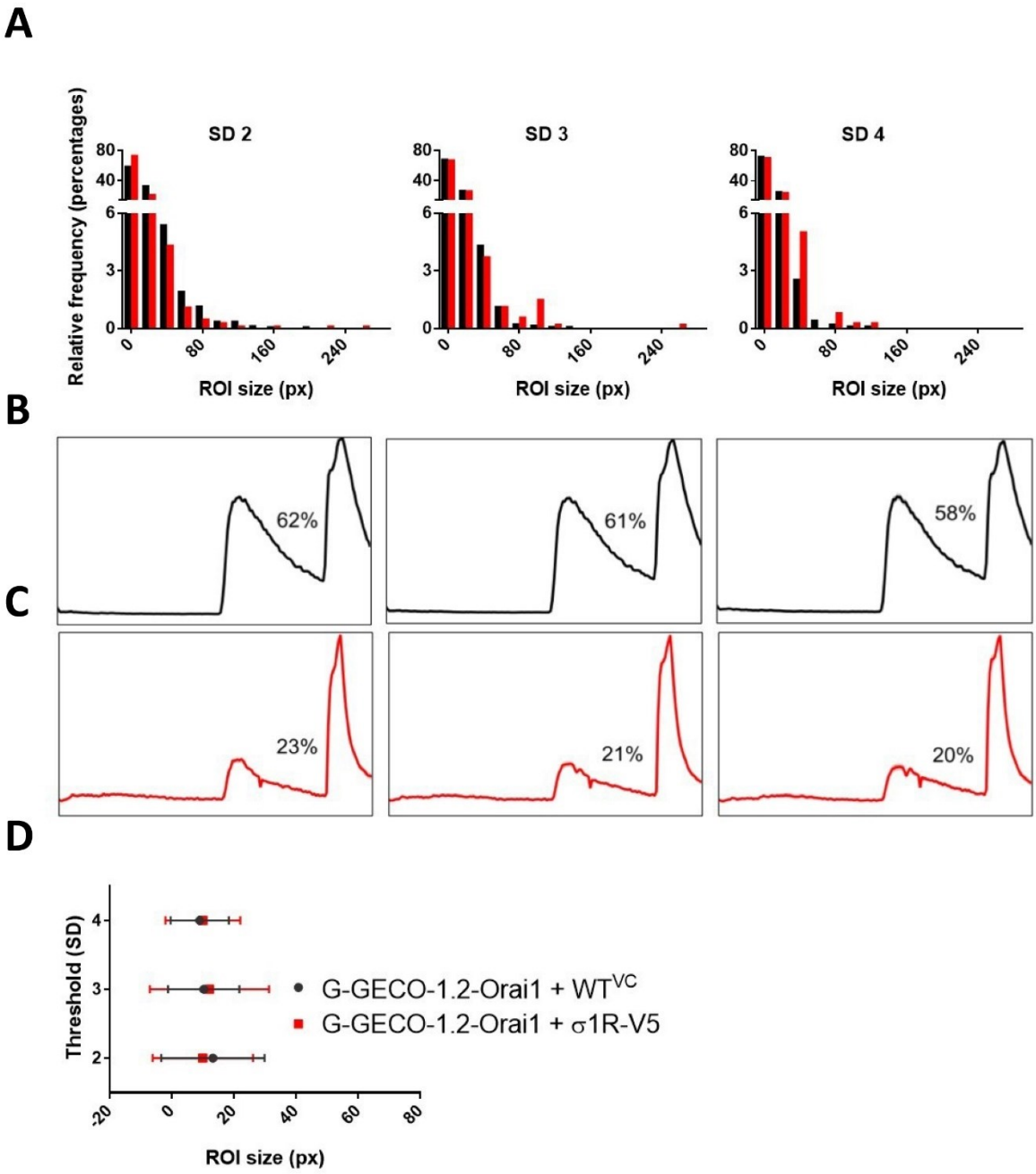


**Fig4.315 Segmentation and ROI size do not affect SOCE quantification.** A) Relative frequency histograms of G-GECO1.2-Orai1 ROI size (pixels) in $WT^{VC}$ (black) and σ1R-V5 (red) HEK293 cells using a threshold of SD2, SD3 and SD4. B) Average G-GECO1.2-Orai1 traces in $WT^{VC}$ HEK293 cells after utilizing different threshold levels. SOCE is expressed as a percentage of $F_{max}$. C) Average G-GECO1.2-Orai1 traces in σ1R-V5 HEK293 cells after utilizing different threshold levels. SOCE is expressed as a percentage of $F_{max}$. D) Average ROI size± SD across three independent experiments (n=3) for $WT^{VC}$ (black) and σ1R-V5 (red) HEK293 cells using TIRFM.

### 4.3.11 σ1R-V5 reduces the frequency of highly-potentiated SOCE and affects its activation and deactivation kinetics

The segmentation method groups neighbouring pixels into ROI based on the provided criteria, such as multiplicity of SD. A grouping as such can potentially hide outliers among the neighbouring pixels whilst providing their average. To understand how segmentation affects measured SOCE, we decided to extract individual pixels from ROIs and measure SOCE within each pixel normalized with its local $F_{max}$ value. The size of the pixel in TIRFM recordings was ~240nm which was closer to the previously reported size of Orai1 cluster (100 – 200nm)[117] than the smallest ROI size (3px = 720nm).

Figure 4.316 compares results for G-GECO1.2-Orai1-measured SOCE in $WT^{VC}$ and σ1R-V5 HEK293 cells obtained using ROIs (column 1) and individual pixels (column 2). Quantification of SOCE at pixel-level also revealed that overexpression of σ1R-V5 significantly reduced this process (0.3528 in $WT^{VC}$HEK293 cells; 0.2289 in σ1R-V5 HEK293; **, $p < 0.009$ ), suggesting that the segmentation method and ROI size did not affect SOCE quantification. However, with this approach, there was an increase in the SOCE range in σ1R-V5 HEK293 cells, suggesting the existence of highly-active Orai1 clusters ( SOCE > 0.5 $F_{max}$ ) which were undetected using ROIs, possibility because of the surrounding, less-active Orai1 clusters. Also, we noticed that most of the SOCE in σ1R-V5 HEK293 cells occurred within a very narrow range between 0.1536 of $F_{max}$ (25% percentile) and 0.2813 of $F_{max}$ (75% percentile). For comparison, most of the SOCE in $WT^{VC}$HEK293 cells occurred within a range between 0.1924 of $F_{max}$ (25% percentile) and 0.5310 of $F_{max}$ (75% percentile). A further comparison of relative frequencies for local SOCE in $WT^{VC}$ and σ1R-V5 HEK293 cells (Figure 4.316B) showed that, while the most frequent activity of local SOCE in both $WT^{VC}$ and σ1R-V5 HEK293 cells was ~0.20 of $F_{max,}$ highly-active Orai1 clusters were more

frequent in $WT^{VC}$HEK293 cells. This result suggested that overexpression of σ1R allowed for tighter regulation of Orai1-mediated SOCE.

Additionally, we compared the kinetics of Orai1-mediated SOCE in $WT^{VC}$ and σ1R-V5 HEK293 cells using dataset normalized at pixel-level. Highly-active Orai1 clusters ( SOCE > 0.5 $F_{max}$ ) were used for the comparison as they provided the more robust fluorescent signal. Figure 4.317A shows fluorescent data containing 50 $F_{max}$-normalised pixels obtained from $WT^{VC}$ and σ1R-V5 HEK293 cells. Figure 4.317B shows five individual traces extracted from the fluorescent data with a similar SOCE (peak) response. Highly-active Orai1 clusters from σ1R-V5 HEK293 cells exhibited slower activation, and steeper deactivation kinetics.

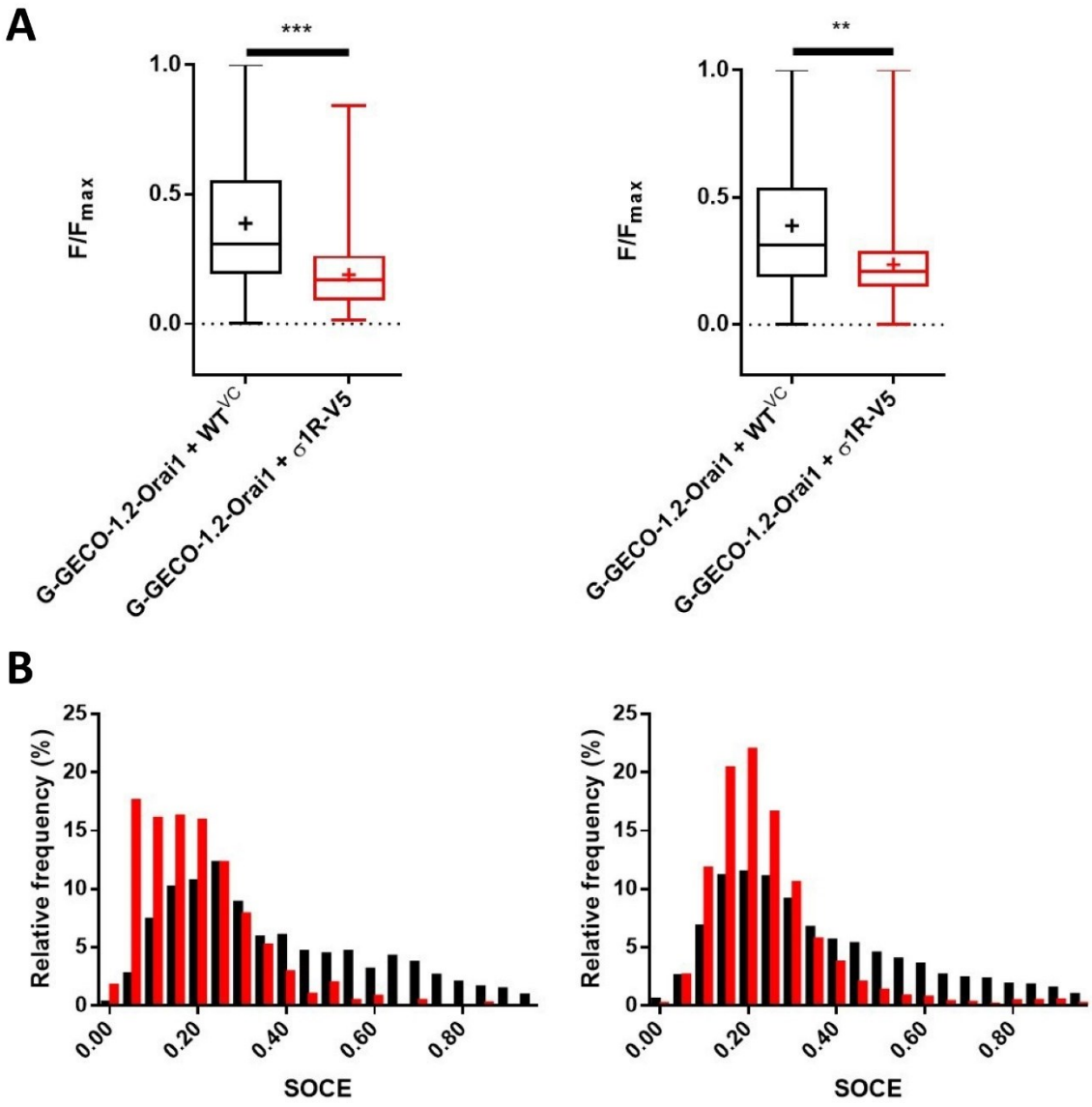


**Fig4.316 Comparison of G-GECO1.2-Orai1-measured SOCE in $WT^{VC}$ and σ1R-V5 HEK293 cells using ROIs and individual pixels.** A) Box-and-whisker plots summarizing SOCE values across three independent experiments (n=3) for $WT^{VC}$ (black) and σ1R-V5 (red) HEK293 cells using TIRFM. A plot in column 1 summarizes SOCE calculated using ROIs. A plot in column 2 summarizes SOCE calculated using individual pixels. B) Relative frequency of local SOCE across three independent experiments (n=3) for $WT^{VC}$ (black) and σ1R-V5 (red) HEK293 cells using TIRFM. A histogram in column 1 summarizes SOCE calculated using ROIs. A histogram in column 2 summarizes SOCE calculated using individual pixels.

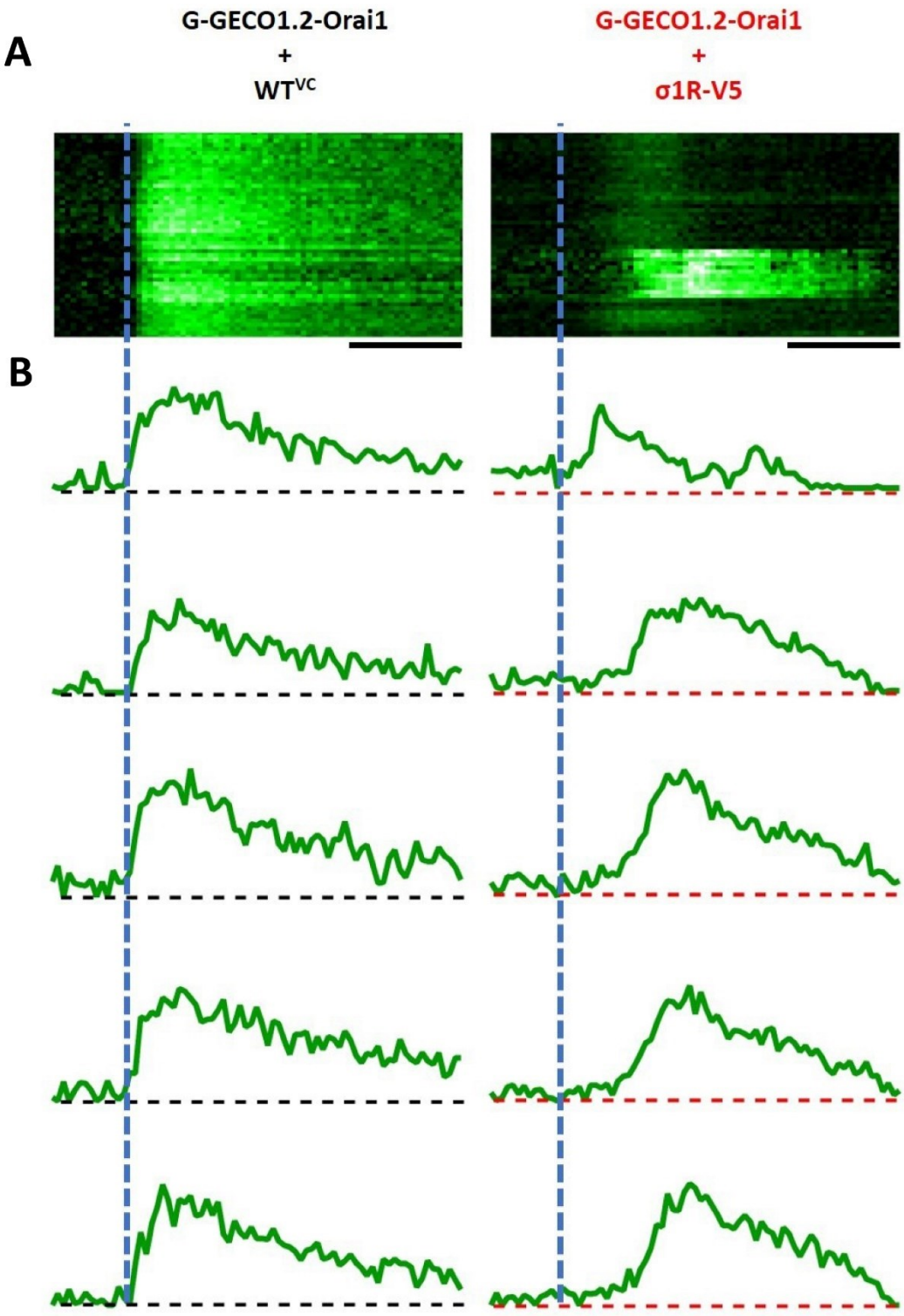


**Fig4.317 Comparison of highly-active Orai1 clusters in $WT^{VC}$ and σ1R-V5 HEK293 cells.** A) Fluorescence data of 50 pixels from G-GECO1.2-Orai1 representative recordings in $WT^{VC}$ (black) and σ1R-V5 (red) HEK293 cells using TIRFM. Scale bar = 100 s. B) Individual traces showing pixel-normalized SOCE in $WT^{VC}$ and σ1R-V5 HEK293 cells. Vertical dashed line = addition of 2mM $Ca^{2+}$. Horizontal dashed line = baseline.

## 4.4 Discussion

### 4.4.1 σ1R reduces frequency of highly active G-GECO1.2-Orai1 clusters

As in Chapter III, enhanced expression of σ1R-V5 in HEK293 cells reduced cumulative SOCE. Co-expression of G-GECO1.2-Orai1 with ER- and PM-markers (Section 4.31-4.32) confirmed that these SOCE measurements occurred at ER-PM junctions where TIRFM allowed for optical sectioning of fluorescent molecules within the immediate vicinity of the PM. Introducing dominant-negative mutant G-GECO1.2-Orai1$^{R91W}$ into the experimental design facilitated characterisation of measured $Ca^{2+}$ influx as SOCE. SOCE measured by G-GECO1.2-Orai1 was significantly higher compared to SOCE measured with GECO1.2-Orai1 $^{R91W}$ (****, $P < 0.0001$) (Section 4.37-4.38), indicating that G-GECO1.2-Orai1 truly measured $Ca^{2+}$ entry occurring through the SOCE/CRAC channel and that there was a minimal contamination by $Ca^{2+}$ entry through a different route. This also implies that enhanced expression of σ1R results in the inhibition of SOCE, as observed in Section 4.39, right at the point of $Ca^{2+}$ entry

Several advantages of utilizing G-GECO1.2-Orai1 construct over electrophysiological techniques include reduced invasiveness and improved spatial information with regards to the location of the SOCE response. Surprisingly, overexpression of σ1R-V5 had more modest local effect within SOCE microdomain than initially predicted. This prediction had several previously established premises. Overexpression of Orai1 can result in changes of Orai1/STIM stoichiometry which determines the effectiveness of Orai1 channel activation[126]. Also, Srivats et al. proposed that by translocating with STIM1 to ER-PM junctions, σ1R reduced effectiveness of STIM1-binding to Orai1[34].Thus, I initially predicted that due to overexpression of G-GECO1.2-Orai1, σ1R would exert greater inhibitory effect within SOCE microdomains than observed during the measurements of

global $Ca^{2+}$ influx. However, the comparison of SOCE frequencies (Fig. 4316) revealed that enhanced expression of σ1R simply resulted in a tighter control of $Ca^{2+}$influx when compared to $WT^{VC}$ HEK293 cells. This result calls for further investigation as current model of SOCE modulation by σ1R - where σ1R simply reduces effectiveness of STIM1 binding to Orai1- does not entirely explain this result. Reduced frequency of highly active G-GECO1.2-Orai1 clusters, while maintaining clusters of lower activity would suggest that σ1R exerts its inhibitory effect by lowering the effectiveness of Orai1 activation, but not necessary the effectiveness of STIM1 binding to Orai1. This could be better explained by reduced number of STIM oligomers within STIM1/Orai1 complex, as observed by Srivats et al[34]. This study also proposed that σ1R requires STIM1 to translocate to ER-PM junction. Thus, to modulate SOCE, σ1R requires transport with its STIM1 "carrier" to the location of Orai1 activation, possibly reducing interaction of STIM oligomers in a process and number of STIM oligomers within SOCE microdomain complex.

Further insights in the mechanism of SOCE modulation by σ1R could perhaps be withdrawn from the studies of its ability to modulate NMDARs. σ1R modulate synaptic plasticity, by enhancing NMDARs' function[202]. At the first sight, this contradicts with the neuroprotective role of σ1R as excessive $Ca^{2+}$ influx via activated NMDAR can cause excitotoxicity. However, while enhancing NMDARs' function allowing $Ca^{2+}$ influx, σ1R also inhibits interaction of GluN2B, NMDAR subunit, with other interactive partners preventing excitotoxicity. Hence, during modulation of NMDARs, σ1R exerts dual role. It is also possible that during Orai1 activation, σ1R modulates SOCE complex in several ways promoting its partial activation but simultaneously preventing large $Ca^{2+}$ influx. Comparison of highly active Orai1 clusters between $WT^{VC}$ and σ1R-V5 HEK293 (Fig.4.317) revealed slower activation but also steeper deactivation kinetics in the presence of σ1R. This suggest more complex role of σ1R within the SOCE complex and requires further investigation.

# 5 Chapter V

## Investigating the functional role of σ1R$^{E102Q}$ in the regulation of SOCE

## 5.1 Introduction

Amyotrophic lateral sclerosis (ALS) emerges as the selective degeneration of motor neurons in the brain and spinal cord, resulting in the muscle weakness. σ1R is neuroprotective ER chaperone. E102Q mutation of σ1R has been identified as a cause of the juvenile-onset form of ALS[36]. Also, intracellular aggregates of $\sigma1R^{E102Q}$ have been reported as part of ALS pathology in lymphoblastoid cells of fALS patient, inducing mitochondrial toxicity and disrupting $Ca^{2+}$ exchange at the MAM[159,203].

In 2017, Dreser et al. reported that activation of SOCE by ionomycin treatment significantly increased intracellular $Ca^{2+}$ in breast cancer cell line MCF-7 expressing σ1R, but not in MCF-7 cells expressing $\sigma1R^{E102Q}$ [159]. Considering expression of $\sigma1R^{E102Q}$ also disrupted $Ca^{2+}$ exchange at the MAM, this study characterised $\sigma1R^{E102Q}$ as loss-of-function mutant. However, reported effect of $\sigma1R^{E102Q}$ supports one[14], but conflicts with other two studies on the regulation of SOCE by σ1R[34,158] . The conclusions of latter studies are experimentally supported in Chapter III and Chapter IV of this thesis.

### 5.1.1 Aims

(1) To determine whether the enhanced expression of ALS-inducing mutant $\sigma1R^{E102Q}$ affects SOCE.

## 5.2 Results

### 5.2.1 The σ1R-V5$^{E102Q}$ mutant is detected as a dimer using Western blot analysis

To create cDNA for the σ1R-V5$^{E102Q}$ mutant, the single-point mutation was introduced into cDNA for σ1R-V5. Additionally, cDNA for "untagged" σ1R was created introducing stop codon into σ1R-V5 cDNA before the sequence for V5-epitope. A newly-created σ1R plasmid was used to create σ1R$^{E102Q}$. All new cDNAs were verified by sequencing. The expression of σ1R, σ1R$^{E102Q}$, σ1R-V5, and σ1R-V5$^{E102Q}$ in HEK293 cells was analysed by Western blotting.

Fig5.21A shows protein levels of σ1R in lysates of HEK293 cells 24h and 48h after transfection with mock (WT), σ1R, σ1R$^{E102Q}$ and si-σ1R RNA. Overexpression of plasmid coding for σ1R resulted in increased levels of σ1R detected at ~ 25kDa – which is predicted protein size of σ1R monomer. Overexpression of σ1R$^{E102Q}$ resulted in no detectable upregulation of σ1R at ~ 25kDa.

Fig5.21B shows protein levels of σ1R-V5 in lysates of HEK293 cells 24h and 48h after transfection with mock (WT), σ1R-V5, and σ1R-V5$^{E102Q}$. Overexpression of plasmid coding for σ1R-V5 resulted in increased levels of σ1R slightly above 25kDa. Overexpression of σ1R-V5$^{E102Q}$ resulted in lesser protein levels of σ1R at the same molecular weight. The detected expression of σ1R-V5$^{E102Q}$ using 20μg of lysate was lower than the expression of σ1R-V5 using 10μg of lysates collected at 24h and 48h post-transfection.

Further Western blot analysis of σ1R-V5$^{E102Q}$ expression in HEK293 cells resulted in detection of σ1R expression at higher molecular weight, slightly above 50kDa (Fig5.22). The expression of σ1R-V5 was also detected at a similar molecular weight (Fig5.22B) but in

a lesser amount (Fig5.22). Additionally, the expression of σ1R was detected slightly below 50kDa (Fig5.22B). Considering cDNAs of σ1R, σ1R-V5, and σ1R-V5$^{E102Q}$ are delivered into the cell using the same type of vector (pcDNA3.1/V5-His-TOPO), and that the size of detected band changes with expression of V5-tagged and untagged protein, this result suggests increased clustering of σ1R-V5$^{E102Q}$ mutant. This result is also in agreement with the initial report about E102Q mutation where σ1R$^{E102Q}$ was detected as a complex at ~ 50kDa (instead of ~25kDa) even in the buffers containing 150mM DTT and 2% Triton-X[36].

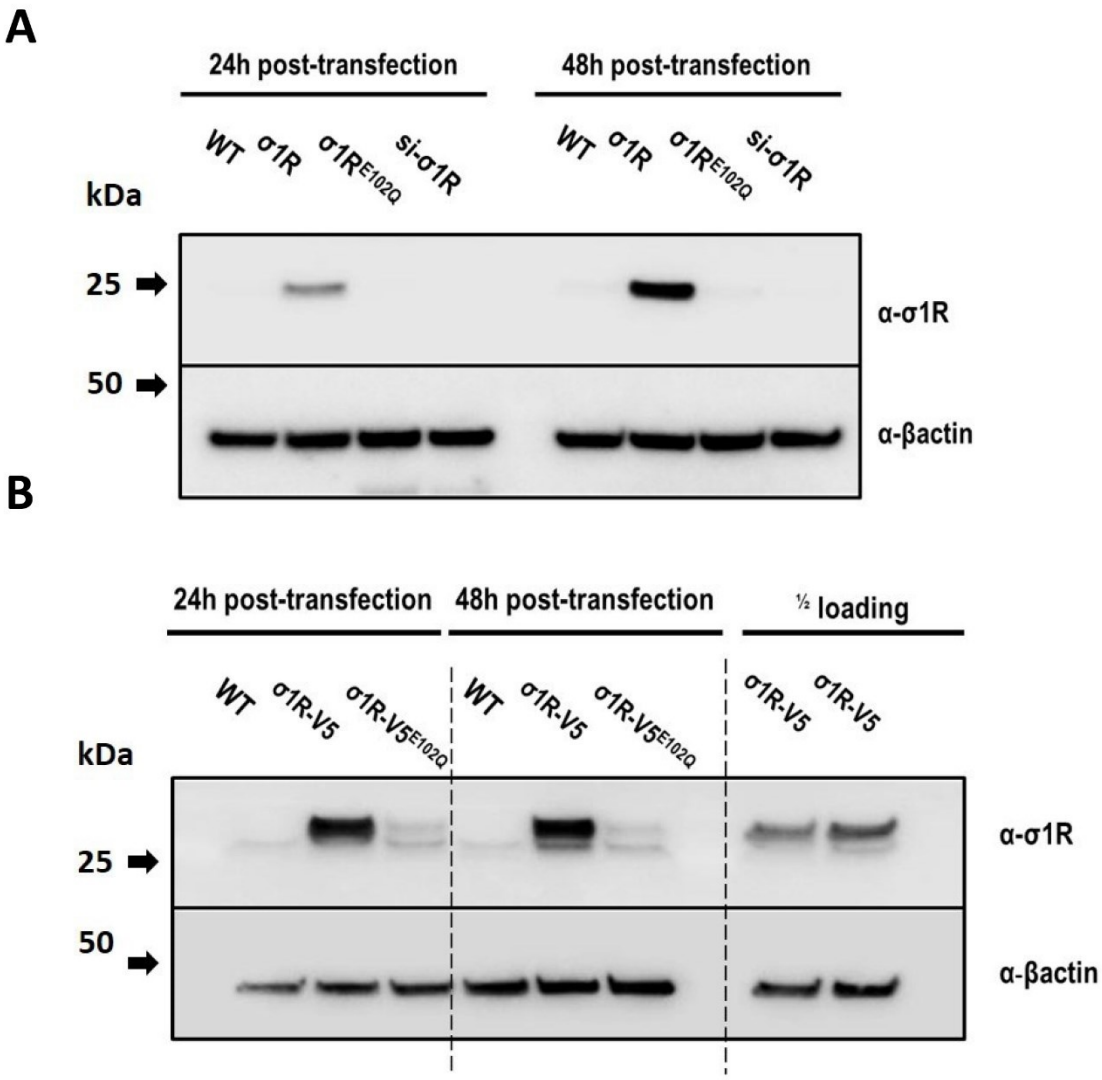


**Fig5.21 Western blot analysis of σ1R, σ1R$^{E102Q}$ and σ1R-V5$^{E102Q}$ expression in HEK293 cells. A)** Nitrocellulose membranes blotted with α-σ1R, and α-βactin showing protein levels of σ1R in WT HEK293 cells and HEK293 expressing σ1R, σ1R$^{E102Q}$, and σ1R siRNA 24 and 48h post-transfection. **B)** Nitrocellulose membranes blotted with α-σ1R, and α-βactin showing protein levels of σ1R in WT HEK293 cells and HEK293 expressing σ1R-V5 and σ1R–V5$^{E102Q}$ in HEK293 cells 24 and 48h post-transfection.

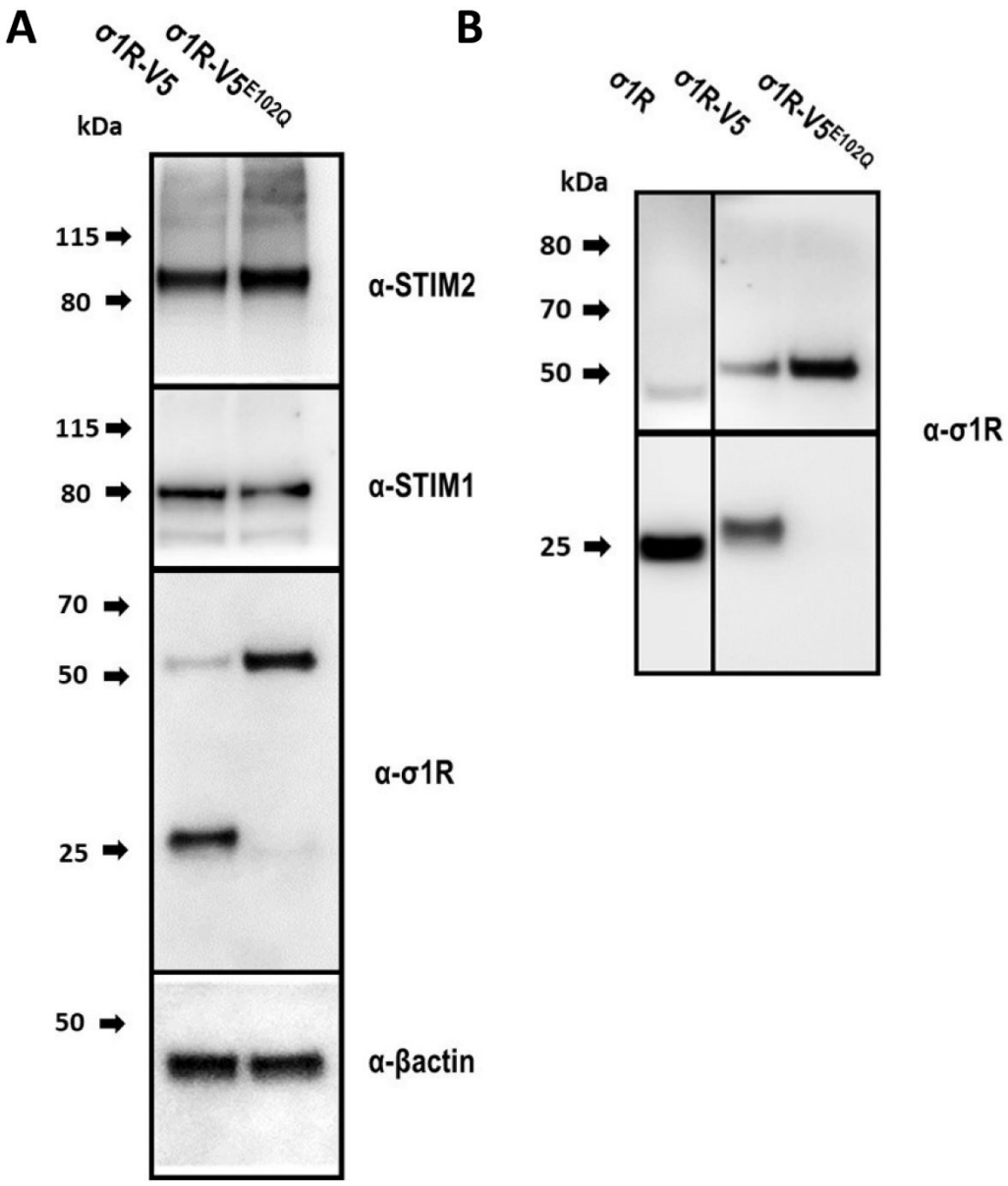


**Fig5.22 Western blot analysis of σ1R-V5$^{E102Q}$ expression in HEK293 cells. A)** Nitrocellulose membranes blotted with α-σ1R showing protein levels of σ1R-V5 and σ1R-V5$^{E102Q}$ in HEK293 cells 48h post-transfection. Additionally, membranes were blotted with α-STIM2, α-STIM1 and α-βactin to target endogenous levels of STIM2, STIM1 and βacting, respectively. **B)** Nitrocellulose membranes blotted with α-σ1R showing protein levels of overexpressed σ1R, σ1R-V5 and overexpressed σ1R–V5$^{E102Q}$ in HEK293 cells 48h post-transfection.

### 5.2.2 Overexpression of σ1R-V5$^{E102Q}$ fails to inhibit SOCE in HEK293 cells

To investigate the functional role of σ1R$^{E102Q}$ in the regulation of SOCE, the σ1R-V5$^{E102Q}$ was overexpressed in HEK293 cells and changes in $[Ca^{2+}]_{cyt}$ were measured using GCaMP6f and Flexstation III microplate reader 48h post-transfection.

Fig5.23 shows GCaMP6f traces of HEK293 cells expressing GCaMP6f-only (WT; black), σ1R (red), σ1R-V5 (green) and σ1R-V5$^{E102Q}$ (purple). Cells were treated with 1μM of thapsigargin in nominal $Ca^{2+}$-free NES followed by the restoration of 2 mM extracellular $Ca^{2+}$. SOCE peaks of HEK293 cells were compared with one-way ANOVA using α of 0.05. The overexpression of σ1R and σ1R-V5 resulted in a significant decrease of SOCE (Fig5.23B, ****, $P < 0.0001$). The overexpression of σ1R-V5$^{E102Q}$ resulted in SOCE which was not significantly different in comparison to WT cells (Fig5.23B, n.s., $P>0.05$), but significantly increased in comparison to HEK293 cells expressing σ1R-V5 (Fig5.23B, ****, $P < 0.0001$). Results of statistical analysis have been summarized in Table 5.21.

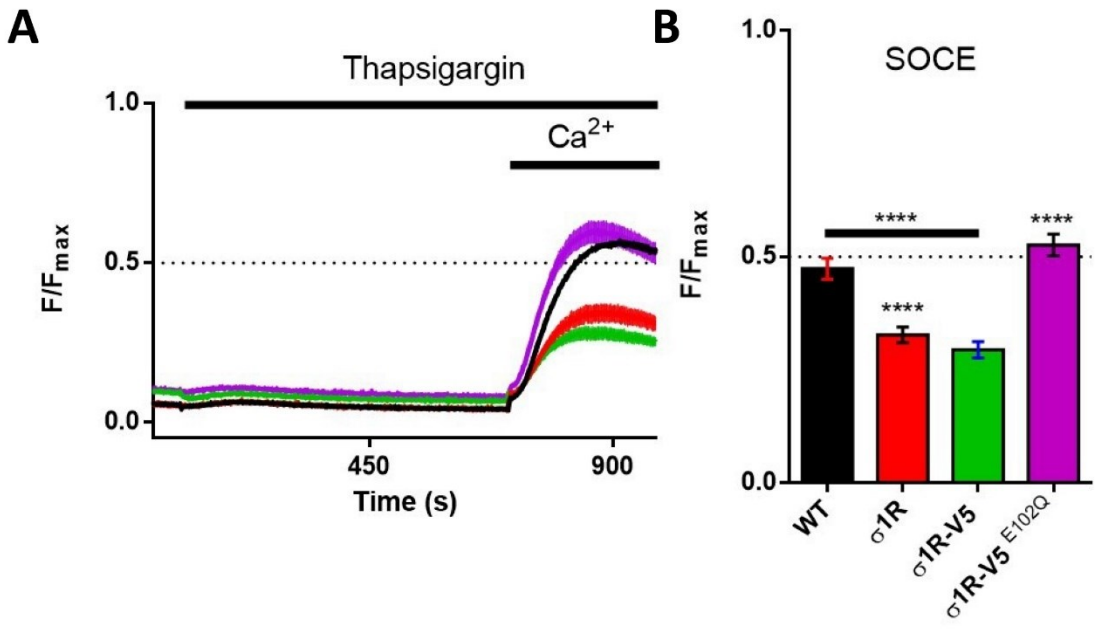


**Fig5.23 Overexpression of σ1R-V5$^{E102Q}$ fails to inhibit SOCE in a σ1R- and σ1R-V5- manner A)** Representative GCaMP6f average±SEM traces of HEK293 cells expressing GCaMP6f-only (WT; black), σ1R (red), σ1R-V5 (green) and σ1R-V5$^{E102Q}$ treated with 1µM thapsigargin in nominal $Ca^{2+}$-free NES followed by the restoration of 2 mM extracellular $Ca^{2+}$ **B)** Results summary of SOCE (peak) values across n=3. One-way ANOVA.****, P < 0.0001.

.

| Group | SOCE Mean± SEM | N | ANOVA SOCE σ1R | ANOVA SOCE σ1R-V5 | ANOVA SOCE σ1R-V5$^{E102Q}$ |
|---|---|---|---|---|---|
| WT | 0.4736 ±0.02305 | 18 | ****, P < 0.0001 | ****, P < 0.0001 | n.s, P > 0.05 |
| σ1R | 0.3275 ±0.01733 | 18 | | n.s, P > 0.05 | ****, P < 0.0001 |
| σ1R-V5 | 0.2948 ±0.01774 | 18 | | | ****, P < 0.0001 |
| σ1R-V5$^{E102Q}$ | 0.5263± 0.02414 | 18 | | | |

**Table 5.2-1 Summary of one-way ANOVA tests for GCaMP6f-measured SOCE during overexpression of different σ1R constructs.** SOCE measurements (Peaks, Fig 5.23) were taken across three independent experiments (n=3). A population of HEK293 cells within one well of 96W plate was used as a biological replicate (N) for statistical analysis.

### 5.2.3 The comparison of σ1R-mKate and σ1R-mKate$^{E102Q}$ expression in HeLa cells

In addition to previously introduced σ1R and σ1R$^{E102Q}$ constructs, I also created E102Q σ1R-mutant using σ1R-mKate construct which had been utilized in TIRFM studies by Srivats et al[34]. Srivats et al. demonstrated that σ1R-mKate co-localizes with Orai1-EGFP following $Ca^{2+}$ store-depletion of HeLa cells expressing HA-STIM1. Before the investigation of σ1R$^{E102Q}$ functional role in SOCE microdomains utilizing novel σ1R-mKate$^{E102Q}$ construct, its subcellular and cellular expression was compared to σ1R-mKate using confocal microscopy.

Fig5.24 shows the subcellular distribution of σ1R-mKate in HeLa cells 48h after transfection. Fig5.25 shows the subcellular distribution of σ1R-mKate$^{E102Q}$ in HeLa cells 48h after transfection. Both mKate-tagged σ1Rs expressed in a predominantly reticular shape. No significant aggregation of intracellular σ1R-mKate$^{E102Q}$ has been detected which contradicts results of the previous study by Dreser et al [159]. Their study reported σ1R$^{E102Q}$ aggregates in primary lymphoblastoid cells derived from E102Q-SigR1 fALS patients, and in the MCF-7 cells.

Fig5.26 compares the cellular expression of σ1R-mKate and σ1R-mKate$^{E102Q}$ in three different populations of HeLa cells 48h after transfection. Under identical recording conditions, higher intensity of σ1R-mKate was detected in comparison to σ1R-mKate$^{E102Q,}$ suggesting higher levels of σ1R-mKate expression.

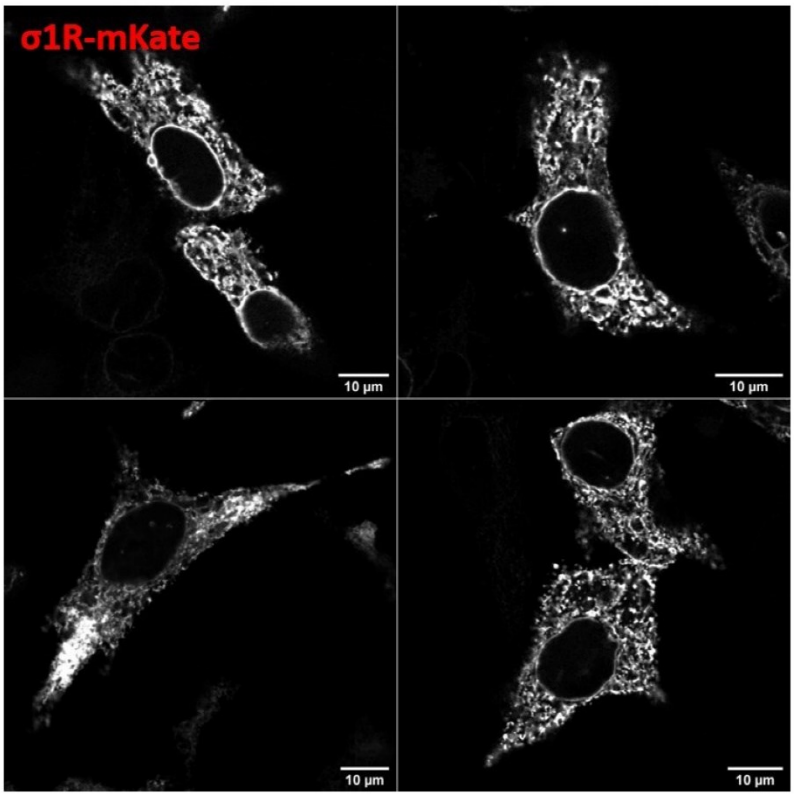


**Fig5.24 Subcellular distribution of σ1R-mKate**. Confocal images of HeLa cells 48h post-transfection with of σ1R-mKate.Scale bar = 10µm.

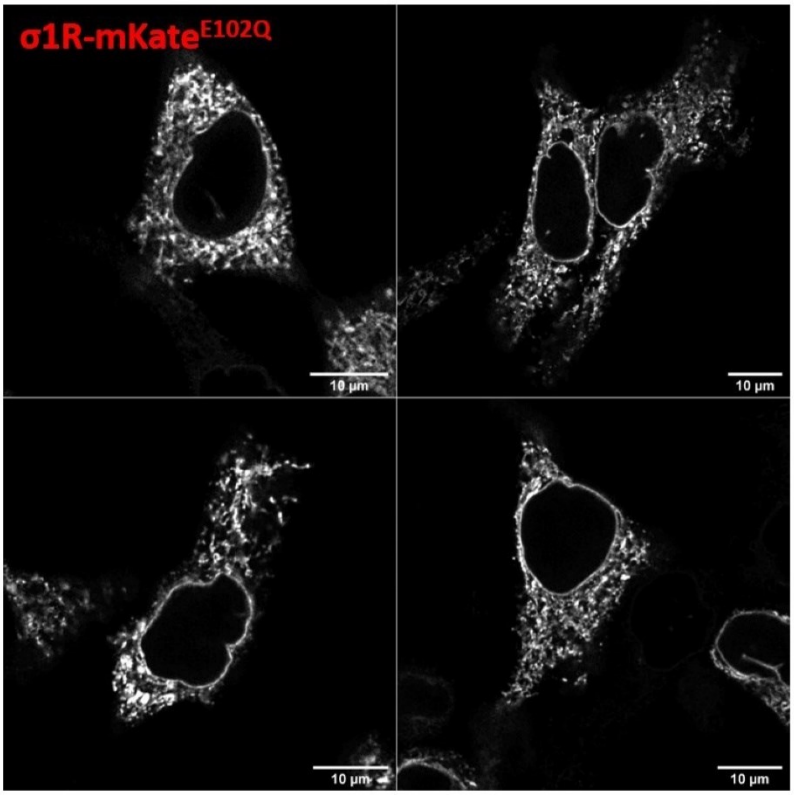


**Fig5.25 Subcellular distribution of σ1R-mKate$^{E102Q}$**. Confocal images of HeLa cells 48h post-transfection with of σ1R-mKate$^{E102Q}$.Scale bar = 10µm.

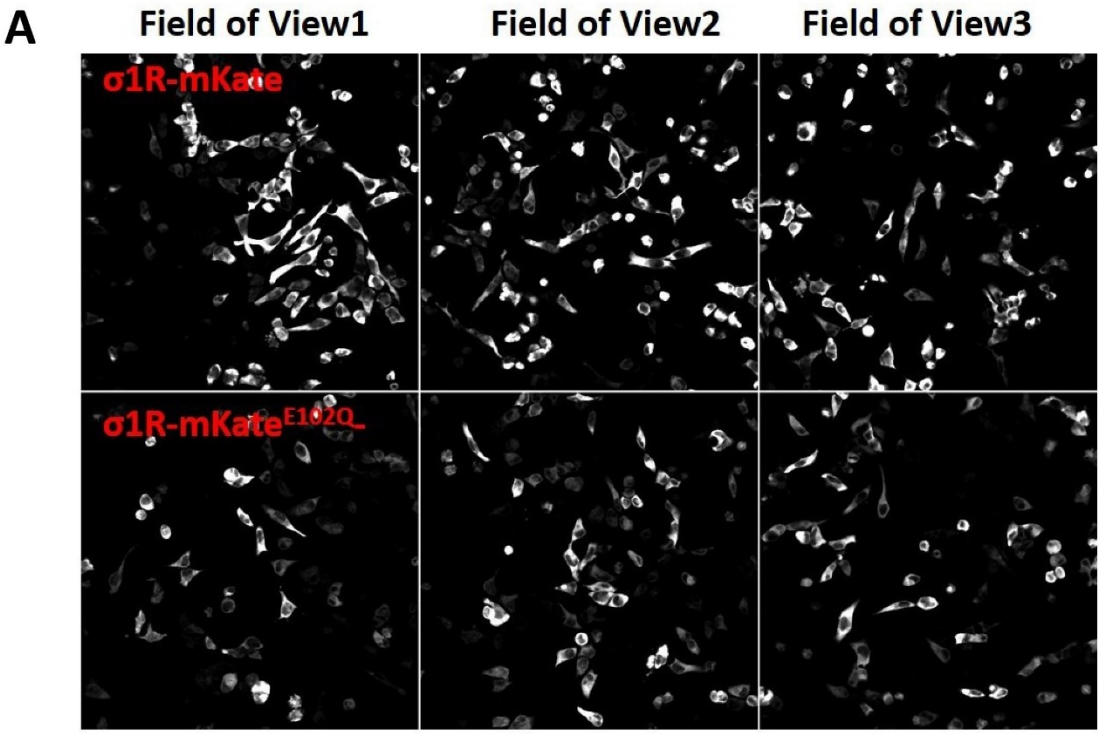


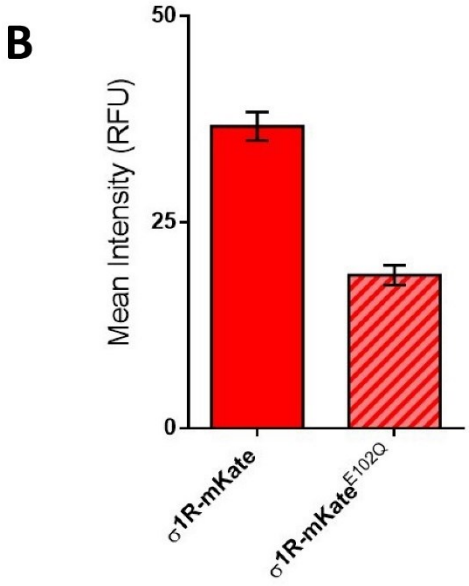


**Fig5.26 Comparison of σ1R-mKate and σ1R-mKate$^{E102Q}$ expression 48h post-transfection A)** HeLa cells expressing σ1R-mKate (row 1) and σ1R-mKate$^{E102Q}$ (row 2) 48h post-transfection. **B)** Comparison of σ1R-mKate and σ1R-mKate$^{E102Q}$ intensities from three field of views

.

### 5.2.4 σ1R-mKate$^{E102Q}$ fails to inhibit $Ca^{2+}$ influx in SOCE microdomains

To investigate the functional role of σ1R$^{E102Q}$ in SOCE microdomains, σ1R-mKate and σ1R-mKate$^{E102Q}$ were co-expressed with G-GECO1.2-Orai1 in HEK293 cells. Additionally, G-GECO1.2-Orai1 was co-expressed with ER-dsRED to mimic the σ1R's ER distribution and the expression for the red channel. Changes in $[Ca^{2+}]_{cyt}$ within SOCE microdomains were measured in HEK293 cells 48h post-transfection with G-GECO1.2-Orai1 and using TIRFM.

Fig5.27 shows representative TIRFM images of G-GECO1.2-Orai1 co-expressed with ER-dsRed (row1), σ1R-mKate (row2) and σ1R-mKate$^{E102Q}$ in 0.1 mM EGTA (column 1), 2mM $Ca^{2+}$ (column 2) and 2mM $Ca^{2+}$ with 5 μM Ionomycin (column 3). G-GECO1.2-Orai1-measured SOCEs (peaks) were compared with the Kruskal-Wallis test using α of 0.05. In comparison to ER-dsRED, overexpression of σ1R-mKate significantly inhibited SOCE (Fig5.28, ***, $P < 0.001$). In comparison to ER-dsRED, overexpression of σ1R-mKate$^{E102Q}$ failed to significantly inhibit SOCE (Fig5.28, ***, $P < 0.001$). Results of statistical analysis have been summarized in Table 5.22.

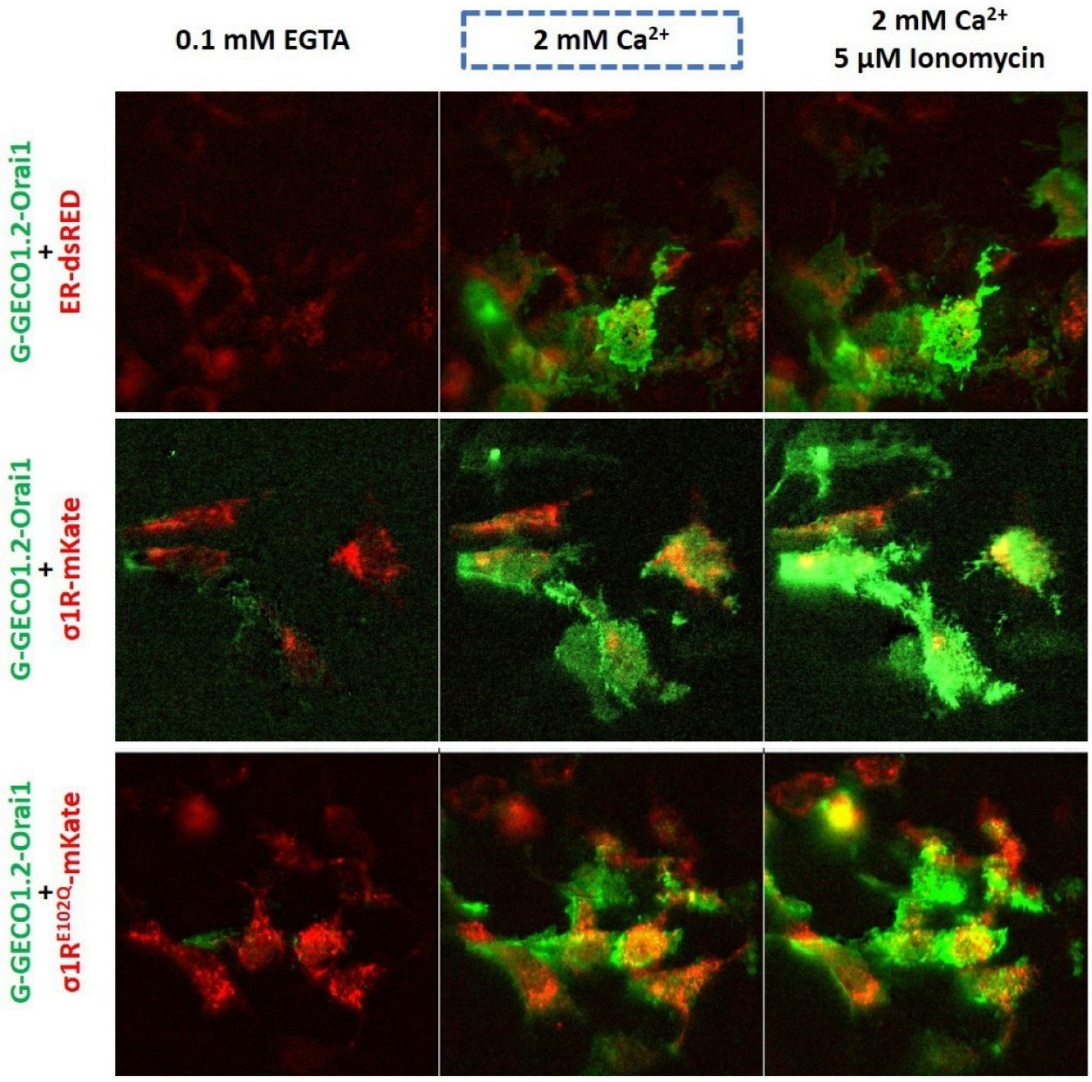


**Fig5.27 The functional effect of σ1R-mKate and σ1R$^{E102Q}$-mKate on Tg-evoked G-GECO1.2Orai1-mediated SOCE in HEK293 cells.** TIRFM images of G-GECO1.2-Orai1-measured SOCE in HEK293 cells expressing ER-dsRED (row1), σ1R-mKate (row2) and σ1R$^{E102Q}$-mKate (row3) in 0.1 mM EGTA (pre-treatment; column 1), 2mM $Ca^{2+}$ (post-treatment with 1 µM Thapsigargin; column 2) and 2mM $Ca^{2+}$ with 5 µM Ionomycin (column 3).

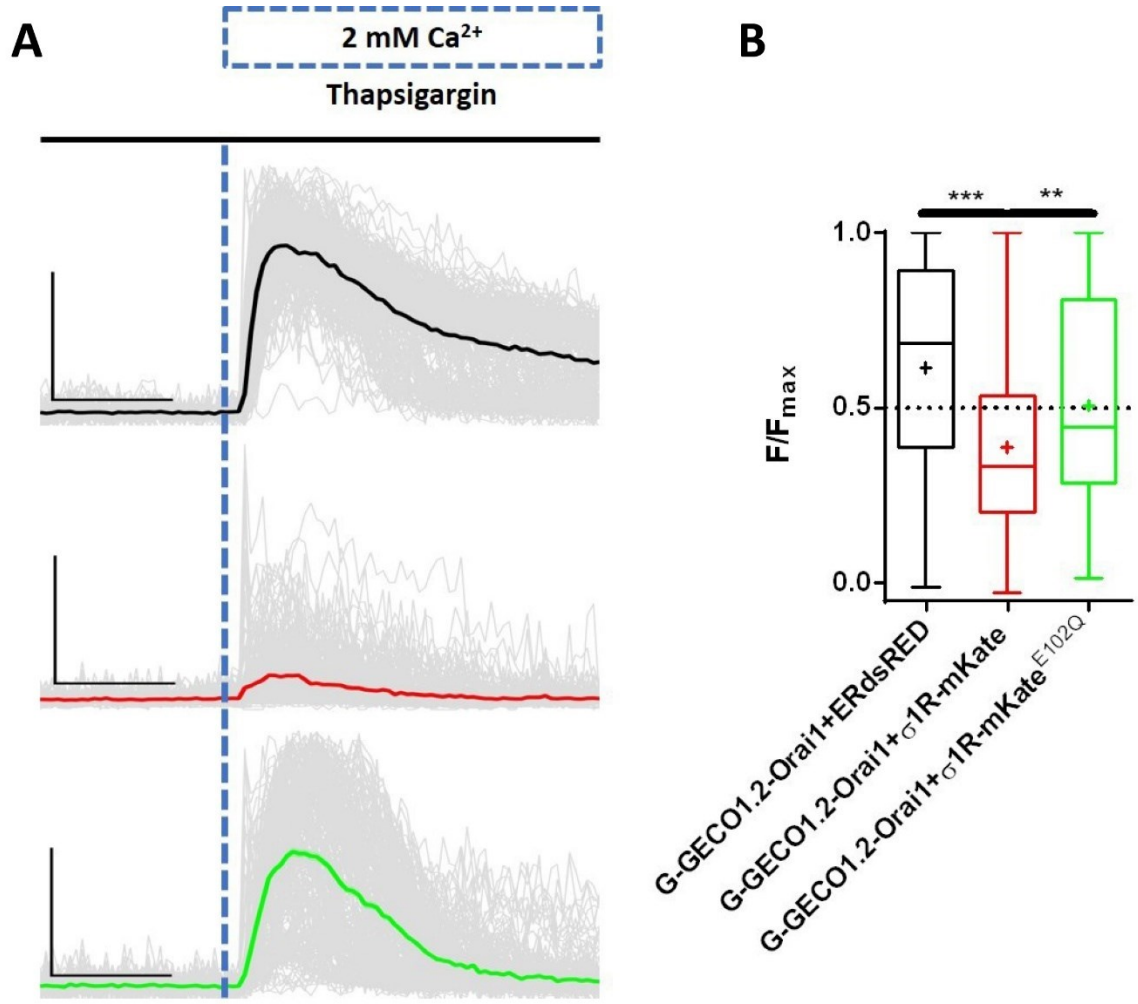


**Fig5.28 Quantification of G-GECO1.2-Orai1-measured SOCE (peak) HEK293 cells expressing ER-dsRED, σ1R-mKate and σ1R$^{E102Q}$-mKate** A) Representative G-GECO1.2-Orai1 average±SEM traces of HEK293 cells expressing ER-dsRED (black), σ1R-mKate (red) and σ1R$^{E102Q}$-mKate (green) during SOCE. Grey traces show individual measurements within the TIRFM recordings. Scale bar = 50% F/Fmax in y-direction and 100 s in x-direction. B) Box-and-whisker plot summarizing SOCE (peak) across three independent experiments (n=3) using TIRFM. Result shows difference between medians compared with the Kruskal-Wallis test. (**, $P < 0.01$, ***, $P < 0.001$).

| Group | Median | Mean±SEM | N | Kruskal-Wallis G-GECO1.2-Orai1+ σ1R-mKate | Kruskal-Wallis G-GECO1.2-Orai1+ σ1R-mKate$^{E102Q}$ |
|---|---|---|---|---|---|
| G-GECO1.2-Orai1+ER-dsRED | 0.6330 | 0.6155±0.05699 | 30 | ***, P < 0.001 | n.s, P > 0.05 |
| G-GECO1.2-Orai1+σ1R-mKate | 0.3322 | 0.3490±0.03638 | 36 | | **, P < 0.01 |
| G-GECO1.2-Orai1+σ1R-mKate$^{E102Q}$ | 0.4639 | 0.5396±0.04202 | 30 | | |

**Table 5.2-2 Summary of Kruskal-Wallis test for G-GECO1.2-Orai1-measured SOCE during overexpression of σ1R-mKate and σ1R-mKate$^{E102Q}$ constructs**. SOCE measurements (Peaks, Fig 5.28) were taken across three independent experiments (n=3). Positionally-grouped ROIs were used as a biological replicate (N) for statistical analysis.

## 5.3 Discussion

### 5.3.1 σ1R$^{E102Q}$ fails to effectively inhibit SOCE

In this chapter, the effect of σ1R$^{E102Q}$ in the regulation of SOCE was tested using both GCaMP6f and G-GECO1.2-Orai1. Enhanced expression of σ1R-V5 $^{E102Q}$ failed to inhibit SOCE in the population of HEK293 cells while σ1R-mKate$^{E102Q}$ exerted similar cumulative effect in SOCE microdomains. During western blot analysis of total protein expression, σ1R-V5 $^{E102Q}$ was detected as a complex at ~ 50kDa (instead of ~25kDa) which is in agreement with previous report[36]. During fluorescent analysis of σ1R-mKate$^{E102Q}$ no significantly different protein aggregation was detected when compared to σ1R-mKate. This result is not in agreement with the most recent study which reported increased aggregation of σ1R-V5 $^{E102Q}$ in primary lymphoblastoid cells (PLCs) derived from E102Q-SigR1 fALS patients, and MCF-7 cell line[159].

Genotyping studies using single nucleotide polymorphism (SNP) approach identified E102Q-mutant of σ1R in the genomic DNA of patients diagnosed with juvenile-onset of ALS[36]. This study reported a shift of the σ1R$^{E102Q}$ to membranes of lower density during sucrose gradient fractionation and the strong hydrophobic interaction between the monomers even in the buffers containing 150mM DTT and 2% Triton-X [36]. The results of the western blot analysis in this chapter support this report. When compared to the overexpression of “untagged” σ1R and σ1R-V5, overexpression of σ1R-V5$^{E102Q}$resulted in the formation of complex detected slightly above 50kDa (Fig 5.22). Faint bands of similar sizes were also detected when overexpressing “untagged” σ1R and σ1R-V5, but majority of their protein expressions was still detected at size predicted for σ1R monomers. This suggests that E102Q-mutation indeed increases interaction between the monomers, especially considering all three constructs were delivered using the same type of vector

(pcDNA3.1/V5-His-TOPO). Functionally, the enhanced expression of both “untagged” σ1R and σ1R-V5 inhibited SOCE, suggesting that the small V5 epitope does not alter protein’ s function. Overexpression of σ1R-V5$^{E102Q}$ failed to inhibit SOCE, suggesting that E102Q point mutation results in the loss-of-function mutant.

Following overexpression of σ1R-mKate$^{E102Q}$ in HeLa cells, no significantly different levels of protein aggregation were detected in comparison to σ1R-mKate. This result diverges from previous reports[36,159], and suggests that fusion of large mKate fluorescent tag may have altered its subcellular distribution. However, earlier investigations of σ1R role in lipid trafficking reported only large-epitopes fused to its N-terminus to alter σ1R’s distribution and function, but not the epitopes fused to its C-terminus[59]. Additionally, the expression of σ1R-mKate and σ1R-mKate$^{E102Q}$ was compared in HeLa cells 48h after transfection. Less σ1R-mKate$^{E102Q}$ expression was detected across three wide field-of-views using confocal microscopy. However, using TIRFM, the rich expression σ1R-mKate$^{E102Q}$ was successfully detected in SOCE microdomains (Fig 5.27). Calcium assay using G-GECO1.2-Orai1 resulted in overall failure of σ1R-mKate$^{E102Q}$ to inhibit SOCE. However, comparing G-GECO1.2-Orai1-measured SOCE peaks of cells expressing ER-dsRED and σ1R-mKate $^{E102Q}$ there is notable lower average, median and 25$^{th}$ percentile in cells expressing σ1R-mKate $^{E102Q}$. Comparing their traces, cells expressing σ1R-mKate $^{E102Q}$ have mixture of responses resembling both highly active G-GECO1.2-Orai1 clusters of ER-dsRED group, as well as reduced-activity of G-GECO1.2-Orai1 clusters observed in σ1R-mKate. These results suggest that σ1R-$^{E102Q}$ may still have ability to inhibit SOCE but increase in the hydrophobic interaction between its monomers decreases its effectiveness to do so.

# 6 Chapter VI

## Investigating the interaction of σ1R with STIM1 and STIM2 during store-depletion

## 6.1 Introduction

The results of Srivats et al.[34] suggest that σ1Rs inhibit SOCE by interacting with STIM1 and attenuating its coupling to Orai1. In addition to STIM1, Orai1-mediated SOCE can be regulated by another member of STIM protein family, STIM2, including its splice variant STIM2.1[116,204]. Despite STIM proteins sharing a highly conserved protein structure, there are some differences in their N-terminal $Ca^{2+}$ sensing domains and Orai1-coupling SOAR domains which result in distinct functional properties[103]. This prompted us to address whether σ1R also regulates STIM2/Orai1-mediated SOCE.

In comparison to STIM1, STIM2 binds $Ca^{2+}$ with lower affinity and has been identified as a weaker coupling partner to Orai1[103]. While STIM1 has been identified as a main activator of SOCE in non-excitable cells, STIM2 has been proposed to be a regulator of basal SOCE, responding to relatively small drops in the ER [$Ca^{2+}$]. In 2015, two groups independently identified STIM2 splice variants STIM2.1, and STIM2.2[116,204]. Using conventional PCR, Miederer et al.[116] tested for splice-specific expression in several cell lines and tissues and detected STIM2.1 and STIM2.2 in all tested human cell lines and primary cells, identifying STIM2.2 as a predominant expressed variant. Functional analysis of these two variants revealed that STIM2.1 is a negative regulator of SOCE in contrast to STIM2.2 which is a positive regulator. Additionally, Rana et al.[204] proposed that STIM2.1 exerts a dominant negative effect on STIM1, although this was disputed by Zhou et al.[117], who showed that concatenated STIM1/STIM2.1 SOAR heterodimers fully activate Orai1 channels.

### 6.1.1 Aim

Given the importance of STIM2 as a regulator of SOCE, particularly in the central nervous system where it is known to have a neuroprotective role, the aim of my study was as follows:

(1) To determine whether σ1R interact with both STIM1 and STIM2 isoforms *in situ*.

## 6.2 Methods

### 6.2.1 Immunofluorescence (IF)

HeLa cells were seeded onto sterile, PBS-rinsed, collagen-coated 13 mm coverslips individually placed into 24W plates. Cells were transduced with either $WT^{VC}$ or σ1R-V5 baculovirus as previously described Chapter II, Section 2.4. Before fixation, cells were washed once with pre-warmed HBSS (37 °C). Cells were fixed with 4% paraformaldehyde for 20 minutes at room temperature, followed by three washes in PBS. Blocking and permeabilization was performed by applying Blocking Solution I (1% saponin, Sigma-Aldrich; UltraCruz blocking solution, Santa Cruz) for 30 minutes. This was replaced with an appropriate mix of primary antibodies diluted into Blocking Solution I (Table 6.21) and incubated at 4°C overnight. Cells were washed three times with Blocking Solution I and secondary antibodies, Alexa Fluor 488 goat anti-mouse IgG and Alexa Fluor 647 goat anti-rabbit IgG (1:800 dilution; H+L, ThermoFisher) applied in Blocking Solution I for 1h at the room temperature in the dark. Finally, cells were washed three times with PBS and mounted using 15 µl of Fluoroshield with DAPI.

### 6.2.2 Proximity ligation assay (PLA)

STIM1/Orai1, STIM2/Orai1, STIM1/σ1R, and STIM2/σ1R interactions were detected with Duolink® In Situ Detection Reagents Orange starter kit (Sigma Aldrich). This assay relies upon detection of the two proteins of interest with antibodies from different species (in this case mouse and rabbit). Following binding of the primary antibodies, secondary antibodies with complimentary oligonucleotides attached are added. If the two bound primary antibodies are sufficiently close (<40 nm), an in-situ PCR reaction is triggered upon

binding of the secondaries, and it is this amplification which is subsequently detected by confocal fluorescence microscopy (Fig 6.21 ).

The starter kit contained secondary PLA probes, a Blocking Solution II, antibody diluents, a ligation solution, an amplification solution, A and B wash buffers, ligase, and polymerase (Table 6.22). Primary antibodies (Table 6.21), PBS, 4% paraformaldehyde, and a Blocking Solution I were prepared separately.

24 h before the assay, HeLa cells were seeded onto collagen-coated coverslips and transduced with either $WT^{VC}$ or σ1R-V5 baculovirus as previously described in Chapter II, Section 2.4. Before fixation, cells were washed once with pre-warmed HBSS (37 °C) followed by 15 min treatment at 37°C in either HBSS (Basal) or $Ca^{2+}$-free HBSS containing 0.1 mM EGTA and 1μM thapsigargin (SOCE). Cells were fixed with 4% paraformaldehyde for 20 minutes at room temperature, followed by 3x washes in PBS. Blocking and permeabilization was performed by applying Blocking Solution I for 30 minutes. This was replaced with Blocking Solution II for another 20 min. Cells were incubated at 4°C overnight with Blocking Solution I containing primary antibodies directed against each of the two proteins of interest. For negative controls, only one or no primary antibody was included. Cells were washed 3x with Blocking Solution I before adding the PLA mix and incubating for 30 min at 37°C. The PLA mix was prepared by diluting both 5x plus and minus PLA probes in antibody diluent and leaving for 10 min at room temperature prior to adding to cells. Cells were washed 2x with Wash Buffer A for 5 minutes under gentle agitation. The Ligase and Ligation solution were mixed according to the manufacturer's instructions, vortexed, and applied to the cells for 30 minutes at 37˚C. Following 2x 5 min washes in Wash Buffer A the Amplification mix (polymerase plus amplification solution) was applied to cells and incubated for 2 hours at 37˚C. This was followed by 2x wash in Wash Buffer B for 10 minutes and a

final wash in 1x Wash Buffer B for 1 minute. The cells were mounted using 15 µl of Fluoroshield with DAPI and stored at 4˚C for <30 h before imaging.

### 6.2.3 Confocal imaging of cells following IF and image processing

Images were recorded sequentially using a Leica SP8 confocal microscope and oil-immersion 63x objective. Z-stack image acquisition was performed to obtain focal middle and top plane of cells of interest. Photo excitation was achieved by the illumination of a) DAPI using 405 nm laser with emission collected between 450-480 nm, b) Alexa Fluor 488 using Argon 488 nm laser with emission collected between 510-530 nm, and c) Alexa Fluor 647 using 633 nm laser with emission collected between 660-690 nm. Images were processed applying ImageJ in-built background subtraction and Gaussian filter (1 px).

### 6.2.4 Confocal imaging of cells following PLA and image processing

Images were recorded sequentially using Leica SP8 confocal microscope and oil-immersion 63x objective. Z-stack image acquisition was performed to obtain ~18-20 images through the cells. Photo excitation was achieved by the illumination of a) DAPI using 405 nm laser with emission collected between 450-480 nm, and b) the fluorophore for the PLA Amplification Orange signal using 543 nm laser with emission wavelength of 570-590 nm. Each PLA dot represents a high concentration of fluorescence as a result of the probe proximity, which can be quantified independently of the intensity. “Z-projection" using the maximum intensity was applied to recorded stacks to quantify PLA interactions within the cells. DAPI and PLA Z-projections were processed using 3x3 mean filter (1 px) and analysed seperatelly using IMCF segmentation toolbar in ImageJ. The “Renyi Entropy-Threshold” command was used to isolate both nuclei and PLA signals, while "Analyse particles"

command was used to count their number in binary image. DAPI and PLA counts were recorded in GraphPad Prism where their ratio was calculated.

| Name | Species | Antigen | Concentration | Reference |
|---|---|---|---|---|
| α-STIM1 | rabbit | 2-350aa of STIM1 | 1:100 | Protein Tech |
| α-STIM2 | rabbit | 583-597 aa of human STIM2 | 1:100 | Alomone lab |
| α-σ1R | mouse | 1-223 aa of human σ1R | 1:100 | (F-5) Santa Cruz biotechnology |
| α-Orai1 | mouse | synthetic peptide near the C-terminus of human Orai1 | 1:100 | Sigma |

**Table 6.2-1 List of antibodies and their respective dilutions as used in IF method and PLA assay**

| Duolink® In Situ Detection Reagents | Function [a] |
|---|---|
| PLA probe anti-mouse minus | A secondary antibody that binds to mouse primary antibodies. |
| PLA probe anti-rabbit plus | A secondary antibody that binds to primary rabbit antibodies. |
| Blocking Solution II | The blocking solution that prevents unspecific binding of the antibodies . |
| Antibody diluent | A mix of salts, detergents, and blocking solution provided to dilute antibodies. |
| Ligation solution | A solution that contains two different connector oligonucleotides which hybridize to the two PLA probe oligonucleotides. |
| Ligase | An enzyme that ligates the oligonucleotides together to form a closed circle which serves as a template for rolling circle amplification. |
| Amplification solution | A solution that contains nucleotides used to produce a single-stranded fluorophore during rolling circle amplification (ex/em = 554/579nm). |
| Polymerase | An enzyme that uses the ligated circle as a template for rolling circle amplification. |
| Wash buffer A and B | Wash buffer A was used after incubation with primary antibodies, PLA probes and ligation ligase solution. Wash buffer B was used after incubation with the amplification-polymerase solution |

**Table 6.2-2 Reagents included in Duolink® In Situ Detection Reagents Orange kit.**

**[a] The function of reagents in the PLA assay.**

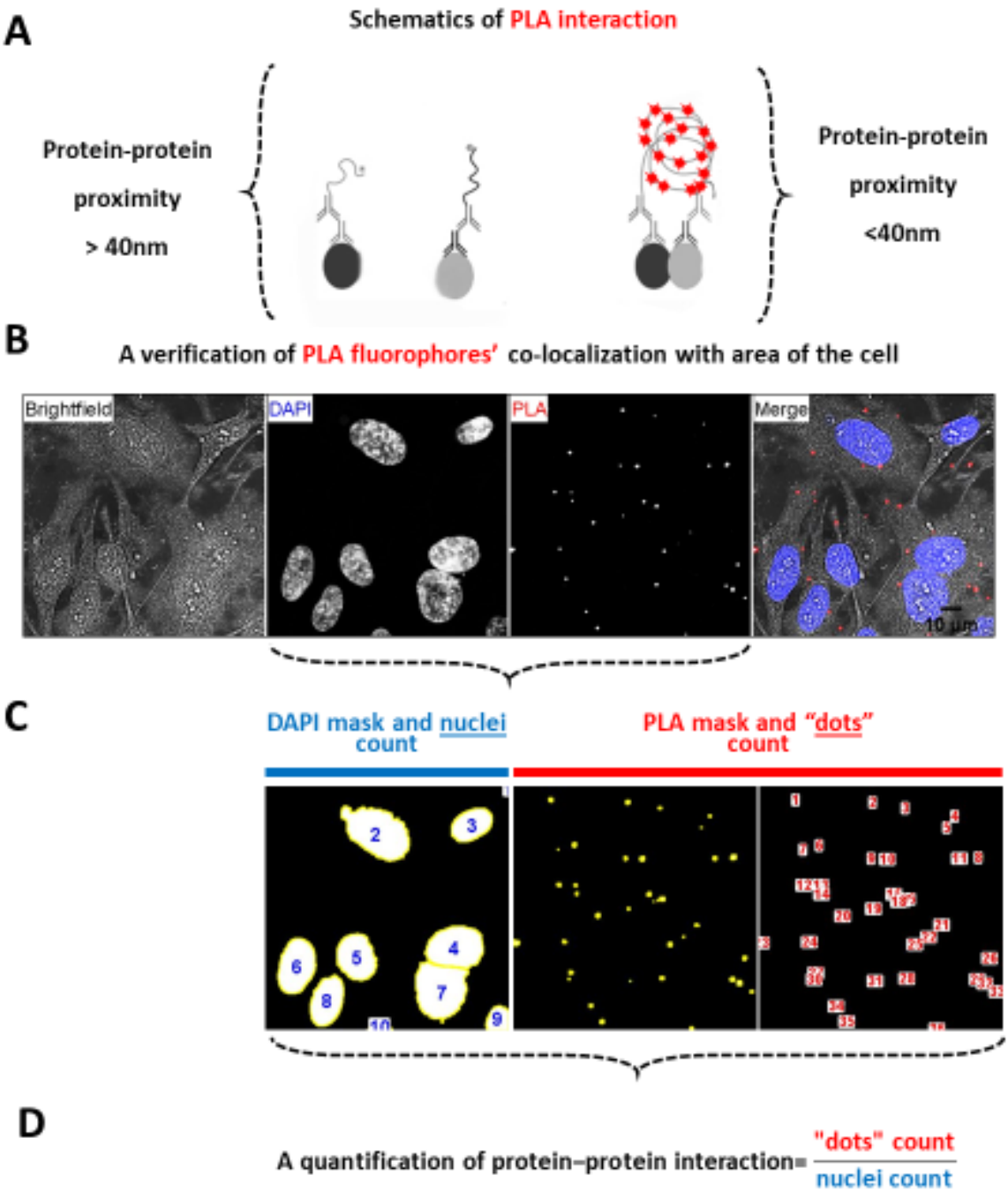


**Fig6.21 A schematic diagram of PLA assay analysis.** A) A PLA assay enables a fluorescent detection of protein-protein proximity ranging from 0-40 nm. A distance between antibody-targeted proteins that are further than 40 nm apart results in no signal. B) A positive PLA signal for STIM1-Orai1 interaction after prolonged thapsigargin (Tg) treatment of HeLa cells. Max projection images of brightfield, DAPI and PLA Z-stacks. A detected PLA signal co-localized with the area of HeLa cells. C) Following the verification that PLA fluorophores corresponding area of HeLa cells, DAPI and PLA images were segmented and analysed using in-built plugins in ImageJ. D) Protein-protein interaction is quantified and estimated using PLA "dots"/DAPI "Nuclei" ratio per analysed image.

## 6.3 Results

### 6.3.1 Expression of endogenous STIM1, STIM2, Orai1, and σ1R in HeLa cells

For the PLA assay, HeLa cells were chosen due to their large size and flat footprint which provides better resolution of the subcellular distribution of proteins in confocal images. The expression and distribution of endogenous STIM1, STIM2 and Orai1 in HeLa was examined by immunostaining using the primary antibodies listed in Table 6.21 and either the anti-mouse (Alex 488) or anti-rabbit (Alexa 647) secondary antibodies. The confocal images in Figs 6.31 and 6.32 show the distribution of endogenous STIM1 and STIM2, respectively. Both STIM isoforms exhibited an intracellular reticular-like distribution whereas Orai1 had a PM-like distribution, labelling the edges of cells in a cross-section through the middle. Endogenous expression of STIM proteins and σ1R in HeLa cells was also analysed by Western blot analysis. Fig 6.33 shows bands identified at the expected molecular mass for STIM1, STIM2, and σ1R, after loading 20 µg of protein. Together with immunostaining data, this result confirms the endogenous expression of STIM1, STIM2, σ1R, and Orai1 in HeLa cells. Also, it confirmed the selectivity of the primary antibodies against STIM1 and STIM2, with no detection of STIM1 with a-STIM2 and vice versa, allowing us to proceed towards the PLA assay .

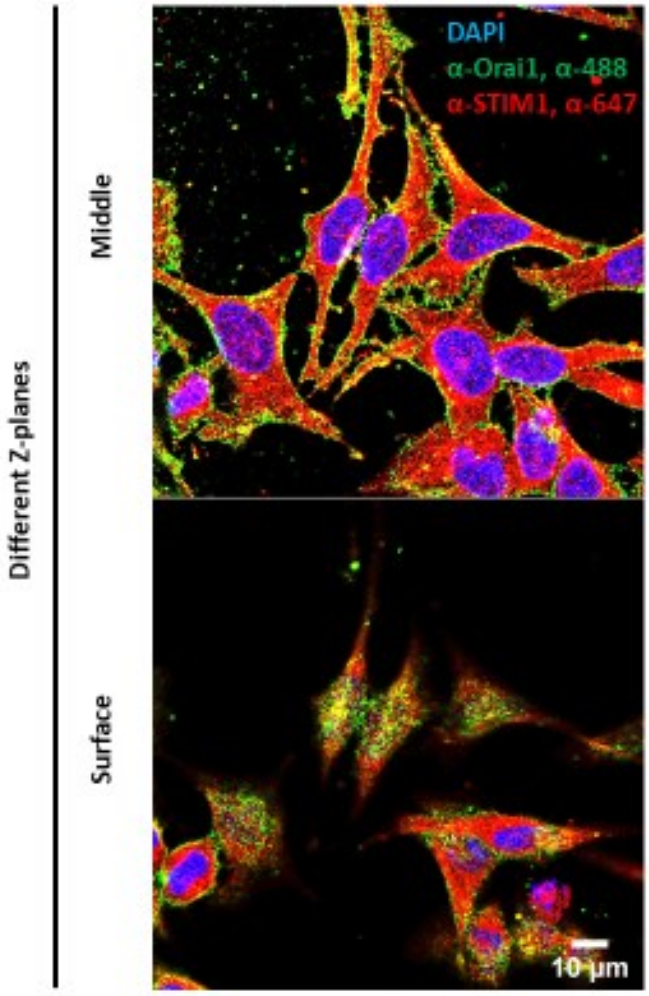


**Fig6.31 Subcellular localization of STIM1 and Orai1 in HeLa cells.** Confocal images of HeLa cells immunostained with α-STIM1 (α-647; red) and α-Orai1 (α-488; green) showing middle and surface cross-sections of the cell.

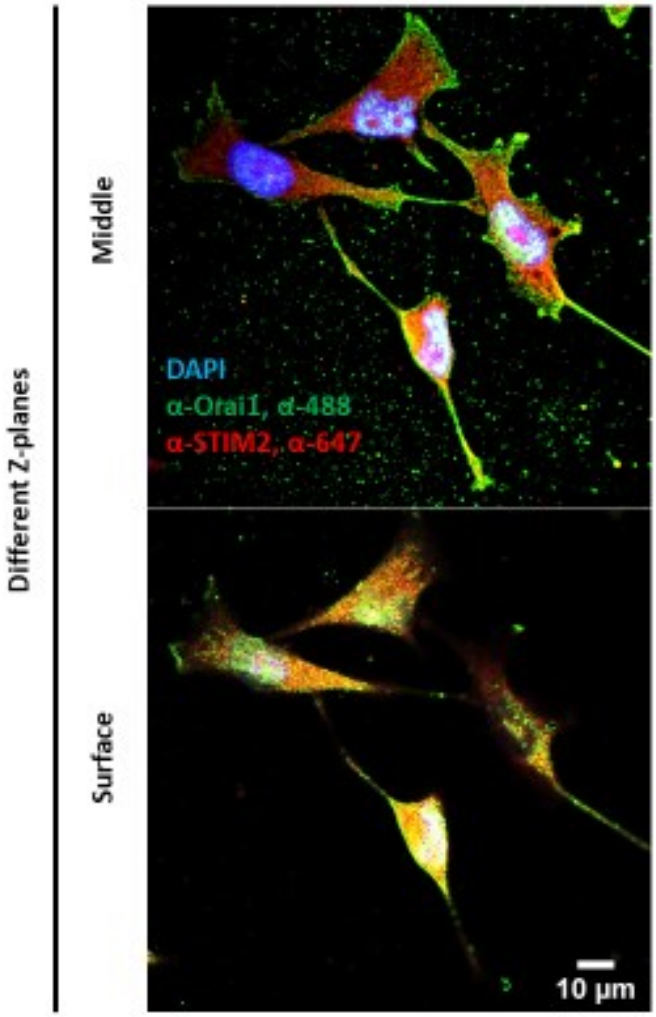


**Fig6.32 Subcellular localization of STIM2 and Orai1 in HeLa cells.** Confocal images of HeLa cells immunostained with α-STIM2 (α-647; red) and α-Orai1 (α-488; green) showing middle and surface cross-sections of the cell.

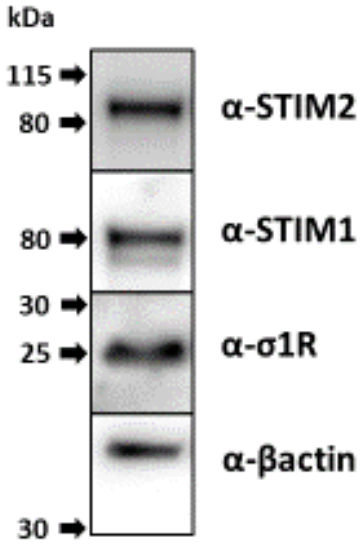


**Fig6.33 Western blot analysis of endogenous protein levels STIM2, STIM1, and σ1R in HeLa cells.** HeLa cells express STIM2, STIM1, and σ1R endogenously.

### 6.3.2 σ1R interacts with STIM1 *in situ*, but overexpression of σ1R-V5 did not inhibit STIM1-Orai1 interaction

Previous co-immunoprecipitation experiments with heterologously expressed STIM1-Myc, σ1R-V5 and Orai1-HA constructs suggested that there is an association between STIM1 and σ1R in unstimulated HEK293 cells, and that σ1R also associates with plasma membrane STIM1-Orai1 complexes following thapsigargin treatment[34]. To investigate interactions between the endogenous proteins in situ, the PLA assay was used with antibodies indicated in Table 6.21.

Initially, negative controls were performed to ensure that detection of fluorescent puncta by the PLA was dependent upon inclusion of antibodies to both proteins of interest. Confocal images obtained from cells where either no primary antibody was added, or only one of α-STIM1, α-STIM2 or α-σ1R was included, are shown in Fig 6.34. In all four conditions, the fluorescent signal detected was negligible, ranging from 0.08 to 0.22 PLA-puncta per cell. Detected range is marked as a 'Background" on the graph summaries.

Following these controls, antibodies against STIM1 and Orai1 were included to investigate the interaction of these two proteins under basal conditions and following $Ca^{2+}$ store depletion, both with and without over-expression of σ1R (Fig 6.35). Upon seeding, HeLa cells were transduced with either $WT^{VC}$ or σ1R-V5 baculovirus and then analysed 24h later. Prior to fixation, HeLa cells were treated with either HBSS (Basal) or 1μM thapsigargin (Tg) in 0.1 mM EGTA nominal $Ca^{2+}$-free HBSS for 15 min at 37°C. The prediction was that the STIM1-Orai1 interaction would increase following $Ca^{2+}$ store depletion triggered by Tg treatment. Images of HeLa cells treated with HBSS revealed very few fluorescent puncta per cell (0.15 ± 0.06 for $WT^{VC}$ and 0.11 ± 0.04 for σ1R-V5) which resembled background

levels. Following treatment with Tg in $Ca^{2+}$ free HBSS there was a dramatic, ~36-fold, increase in the number of fluorescent puncta per cell for the $WT^{VC}$ HeLa cells (5.4± 0.6). Following statistical analysis with a one-way ANOVA with Tukey post-hoc test, this increase is highly significant (****, $P < 0.0001$). Similarly, in cells over-expressing σ1R-V5 the number of puncta increased ~42-fold following Tg treatment (4.6 ± 0.6; ***, $p < 0.001$)). The frequency of the fluorescent puncta should provide a measure of STIM1-Orai1 interactions and its strong dependence upon $Ca^{2+}$ store depletion is evidence towards the reliability of this assay. Although the increase in puncta frequency per cell was slightly less in cells expressing σ1R-V5, the difference between these cells and cells transduced with the $WT^{VC}$ type virus was not significant (n.s., $P>0.05$)**.** These results suggest that σ1R does not exert a strong inhibitory effect on STIM1-Orai1 interactions.

Fig 6.36 shows the PLA analysis of STIM1-σ1R interactions for both endogenous σ1R ($WT^{VC}$) and following over-expression of σ1R-V5. In $WT^{VC}$ cells, puncta were detected under basal conditions (9.2 ± 0.8 per cell, n=3) and following Tg-induced store-depletion this increased ~2-fold (19.4± 1.6, n=3). This increase was statistically significant (***, $P < 0.001$). These results suggest that STIM1 and σ1R interact with one another and that depletion of the $Ca^{2+}$ store promotes this interaction further. The overexpression of σ1R enhanced the interaction under basal conditions, but the lack of any further increase upon store depletion could be because the endogenous levels of STIM1 were limiting.

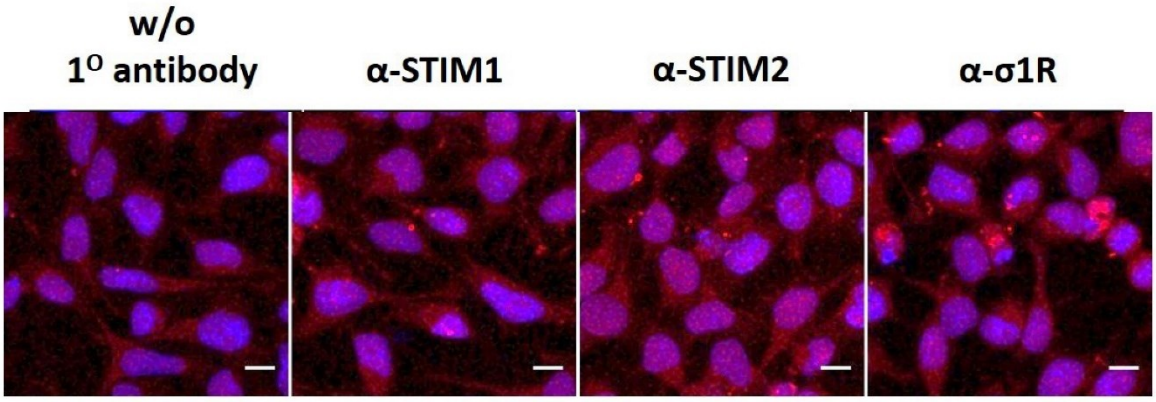


**Fig6.34 Negative controls for PLA assay.** Maximal Z-projections of confocal images of $WT^{VC}$ HeLa cells under basal conditions. HeLa cells were stained with the nuclear marker DAPI (blue). The PLA signal, recognized as a fluorescent red dot, depends on the simultaneous targeting of two antigens during the assay. A negative controls consisting of no primary antibodies (column 1), only α-STIM1 (column 2), α-STIM2 (column 3), and α- σ1R (column 4) resulted in insignificant PLA-positive detection.

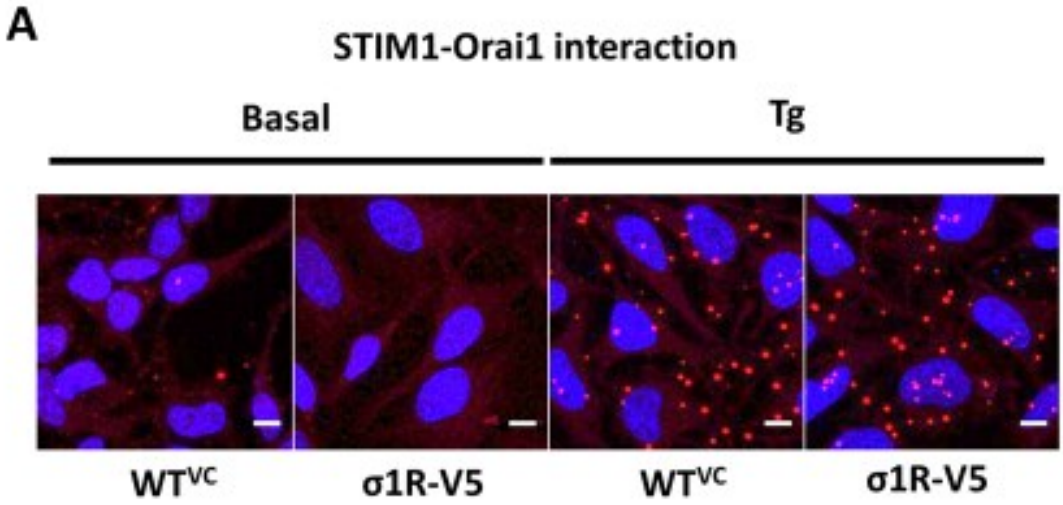


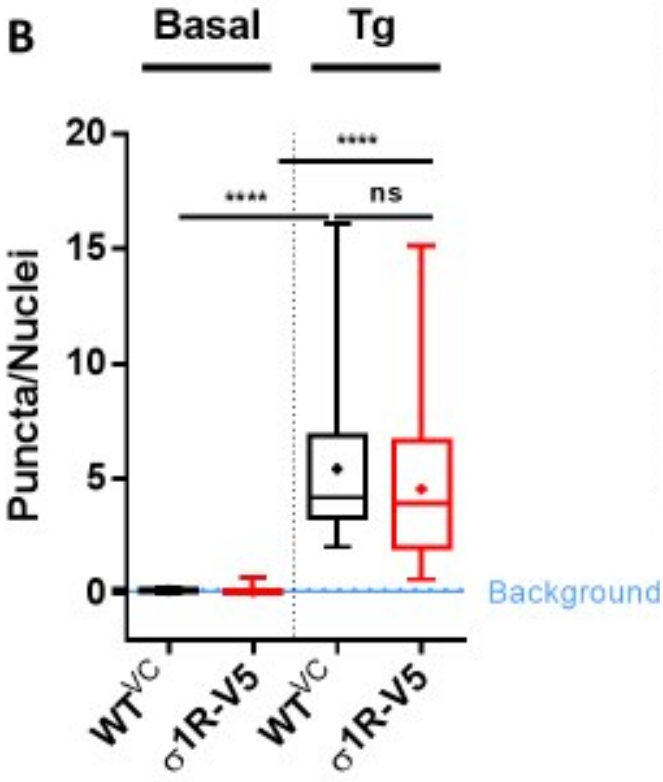


**Fig6.35 STIM1 interacts with Orai1 after thapsigargin (Tg) treatment.** A) Maximal Z-projections of confocal images of $WT^{VC}$ and σ1R-V5 HeLa cells under basal and store-depleted (Tg) conditions. HeLa cells were stained with the nuclear marker DAPI (blue). The PLA signal, recognised as a fluorescent red dot, detects the proximity of STIM1 and Orai1 antibodies. B) Box plots summarising results across three independent experiments (n=3) compared with one-way ANOVA. n.s., $P>0.05$, ****, $P<0.0001$. Scale bar = 10 μm.

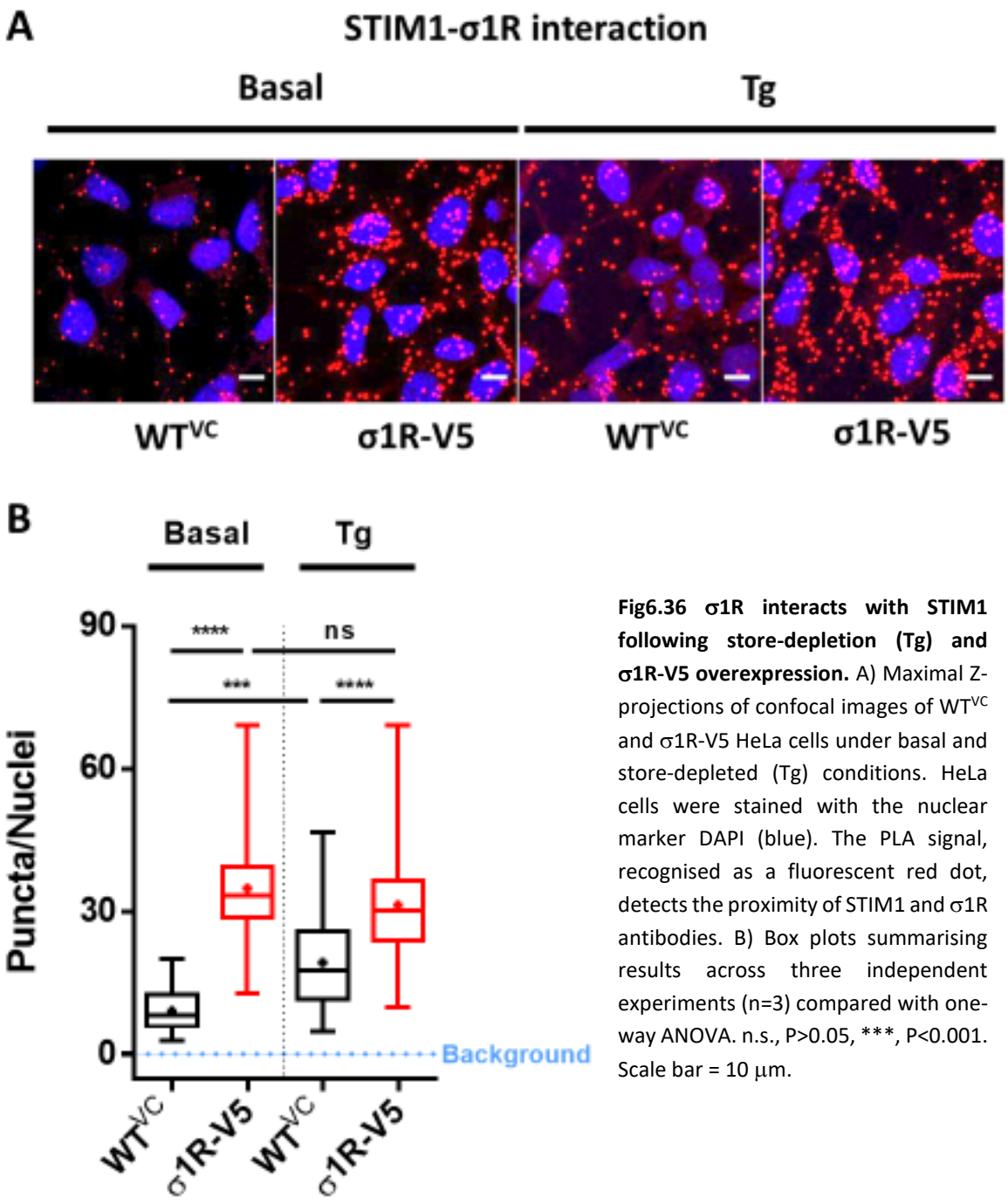


**Fig6.36 σ1R interacts with STIM1 following store-depletion (Tg) and σ1R-V5 overexpression.** A) Maximal Z-projections of confocal images of $WT^{VC}$ and σ1R-V5 HeLa cells under basal and store-depleted (Tg) conditions. HeLa cells were stained with the nuclear marker DAPI (blue). The PLA signal, recognised as a fluorescent red dot, detects the proximity of STIM1 and σ1R antibodies. B) Box plots summarising results across three independent experiments (n=3) compared with one-way ANOVA. n.s., P>0.05, ***, P<0.001. Scale bar = 10 μm.

### 6.3.3 σ1R interacts with STIM2 in unstimulated cells and its upregulation promotes STIM2-Orai1 basal interaction.

Similar experiments were carried out to determine the interaction of endogenous STIM2 with Orai1 and σ1R (Figs 6.37 and 6.38). The number of STIM2-Orai1 fluorescent puncta under basal conditions was low (1.4 ± 0.16, n=3) and surprisingly it decreased ~5-fold post-Tg treatment (0.19 ± 0.05, n = 3, *, P < 0.05) in contrast to what was observed for STIM1-Orai1. The overexpression of σ1R-V5 increased the number of puncta per cell by ~4-fold under basal conditions (4.4 ± 0.41), suggesting it promotes STIM2-Orai1 association, but again there was a ~4.5-fold decrease post Tg treatment (1.3± 0.10, n = 3 and,**** P < 0.0001). PLA analysis of STIM2-σ1R interactions showed that for the endogenous proteins (cells expressing $WT^{VC}$) the number of fluorescent puncta per cell also decreased ~3-fold following Tg-treatment from 3.3 ± 0.26 to 1.23 ± 0.14. In cells expressing σ1R-V5 there was instead an increase in puncta post Tg treatment (3.6± 0.42 for basal and 5.9 ± 0.53 post-Tg, n = 3, ***, P < 0.001). The apparent reduction in STIM2 interaction with both Orai1 and σ1R post-Tg treatment could be related to the enhanced binding of STIM1 to both proteins under these conditions. Unlike STIM1, STIM2 is expected to show some translocation to ER-PM junctions and interaction with Orai1 under basal conditions. Upon $Ca^{2+}$ store depletion, STIM1 will also translocates to these junctions and might therefore compete with STIM2 for binding Orai1. Similarly, enhanced STIM1-σ1R interactions could account for reduced STIM2- σ1R interactions. Under conditions of store depletion, the over-expression of σ1R increased the number of puncta seen using a combination of anti-STIM2 and anti-σ1R by 6-fold, which supports the idea that the puncta frequency is providing a read-out of STIM2-σ1R interactions.

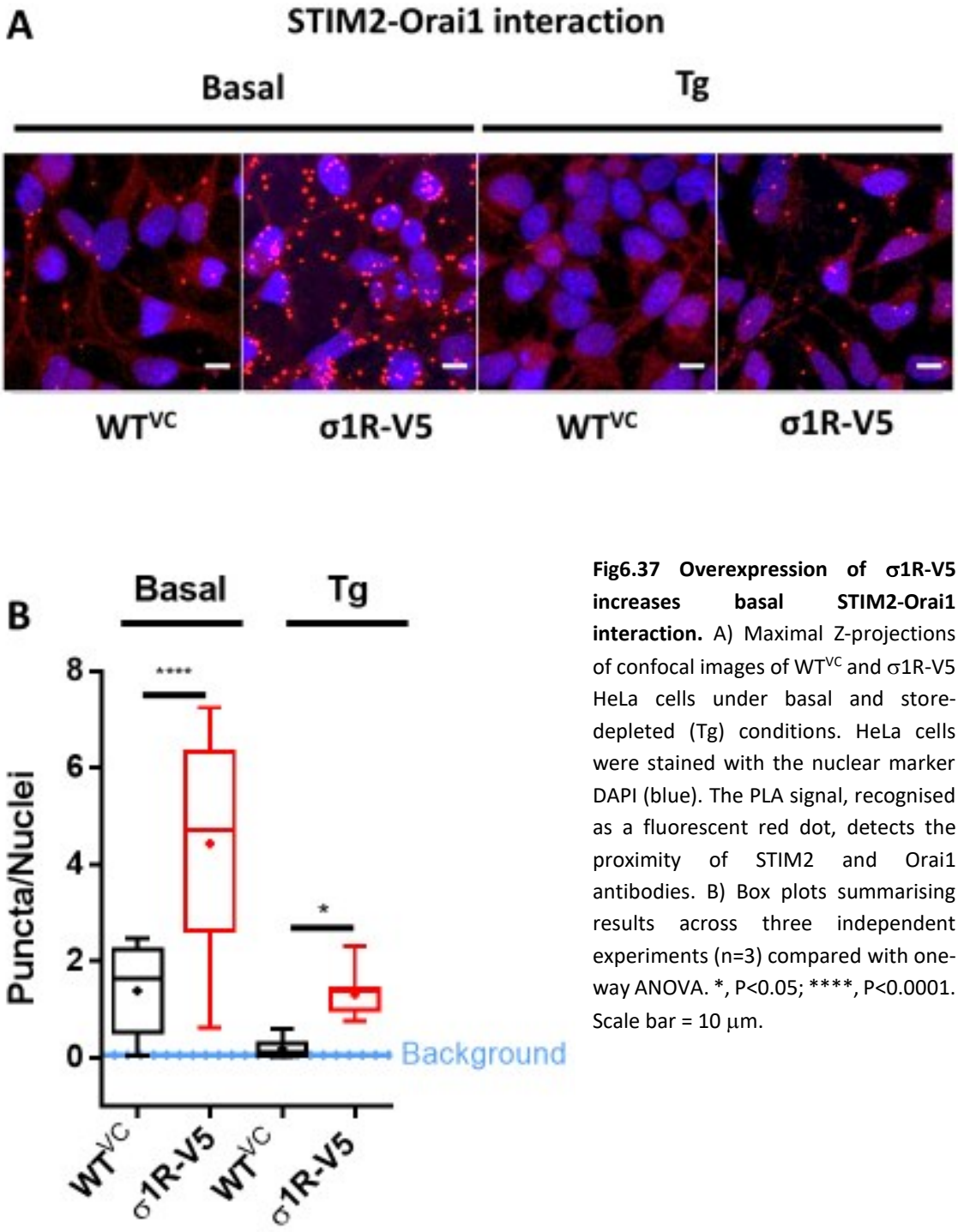


**Fig6.37 Overexpression of σ1R-V5 increases basal STIM2-Orai1 interaction.** A) Maximal Z-projections of confocal images of $WT^{VC}$ and σ1R-V5 HeLa cells under basal and store-depleted (Tg) conditions. HeLa cells were stained with the nuclear marker DAPI (blue). The PLA signal, recognised as a fluorescent red dot, detects the proximity of STIM2 and Orai1 antibodies. B) Box plots summarising results across three independent experiments (n=3) compared with one-way ANOVA. *, P<0.05; ****, P<0.0001. Scale bar = 10 μm.

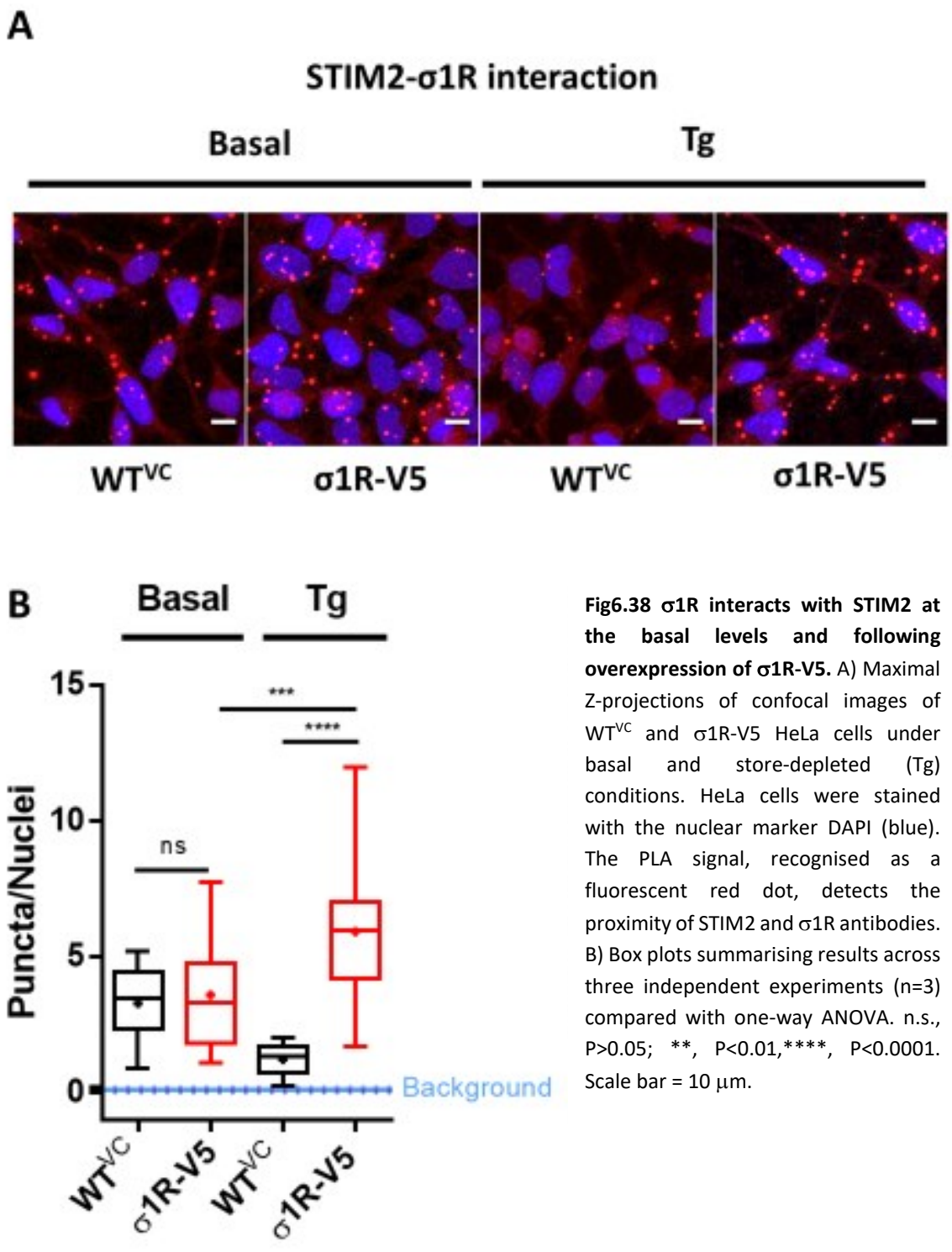


**Fig6.38 σ1R interacts with STIM2 at the basal levels and following overexpression of σ1R-V5.** A) Maximal Z-projections of confocal images of $WT^{VC}$ and σ1R-V5 HeLa cells under basal and store-depleted (Tg) conditions. HeLa cells were stained with the nuclear marker DAPI (blue). The PLA signal, recognised as a fluorescent red dot, detects the proximity of STIM2 and σ1R antibodies. B) Box plots summarising results across three independent experiments (n=3) compared with one-way ANOVA. n.s., P>0.05; **, P<0.01,****, P<0.0001. Scale bar = 10 μm.

### 6.3.4 σ1R and STIM2 co-localize in sub-PM puncta under basal conditions and post-thapsigargin treatment.

Further investigation of a possible interaction between STIM2 and σ1R was carried out by analysing their subcellular distributions and co-localization under basal and store-depleted conditions. STIM2.2-mCh and σ1R-EGFP were over-expressed in HeLa cells, and their expression in the vicinity of the plasma membrane was imaged using TIRFM. In the majority of cells, STIM2.2-mCh was already translocated to sub-PM puncta under basal conditions (normal HBSS) and was unresponsive to Tg-induced store-depletion. Within these puncta, STIM2.2-mCh clearly co-localized with σ1R-EGFP (Fig. 6.39). There were, however, some cells in which the translocation of both STIM2.2-mCh and σ1R-EGFP to the PM was enhanced by treating cells with 1 μM Tg for 6 min in $Ca^{2+}$- free HBSS, and an example is shown in Fig 6.310.

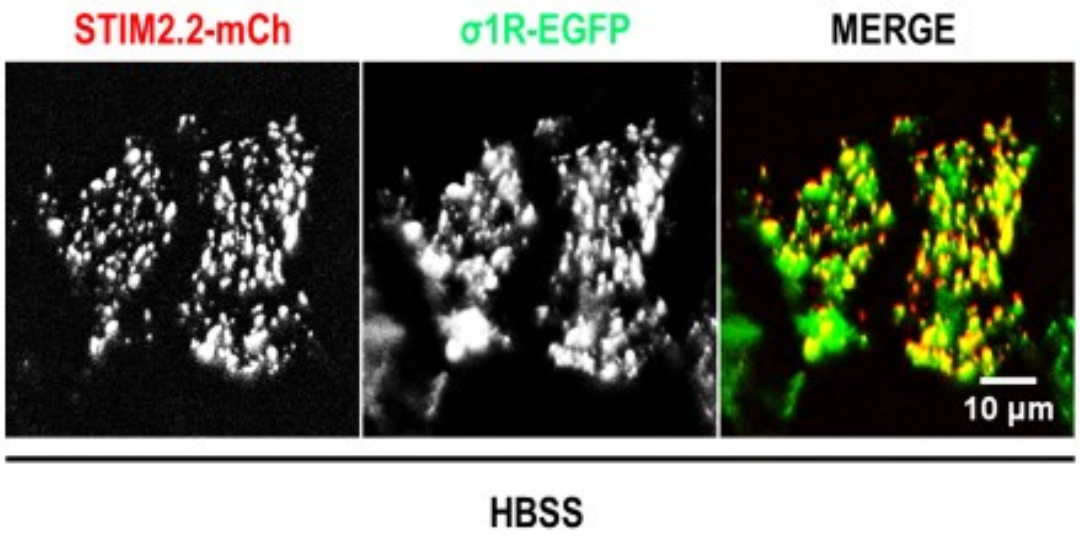


**Fig6.39 σ1R-EGFP co-localizes with STIM2.2-mCh at sub-PM regions under basal conditions (HBSS).** TIRFM images of HeLa cells co-transfected with STIM2.2-mCh (column 1) and σ1R-EGFP (column 2). Two proteins co-localize at sub-PM regions in puncta-like structures.

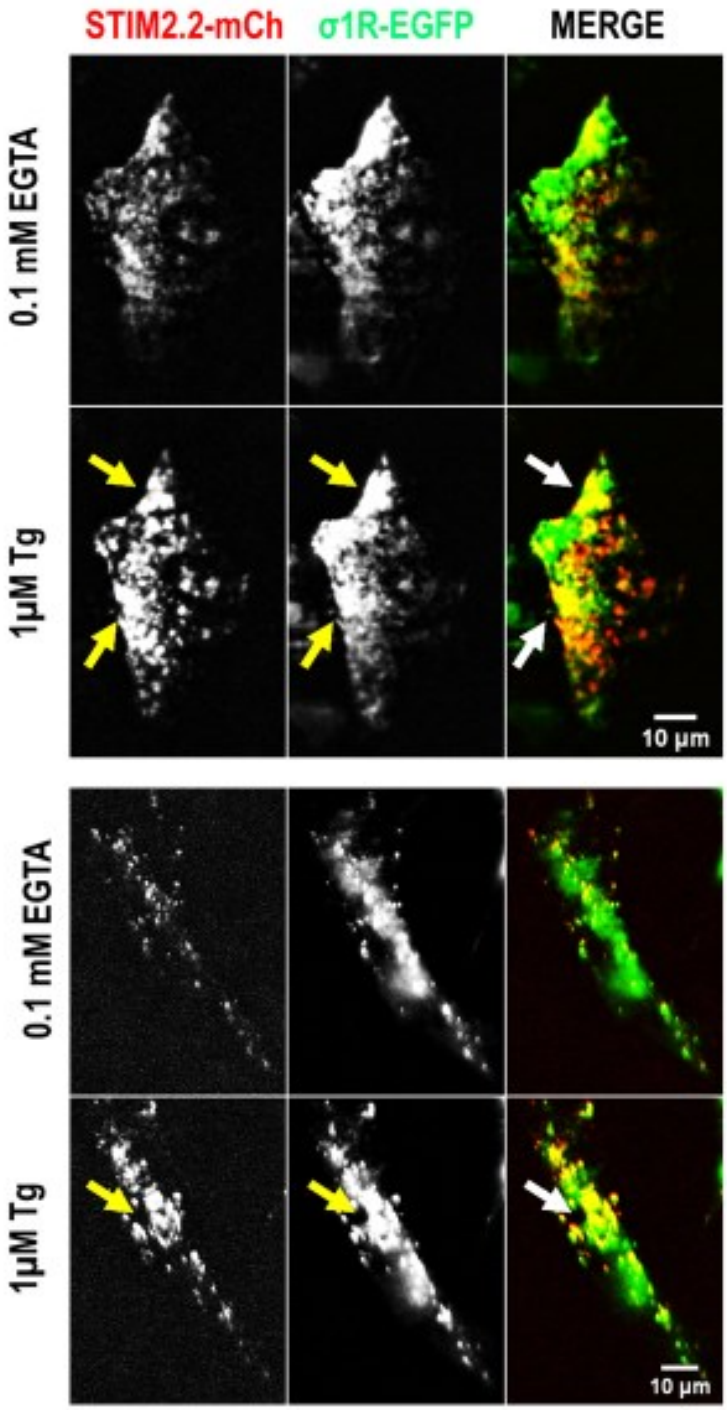


**Fig6.310 σ1R-EGFP co-localizes with STIM2.2-mCh at sub-PM regions following store-depletion.** TIRFM images of HeLa cells co-transfected with STIM2.2-mCh (column 1) and σ1R-EGFP (column 2). As no puncta-like structures were observed in 0.1 mM EGTA, cells were treated with 1 μM thapsigargin (Tg) for 6 min causing translocation of both proteins into the puncta-like structure at sub-PM regions.

## 6.4 Discussion

### 6.4.1 σ1R interacts in situ with both STIM homologs

Targeting σ1R and STIM proteins with primary antibodies (Table 6.21) allows for detection of their interaction in-situ using PLA method. If two proteins are sufficiently close (<40 nm), an in-situ PCR reaction is triggered upon binding of the secondaries resulting in the amplified signal that can be detected by confocal fluorescence microscopy. To test the specificity of detected PLA signals, I first took advantage of molecular mechanism of SOCE activation where STIM1 and Orai1 interaction occurs only after store-depletion. Following treatment of $WT^{VC}$ HeLa cells with Tg in $Ca^{2+}$ free HBSS there was a dramatic, ~36-fold, increase in the number of fluorescent puncta per cell (Fig 6.35) while the signal in untreated cells remained at the level of background. Similar results were also observed σ1R-V5 HeLa cells showing strong dependence upon $Ca^{2+}$ store depletion, and hence, supporting the reliability of this assay. Interestingly, the frequency of STIM1/Orai1 puncta between $WT^{VC}$ and σ1R-V5 HeLa cells was not significant (n.s., P>0.05)**,** suggesting that σ1R does not exert a strong inhibitory effect on STIM1-Orai1 interactions as it was previously reported[34].

Using the approach, STIM1-σ1R interactions were tested in the presence of endogenous σ1R ($WT^{VC}$ HeLa cells) and following over-expression of σ1R-V5. In $WT^{VC}$ HeLa cells, puncta were detected under basal conditions suggesting that σ1R and STIM1 can interact in unstimulated cells. Following Tg-induced store-depletion, the interaction between two proteins increased ~ 2 fold which is in agreement with earlier reports of σ1R's "active mode" after dissociating from BiP, and attenuation of SOCE after associating with STIM1[22,34]. Hence, these results suggest that STIM1 and σ1R interact with one another and that depletion of the $Ca^{2+}$ store promotes this interaction further. The overexpression of σ1R enhanced this interaction already under basal conditions, suggesting it can occur

independently of store-depletion depending on the availability of both STIM1 and σ1R as interactive partners.

Similar experiments were carried out to determine the interaction of endogenous STIM2 with Orai1 and σ1R (Figs 6.37 and 6.38). The number of STIM2-Orai1 fluorescent puncta under basal conditions was low (1.4 ± 0.16, n=3) and surprisingly it decreased after Tg treatment which is in contrast to what was observed for STIM1-Orai1 interaction. A possible explanation could be that, in comparison to STIM2, STIM1 possesses lower SAM stability and less robust EF-SAM interface. Hence, STIM1 exhibits increased kinetics of oligomerisation compared to STIM2 after thapsigargin treatment[106,108]. Also, the increased stability of STIM2 EF-SAM domain decreases protein's propensity for oligomerisation, which attenuates STIM2-association kinetics and prevents hyperactivation of SOCE due to low drops in intraluminal $Ca^{2+}$[106]. Thus, a decreased kinetics and propensity of oligomerisation may also result in less STIM2-Orai1 interaction after prolonged treatment with thapsigargin, especially when competing for Orai1-anchoring sites with stronger activator such as STIM1. Interestingly, the overexpression of σ1R-V5 increased the number of puncta per cell by ~4-fold under basal conditions (4.4 ± 0.41), suggesting σ1R-V5 promotes or perhaps, stabilises STIM2-Orai1 association. Following thapsigargin treatment, there was again significant decrease in STIM2-Orai1 interactive puncta 1.3± 0.10, n = 3 and,**** P < 0.0001).

PLA analysis of STIM2-σ1R interactions showed that for the endogenous proteins ($WT^{VC}$ HeLa cells) the number of fluorescent puncta per cell also decreased ~3-fold following thapsigargin treatment (from 3.3 ± 0.26 to 1.23 ± 0.14). On contrary, in cells expressing σ1R-V5 there was instead an increase in puncta post thapsigargin treatment (3.6± 0.42 for basal and 5.9 ± 0.53 post-Tg; ***, P < 0.001) across three independent experiments (n=3).This suggests that the reduction in STIM2 interaction with endogenous σ1R under stress

conditions could be related to the enhanced binding of STIM1 to both proteins under these conditions.

Unlike STIM1, STIM2 is expected to show some translocation to ER-PM junctions and interaction with Orai1 under basal conditions. Also, the polybasic tail of STIM proteins plays a crucial role in stabilising STIM proteins at contact sites between ER and PM allowing STIM proteins to interact with the proteins at the PM. In comparison to STIM1, STIM2 has a higher affinity of the polybasic tail for lipids that stabilises protein's localisation at the PM even at the resting conditions[111]. However, upon $Ca^{2+}$ store depletion, STIM1 also translocates to these junctions and might therefore compete with STIM2 for binding Orai1. Similarly, enhanced STIM1- σ1R interactions could account for reduced STIM2-σ1R interactions, where the interplay between σ1R and STIM homologs could play important role in the regulation of SOCE and consequently $Ca^{2+}$ homeostasis. Under stress conditions, the over-expression of σ1R increased the number of puncta seen using a combination of anti-STIM2 and anti-σ1R by 6-fold, which supports the idea that the puncta frequency is providing a read-out of STIM2- σ1R interactions and that the availability of σ1R as interactive partner may be essential in regulation of different pathways. Additionally, TIRFM recordings of STIM2.2-mCh and σ1R-EGFP supported PLA data, indicating these two proteins can co-localise at ER-PM junctions under both basal and store-depleted conditions. However, while our PLA results for STIM1-σ1R interaction are supported by current body of evidence, additional FRET or CoIP experiments are required for further characterisation of STIM2-σ1R interactions.

# 7 Chapter VII

## The functional role of σ1Rs in regulation of STIM2.2/Orai1 mediated SOCE.

## 7.1 Introduction

STIM1 is the most studied member of the STIM protein family and the main activator of SOCE in non-excitable cells. The exact role of its homolog, STIM2, has been a matter of debate[98]. STIM2 has been proposed to be the regulator of basal SOCE, and it has also emerged as more relevant STIM protein in the regulation of neuronal SOCE (nSOCE) due to its predominant expression within mouse spinal cord dorsal horn neurons, forebrain and hippocampus.

Results presented in the previous chapter, provide evidence that σ1R, a neuroprotective ER chaperone, interacts with both STIM1 and STIM2 *in situ*. This interaction was dependent on (1) the levels of $[Ca^{2+}]_{ER}$, and (2) the level of σ1R expression. The STIM1-σ1R interaction was promoted by prolonged store depletion (stress conditions), whilst the highest PLA signal for σ1R-STIM2 was observed under basal conditions.

In this chapter, the effect of σ1R on the function of STIM2 splice variants – STIM2.2 and STIM2.1 – was examined in HEK293 cells. The aims were as follows:

(1) To determine whether σ1R regulates STIM2.2-mediated SOCE in a population of HEK293 cells.
(2) To investigate whether σ1R regulates STIM2.2-dependent $Ca^{2+}$ influx within SOCE microdomains under basal conditions and following prolonged store-depletion.

## 7.2 Methods

### 7.2.1 Experimental timeline of Chapter VII

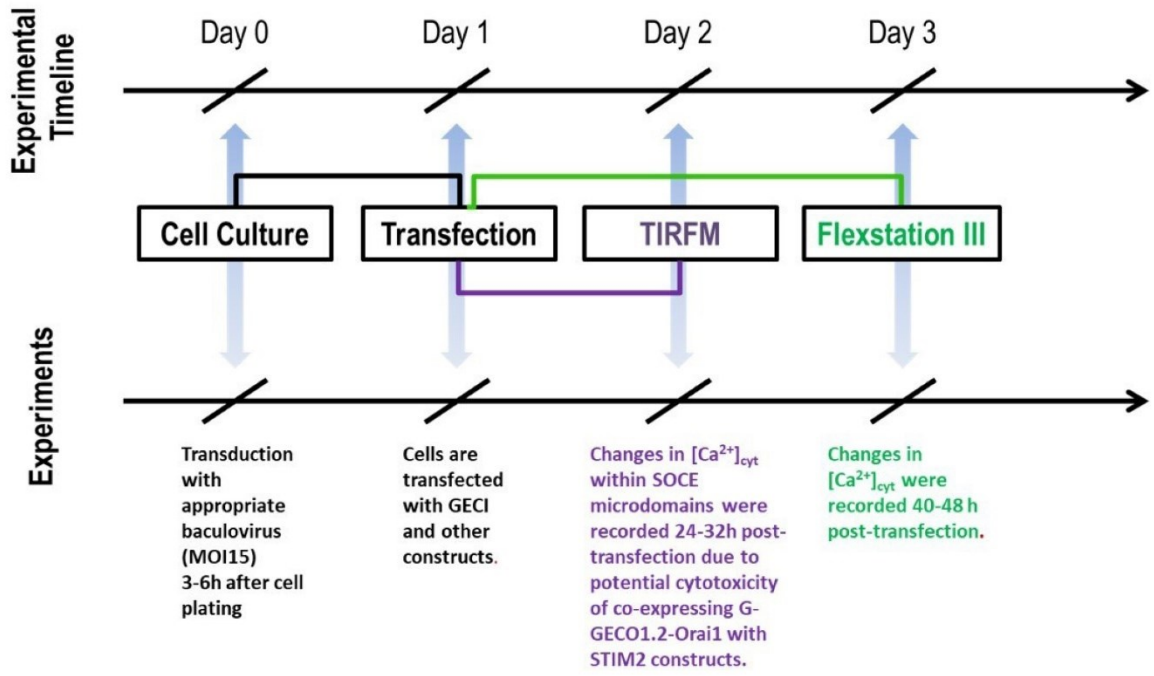


**Fig7.21.Experimental timeline of TIRFM and Flexstation III experiments in Chapter VII** (Day 0) Cell culture and plating of cells on the appropriate recording dishes, followed by baculovirus transduction. (Day 1) Transfection using PEI for Flexstation III experiments, and Lipofectamine 2000 for TIRFM experiments. (Day 2) TIRFM experiments. (Day 3) Flexstation III experiments.

## 7.3 Results

### 7.3.1 σ1R-V5 inhibits STIM1 and STIM2.2-potentiated SOCE in HEK293 cells

Having shown in Chapter VI that STIM2 interacts with σ1R in situ, I compared the inhibitory effects of σ1R-V5 on STIM1- and STIM2.2-mediated SOCE in HEK293 cells. For these experiments, in addition to using STIM2.2-mCh, the untagged STIM2.2 was also tested, whereas for the overexpression of STIM1, mCh-STIM1 and HA-STIM1 were used. Before transfection with STIM plasmids, HEK293 cells were transduced with either $WT^{VC}$ or σ1R-V5 baculovirus. 40-48 h after transfection (60-72h after transduction), SOCE was measured in a population of HEK293 cells using Flexstation III and GcAMP6f.

The results of these experiments are shown in Fig 7.31. For each group, SOCE peaks from 18 biological replicates (N=18) across three independent experiments (n=3) were compared using one-way ANOVA with α=0.05. SOCE in σ1R-V5 HEK293 cells was significantly reduced in comparison to $WT^{VC}$ HEK293 cells (0.47 ± 0.018 for $WT^{VC}$ versus 0.26 ± 0.021 for σ1R-V5, ****,$P < 0.0001$). Overexpression of HA-STIM1 and STIM2.2 in $WT^{VC}$ HEK293 cells significantly potentiated SOCE in comparison to $WT^{VC}$ HEK293 cells (0.75 ± 0.023 for $WT^{VC}$ + HA-STIM1 and 0.82 ± 0.032 for $WT^{VC}$ + STIM2.2, ****,$P < 0.0001$). Overexpression of HA-STIM1 and STIM2.2 in σ1R-V5 HEK293 cells restored SOCE to $WT^{VC}$ levels, but it was significantly lower in comparison to HA-STIM1- and STIM2.2-potentiated SOCE in $WT^{VC}$ HEK293 cells (0.48 ± 0.023 for σ1R-V5 + HA-STIM1 and 0.46 ± 0.031 for σ1R-V5 + STIM2.2, n.s, $P > 0.05$,****,$P < 0.0001$). This suggest that σ1R-V5 inhibits both HA-STIM1 and STIM2.2-potentiated SOCE in HEK293 cells.

Results from similar experiments but using the mCherry-tagged STIM constructs are shown in Fig 7.31C and D. Again, they show that σ1R-V5 inhibits mCh-STIM1 and STIM2.2-

mCh-potentiated SOCE in HEK293 cells. A comparison between these results suggests that STIM2.2-mCh behaves similarly to un-tagged STIM2.2.

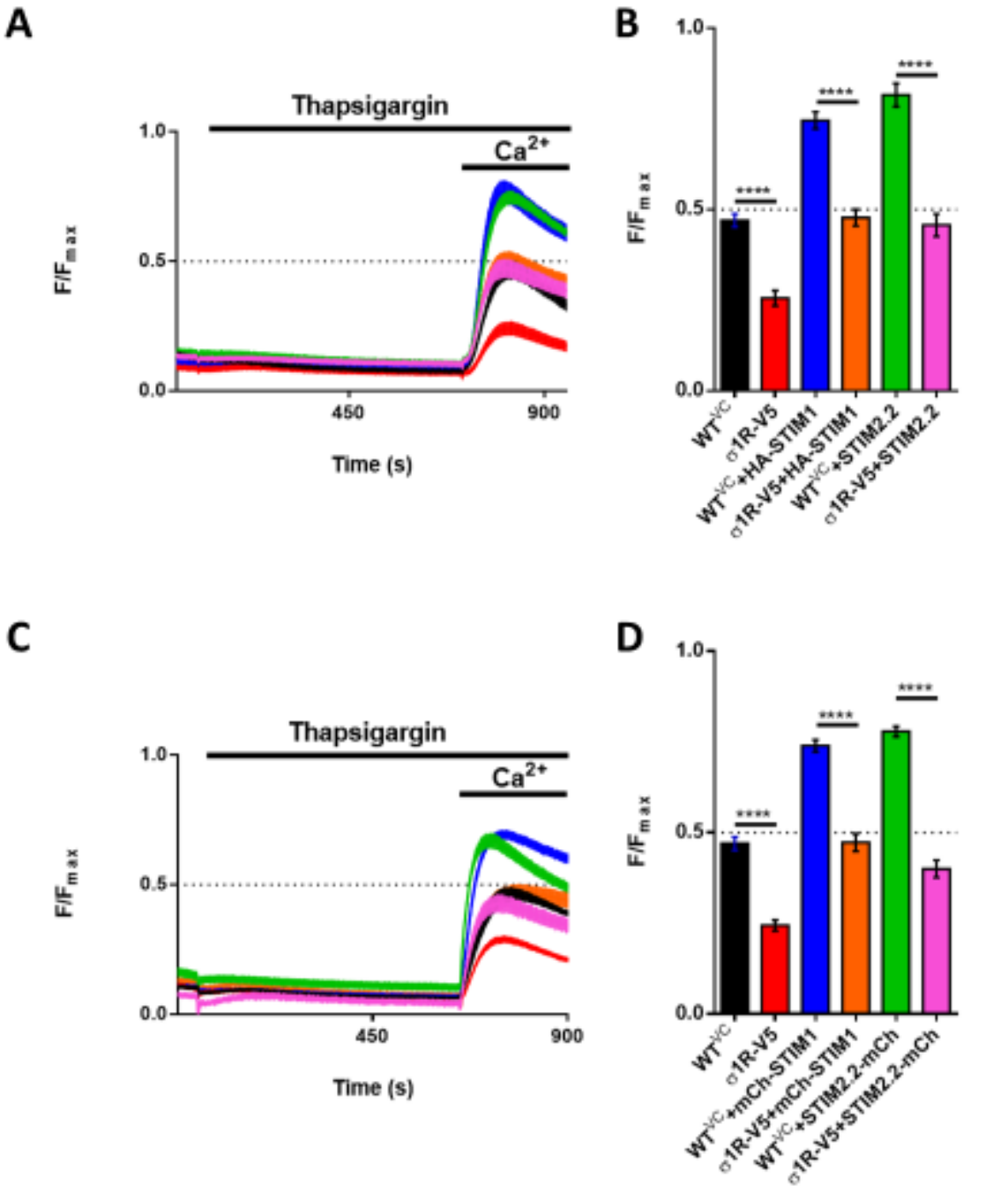


**Fig7.31 σ1R-V5 inhibits STIM1- and STIM2.2-potentiated SOCE in HEK293 cells.** A) GcAMP6f traces during treatment by 1 μM thapsigargin followed by restoration of 2 mM extracellular $Ca^{2+}$ in HEK293 cells expressing $WT^{VC}$ (black), σ1R-V5 (red), $WT^{VC}$+HA-STIM1 (blue), σ1R-V5+HA-STIM1 (orange), $WT^{VC}$+STIM2.2 (green), and σ1R-V5 + STIM2.2 (pink). C) GcAMP6f traces under same treatment and conditions as above (A) where STIM2.2 is expressed using STIM2.2-mCH construct. B) and D) Summary results showing SOCE from 18 biological replicates (N=18) across three independent experiments (n=3). A population of HEK293 cells within one well of 96W plate was used as a biological replicate (N) for statistical analysis. SOCE peaks were compared with one-way ANOVA, ****, P<0.0001.

### 7.3.2 STIM1 mediates the majority of Tg-evoked SOCE in HEK293 cells

HEK293 cells have endogenous levels of both STIM1 and STIM2 proteins (Chapter III, Fig3.38). To further characterize thapsigargin-evoked SOCE in HEK293 cells, endogenous STIM1 levels were knocked-down using STIM1 specific siRNA (Fig7.32C). SOCE was measured in a population of HEK293 cells using a Flexstation III and the $Ca^{2+}$ reporter GcAMP6f.

Fig7.32 shows GcAMP6f responses from cells transfected with either siRNA for STIM1 or a control siRNA (siControlA). Cells were treated with 1 μM thapsigargin (Tg) in nominal $Ca^{2+}$-free NES followed by restoration of 2 mM extracellular $Ca^{2+}$ and the peak of the SOCE response was compared using 18 biological replicates (N=18) across three independent experiments (n=3) with a Student' t-test using α of 0.05. Knockdown of STIM1 significantly reduced the amplitude of the SOCE response (****, $P<0.0001$). This reduction in SOCE suggests that endogenous STIM1 mediates the majority of Tg-evoked SOCE in HEK293 cells.

The knockdown of endogenous STIM1 was confirmed with Western blot analysis. Fig7.32C shows endogenous levels of STIM1 in (1) mock-transfected HEK293 cells, (2) cells transfected with siRNA control and (3) siSTIM1 transfected cells.

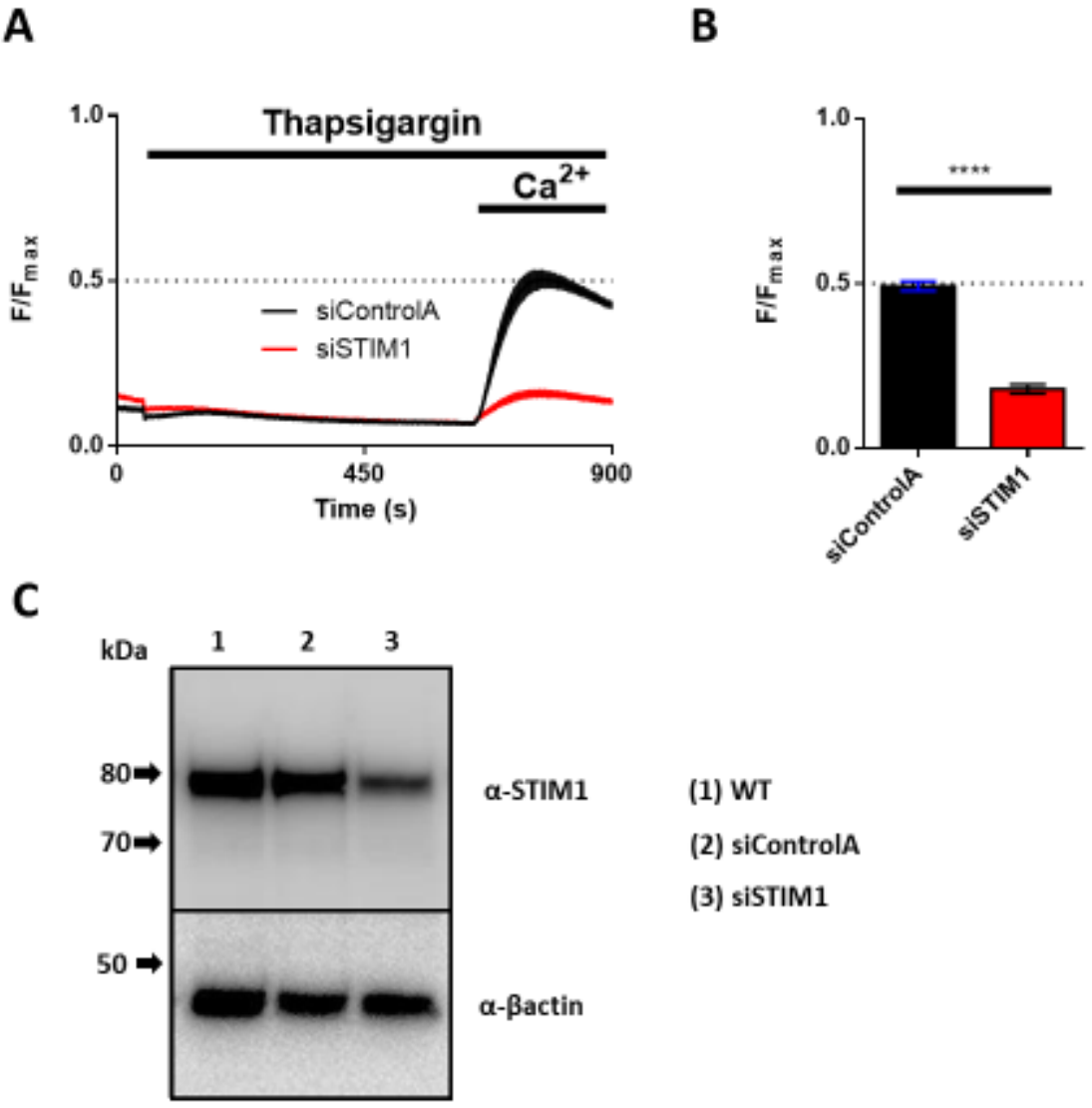


**Fig7.32 STIM1 mediates the majority of Tg-evoked SOCE in HEK293 cells.** A) GcAMP6f traces during treatment by 1 μM thapsigargin followed by restoration of 2 mM extracellular $Ca^{2+}$ in HEK293 cells expressing siControlA (black) and siSTIM1 (red). B) Summary results showing SOCE from 18 biological replicates (N=18) across three independent experiments (n=3). A population of HEK293 cells within one well of 96W plate was used as a biological replicate (N) for statistical analysis. SOCE peaks were compared with Student's t-test. ****, P<0.0001. C) Western blot analysis of endogenous STIM1 in (1) wild-type (WT) HEK293 cells, and cells expressing (2) siControlA, and (3) siSTIM1.

### 7.3.3 Overexpression of STIM2.2-mCh rescues SOCE in siSTIM1 HEK293 cells

After demonstrating that the majority of Tg-evoked SOCE in HEK293 cells is STIM1-dependent, I tested whether overexpression of STIM2.2-mCh can rescue SOCE in siSTIM1 HEK293 cells. To overexpress STIM2 proteins, STIM2.2-mCh and STIM2.1-mCh constructs were used. These constructs were provided by Barbara Niemeyer who characterized STIM2.2 and STIM2.1 variants as positive and negative regulators of SOCE, respectively[116]. Endogenous STIM1 levels were knocked down using STIM1 siRNA and SOCE was measured in the population of HEK293 cells using the Flexstation III and GCaMP6f.

Responses are shown in Fig7.33 for cells expressing siControlA (black), siControlA + STIM2.2-mCh (green), siControlA + STIM2.1-mCh (blue), siSTIM1(red), siSTIM1 + STIM2.2-mCh (pink) and siSTIM1 + STIM2.2-mCh (orange). HEK293 cells were treated with 1 μM Thapsigargin in nominal $Ca^{2+}$-free NES followed by restoration of 2 mM extracellular $Ca^{2+}$ to measure SOCE. SOCE peaks from 18 biological replicates (N=18) across three independent experiments (n=3) were compared using one-way ANOVA with α of 0.05. The knockdown of endogenous STIM1 inhibited SOCE (0.51 ± 0.018 for siControlA versus 0.21 ± 0.019 for siSTIM1, ****,$P < 0.0001$). Overexpression of STIM2.2-mCh significantly potentiated SOCE whilst overexpression of STIM2.1-mCh significantly reduced it (0.86 ± 0.030 for siControlA + STIM2.2-mCh, ****,$P < 0.0001$ and 0.35 ± 0.025 for siControlA + STIM2.1-mCh, ****,$P < 0.0001$). Overexpression of STIM2.2-mCh combined with siSTIM1 rescued SOCE to similar levels of control cells (0.58 ± 0.023), whereas overexpression of STIM2.1-mCh did not (0.20 ± 0.0061).

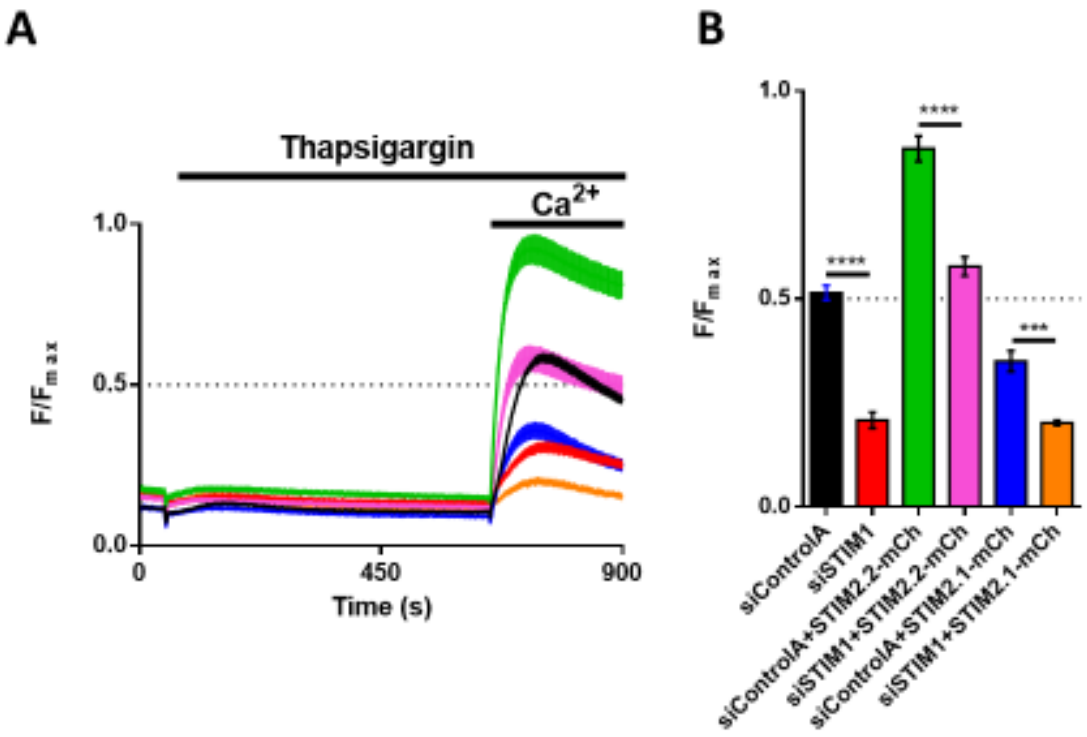


**Fig7.33 Overexpression of STIM2.2-mCh rescues SOCE in siSTIM1 HEK293 transients.** A) GcAMP6f traces during treatment by 1 μM thapsigargin followed by restoration of 2 mM extracellular $Ca^{2+}$ in HEK293 cells expressing siControlA (black), siSTIM1 (red), siControlA+STIM2.2-mCh (green), siSTIM1+STIM2.2-mCh (pink), siControlA+STIM2.1-mCh (blue) and siSTIM1+STIM2.1-mCh (orange). B) Summary results showing SOCE from 18 biological replicates (N=18) across three independent experiments (n=3). A population of HEK293 cells within one well of 96W plate was used as a biological replicate (N) for statistical analysis. SOCE peaks were compared with one-way ANOVA. ***,P<0.001; ****, P<0.0001.

### 7.3.4 σ1R-V5 inhibits STIM2.2-mediated SOCE in siSTIM1 HEK293 cells

Srivats et al. showed that σ1R inhibits SOCE by attenuating coupling of STIM1 to Orai1[34]. As σ1R-V5 limited STIM2.2-potentiated SOCE in HEK293 cells, we tested whether σ1R-V5 reduces STIM2.2-mediated SOCE independently of STIM1. To simultaneously overexpress STIM2.2 and knockdown STIM1, cells were transfected with STIM2.2 (untagged) and siSTIM1 RNA following transduction with either $WT^{VC}$ or σ1R-V5 baculovirus. 40-48 h post transfection, SOCE was measured using the Flexstation III and GcAMP6f. Additionally, Western blot analysis was performed using lysates from cells treated in the same way as for the functional assay.

SOCE responses are shown in Fig7.34 for HEK293 cells expressing σ1R-V5 (blue), $WT^{VC}$ + siSTIM1 (red), $WT^{VC}$ + STIM2.2 (green), σ1R-V5 + STIM2.2 (grey), $WT^{VC}$ + STIM2.2 + siSTIM1 (pink), and σ1R-V5 + STIM2.2 + siSTIM1 (orange). As in previous experiments, overexpression of σ1R-V5 and siSTIM1 significantly reduced SOCE. Overexpression of STIM2.2 in $WT^{VC}$ cells increased SOCE and it was significantly lower in σ1R-V5 + STIM2.2 cells. Co-expression of siSTIM1 and STIM2.2 resulted in significantly lower SOCE in σ1R-V5 HEK293 cells when compared to $WT^{VC}$ cells, indicating that σ1R-V5 inhibits STIM2.2-mediated SOCE independently of endogenous STIM1. Statistical analysis for was performed using one-way ANOVA with α of 0.05. Number of biological replicates and the results are summarized in Table 7.31.

Fig7.35 shows Western blot analysis of (1) $WT^{VC}$ + STIM2.2, (2) σ1R-V5 + STIM2.2, (3) $WT^{VC}$ + STIM2.2 + siSTIM1, (4) σ1R-V5 + STIM2.2 + siSTIM1, (5) $WT^{VC}$ + siSTIM1, and (6) σ1R-V5 + siSTIM1 HEK293 lysates 40 hours after co-transfection with GcAMP6f to mimic the conditions of the FlexStation III experiments. Fig7.35B, C and D summarize normalized STIM2.2, STIM1, and σ1R-V5 intensity across three independent experiments

(n=3) analyzed with one-way ANOVA using α of 0.05. Overexpression of σ1R-V5 significantly reduced STIM2.2 overexpression and endogenous STIM1 protein levels in comparison to the $WT^{VC}$ HEK293 cells, suggesting σ1R-V5 inhibits SOCE by reducing levels of both STIM proteins. However, there was no significant difference in overexpressed STIM2.2 and endogenous STIM1 protein levels following overexpression of siSTIM1 in $WT^{VC}$ and σ1R-V5 HEK293 cells. Considering that during Flexstation III experiments σ1R-V5 +STIM2.2+siSTIM1 HEK293 cells had significantly lower $Ca^{2+}$ influx in comparison to the $WT^{VC}$+STIM2.2+siSTIM1 cells, similar protein levels between these two groups indicate σ1R-V5 also inhibits STIM2.2-mediated SOCE through additional mechanism.

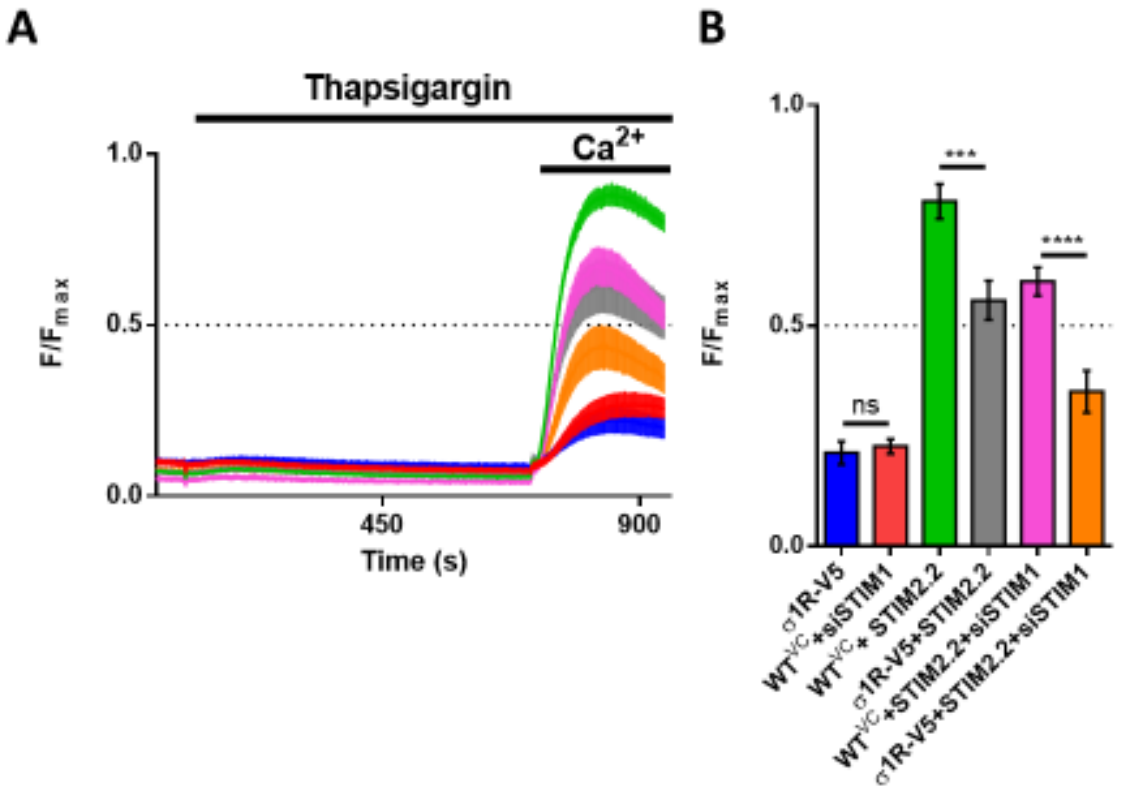


**Fig7.34 σ1R-V5 inhibits STIM2.2-mediated SOCE in HEK293 cells.** A) GcAMP6f traces during treatment by 1 μM thapsigargin followed by restoration of 2 mM extracellular $Ca^{2+}$ in HEK293 cells expressing σ1R-V5 (blue), $WT^{VC}$+siSTIM1 (red), $WT^{VC}$+STIM2.2 (green), σ1R-V5+STIM2.2 (grey), $WT^{VC}$+STIM2.2+siSTIM1 (pink), and σ1R-V5+STIM2.2+siSTIM1 (orange). B) Summary results showing SOCE from 18 biological replicates (N=18) across three independent experiments (n=3). A population of HEK293 cells within one well of 96W plate was used as a biological replicate (N) for statistical analysis. SOCE peaks were compared with one-way ANOVA. n.s., P>0.05; ***,P<0.001; ****, P<0.0001.

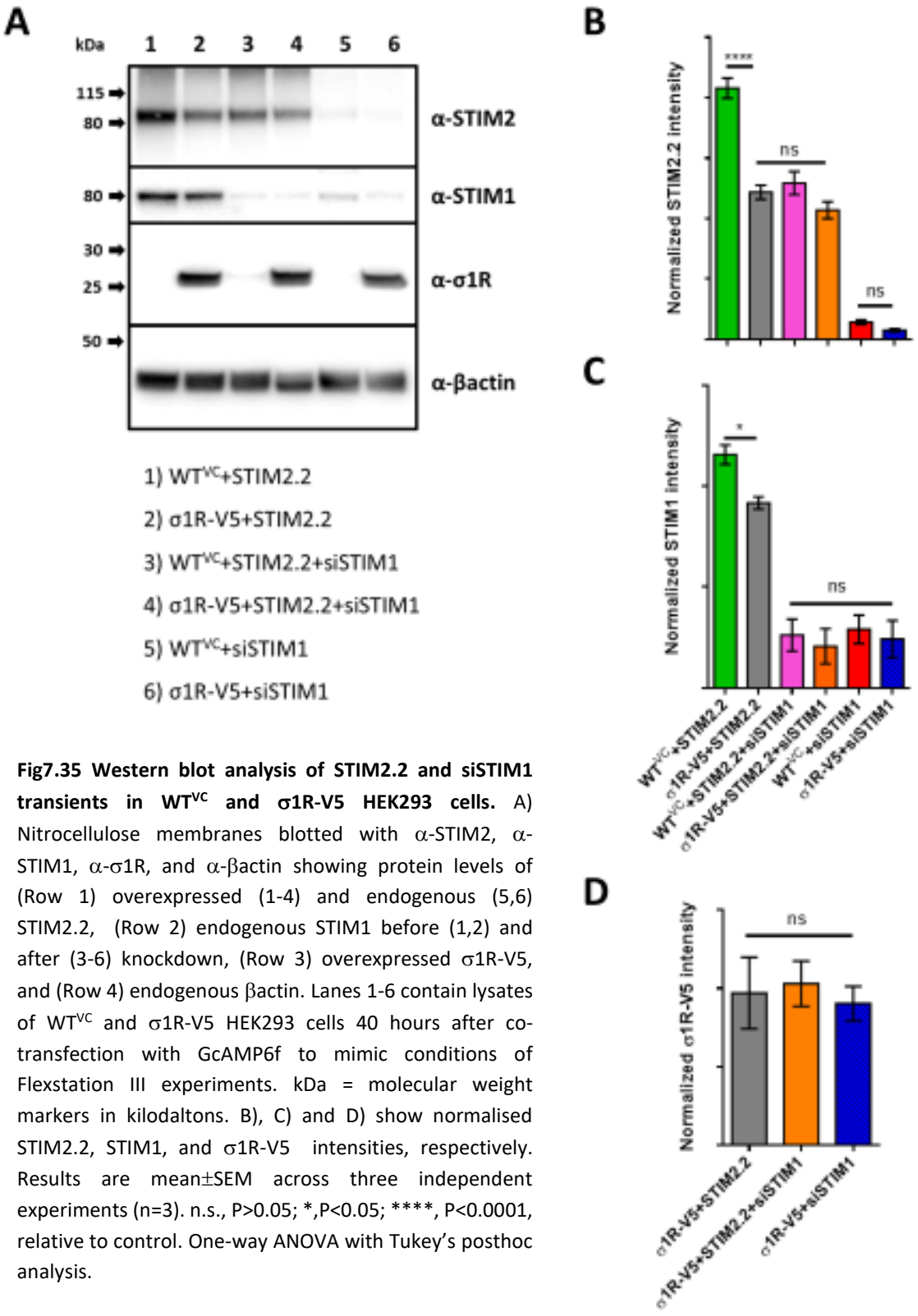


**Fig7.35 Western blot analysis of STIM2.2 and siSTIM1 transients in $WT^{VC}$ and σ1R-V5 HEK293 cells.** A) Nitrocellulose membranes blotted with α-STIM2, α-STIM1, α-σ1R, and α-βactin showing protein levels of (Row 1) overexpressed (1-4) and endogenous (5,6) STIM2.2, (Row 2) endogenous STIM1 before (1,2) and after (3-6) knockdown, (Row 3) overexpressed σ1R-V5, and (Row 4) endogenous βactin. Lanes 1-6 contain lysates of $WT^{VC}$ and σ1R-V5 HEK293 cells 40 hours after co-transfection with GcAMP6f to mimic conditions of Flexstation III experiments. kDa = molecular weight markers in kilodaltons. B), C) and D) show normalised STIM2.2, STIM1, and σ1R-V5 intensities, respectively. Results are mean±SEM across three independent experiments (n=3). n.s., P>0.05; *,P<0.05; ****, P<0.0001, relative to control. One-way ANOVA with Tukey's posthoc analysis.

| Group | Mean± SEM | N | (1) | (2) | (3) | (4) | (5) | (6) |
|---|---|---|---|---|---|---|---|---|
| (1) σ1R-V5 | 0.2118± 0.02616 | 18 | | n.s, P > 0.5 | ****, P < 0.0001 | ****, P < 0.0001 | ****, P < 0.0001 | n.s, P > 0.5 |
| (2) $WT^{VC}$+siSTIM1 | 0.2266± 0.01651 | 18 | | | ****, P < 0.0001 | ****, P < 0.0001 | ****, P < 0.0001 | n.s, P > 0.5 |
| (3) $WT^{VC}$+STIM2.2 | 0.7816± 0.03935 | 18 | | | | ***, P < 0.001 | **, P < 0.01 | ****, P < 0.0001 |
| (4) σ1R-V5+STIM2.2 | 0.6000± 0.03201 | 18 | | | | | n.s, P > 0.5 | ***, P < 0.001 |
| (5) $WT^{VC}$+STIM2.2 +siSTIM1 | 0.5571± 0.04415 | 18 | | | | | | ****, P < 0.0001 |
| (6) σ1R-V5+STIM2.2 + siSTIM1 | 0.3507± 0.04771 | 18 | | | | | | |

**Table 7.3-1 Summary of one-way ANOVA with Tukey posthoc analysis for the thapsigargin-evoked SOCE.** SOCE measurements (Peaks, Fig 7.34) were taken across three independent experiments (n=3). A population of HEK293 cells within one well of 96W plate was used as a biological replicate (N) for statistical analysis.

### 7.3.5 STIM1 mediates the majority of Tg-evoked, G-GECO1.2-Orai1 measured SOCE in HEK293 cells

Next I measured SOCE in single cells expressing G-GECO1.2-Orai1 using epifluorescence microscopy. Representative images are shown in Fig7.36 and the knockdown of STIM1 clearly inhibited the majority of the G-GECO1.2-Orai1-mediated $Ca^{2+}$ response. G-GECO1.2-Orai1$^{R91W}$ expressing cells were used as a negative control (Fig7.36, row 3). A summary of the results is shown in Fig 7.37. SOCE peaks from 18 biological replicates (N=18) across the three independent experiments (n=3) were analyzed using the Kruskal-Wallis and Dunn's multiple comparison tests with α of 0.05. Positionally-grouped ROIs were used as a one biological replicate. In cells transfected with siSTIM1 there was a >3-fold inhibition of the G-GECO1.2-Orai1-mediated SOCE. There was also a significant difference between the SOCE response for siSTIM1 expressing cells and the G-GECO1.2-Orai1$^{R91W}$ response, indicating that siSTIM1 did not abolish G-GECO1.2-Orai1-mediated SOCE. Altogether these results demonstrate that the majority of Tg-evoked SOCE in HEK293 cells is STIM1-mediated.

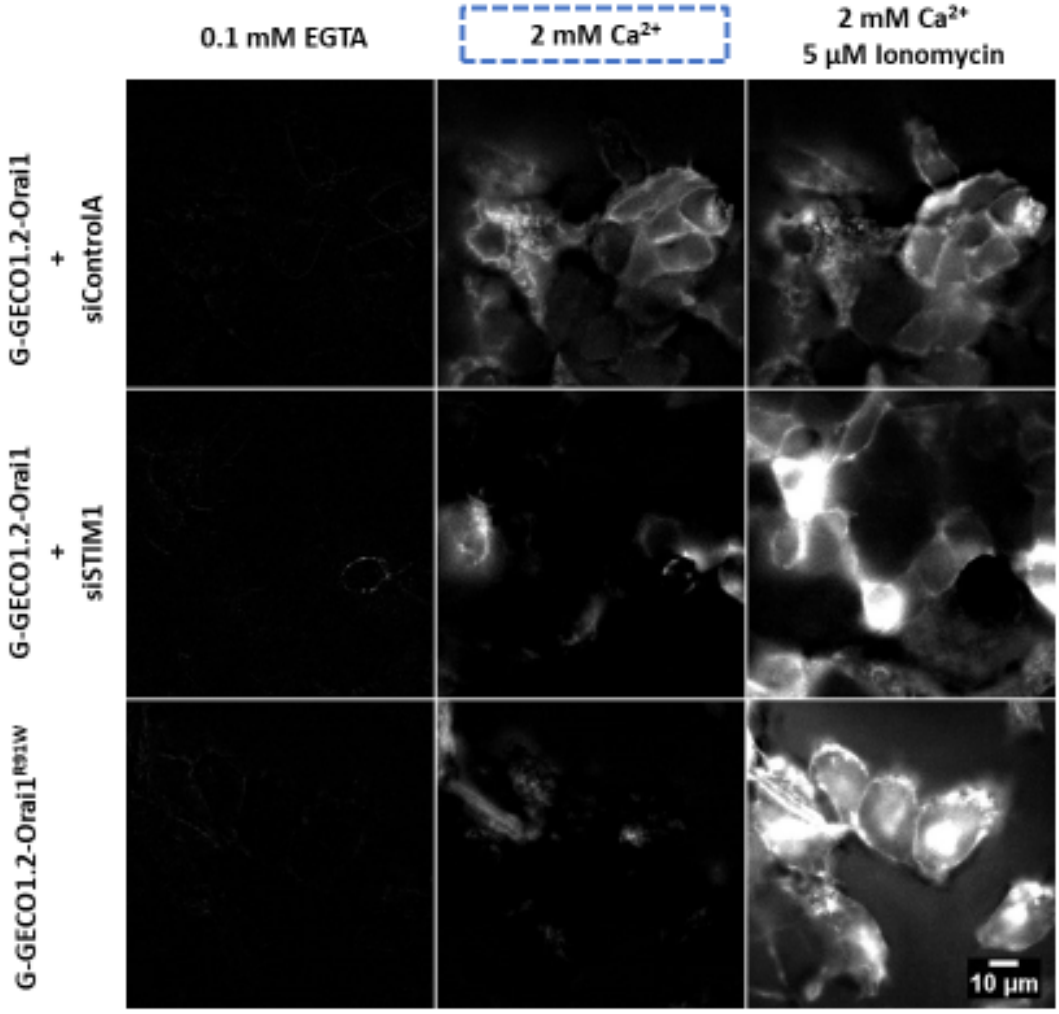


**Fig7.36 STIM1 knockdown reduced the majority of G-GECO1.2-Orai1-mediated SOCE.** Epifluorescent images of G-GECO1.2-Orai1 and G-GECO1.2-Orai1$^{R91W}$ HEK293 transients in 0.1 mM EGTA (pre-treatment; column 1), 2 mM $Ca^{2+}$ (post-treatment with 1 µM thapsigargin; column 2), and 2 mM $Ca^{2+}$ with 5 µM Ionomycin ( column 3) co-transfected with either siControlA (row 1) and siSTIM1 (row 2). Scale bar = 10 µM.

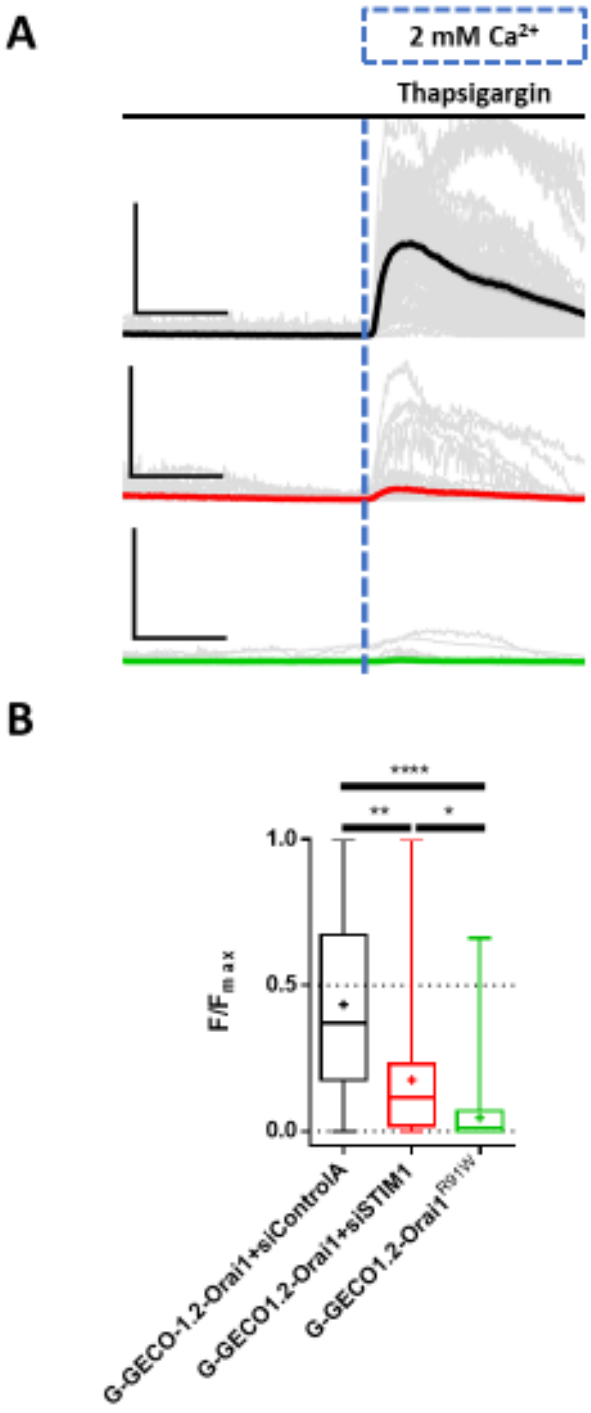


**Fig7.37 Quantification of G-GECO1.2-Orai1-mediated SOCE during STIM1 knockdown in HEK293 cells** A) Representative mean±SEM traces of G-GECO1.2-Orai1+siControlA (black), G-GECO1.2-Orai1+siSTIM1 (red), and G-GECO1.2-Orai1$^{R91W}$ during SOCE. Grey traces show individual measurements within the recordings. Blue dashed line indicates the addition of 2 mM $Ca^{2+}$ following store depletion. Scale bare = 50% $F/F_{max}$ (y-axis) and 100 s (x-axis). B) Box and whiskers plot of SOCE (peaks) values from 18 biological replicates (N=18) across three independent experiments (n=3) compared with Kruskal-Wallis test. Positionally-grouped ROIs were used as one biological replicate. *, P<0.05; **<0.01;****,P< 0.0001.

### 7.3.6 σ1R-V5 inhibits Tg-evoked STIM2.2-mediated $Ca^{2+}$ influx in SOCE microdomains

Having investigated the effects of σ1R on STIM2.2 mediated SOCE using the Flexstation III, which measures global $[Ca^{2+}]_{cyt}$, I moved to testing the effects of σ1R on STIM2.2-enriched SOCE microdomains using G-GECO1.2-Orai1 and STIM2.2-mCh and TIRFM. The overexpression of STIM2.1-mCh was used as a negative control. Fig 7.38 shows representative TIRFM images of HEK293 cells expressing (row 1) $WT^{VC}$ + G-GECO1.2-Orai1 + STIM2.2-mCh, (row 2) σ1R-V5 + G-GECO1.2-Orai1 + STIM2.2-mCh, and (row 3) $WT^{VC}$ + G-GECO1.2-Orai1 + STIM2.1-mCh. TIRFM images are shown at different time points throughout the experiment to show the baseline fluorescence (column 1), the SOCE response after 6-min treatment with 1 μM Thapsigargin (column 2) and the maximal response obtained using 5 μM ionomycin (column 3). When comparing the three experimental groups, the Tg-induced SOCE in STIM2.2-mCh enriched microdomains is visibly lower in cells expressing σ1R-V5 (row 2) compared to $WT^{VC}$ cells (row 1). SOCE detected in $WT^{VC}$ cells expressing STIM2.1-mCh was also significantly lower.

Fig7.39 summarizes the results of the TIRFM experiments. Statistical analysis of SOCE peaks from 36 biological replicates from (N=36) across three independent experiments (n=3) was performed using Kruskal-Wallis and Dunn's multiple comparison tests with α of 0.05. Tg-evoked SOCE within STIM2.2-mCh enriched microdomains of σ1R-V5 HEK293 cells was significantly reduced in comparison to SOCE in $WT^{VC}$ HEK293 cell, but not significantly different when compared to STIM2.1-mCh enriched SOCE microdomains in $WT^{VC}$ HEK293 cells. This result suggests that σ1R-V5 significantly reduces $Ca^{2+}$ influx within STIM2.2-enriched SOCE microdomains. Results of statistical analysis have been summarized in Table 7.32.

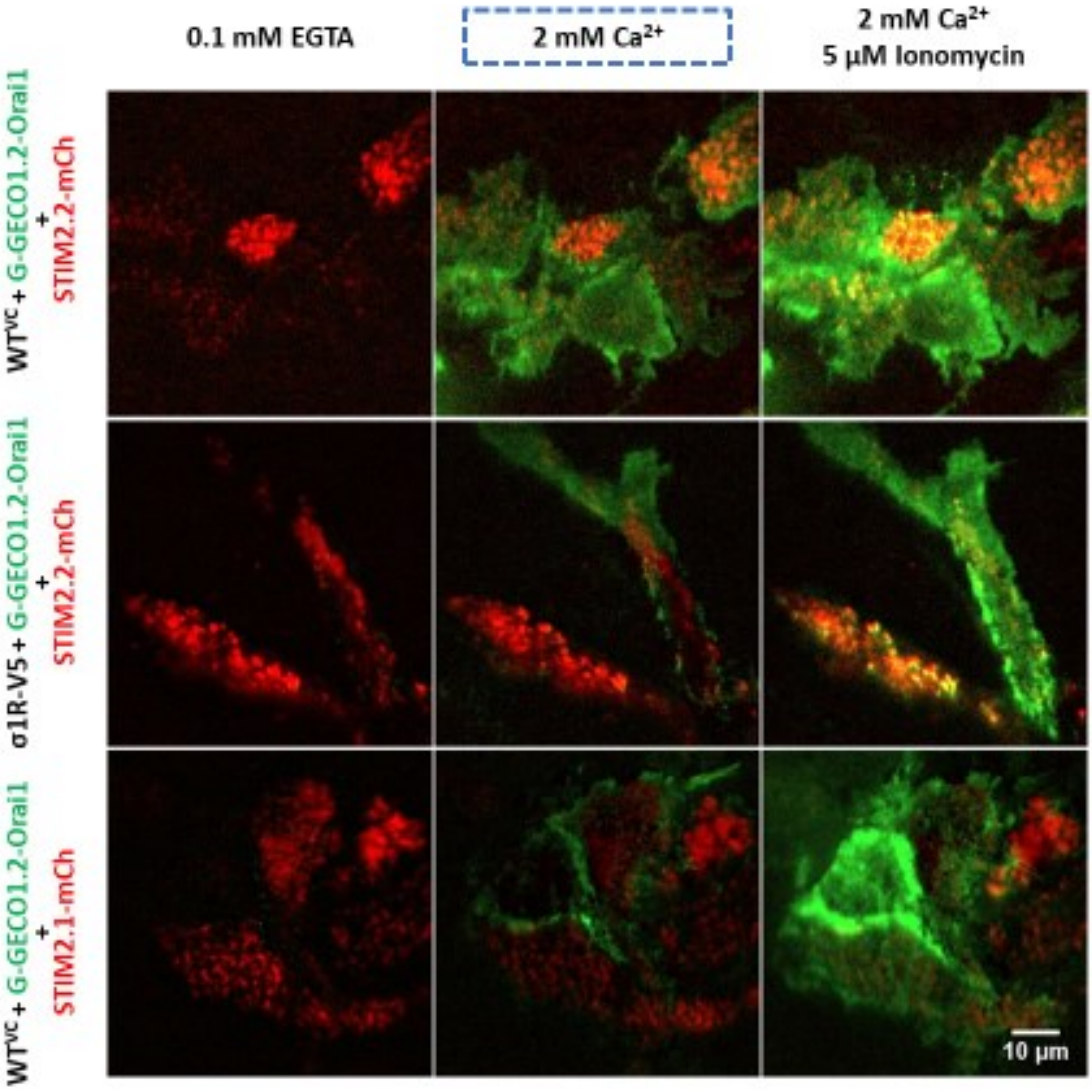


**Fig7.38 σ1R-V5 reduces Tg-evoked STIM2.2/Orai1-mediated SOCE in HEK293 cells.** TIRFM images of G-GECO1.2-Orai1-measured SOCE in HEK293 cells expressing (row 1 ) $WT^{VC}$+STIM2.2-mCh, (row 2) σ1R-V5+STIM2.2-mCh, and (row 3) $WT^{VC}$+STIM2.1-mCh in 0.1 mM EGTA (pre-treatment; column 1), 2 mM $Ca^{2+}$ (post-treatment with 1 μM thapsigargin; column 2), and 2 mM $Ca^{2+}$ with 5 μM Ionomycin (column 3). Scale bar = 10 μM.

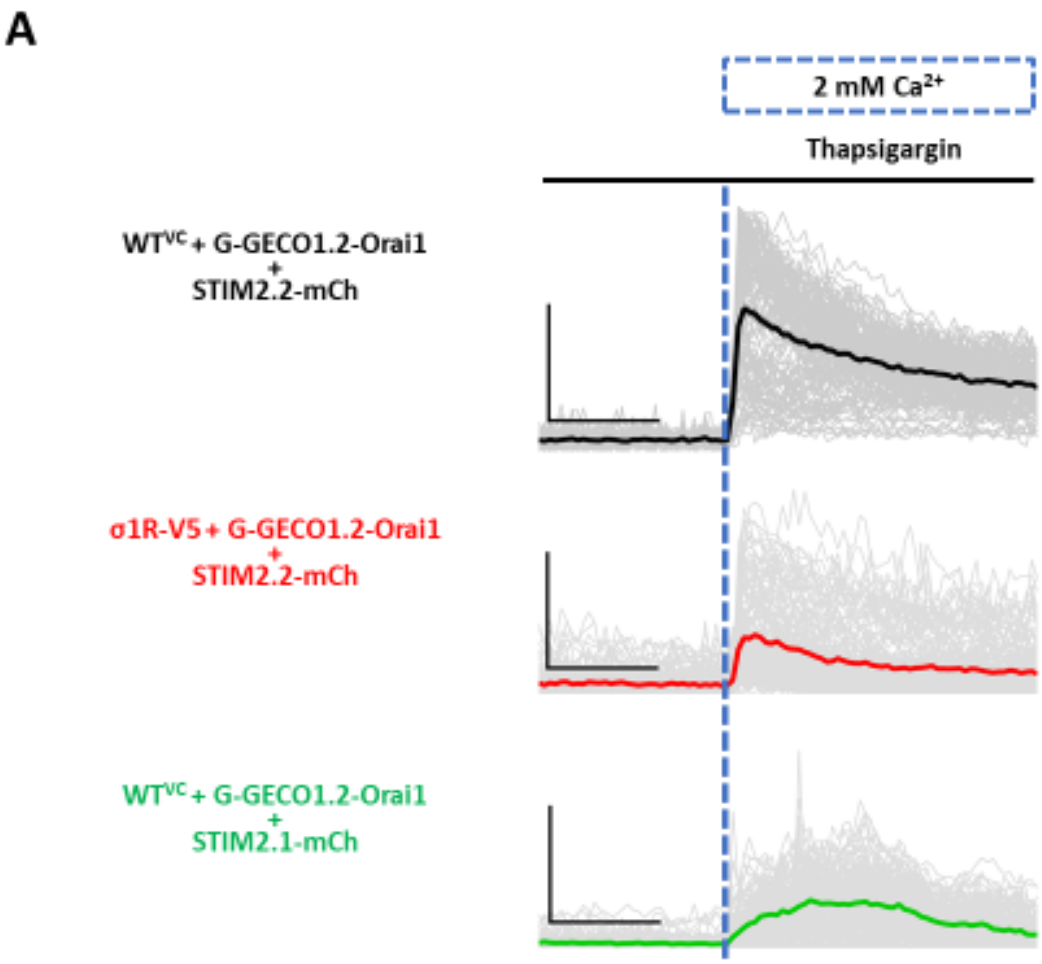


**Fig7.39 Quantification of Tg-evoked STIM2.2/Orai1-mediated SOCE in HEK293 cells** A) Representative G-GECO1.2-Orai1 mean±SEM traces of HEK293 cells expressing $WT^{VC}$+STIM2.2-mCh (black), σ1R-V5+STIM2.2-mCh (red), and $WT^{VC}$+STIM2.1-mCh (green) during SOCE. Grey traces show individual measurements within the recordings. Blue dashed line indicates the addition of 2 mM $Ca^{2+}$ following store depletion. Scale bare = 50% $F/F_{max}$ (y-axis) and 100 s (x-axis). B) Box and whiskers plot of SOCE (peaks) values from 36 biological replicates (N=36) across three independent experiments (n=3) compared with Kruskal-Wallis test. One biological replicate consists of positionally grouped ROIs. n.s., P>0.05;**, P<0.01; **<0.01;***,P< 0.001.

| Group | Median | Mean±SEM | N | Kruskal-Wallis summary σ1R-V5+G-GECO1.2-Orai1+STIM2.2-mCh | Kruskal-Wallis summary $WT^{VC}$+G-GECO1.2-Orai1+STIM2.1-mCh |
|---|---|---|---|---|---|
| $WT^{VC}$+G-GECO1.2-Orai1+STIM2.2-mCh | 0.4592 | 0.5080±0.03842 | 36 | ***, P < 0.001 | **, P < 0.01 |
| σ1R-V5+G-GECO1.2-Orai1+STIM2.2-mCh | 0.2669 | 0.2864±0.02659 | 36 | | n.s, P > 0.05 |
| $WT^{VC}$+G-GECO1.2-Orai1+STIM2.1-mCh | 0.2848 | 0.3356±0.03890 | 36 | | |

**Table 7.3-2 Summary of Kruskal-Wallis with Dunn's multiple comparison analysis for Tg-evoked $Ca^{2+}$ influx in STIM2-enriched SOCE microdomains.** SOCE measurements (Peaks, Fig 7.39) were taken from 36 biological replicates (N=36) across three independent experiments (n=3). Positionally-grouped ROIs were used as a biological replicate (N) for statistical analysis.

### 7.3.7

### 7.3.8 σ1R-V5 fails to inhibit EGTA-evoked SOCE in STIM2.2-enriched microdomains of HEK293 cells

STIM2 is proposed to regulate basal SOCE[98] and the PLA results shown in the previous chapter provide evidence for a STIM2/σ1R interaction *in situ* under basal conditions. Therefore, I tested whether σ1Rs functionally inhibits SOCE in STIM2.2-mCh enriched microdomains when ER $Ca^{2+}$ stores are not severely depleted by thapsigargin (Tg) treatment but instead are incubated in a $Ca^{2+}$ free HBSS containing 0.1 mM EGTA to produce a more modest reduction in ER [$Ca^{2+}$].Fig7.310 shows representative TIRFM images of HEK293 cells expressing (row 1) $WT^{VC}$ + G-GECO1.2-Orai1 + STIM2.2-mCh, (row 2) σ1R-V5 + G-GECO1.2-Orai1 + STIM2.2-mCh, (row 3) $WT^{VC}$ + G-GECO1.2-Orai1 + STIM2.1-mCh, and (row 4) $WT^{VC}$ + G-GECO1.2-$Orai1^{R91W}$ + STIM2.2-mCh. The G-GECO1.2-$Orai1^{R91W}$ construct was included as a negative control to ensure that measured changes in fluorescence within the SOCE microdomains correspond to $Ca^{2+}$ influx through the Orai1 channel.

Statistical analysis of SOCE peaks from 24-54 biological replicates (N=24-54, Table 7.33) across three independent experiments (n=3) was performed using Kruskal-Wallis and Dunn's multiple comparison tests with α of 0.05. Following treatment with 0.1 mM EGTA, there was no significant difference in the SOCE response measured within STIM2.2-mCh-enriched SOCE microdomains of $WT^{VC}$ and σ1R-V5 HEK293 cells. This result suggests that the inhibitory effect of σ1R on STIM2.2-mediated SOCE requires a large depletion of $[Ca^{2+}]_{ER}$. The significantly reduced SOCE response in $WT^{VC}$ HEK293 cells co-expressing either STIM2.1-mCh with G-GECO1.2-Orai1, or mutant G-GECO1.2-$Orai1^{R91W}$ with STIM2.2-mCh were as expected and provide evidence that the responses are mediated by

the G-GECO1.2-Orai1 channel. The results of the statistical analysis are summarized in Fig 7.311 and Table 7.33.

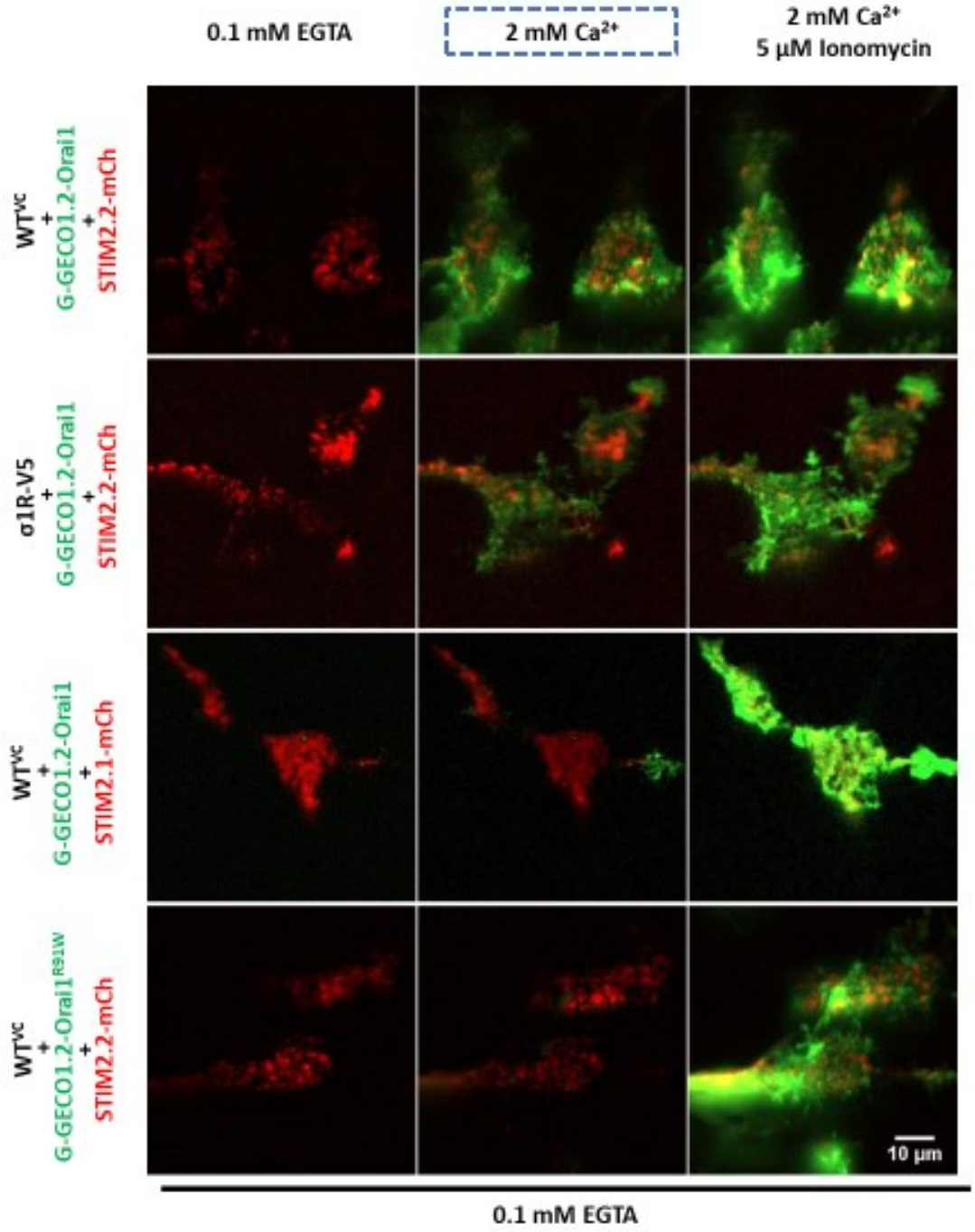


**Fig7.310 σ1R-V5 fails to inhibit EGTA-evoked STIM2.2/Orai1-mediated SOCE in HEK293 cells.** TIRFM images of G-GECO1.2-Orai1-measured SOCE in HEK293 cells expressing (row 1 ) $WT^{VC}$+STIM2.2-mCh, (row 2) σ1R-V5+STIM2.2-mCh, and (row 3) $WT^{VC}$+STIM2.1-mCh, and G-GECO1.2-$Orai1^{R91W}$-measured SOCE in HEK293 cells expressing (row 4) $WT^{VC}$+STIM2.2-mCh. Images shows cells in 0.1 mM EGTA (pre-treatment; column 1), 2 mM $Ca^{2+}$ (post-treatment with 1 µM thapsigargin; column 2), and 2 mM $Ca^{2+}$ with 5 µM Ionomycin (column 3). Scale bar = 10 µM.

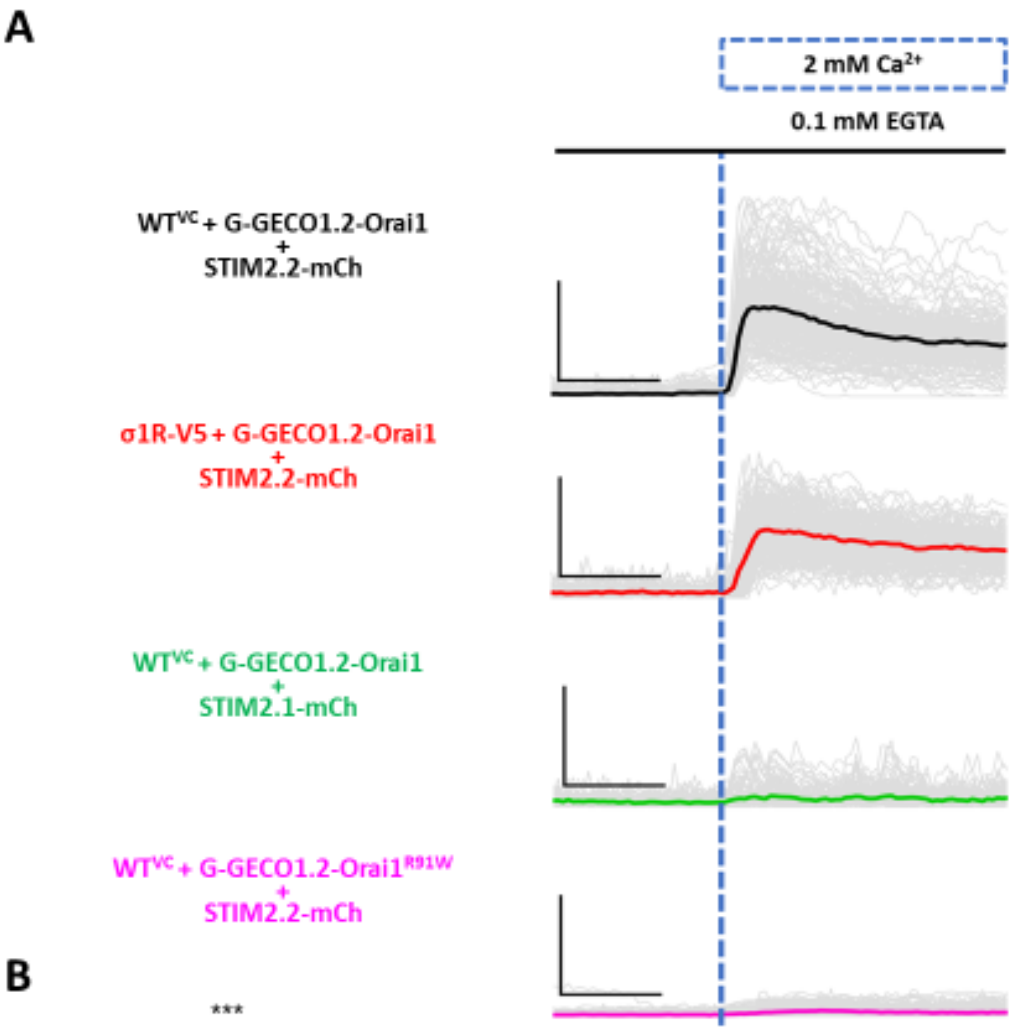


**Fig7.311 Quantification of EGTA-evoked STIM2.2/Orai1-mediated SOCE in HEK293 cells** A) Representative G-GECO1.2-Orai1 mean±SEM traces of HEK293 cells expressing $WT^{VC}$+STIM2.2-mCh (black), σ1R-V5+STIM2.2-mCh (red), and $WT^{VC}$+STIM2.1-mCh (green) during SOCE. G-GECO1.2-$Orai1^{R91W}$ mean±SEM traces of HEK293 cells expressing $WT^{VC}$+STIM2.2-mCh (pink).Grey traces show individual measurements within the recordings. Blue dashed line indicates the addition of 2 mM $Ca^{2+}$ following store depletion. Scale bare = 50% $F/F_{max}$ (y-axis) and 100 s (x-axis). B) Box and whiskers plot of SOCE (peaks) values from 24-54 biological replicates (N=24-54) across three independent experiments (n=3) compared with Kruskal-Wallis test. One biological replicate consists of positionally grouped ROIs. n.s., P>0.05;**, P<0.01; **<0.01;***,P< 0.001.

| Group | Median | Mean± SEM | N | Kruskal-Wallis summary σ1R-V5+G-GECO1.2-Orai1+STIM2.2-mCh | Kruskal-Wallis summary $WT^{VC}$+G-GECO1.2-Orai1+STIM2.1-mCh | Kruskal-Wallis summary $WT^{VC}$+G-GECO1.2-$Orai1^{R91W}$+STIM2.2-mCh |
|---|---|---|---|---|---|---|
| $WT^{VC}$+G-GECO1.2-Orai1+STIM2.2-mCh | 0.3264 | 0.4047± 0.03204 | 54 | n.s, P > 0.5 | ***, P < 0.001 | ****, P < 0.0001 |
| σ1R-V5+G-GECO1.2-Orai1+STIM2.2-mCh | 0.4289 | 0.4493± 0.02969 | 54 | | ****, P < 0.0001 | ****, P < 0.0001 |
| $WT^{VC}$+G-GECO1.2-Orai1+STIM2.1-mCh | 0.1201 | 0.1703± 0.02966 | 24 | | | n.s, P > 0.5 |
| $WT^{VC}$+G-GECO1.2-$Orai1^{R91W}$+STIM2.2-mCh | 0.1163 | 0.1413± 0.01947 | 36 | | | |

**Table 7.3-3 Summary of Kruskal-Wallis with Dunn's multiple comparison tests for EGTA-evoked $Ca^{2+}$ influx in STIM2-enriched SOCE microdomains.** SOCE measurements (Peaks, Fig 7.311) were taken from 24-54 biological replicates (N=24-54) across three independent experiments (n=3). Positionally-grouped ROIs were used as a biological replicate (N) for statistical analysis.

## 7.4 Discussion

### 7.4.1 σ1R inhibits STIM2.2/Orai1 mediated SOCE after profound store-depletion

After demonstrating that σ1R can interact with both STIM homologs in Chapter VI, in Chapter VII I have demonstrated that enhanced expression of σ1R can also inhibit thapsigargin-evoked STIM2.2/Orai1-mediated SOCE. During measurements of $[Ca^{2+}]_{cyt}$ in the population of HEK293 cells using GCaMP6f, σ1R inhibited (1) STIM2.2-potentiated SOCE, and (2) STIM2.2-potentiated SOCE during STIM1 knockdown. σ1R also inhibited STIM2.2-potentiated SOCE when measured by G-GECO1.2-Orai1 in STIM2.2 enriched microdomains (Fig 7.38-9). SOCE was also detected by G-GECO1.2-Orai1 in STIM2.2 enriched microdomains during basal conditions (Fig. 7.310-11). To confirm that these measurements of $Ca^{2+}$ influx truly correspond to the measurements of SOCE at ER-PM junctions, additional controls were run using negative regulator of SOCE, STIM2 splice variant STIM2.1, and dominant-negative mutant G-GECO1.2-Orai1$^{R91W}$. Similar levels of $Ca^{2+}$ influx were detected under both conditions, supporting initial hypothesis that small changes in ER $[Ca^{2+}]$ are sufficient to evoke STIM2.2/Orai1 mediated SOCE. However, enhanced expression of σ1R failed to inhibit STIM2.2-mediated SOCE during basal conditions (Fig. 7.310-11)

The inhibition of STIM2.2-potentiated SOCE by σ1R in the population of HEK293 cells can simply be explained as a result of reduced levels of STIM2.2 proteins that were detected by western blot analysis in the presence of σ1R ( Fig 7.35). However, potentiation of SOCE that occurs during STIM1 knockdown by overexpressing STIM2.2 (Fig 7.33) suggests that STIM2.2 can rescue Tg-evoked SOCE in the absence of STIM1 proteins, and σ1R exerted same inhibitory effect under those conditions (Fig. 7.34). In broader context,

during the overexpression of σ1R, thapsigargin treatment can also potentiate STIM2/ σ1R interaction, as observed in previous chapter. Altogether, these results suggest more than one underlying mechanism by which σ1R exerts its inhibitory effect on SOCE. Importantly, these results also demonstrate that σ1R can interact with STIM2.2 (Chapter VI) and modulate STIM2.2-mediated SOCE (Chapter VII). Recently, STIM2.2-mediated nSOCE came into focus during investigations of its role during pathologies of CNS. Several studies have shown that the downregulation of STIM2, but not STIM1, decreased apoptosis and improved neuronal survival, by reducing ER [$Ca^{2+}$] release and $Ca^{2+}$ overload[205]. Here, I have demonstrated that σ1R inhibits G-GECO1.2-Orai1-measured SOCE in STIM2.2 enriched microdomains only during profound store-depletion using thapsigargin. During the basal activation of STIM2.2/Orai1-mediated SOCE using only 0.1 mM EGTA, similar results were observed in both presence and absence of σ1R. These results suggest that the modulation of STIM2.2-mediated SOCE by σ1R could also be part of its neuroprotective role.

# 8 Conclusion

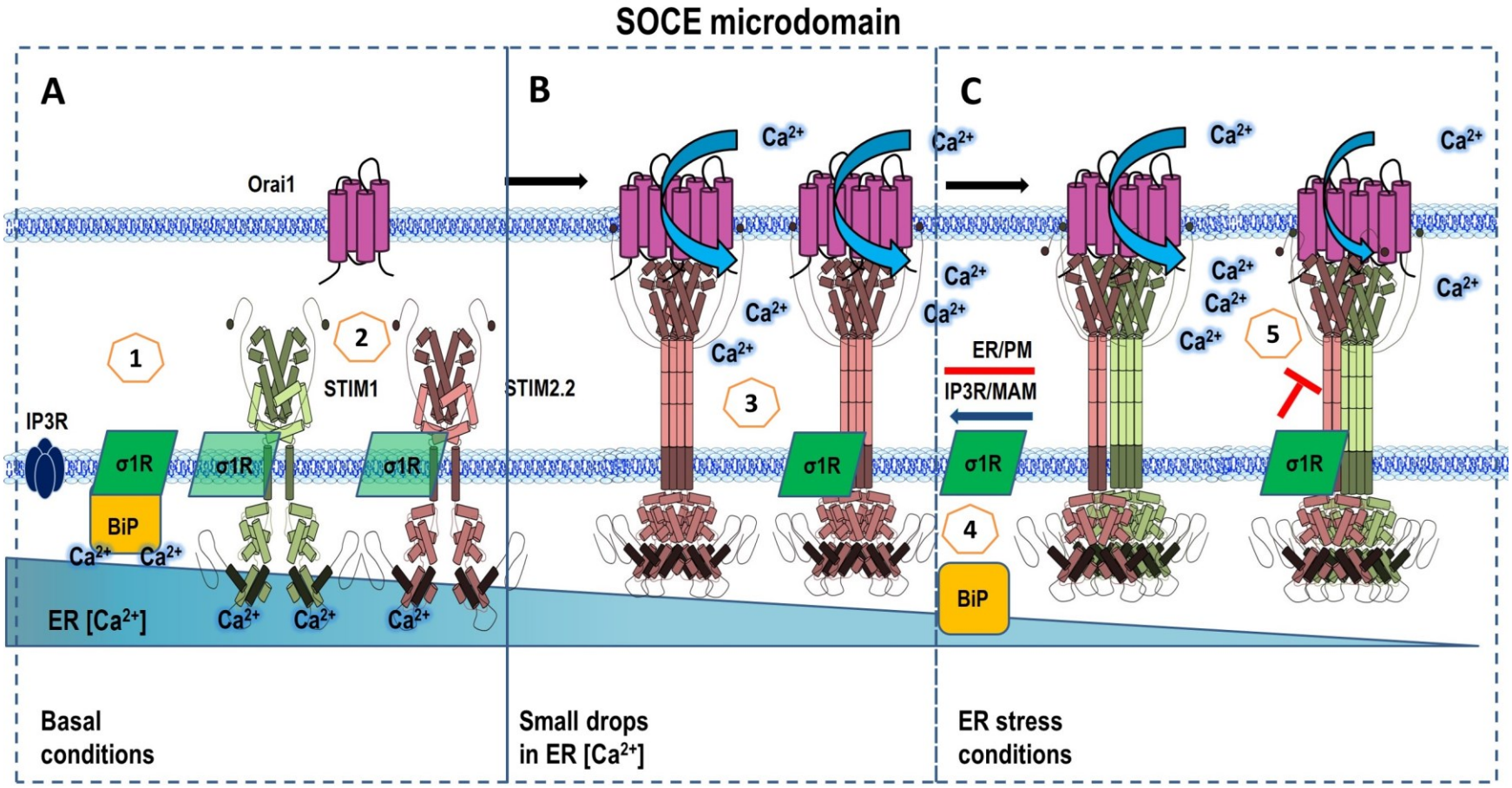


**Figure 8.1 The proposed mechanism of σ1R in SOCE microdomain as explained in Section 8.12 of this chapter.**

### 8.1.1 σ1R inhibits STIM1/Orai1- and STIM2.2/Orai1-mediated SOCE under ER stress conditions

Tight and precise regulation of SOCE is crucial for numerous cellular processes, such as the replenishment of intracellular $Ca^{2+}$ in non-excitable cells, or the maintenance of $Ca^{2+}$ homeostasis in excitable cells[115,139]. σ1R is a neuroprotective ER chaperone with established therapeutic potential that has been proposed as a functional regulator of Orai1-mediated SOCE[14,34]. However, σ1R has been reported to inhibit, promote, and even potentiate SOCE in different cell lines requiring further investigation[14,34,158,159]

In this doctoral work, the role of the σ1R in the regulation of SOCE has been investigated using measurements of changes in $[Ca^{2+}]_{cyt}$ in the population of cells, but also at the point of $Ca^{2+}$ entry – SOCE microdomains. In both experimental conditions, the enhanced expression of σ1R inhibited SOCE under ER stress conditions, as it was previously reported by Srivats et al[34]. However, the experimental evidence collected within this work suggests more subtle and organised inhibitory effect than previously reported.

The comparison of SOCE frequencies at ER-PM junctions revealed that enhanced expression of σ1R in HEK293 cells results in a tighter control of G-GECO1.2-Orai1-measured $Ca^{2+}$influx when compared to $WT^{VC}$ HEK293 cells. This effect was confirmed by overexpression of mKate-tagged σ1R construct compared to the reported loss-of-function mKate-tagged mutant $σ1R^{E102Q}$ where expression of E102Q mutant resulted in increased number of highly potentiated G-GECO1.2-Orai1 puncta. These results suggest that σ1R possesses mechanism to reduce, rather than to completely diminish SOCE, and exerts it within SOCE microdomains during ER stress conditions. This underlying mechanism of SOCE modulation by σ1R is independent of σ1R's interactive partner IP3R, and of efflux of intracellular $K^+$, which was observed in colorectal and breast cancer cells[14].

Under basal conditions, σ1R was shown to interact with both STIM1 and STIM2.2 proteins. The frequency of STIM/σ1R interaction *in situ* has been promoted by enhanced expression of σ1R, suggesting that the effect of σ1R may depend on its availability as interactive partner. Recent reports suggest that the downregulation of STIM2, but not STIM1, decreased apoptosis and improved neuronal survival by reducing ER [$Ca^{2+}$] release and $Ca^{2+}$ overload[205]. PLA analysis of STIM1-σ1R and STIM2-σ1R interactions in HeLa cells showed that during limited expression σ1R, profound store-depletion increases STIM1--σ1R interaction while decreasing STIM2-σ1R, suggesting that the availability of σ1R as interactive partner may be essential in the regulation of STIM1-mediated and STIM2-mediated SOCE. Contrary to previously proposed model of STIM1-Orai1- σ1R, enhanced expression of σ1R increased STIM2/Orai1 interaction. The greatest increase was observed during basal conditions and it was reduced by profound store-depletion. These results suggest that the reduction in STIM2 interaction with endogenous σ1R post-thapsigargin treatment could be related to the enhanced binding of STIM1 to both proteins under these conditions. These results also show that in addition to STIM1, σ1R can also interact with STIM2.

σ1R is widely expressed in CNS where it exhibits neuroprotective properties[12]. σ1R confers a neuroprotective role in pre-clinical models of neurodegenerative disorders, but the mechanisms by which σ1R exhibits its neuroprotective role remain elusive. The results of this doctoral work show that σ1R can counter STIM2.2-mediated SOCE during profound ER [$Ca^{2+}$] release (ER stress conditions), indicating that its ability to modulate STIM2.2/Orai1-mediated SOCE could be part of the mechanism underlying its neuroprotective ability.

### 8.1.2 The proposed mechanism of σ1R in SOCE microdomain

On the base of the previous studies[14,22,34,116,139] and our findings, we propose a model (Fig8.1) where σ1R modulates Orai1 channel function in STIM-dependent manner:

A) Basal conditions:

1. At rest, σ1R is associated with well-characterized intraluminal chaperone BiP that binds luminal $Ca^{2+}$.
2. During same conditions, σ1R also interacts with STIM1 and STIM2.2. proteins. However, the STIM/σ1R interaction may be limited by the availability of σ1R as an interactive partner.

B) Small drops in ER [$Ca^{2+}$]:

3. As the interactive partner of STIM proteins, σ1R has ability to translocate to ER-PM junctions in STIM-dependent manner. As the interactive partner of STIM2.2, σ1R can translocate to ER-PM junctions where it co-localises with STIM2.2. The evidence suggests that enhanced expression of σ1R may promote STIM2.2/Orai1 interaction. However, no inhibitory effect of the σ1R was detected during STIM2.2/Orai1-mediated SOCE under these conditions.

C) ER stress conditions:

4. The switch from “inactive mode” (σ1R is bound to BiP) to “active mode” of σ1R (σ1R dissociates from BiP) is conditioned by the levels of luminal $Ca^{2+}$. Following severe drop in ER [$Ca^{2+}$], σ1R dissociates from BiP and it is available for interaction with other proteins, such as IP3Rs at MAMs or STIM proteins at ER-PM junctions.

5. As the interactive partner of STIM proteins, the σ1R has ability to translocate to ER-PM junctions in STIM-dependent manner. Hence, σ1R's ability to modulate SOCE will be conditioned by the levels of luminal $Ca^{2+}$, and the $Ca^{2+}$ affinity of STIM homologs. As part of SOCE microdomain complex, σ1R inhibits Orai1-mediated $Ca^{2+}$ influx.

There are several additional mechanisms to explain how the σ1R inhibits $Ca^{2+}$ influx as a part of SOCE microdomain complex. Based on our results, it is possible that, by binding to STIM proteins, σ1R restricts the stoichiometry of STIM/Orai interaction preventing maximum activation of SOCE. Current evidence suggests that Orai1 channel is a hexameric structure requiring two STIM proteins per Orai1 unit to achieve maximum activation and $Ca^{2+}$ influx[126]. While binding to STIM proteins, σ1R possibly restricts their ability to form compact and sizable homo- or heterooligomers that would ensure the most efficient activation of Orai1 channel or perhaps, the most efficient crosslinking of Orai1 clusters. For example, inhibitory splice variant of STIM2, STIM2.1, inhibits $Ca^{2+}$ influx by reducing STIM1's ability to crosslink multiple Orai1 clusters once part of STIM1/STIM2.1 heterooligomer[117].

σ1R's restriction of STIM/Orai stoichiometry would also explain no significant reduction of STIM2.2/Orai1-mediated SOCE induced by small changes in ER [$Ca^{2+}$]. The comparison of STIM1 and STIM2 respective EF-SAM domains identified functionally relevant differences in the stability of two homologues. In comparison to STIM2, STIM1 possesses lower SAM stability and less robust EF-SAM interface. Hence, STIM1 exhibits increased kinetics of oligomerisation compared to STIM2[106,108]. The increased stability of STIM2 EF-SAM domain decreases protein's propensity for oligomerisation. Hence, during small changes in ER [$Ca^{2+}$], STIM2.2 most likely activates basal SOCE at less efficient stoichiometry, diminishing the effect of σ1R as its interactive partner.

It is possible that σ1R modulates SOCE using similar mechanism as SARAF. Following SOCE activation, global increases in [$Ca^{2+}$] activate SCDI that then occurs gradually in tens of seconds. SCDI is reported to be regulated by various proteins, including SARAF, caveolin, E-syt1, septin4, and PI(4,5)P2[130,131]. To regulate SCDI, SARAF has to interact with STIM1 interaction and STIM1-Orai1 complex has to form within microdomain[206]. Upon $Ca^{2+}$ store depletion, SARAF replaces STIM1, as its interactive partner, for the C-terminal region of Orai1. Following the raise in cytosolic $Ca^{2+}$, SARAF dissociates from Orai1 to re-interact with STIM1[206]. This re-association of SARAF and STIM1 possibly promotes inactivation of SOCE microdomain complex, aiding SCDI.

### 8.1.3 Future directions

In this doctoral work, we have shown that σ1R inhibits STIM1/Orai1- and STIM2.2/Orai1-mediated SOCE during ER stress conditions. The evidence that σ1R acts as a STIM interactive partner *in situ* was obtained mostly using PLA-approach that relies on the binding specificity of antibodies and oligonucleotides used in the process. Antibodies targeting Orai1, STIM1, STIM2 and σ1R were chosen based on the reported location of their epitopes and the specificity shown during Western blot and immunostaining analyses. Using manufacturer information, all epitopes were predicted to be cytosolic. Cytosolic epitope of σ1R was targeted based on the novel structure of σ1R that positions the majority of protein outside ER[28].

Undertaken PLA analysis verified earlier study that reported STIM1/Orai1 and STIM1/σ1R interactions using co-immunoprecipitation approach and targeting of HA-, myc- and FLAG-tagged proteins[34]. However, PLA results reporting STIM2/Orai1 and STIM2/ σ1R interactions within this thesis identify STIM2 as a new interactive partner of σ1R and require further investigation. The limitation of PLA approach lies in the specificity of the primary

antibody that influences proper data interpretation. Unspecific, off-target effects could yield false-positive interaction. Hence, the work performed in this thesis cannot fully exclude off-target effects of α-STIM2, especially considering high sequence similarity of two STIM homologs. To verify STIM2/σ1R interaction, we propose creating recombinant STIM2 and σ1R proteins that will allow us to perform co-immunoprecipitation studies and more specific targeting using tag-antibodies. Additionally, this approach can be combined with introduction of different mutations to the sequence of STIM proteins, as well as C-terminal truncation of STIM proteins via PCR. This additional approach will allow us to identify domain(s) involved in STIM/ σ1R interactions.

The measurements of SOCE via G-GECO1.2-Orai1 allows optical recording of changes in cytosolic [$Ca^{2+}$] 8nm below channel pore. This spatial restriction of optical recording, as well as the expression of dominant negative G-GECO1.2-Orai1$^{R91W}$, can be advantage when studying neuronal SOCE using research models where voltage-gated $Ca^{2+}$ channels and glutamate receptor channels dominate $Ca^{2+}$ signalling. One such a model are cultured hippocampal neurons from WT and STIM2−/− mice where STIM2 (but not STIM1) was found essential for intracellular $Ca^{2+}$ accumulation during cerebral ischemia[114]. In hippocampal neurons from STIM2-/- mice, the absence of STIM2 decreased $Ca^{2+}$ overload during an ischemic challenge[114]. To investigate whether STIM2.2/ σ1R interaction underlies neuroprotective role of σ1R, we propose using the same model and translating the approach demonstrated throughout this thesis. This would allow us to test whether enhanced expression of σ1R counteracts STIM2.2-mediated $Ca^{2+}$ overload during an ischemic challenge. Additionally, we could determine the contribution of Orai1-mediated $Ca^{2+}$ influx to the development of cerebral ischemia.

# 9 References


1. Martin, W. R., Eades, C. G., Thompson, J. A., Huppler, R. E. & Gilbert, P. E. The effects of morphine- and nalorphine- like drugs in the nondependent and morphine-dependent chronic spinal dog. *J. Pharmacol. Exp. Ther.* **197**, 517–532 (1976).

2. Chu, U. B., Ramachandran, S., Hajipour, A. R. & Ruoho, A. E. Photoaffinity labeling of the sigma-1 receptor with N-[3-(4-nitrophenyl)propyl]-N-dodecylamine: evidence of receptor dimers. *Biochemistry* **52**, 859–868 (2013).

3. Khazan N, Young GA, El-Fakany EE, Hong O, Calligaro D. Sigma receptors mediated the psychotomimetic effects of N-allylnormetazocine (SKF-10,047), but not its opioid agonistic-antagonistic properties. Neuropharmacology. 1984 Aug;23(8):983-7. PubMed PMID: 6090969. *Neuropharmacology* **8**, 983–7 (1984).

4. Su, T. P. Evidence for sigma opioid receptor: binding of [3H]SKF-10047 to etorphine-inaccessible sites in guinea-pig brain. *J. Pharmacol. Exp. Ther.* **223**, 284–290 (1982).

5. Tam, S. W. (+)-[3H]SKF 10,047, (+)-[3H]ethylketocyclazocine, mu, kappa, delta and phencyclidine binding sites in guinea pig brain membranes. *Eur. J. Pharmacol.* **109**, 33–41 (1985).

6. Hellewell, S. B. & Bowen, W. D. A sigma-like binding site in rat pheochromocytoma (PC12) cells: decreased affinity for (+)-benzomorphans and lower molecular weight suggest a different sigma receptor form from that of guinea pig brain. *Brain Res.* **527**, 244–253 (1990).

7. Hanner, M. *et al.* Purification, molecular cloning, and expression of the mammalian sigma1-binding site. *Proc. Natl. Acad. Sci. U. S. A.* **93**, 8072–8077 (1996).

8. Hellewell, S. B. *et al.* Rat liver and kidney contain high densities of sigma 1 and sigma 2 receptors: characterization by ligand binding and photoaffinity labeling. *Eur. J. Pharmacol.* **268**, 9–18 (1994).

9. Kekuda, R., Prasad, P. D., Fei, Y. J., Leibach, F. H. & Ganapathy, V. Cloning and functional expression of the human type 1 sigma receptor (hSigmaR1). *Biochem. Biophys. Res. Commun.* **229**, 553–558 (1996).

10. Mei, J. & Pasternak, G. W. Molecular cloning and pharmacological characterization of the rat sigma1 receptor. *Biochem. Pharmacol.* **62**, 349–355 (2001).

11. Alon, A. *et al.* Identification of the gene that codes for the σ2 receptor. *Proc. Natl. Acad. Sci. U. S. A.* **114**, 7160–7165 (2017).

12. Rousseaux, C. G. & Greene, S. F. Sigma receptors [σRs]: biology in normal and diseased states. *J. Recept. Signal Transduct.* **36**, 327–388 (2016).

13. Wang, B. *et al.* Expression of sigma 1 receptor in human breast cancer. *Breast Cancer Res. Treat.* **87**, 205–214 (2004).

14. Gueguinou, M. *et al.* The SigmaR1 chaperone drives breast and colorectal cancer cell migration by tuning SK3-dependent Ca2+ homeostasis. *Oncogene* **36**, 3640–3647 (2017).

15. Chantome, A. *et al.* Pivotal Role of the Lipid Raft SK3-Orai1 Complex in Human Cancer Cell Migration and Bone Metastases. *Cancer Res.* **73**, 4852–4861 (2013).

16. Yang, S. The store-operated calcium channels in cancer metastasis from cell migration invasion to metastatic colonization. *Front. Biosci.* **23**, 1241–1256 (2018).

17. Cobos, E. J., Entrena, J. M., Nieto, F. R., Cendán, C. M. & Del Pozo, E. Pharmacology and therapeutic potential of sigma(1) receptor ligands. *Curr. Neuropharmacol.* **6**, 344–366 (2008).

18. Skuza, G. Potential antidepressant activity of sigma ligands. *Pol. J. Pharmacol.* **55**, 923–934 (2003).

19. Nguyen, L., Lucke-Wold, B. P., Mookerjee, S., Kaushal, N. & Matsumoto, R. R. Sigma-1 Receptors and Neurodegenerative Diseases: Towards a Hypothesis of Sigma-1 Receptors as Amplifiers of Neurodegeneration and Neuroprotection. *Adv. Exp. Med. Biol.* **964**, 133–152 (2017).

20. Alonso, G. *et al.* Immunocytochemical localization of the sigma(1) receptor in the adult rat central nervous system. *Neuroscience* **97**, 155–170 (2000).

21. Wu, Y. *et al.* Contacts between the endoplasmic reticulum and other membranes in neurons. *Proc. Natl. Acad. Sci. U. S. A.* **114**, E4859–E4867 (2017).

22. Hayashi, T. & Su, T.-P. Sigma-1 Receptor Chaperones at the ER- Mitochondrion Interface Regulate Ca2+ Signaling and Cell Survival. *Cell* **131**, 596–610 (2007).

23. Hayashi, T. & Su, T.-P. Cholesterol at the endoplasmic reticulum: roles of the sigma-1 receptor chaperone and implications thereof in human diseases. *Subcell. Biochem.* **51**, 381–398 (2010).

24. Csordás, G. *et al.* Structural and functional features and significance of the physical linkage between ER and mitochondria. *J. Cell Biol.* **174**, 915–921 (2006).

25. Hayashi, T. & Su, T.-P. Sigma-1 receptors at galactosylceramide-enriched lipid microdomains regulate oligodendrocyte differentiation. *Proc. Natl. Acad. Sci. U. S. A.* **101**, 14949–14954 (2004).

26. Gebreselassie, D. & Bowen, W. D. Sigma-2 receptors are specifically localized to lipid rafts in rat liver membranes. *Eur. J. Pharmacol.* **493**, 19–28 (2004).

27. Aydar, E., Palmer, C. P., Klyachko, V. A. & Jackson, M. B. The sigma receptor as a ligand-regulated auxiliary potassium channel subunit. *Neuron* **34**, 399–410 (2002).

28. Schmidt, H. R. *et al.* Crystal structure of the human σ1 receptor. *Nature* **532**, 527–530 (2016).

29. Schmidt, H. R., Betz, R. M., Dror, R. O. & Kruse, A. C. Structural basis for σ1 receptor ligand recognition. *Nat. Struct. Mol. Biol.* **25**, 981–987 (2018).

30. Ramachandran, S., Lu, H., Prabhu, U. & Ruoho, A. E. Purification and characterization of the guinea pig sigma-1 receptor functionally expressed in Escherichia coli. *Protein Expr. Purif.* **51**, 283–292 (2007).

31. Gromek, K. A. *et al.* The oligomeric states of the purified sigma-1 receptor are stabilized by ligands. *J. Biol. Chem.* **289**, 20333–20344 (2014).

32. Mishra, A. K. *et al.* The sigma-1 receptors are present in monomeric and oligomeric forms in living cells in the presence and absence of ligands. *Biochem. J.* **466**, 263–271 (2015).

33. Smith, S. B. & Su, T.-P. *Sigma receptors: their role in disease and as therapeutic targets*. (2017).

34. Srivats, S. *et al.* Sigma1 receptors inhibit store-operated Ca $^{2+}$ entry by attenuating coupling of STIM1 to Orai1. *J. Cell Biol.* **213**, 65–79 (2016).

35. Pal, A. *et al.* Identification of regions of the sigma-1 receptor ligand binding site using a novel photoprobe. *Mol. Pharmacol.* **72**, 921–933 (2007).

36. Al-Saif, A., Al-Mohanna, F. & Bohlega, S. A mutation in sigma-1 receptor causes juvenile amyotrophic lateral sclerosis. *Ann. Neurol.* **70**, 913–919 (2011).

37. Tagashira, H., Shinoda, Y., Shioda, N. & Fukunaga, K. Methyl pyruvate rescues mitochondrial damage caused by SIGMAR1 mutation related to amyotrophic lateral sclerosis. *Biochim. Biophys. Acta* **1840**, 3320–3334 (2014).

38. Jahn, H. Memory loss in Alzheimer's disease. *Dialogues Clin. Neurosci.* **15**, 445–454 (2013).

39. Kunitachi, S. *et al.* Phencyclidine-induced cognitive deficits in mice are ameliorated by subsequent subchronic administration of donepezil: role of sigma-1 receptors. *Brain Res.* **1279**, 189–196 (2009).

40. Ishima, T. & Hashimoto, K. Potentiation of nerve growth factor-induced neurite outgrowth in PC12 cells by ifenprodil: the role of sigma-1 and IP3 receptors. *PloS One* **7**, e37989 (2012).

41. Bem, W. T. *et al.* Overexpression of sigma receptors in nonneural human tumors. *Cancer Res.* **51**, 6558–6562 (1991).

42. Thomas, G. E. *et al.* Sigma and opioid receptors in human brain tumors. *Life Sci.* **46**, 1279–1286 (1990).

43. John, C. S., Bowen, W. D., Varma, V. M., McAfee, J. G. & Moody, T. W. Sigma receptors are expressed in human non-small cell lung carcinoma. *Life Sci.* **56**, 2385–2392 (1995).

44. Vilner, B. J., John, C. S. & Bowen, W. D. Sigma-1 and sigma-2 receptors are expressed in a wide variety of human and rodent tumor cell lines. *Cancer Res.* **55**, 408–413 (1995).

45. Crawford, K. W. & Bowen, W. D. Sigma-2 receptor agonists activate a novel apoptotic pathway and potentiate antineoplastic drugs in breast tumor cell lines. *Cancer Res.* **62**, 313–322 (2002).

46. Moody, T. W., Leyton, J. & John, C. Sigma ligands inhibit the growth of small cell lung cancer cells. *Life Sci.* **66**, 1979–1986 (2000).

47. Aydar, E., Onganer, P., Perrett, R., Djamgoz, M. B. & Palmer, C. P. The expression and functional characterization of sigma (sigma) 1 receptors in breast cancer cell lines. *Cancer Lett.* **242**, 245–257 (2006).

48. Hayashi, T. The Sigma-1 Receptor in Cellular Stress Signaling. *Front. Neurosci.* **13**, 733 (2019).

49. Romero, L. & Portillo-Salido, E. Trends in Sigma-1 Receptor Research: A 25-Year Bibliometric Analysis. *Front. Pharmacol.* **10**, 564 (2019).

50. Gething, M.-J. Role and regulation of the ER chaperone BiP. *Semin. Cell Dev. Biol.* **10**, 465–472 (1999).

51. Lièvremont, J.-P., Rizzuto, R., Hendershot, L. & Meldolesi, J. BiP, a Major Chaperone Protein of the Endoplasmic Reticulum Lumen, Plays a Direct and Important Role in the Storage of the Rapidly Exchanging Pool of $Ca^{2+}$. *J. Biol. Chem.* **272**, 30873–30879 (1997).

52. Brailoiu, E. *et al.* Choline Is an Intracellular Messenger Linking Extracellular Stimuli to IP3-Evoked Ca2+ Signals through Sigma-1 Receptors. *Cell Rep.* **26**, 330-337.e4 (2019).

53. Hayashi, T., Rizzuto, R., Hajnoczky, G. & Su, T.-P. MAM: more than just a housekeeper. *Trends Cell Biol.* **19**, 81–88 (2009).

54. Ali, M. M. U. *et al.* Structure of the Ire1 autophosphorylation complex and implications for the unfolded protein response. *EMBO J.* **30**, 894–905 (2011).

55. Iwawaki, T. *et al.* Translational control by the ER transmembrane kinase/ribonuclease IRE1 under ER stress. *Nat. Cell Biol.* **3**, 158–164 (2001).

56. Mori, T., Hayashi, T., Hayashi, E. & Su, T.-P. Sigma-1 receptor chaperone at the ER-mitochondrion interface mediates the mitochondrion-ER-nucleus signaling for cellular survival. *PloS One* **8**, e76941 (2013).

57. Chen, Y.-J., Quintanilla, C. G. & Liou, J. Recent insights into mammalian ER–PM junctions. *Curr. Opin. Cell Biol.* **57**, 99–105 (2019).

58. Hsieh, T.-S., Chen, Y.-J., Chang, C.-L., Lee, W.-R. & Liou, J. Cortical actin contributes to spatial organization of ER-PM junctions. *Mol. Biol. Cell* **28**, 3171–3180 (2017).

59. Hayashi, T. & Su, T.-P. Intracellular Dynamics of σ-1 Receptors ($\sigma_1$ Binding Sites) in NG108-15 Cells. *J. Pharmacol. Exp. Ther.* **306**, 726–733 (2003).

60. Mueller, B. H. *et al.* Sigma-1 receptor stimulation attenuates calcium influx through activated L-type Voltage Gated Calcium Channels in purified retinal ganglion cells. *Exp. Eye Res.* **107**, 21–31 (2013).

61. Pabba, M. *et al.* NMDA Receptors Are Upregulated and Trafficked to the Plasma Membrane after Sigma-1 Receptor Activation in the Rat Hippocampus. *J. Neurosci.* **34**, 11325–11338 (2014).

62. Kinoshita, M., Matsuoka, Y., Suzuki, T., Mirrielees, J. & Yang, J. Sigma-1 receptor alters the kinetics of Kv1.3 voltage gated potassium channels but not the sensitivity to receptor ligands. *Brain Res.* **1452**, 1–9 (2012).

63. Jean-Yves, L. *et al.* Voltage-Gated Ion Channels, New Targets in Anti-Cancer Research. *Recent Patents Anticancer Drug Discov.* **2**, 189–202 (2007).

64. Balasuriya, D. *et al.* The sigma-1 receptor binds to the Nav1.5 voltage-gated Na+ channel with 4-fold symmetry. *J. Biol. Chem.* **287**, 37021–37029 (2012).

65. Cheng, Z.-X. *et al.* Neurosteroid dehydroepiandrosterone sulphate inhibits persistent sodium currents in rat medial prefrontal cortex via activation of sigma-1 receptors. *Exp. Neurol.* **210**, 128–136 (2008).

66. Morales-Lázaro, S. L., González-Ramírez, R. & Rosenbaum, T. Molecular Interplay Between the Sigma-1 Receptor, Steroids, and Ion Channels. *Front. Pharmacol.* **10**, 419 (2019).

67. Balasuriya, D. *et al.* A direct interaction between the sigma-1 receptor and the hERG voltage-gated K+ channel revealed by atomic force microscopy and homogeneous time-resolved fluorescence (HTRF®). *J. Biol. Chem.* **289**, 32353–32363 (2014).

68. Crottès, D. *et al.* Sig1R Protein Regulates hERG Channel Expression through a Post-translational Mechanism in Leukemic Cells. *J. Biol. Chem.* **286**, 27947–27958 (2011).

69. Martina, M., Turcotte, M.-E. B., Halman, S. & Bergeron, R. The sigma-1 receptor modulates NMDA receptor synaptic transmission and plasticity via SK channels in rat hippocampus. *J. Physiol.* **578**, 143–157 (2007).

70. Zhang, H. & Cuevas, J. Sigma receptors inhibit high-voltage-activated calcium channels in rat sympathetic and parasympathetic neurons. *J. Neurophysiol.* **87**, 2867–2879 (2002).

71. Cataldi, M. The changing landscape of voltage-gated calcium channels in neurovascular disorders and in neurodegenerative diseases. *Curr. Neuropharmacol.* **11**, 276–297 (2013).

72. Mattson, M. P. Calcium and neurodegeneration. *Aging Cell* **6**, 337–350 (2007).

73. Zündorf, G. & Reiser, G. Calcium dysregulation and homeostasis of neural calcium in the molecular mechanisms of neurodegenerative diseases provide multiple targets for neuroprotection. *Antioxid. Redox Signal.* **14**, 1275–1288 (2011).

74. Hansen, K. B. *et al.* Structure, function, and allosteric modulation of NMDA receptors. *J. Gen. Physiol.* **150**, 1081–1105 (2018).

75. Monnet, F. P., Debonnel, G., Bergeron, R., Gronier, B. & de Montigny, C. The effects of sigma ligands and of neuropeptide Y on N-methyl-D-aspartate-induced neuronal activation of CA3 dorsal hippocampus neurones are differentially affected by pertussin toxin. *Br. J. Pharmacol.* **112**, 709–715 (1994).

76. Balasuriya, D., Stewart, A. P. & Edwardson, J. M. The σ-1 receptor interacts directly with GluN1 but not GluN2A in the GluN1/GluN2A NMDA receptor. *J. Neurosci. Off. J. Soc. Neurosci.* **33**, 18219–18224 (2013).

77. Maurice, T., Roman, F. J. & Privat, A. Modulation by neurosteroids of the in vivo (+)-[3H]SKF-10,047 binding to sigma 1 receptors in the mouse forebrain. *J. Neurosci. Res.* **46**, 734–743 (1996).

78. Berridge, M. J. Elementary and global aspects of calcium signalling. *J. Physiol.* **499**, 291–306 (1997).

79. Berridge, M. J., Lipp, P. & Bootman, M. D. The versatility and universality of calcium signalling. *Nat. Rev. Mol. Cell Biol.* **1**, 11–21 (2000).

80. Bojarski, L., Herms, J. & Kuznicki, J. Calcium dysregulation in Alzheimer's disease. *Neurochem. Int.* **52**, 621–633 (2008).

81. Schapira, A. H. V. Calcium dysregulation in Parkinson's disease. *Brain J. Neurol.* **136**, 2015–2016 (2013).

82. Kolobkova, Y. A., Vigont, V. A., Shalygin, A. V. & Kaznacheyeva, E. V. Huntington's Disease: Calcium Dyshomeostasis and Pathology Models. *Acta Naturae* **9**, 34–46 (2017).

83. Leal, S. S. & Gomes, C. M. Calcium dysregulation links ALS defective proteins and motor neuron selective vulnerability. *Front. Cell. Neurosci.* **9**, (2015).

84. Stewart, T. A., Yapa, K. T. D. S. & Monteith, G. R. Altered calcium signaling in cancer cells. *Biochim. Biophys. Acta BBA - Biomembr.* **1848**, 2502–2511 (2015).

85. Ashby, M. C. & Tepikin, A. V. ER calcium and the functions of intracellular organelles. *Semin. Cell Dev. Biol.* **12**, 11–17 (2001).

86. Clapham, D. E. Calcium signaling. *Cell* **131**, 1047–1058 (2007).

87. Putney, J. W. A model for receptor-regulated calcium entry. *Cell Calcium* **7**, 1–12 (1986).

88. Putney, J. W. Capacitative calcium entry revisited. *Cell Calcium* **11**, 611–624 (1990).

89. Soboloff, J., Rothberg, B. S., Madesh, M. & Gill, D. L. STIM proteins: dynamic calcium signal transducers. *Nat. Rev. Mol. Cell Biol.* **13**, 549–565 (2012).

90. Hoth, M. & Penner, R. Depletion of intracellular calcium stores activates a calcium current in mast cells. *Nature* **355**, 353–356 (1992).

91. Liou, J. *et al.* STIM is a Ca2+ sensor essential for Ca2+-store-depletion-triggered Ca2+ influx. *Curr. Biol. CB* **15**, 1235–1241 (2005).

92. Roos, J. *et al.* STIM1, an essential and conserved component of store-operated Ca2+ channel function. *J. Cell Biol.* **169**, 435–445 (2005).

93. Feske, S. *et al.* A mutation in Orai1 causes immune deficiency by abrogating CRAC channel function. *Nature* **441**, 179–185 (2006).

94. Vig, M. *et al.* CRACM1 multimers form the ion-selective pore of the CRAC channel. *Curr. Biol. CB* **16**, 2073–2079 (2006).

95. Yeromin, A. V. *et al.* Molecular identification of the CRAC channel by altered ion selectivity in a mutant of Orai. *Nature* **443**, 226–229 (2006).

96. Moccia, F. *et al.* Stim and Orai proteins in neuronal Ca(2+) signaling and excitability. *Front. Cell. Neurosci.* **9**, 153 (2015).

97. Williams, R. T. *et al.* Identification and characterization of the STIM (stromal interaction molecule) gene family: coding for a novel class of transmembrane proteins. *Biochem. J.* **357**, 673–685 (2001).

98. Berna-Erro, A., Jardin, I., Salido, G. M. & Rosado, J. A. Role of STIM2 in cell function and physiopathology. *J. Physiol.* **595**, 3111–3128 (2017).

99. Oritani, K. & Kincade, P. W. Identification of stromal cell products that interact with pre-B cells. *J. Cell Biol.* **134**, 771–782 (1996).

100. Dziadek, M. A. & Johnstone, L. S. Biochemical properties and cellular localisation of STIM proteins. *Cell Calcium* **42**, 123–132 (2007).

101. Hauser, C. T. & Tsien, R. Y. A hexahistidine-Zn2+-dye label reveals STIM1 surface exposure. *Proc. Natl. Acad. Sci. U. S. A.* **104**, 3693–3697 (2007).

102. Zheng, L. *et al.* Auto-inhibitory role of the EF-SAM domain of STIM proteins in store-operated calcium entry. *Proc. Natl. Acad. Sci. U. S. A.* **108**, 1337–1342 (2011).

103. Derler, I., Jardin, I. & Romanin, C. Molecular mechanisms of STIM/Orai communication. *Am. J. Physiol. Cell Physiol.* **310**, C643-662 (2016).

104. Bhardwaj, R., Hediger, M. A. & Demaurex, N. Redox modulation of STIM-ORAI signaling. *Cell Calcium* **60**, 142–152 (2016).

105. Park, C. Y. *et al.* STIM1 Clusters and Activates CRAC Channels via Direct Binding of a Cytosolic Domain to Orai1. *Cell* **136**, 876–890 (2009).

106. Hirve, N., Rajanikanth, V., Hogan, P. G. & Gudlur, A. Coiled-Coil Formation Conveys a STIM1 Signal from ER Lumen to Cytoplasm. *Cell Rep.* **22**, 72–83 (2018).

107. Hoth, M. & Niemeyer, B. A. The neglected CRAC proteins: Orai2, Orai3, and STIM2. *Curr. Top. Membr.* **71**, 237–271 (2013).

108. Luik, R. M., Wang, B., Prakriya, M., Wu, M. M. & Lewis, R. S. Oligomerization of STIM1 couples ER calcium depletion to CRAC channel activation. *Nature* **454**, 538–542 (2008).

109. Prakriya, M. & Lewis, R. S. Store-Operated Calcium Channels. *Physiol. Rev.* **95**, 1383–1436 (2015).

110. Carrasco, S. & Meyer, T. STIM proteins and the endoplasmic reticulum-plasma membrane junctions. *Annu. Rev. Biochem.* **80**, 973–1000 (2011).

111. Parvez, S. *et al.* STIM2 protein mediates distinct store-dependent and store-independent modes of CRAC channel activation. *FASEB J. Off. Publ. Fed. Am. Soc. Exp. Biol.* **22**, 752–761 (2008).

112. Brandman, O., Liou, J., Park, W. S. & Meyer, T. STIM2 is a feedback regulator that stabilizes basal cytosolic and endoplasmic reticulum Ca2+ levels. *Cell* **131**, 1327–1339 (2007).

113. Soboloff, J. *et al.* Orai1 and STIM reconstitute store-operated calcium channel function. *J. Biol. Chem.* **281**, 20661–20665 (2006).

114. Berna-Erro, A. *et al.* STIM2 regulates capacitive Ca2+ entry in neurons and plays a key role in hypoxic neuronal cell death. *Sci. Signal.* **2**, ra67 (2009).

115. Bollimuntha, S., Pani, B. & Singh, B. B. Neurological and Motor Disorders: Neuronal Store-Operated Ca2+ Signaling: An Overview and Its Function. *Adv. Exp. Med. Biol.* **993**, 535–556 (2017).

116. Miederer, A.-M. *et al.* A STIM2 splice variant negatively regulates store-operated calcium entry. *Nat. Commun.* **6**, 6899 (2015).

117. Zhou, Y. *et al.* Cross-linking of Orai1 channels by STIM proteins. *Proc. Natl. Acad. Sci. U. S. A.* **115**, E3398–E3407 (2018).

118. Hou, X., Pedi, L., Diver, M. M. & Long, S. B. Crystal structure of the calcium release-activated calcium channel Orai. *Science* **338**, 1308–1313 (2012).

119. Balasuriya, D., Srivats, S., Murrell-Lagnado, R. D. & Edwardson, J. M. Atomic force microscopy (AFM) imaging suggests that stromal interaction molecule 1 (STIM1) binds to Orai1 with sixfold symmetry. *FEBS Lett.* **588**, 2874–2880 (2014).

120. Yen, M., Lokteva, L. A. & Lewis, R. S. Functional Analysis of Orai1 Concatemers Supports a Hexameric Stoichiometry for the CRAC Channel. *Biophys. J.* **111**, 1897–1907 (2016).

121. Alansary, D., Bogeski, I. & Niemeyer, B. A. Facilitation of Orai3 targeting and store-operated function by Orai1. *Biochim. Biophys. Acta BBA - Mol. Cell Res.* **1853**, 1541–1550 (2015).

122. Vaeth, M. *et al.* ORAI2 modulates store-operated calcium entry and T cell-mediated immunity. *Nat. Commun.* **8**, 14714 (2017).

123. Wang, Y. *et al.* STIM protein coupling in the activation of Orai channels. *Proc. Natl. Acad. Sci.* **106**, 7391–7396 (2009).

124. Penna, A. *et al.* The CRAC channel consists of a tetramer formed by Stim-induced dimerization of Orai dimers. *Nature* **456**, 116–120 (2008).

125. Wettschureck, N. & Offermanns, S. Mammalian G proteins and their cell type specific functions. *Physiol. Rev.* **85**, 1159–1204 (2005).

126. Yen, M. & Lewis, R. S. Numbers count: How STIM and Orai stoichiometry affect store-operated calcium entry. *Cell Calcium* **79**, 35–43 (2019).

127. Lang, S. *et al.* Sec61 complexes form ubiquitous ER $Ca^{2+}$ leak channels. *Channels* **5**, 228–235 (2011).

128. Supnet, C. & Bezprozvanny, I. Presenilins as endoplasmic reticulum calcium leak channels and Alzheimer's disease pathogenesis. *Sci. China Life Sci.* **54**, 744–751 (2011).

129. Manjarrés, I. M., Rodríguez-García, A., Alonso, M. T. & García-Sancho, J. The sarco/endoplasmic reticulum Ca(2+) ATPase (SERCA) is the third element in capacitative calcium entry. *Cell Calcium* **47**, 412–418 (2010).

130. Zweifach, A. & Lewis, R. S. Slow calcium-dependent inactivation of depletion-activated calcium current. Store-dependent and -independent mechanisms. *J. Biol. Chem.* **270**, 14445–14451 (1995).

131. Palty, R., Raveh, A., Kaminsky, I., Meller, R. & Reuveny, E. SARAF inactivates the store operated calcium entry machinery to prevent excess calcium refilling. *Cell* **149**, 425–438 (2012).

132. Maléth, J., Choi, S., Muallem, S. & Ahuja, M. Translocation between PI(4,5)P2-poor and PI(4,5)P2-rich microdomains during store depletion determines STIM1 conformation and Orai1 gating. *Nat. Commun.* **5**, 5843 (2014).

133. Li, X. *et al.* Calmodulin dissociates the STIM1-Orai1 complex and STIM1 oligomers. *Nat. Commun.* **8**, 1042 (2017).

134. Smyth, J. T. *et al.* Activation and regulation of store-operated calcium entry. *J. Cell. Mol. Med.* **14**, 2337–2349 (2010).

135. Ambudkar, I. S., de Souza, L. B. & Ong, H. L. TRPC1, Orai1, and STIM1 in SOCE: Friends in tight spaces. *Cell Calcium* **63**, 33–39 (2017).

136. Kim, M. S. *et al.* Native Store-operated Ca2+ Influx Requires the Channel Function of Orai1 and TRPC1. *J. Biol. Chem.* **284**, 9733–9741 (2009).

137. Huang, G. N. *et al.* STIM1 carboxyl-terminus activates native SOC, I(crac) and TRPC1 channels. *Nat. Cell Biol.* **8**, 1003–1010 (2006).

138. Cheng, K. T., Liu, X., Ong, H. L. & Ambudkar, I. S. Functional requirement for Orai1 in store-operated TRPC1-STIM1 channels. *J. Biol. Chem.* **283**, 12935–12940 (2008).

139. Majewski, L. & Kuznicki, J. SOCE in neurons: Signaling or just refilling? *Biochim. Biophys. Acta* **1853**, 1940–1952 (2015).

140. Feske, S., Prakriya, M., Rao, A. & Lewis, R. S. A severe defect in CRAC Ca2+ channel activation and altered K+ channel gating in T cells from immunodeficient patients. *J. Exp. Med.* **202**, 651–662 (2005).

141. Lacruz, R. S. & Feske, S. Diseases caused by mutations in ORAI1 and STIM1. *Ann. N. Y. Acad. Sci.* **1356**, 45–79 (2015).

142. Maus, M. *et al.* Missense mutation in immunodeficient patients shows the multifunctional roles of coiled-coil domain 3 (CC3) in STIM1 activation. *Proc. Natl. Acad. Sci. U. S. A.* **112**, 6206–6211 (2015).

143. Han, K. A., Rothberg, P. & Kulesz-Martin, M. Altered levels of endogenous retrovirus-like sequence (VL30) RNA during mouse epidermal cell carcinogenesis. *Mol. Carcinog.* **3**, 75–82 (1990).

144. Flourakis, M. *et al.* Orai1 contributes to the establishment of an apoptosis-resistant phenotype in prostate cancer cells. *Cell Death Dis.* **1**, e75 (2010).

145. Schmidt, S. *et al.* Enhanced Orai1 and STIM1 expression as well as store operated Ca2+ entry in therapy resistant ovary carcinoma cells. *Oncotarget* **5**, 4799–4810 (2014).

146. Zhang, Z. *et al.* STIM1, a direct target of microRNA-185, promotes tumor metastasis and is associated with poor prognosis in colorectal cancer. *Oncogene* **34**, 4808–4820 (2015).

147. Yang, S., Zhang, J. J. & Huang, X.-Y. Orai1 and STIM1 are critical for breast tumor cell migration and metastasis. *Cancer Cell* **15**, 124–134 (2009).

148. Li, G. *et al.* Suppression of STIM1 inhibits human glioblastoma cell proliferation and induces G0/G1 phase arrest. *J. Exp. Clin. Cancer Res. CR* **32**, 20 (2013).

149. Hartmann, J. *et al.* STIM1 controls neuronal $Ca^{2+}$ signaling, mGluR1-dependent synaptic transmission, and cerebellar motor behavior. *Neuron* **82**, 635–644 (2014).

150. Baba, A. *et al.* Activity-Evoked Capacitative Ca2Ƨ Entry: Implications in Synaptic Plasticity. 5.

151. Samtleben, S., Wachter, B. & Blum, R. Store-operated calcium entry compensates fast ER calcium loss in resting hippocampal neurons. *Cell Calcium* **58**, 147–159 (2015).

152. Klejman, M. E. *et al.* Expression of STIM1 in brain and puncta-like co-localization of STIM1 and ORAI1 upon depletion of Ca2+ store in neurons. *Neurochem. Int.* **54**, 49–55 (2009).

153. Vlachos, A. *et al.* Synaptopodin regulates plasticity of dendritic spines in hippocampal neurons. *J. Neurosci. Off. J. Soc. Neurosci.* **29**, 1017–1033 (2009).

154. Ng, A. N., Krogh, M. & Toresson, H. Dendritic EGFP-STIM1 activation after type I metabotropic glutamate and muscarinic acetylcholine receptor stimulation in hippocampal neuron. *J. Neurosci. Res.* **89**, 1235–1244 (2011).

155. Garcia-Alvarez, G. *et al.* Impaired spatial memory and enhanced long-term potentiation in mice with forebrain-specific ablation of the Stim genes. *Front. Behav. Neurosci.* **9**, 180 (2015).

156. Zhang, H. *et al.* Store-Operated Calcium Channel Complex in Postsynaptic Spines: A New Therapeutic Target for Alzheimer's Disease Treatment. *J. Neurosci. Off. J. Soc. Neurosci.* **36**, 11837–11850 (2016).

157. Popugaeva, E. *et al.* STIM2 protects hippocampal mushroom spines from amyloid synaptotoxicity. *Mol. Neurodegener.* **10**, 37 (2015).

158. Brailoiu, G. C. *et al.* Cocaine inhibits store-operated Ca2+ entry in brain microvascular endothelial cells: critical role for sigma-1 receptors. *Biochem. J.* **473**, 1–5 (2016).

159. Dreser, A. *et al.* The ALS-linked E102Q mutation in Sigma receptor-1 leads to ER stress-mediated defects in protein homeostasis and dysregulation of RNA-binding proteins. *Cell Death Differ.* **24**, 1655–1671 (2017).

160. ViraPower™ BacMam Expression System and BacMam pCMV-DEST Vector Kit MANUAL. (2014).

161. Kar, P., Nelson, C. & Parekh, A. B. Selective activation of the transcription factor NFAT1 by calcium microdomains near Ca2+ release-activated Ca2+ (CRAC) channels. *J. Biol. Chem.* **286**, 14795–14803 (2011).

162. Chen, T.-W. *et al.* Ultrasensitive fluorescent proteins for imaging neuronal activity. *Nature* **499**, 295–300 (2013).

163. Willoughby, D. *et al.* Direct binding between Orai1 and AC8 mediates dynamic interplay between Ca2+ and cAMP signaling. *Sci. Signal.* **5**, ra29 (2012).

164. Saraiva, N. *et al.* hGAAP promotes cell adhesion and migration via the stimulation of store-operated $Ca^{2+}$ entry and calpain 2. *J. Cell Biol.* **202**, 699 (2013).

165. Grynkiewicz, G., Poenie, M. & Tsien, R. Y. A new generation of Ca2+ indicators with greatly improved fluorescence properties. *J. Biol. Chem.* **260**, 3440–3450 (1985).

166. Minta, A., Kao, J. P. & Tsien, R. Y. Fluorescent indicators for cytosolic calcium based on rhodamine and fluorescein chromophores. *J. Biol. Chem.* **264**, 8171–8178 (1989).

167. Tsien, R. Y. A non-disruptive technique for loading calcium buffers and indicators into cells. *Nature* **290**, 527–528 (1981).

168. Lock, J. T., Parker, I. & Smith, I. F. A comparison of fluorescent $Ca^{2+}$ indicators for imaging local $Ca^{2+}$ signals in cultured cells. *Cell Calcium* **58**, 638–648 (2015).

169. Paredes, R. M., Etzler, J. C., Watts, L. T., Zheng, W. & Lechleiter, J. D. Chemical calcium indicators. *Methods San Diego Calif* **46**, 143–151 (2008).

170. Kim, D. S., Jayaraman, V., Looger, L. L. & Svoboda, K. Engineering Fluorescent Calcium Sensor Proteins for Imaging Neural Activity. 11 (2014).

171. Badura, A., Sun, X. R., Giovannucci, A., Lynch, L. A. & Wang, S. S.-H. Fast calcium sensor proteins for monitoring neural activity. *Neurophotonics* **1**, 025008 (2014).

172. Kost, T. A., Condreay, J. P., Ames, R. S., Rees, S. & Romanos, M. A. Implementation of BacMam virus gene delivery technology in a drug discovery setting. *Drug Discov. Today* **12**, 396–403 (2007).

173. Condreay, J. P. *et al.* Baculoviruses and mammalian cell-based assays for drug screening. *Adv. Virus Res.* **68**, 255–286 (2006).

174. Graham, F. L., Smiley, J., Russell, W. C. & Nairn, R. Characteristics of a Human Cell Line Transformed by DNA from Human Adenovirus Type 5. *J. Gen. Virol.* **36**, 59–72 (1977).

175. Cusick, J. K., Mustian, A., Goldberg, K. & Reyland, M. E. RELT induces cellular death in HEK 293 epithelial cells. *Cell. Immunol.* **261**, 1–8 (2010).

176. Stepanenko, A. A. & Dmitrenko, V. V. HEK293 in cell biology and cancer research: phenotype, karyotype, tumorigenicity, and stress-induced genome-phenotype evolution. *Gene* **569**, 182–190 (2015).

177. Shaw, G., Morse, S., Ararat, M. & Graham, F. L. Preferential transformation of human neuronal cells by human adenoviruses and the origin of HEK 293 cells. *FASEB J.* **16**, 869–871 (2002).

178. Lin, Y.-C. *et al.* Genome dynamics of the human embryonic kidney 293 lineage in response to cell biology manipulations. *Nat. Commun.* **5**, (2014).

179. Thomas, P. & Smart, T. G. HEK293 cell line: A vehicle for the expression of recombinant proteins. *J. Pharmacol. Toxicol. Methods* **51**, 187–200 (2005).

180. Muñoz, E. *et al.* Nonsteroidal anti-inflammatory drugs inhibit vascular smooth muscle cell proliferation by enabling the Ca2+-dependent inactivation of calcium release-activated calcium/orai channels normally prevented by mitochondria. *J. Biol. Chem.* **286**, 16186–16196 (2011).

181. Thillaiappan, N. B., Chavda, A. P., Tovey, S. C., Prole, D. L. & Taylor, C. W. Ca2+ signals initiate at immobile IP3 receptors adjacent to ER-plasma membrane junctions. *Nat. Commun.* **8**, (2017).

182. Sampieri, A., Santoyo, K., Asanov, A. & Vaca, L. Association of the IP3R to STIM1 provides a reduced intraluminal calcium microenvironment, resulting in enhanced store-operated calcium entry. *Sci. Rep.* **8**, (2018).

183. Nelson, H. A., Leech, C. A., Kopp, R. F. & Roe, M. W. Interplay between ER Ca2+ Binding Proteins, STIM1 and STIM2, Is Required for Store-Operated Ca2+ Entry. *Int. J. Mol. Sci.* **19**, (2018).

184. Macian, F. NFAT proteins: key regulators of T-cell development and function. *Nat. Rev. Immunol.* **5**, 472–484 (2005).

185. Feske, S., Draeger, R., Peter, H. H., Eichmann, K. & Rao, A. The duration of nuclear residence of NFAT determines the pattern of cytokine expression in human SCID T cells. *J. Immunol. Baltim. Md 1950* **165**, 297–305 (2000).

186. Su, T.-P., Su, T.-C., Nakamura, Y. & Tsai, S.-Y. The Sigma-1 Receptor as a Pluripotent Modulator in Living Systems. *Trends Pharmacol. Sci.* **37**, 262–278 (2016).

187. Poteser, M. *et al.* PKC-dependent coupling of calcium permeation through transient receptor potential canonical 3 (TRPC3) to calcineurin signaling in HL-1 myocytes. *Proc. Natl. Acad. Sci.* **108**, 10556 (2011).

188. Marasco, C. C. *et al.* Systems-level view of cocaine addiction: the interconnection of the immune and nervous systems. *Exp. Biol. Med. Maywood NJ* **239**, 1433–1442 (2014).

189. Schäuble, N. *et al.* BiP-mediated closing of the Sec61 channel limits Ca2+ leakage from the ER. *EMBO J.* **31**, 3282–3296 (2012).

190. Okeke, E., Dingsdale, H., Parker, T., Voronina, S. & Tepikin, A. V. Endoplasmic reticulum-plasma membrane junctions: structure, function and dynamics. *J. Physiol.* **594**, 2837–2847 (2016).

191. Hogan, P. G. The STIM1-ORAI1 microdomain. *Cell Calcium* **58**, 357–367 (2015).

192. Berridge, M. J. Calcium microdomains: organization and function. *Cell Calcium* **40**, 405–412 (2006).

193. Dynes, J. L., Amcheslavsky, A. & Cahalan, M. D. Genetically targeted single-channel optical recording reveals multiple Orai1 gating states and oscillations in calcium influx. *Proc. Natl. Acad. Sci. U. S. A.* **113**, 440–445 (2016).

194. Sanderson, M. J., Smith, I., Parker, I. & Bootman, M. D. Fluorescence Microscopy. *Cold Spring Harb. Protoc.* **2014**, pdb.top071795-pdb.top071795 (2014).

195. Dorostkar, M. M., Dreosti, E., Odermatt, B. & Lagnado, L. Computational processing of optical measurements of neuronal and synaptic activity in networks. *J. Neurosci. Methods* **188**, 141–150 (2010).

196. Burger, W. & Burge, M. J. *Principles of digital image processing. 3: Advanced methods*. (Springer, 2013).

197. Mattheyses, A. L., Simon, S. M. & Rappoport, J. Z. Imaging with total internal reflection fluorescence microscopy for the cell biologist. *J. Cell Sci.* **123**, 3621–3628 (2010).

198. Martin-Fernandez, M. L., Tynan, C. J. & Webb, S. E. D. A 'pocket guide' to total internal reflection fluorescence: A 'POCKET GUIDE' TO TOTAL INTERNAL REFLECTION FLUORESCENCE. *J. Microsc.* **252**, 16–22 (2013).

199. Cai, X. *et al.* Pore properties of Orai1 calcium channel dimers and their activation by the STIM1 ER calcium sensor. *J. Biol. Chem.* **293**, 12962–12974 (2018).

200. Thompson, J. L., Mignen, O. & Shuttleworth, T. J. The Orai1 severe combined immune deficiency mutation and calcium release-activated Ca2+ channel function in the heterozygous condition. *J. Biol. Chem.* **284**, 6620–6626 (2009).

201. Gwack, Y. *et al.* Biochemical and Functional Characterization of Orai Proteins. *J. Biol. Chem.* **282**, 16232–16243 (2007).

202. Pabba, M. & Sibille, E. Sigma-1 and N-Methyl-d-Aspartate Receptors: A Partnership with Beneficial Outcomes. *Mol. Neuropsychiatry* **1**, 47–51 (2015).

203. Watanabe, S. *et al.* Mitochondria-associated membrane collapse is a common pathomechanism in SIGMAR1- and SOD1-linked ALS. *EMBO Mol. Med.* **8**, 1421–1437 (2016).

204. Rana, A. *et al.* Alternative splicing converts STIM2 from an activator to an inhibitor of store-operated calcium channels. *J. Cell Biol.* **209**, 653–669 (2015).

205. Serwach, K. & Gruszczynska-Biegala, J. STIM Proteins and Glutamate Receptors in Neurons: Role in Neuronal Physiology and Neurodegenerative Diseases. *Int. J. Mol. Sci.* **20**, (2019).

206. Albarran, L. *et al.* Dynamic interaction of SARAF with STIM1 and Orai1 to modulate store-operated calcium entry. *Sci. Rep.* **6**, 24452 (2016).